GCOS
Reference
Upper-
Air
Network

GRUAN Technical Document

Technical characteristics and GRUAN data processing for the Meisei RS-11G and iMS-100 radiosondes

Nobuhiko Kizu, Takuji Sugidachi, Eriko Kobayashi, Shunsuke Hoshino, Kensaku Shimizu, Ryota Maeda and Masatomo Fujiwara

Publisher
GRUAN Lead Centre

Number & Version
GRUAN-TD-5
Rev 1.0 (2018-02-21)

Document info

Title:	*Technical characteristics and GRUAN data processing for the Meisei RS-11G and iMS-100 radiosondes*
Topic:	Data product
Authors:	Nobuhiko Kizu, Takuji Sugidachi, Eriko Kobayashi, Shunsuke Hoshino, Kensaku Shimizu, Ryota Maeda and Masatomo Fujiwara
Publisher:	GRUAN Lead Centre, DWD
Document type:	Technical Document
Document number:	GRUAN-TD-5
Page count:	152
Version:	Rev 1.0 (2018-02-21)

Abstract

The GCOS (Global Climate Observing System) Reference Upper-Air Network (GRUAN) data processing for the Meisei RS-11G and iMS-100 radiosondes has been developed to meet the criteria for reference measurements. Since July 2013, the RS-11G radiosonde has been regularly launched at Tateno (36.06°N, 140.13°E, 25.2 m; Aerological Observatory of the Japan Meteorological Agency), Japan. Also, a smaller version, the Meisei iMS-100 radiosonde has been developed, with the same sensors as those of the RS-11G radiosonde, and will be used at Tateno in the future. This technical document describes the algorithms including the corrections to obtain pressure (or geopotential height), temperature, relative humidity (RH), and horizontal wind data from the RS-11G and iMS-100 radiosonde raw data. It also discusses the uncertainty evaluation for each variable obtained from these radiosondes. The corrections compensate various known systematic biases, which are mainly the solar radiation error, calibration error, and heat spike error for the temperature measurements, and the dry biases due to solar heating, time-lag error, and calibration error at low temperature conditions for the RH measurements. The measurement uncertainty for each variable was evaluated by laboratory experiments and verified by comparison flights. The uncertainty for the temperature measurements is mainly determined by that of the corrections for the solar radiation error and calibration error. Its uncertainty increases with altitude, and reaches 0.8 K at 30 km. Up to ∼15 km, the calibration-error correction is the dominant factor to the total uncertainty of the temperature measurements, while in the stratosphere, the radiation correction is the dominant factor. Because the actual sounding conditions are different from the assumed condition (e.g., surface and cloud albedo), it is considered that additional information for each sounding, such as the cloud condition, is necessary to reduce the uncertainty. Also, the uncertainty due to heat spikes needs to be considered for particular flight configurations (e.g., the case with a shorter string of 15 m and a 600 g balloon). A large payload and a rig for multiple-payload sounding may introduce additional heat spikes and thus larger uncertainty. The uncertainty of the RH measurements is maximal around the tropopause because of the large and sudden change in RH between the wet troposphere and dry stratosphere and of the coldness there, leading to large time-lag correction component. The uncertainty from the calibration-error correction is relatively large at low temperatures because the evaluation is difficult there. Solar heating on the RH sensor leads to dry bias; thus, this bias is corrected by considering the difference between the sensor

temperature and air temperature. The uncertainty from the solar heating dry bias correction is derived from the sensor temperature measurement uncertainty (± 0.3 K). The sensor temperature is measured with the dedicated thermistor for the iMS-100, and is estimated by the solar radiation correction and thermal-lag for the RS-11G. There are other minor factors contributing to the total RH uncertainty, though they are currently not quantified. The hysteresis bias arises only when the RH changes from wet to dry. The contamination error causes wet biases only under rainy conditions, though its quantification is currently not possible because the RH reference measurements do not exist under rainy conditions. The uncertainty for the geopotential height is determined by the accuracy of the Global Positioning System (GPS) antenna and module in use (as the RS-11G and iMS-100 radiosondes are usually not equipped with a pressure sensor). The 3 dimensional error of the GPS for the RS-11G and iMS-100 is typically less than 10 m. The pressure is calculated from the GPS geopotential height using the relationship of the hydrostatic equation and thus using temperature and RH data. Therefore, the uncertainties in the GPS-based geopotential-height, temperature, and RH measurements propagate to the uncertainty of the pressure measurement. In addition, the uncertainty of surface pressure measurement affects the total pressure uncertainty. The geopotential-height uncertainty is the main factor for the pressure uncertainty at lower altitudes, while the temperature uncertainty is the main factor at higher altitudes. Also, the uncertainty of the surface pressure measurement contributes to the pressure uncertainty at all levels. The uncertainty (1σ) of the GPS Doppler speed measurements is less than 0.01 m s^{-1}, and thus this is not the main factor of the uncertainty for the GPS-based horizontal wind measurements. The main factor comes from the radiosonde pendulum motions during the flight. Such oscillations are removed by a software filter (in particular for operational sounding data). Because of this filtering, smaller-scale variabilities with the periods less than the pendulum period cannot be obtained. The period of the pendulum motion is 7.8 s for the string of 15 m length, and the uncertainty due to these oscillations are typically 1 – 3 m s^{-1}, being larger at higher altitudes.

Revision history

Version	Author / Editor	Description
Rev 1.0 (2018-02-21)	Nobuhiko Kizu, Takuji Sugidachi, Eriko Kobayashi, Shunsuke Hoshino, Kensaku Shimizu, Ryota Maeda and Masatomo Fujiwara	First published version as GRUAN Technical Document 5 (GRUAN-TD-5)

Table of Contents

1 Introduction

1.1 Motivation

Since the 1930s, routine radiosonde observations have been carried out in Japan, and it was 1957 when the radiosonde network in Japan was established by the JMA (*JMA*, 1975). These radiosonde data provide the longest record of upper air temperature, relative humidity (RH), geopotential height, pressure, and horizontal winds. These data have a great potential for climate research. However, the original radiosonde record contains various errors and biases because of changes in instrumentation and observational practices, which cause non-climate-related changes or inhomogeneities (e.g. *Seidel et al.*, 2009). This is because the original (and still current) motivation of the operational radiosonde observations was to support weather forecast activities. Such inhomogeneities in the data record have severely hampered the application of radiosonde data in climate studies.

The Global Climate Observing System (GCOS) Reference Upper Air Network (GRUAN) was established in 2008 to provide long-term and high-quality climate data records from the surface, through the troposphere, and into the stratosphere (*Seidel et al.*, 2009; *Bodeker et al.*, 2016). The primary goals of the GRUAN are to provide the GRUAN data product, that is, vertical profiles of reference measurements suitable for reliably detecting climate change on decadal time scales. To prevent the inhomogeneities by the instrumental change in the radiosonde record, the GRUAN data product must be open, documented in peer-reviewed literatures, traceable to SI (International System of Units) standards, and must contain best possible estimates of the measurement uncertainties. For operational upper-air observations from radiosondes, metadata are often incomplete. The GRUAN data product is expected to be the processed data together with the complete metadata (including raw data, and the information on the sonde type, software version, payload configuration, etc.).

The RS-11G and iMS-100 radiosondes have been recently developed by a Japanese company Meisei Electric Co. Ltd. The RS-11G radiosonde has been used at the Japan Meteorological Agency (JMA) operational stations including Tateno station which is a to-be-certified GRUAN site. The iMS-100 radiosonde is a smaller version of RS-11G, with the same sensors as those of RS-11G, and will be used at some JMA sites in the future. In this technical document, the technical details, processing algorithms, and uncertainty evaluation of the Meisei RS-11G and iMS-100 radiosondes will be explained, so that their data product would meet the criteria for a GRUAN data product. The rest of this chapter describes the historical overview of the operational radiosonde soundings in Japan (Chapter 1.2) and the JMA's contributions to the GRUAN (Chapter 1.3).

1.2 Historical overview of the operational radiosonde soundings in Japan

The technologies used in the RS-11G and iMS-100 radiosondes is a compilation of the technologies that Meisei (in collaboration with the JMA for many cases) has developed in the past $\sim$80 years. The main motivations of the development of the latest two radiosonde models are to produce an environmentally friendly, light-weight, and high-precision radiosonde. This section briefly describes the 80-year history of the technical development leading up to the latest two radiosonde models.

The routine radiosonde observations were started in June 1938 at three sites in Japan (*JMA*, 1975). At that time, the radiosonde called "Central Meteorological Observatory Type No.1" (also called as "S38 radiosonde", Central Meteorological Observatory (CMO) was the forerunner organization of JMA) was used, which consists of an aneroid type barometer (for pressure), bimetal thermometer (temperature), and hair hygrometer (humidity) (Figure 1.1). Each sensor has an independent transmitter, with the carrier radiowave frequency changing in accordance with changing values of each variable. After the World War II, the CMO was no longer able to manufacture the S38 type radiosonde. Therefore, the CMO decided to employ the Imperial Japanese Army's radiosonde called Type 3 Temperature and Humidity Transmitter (also called as S43 radiosonde, Figure 1.2). This radiosonde had been manufactured by Meisei during the World War II. This radiosonde was equipped with a mercury thermometer and also used three changing carrier frequencies similar to the S38 radiosonde. In 1947 CMO introduced the S43K radiosonde. The temperature sensor was replaced with a bimetal thermometer so that it became possible to measure temperatures below -60°C. The major problem of the S43 and S43K radiosondes is their wide bandwidth which results in interfering with other radiofrequencies. Therefore, the S48 radiosonde was developed in 1949 (Figure 1.3), whose carrier frequency was fixed at 27.7 MHz and whose data were transmitted by the Morse code. Thereafter, some minor changes were made: The carrier frequency was changed to 402 MHz in 1949 following the International Telecommunication Convention (the S49 radiosonde); the weight was reduced in 1950 (the S50 radiosonde, Figure 1.4); and the Morse code conversion board was improved in 1952 (the S52 radiosonde). During this time period, a rawinsonde (radar-wind sonde) system that can obtain horizontal wind data was developed (the RS52 rawinsonde, 1952), with the improved directivity of the data receiving antenna and the development of a method to manually acquire the ground antenna-to-radiosonde direction data. At the same time, the radiosonde carrier frequency was changed to 408 MHz. However, the manual operation method using the radio wave axis in those days was poor in accuracy compared to the elevation-azimuth angle measurements with the optical theodolite. Thus, the angle measurements with the optical method was used while the rawinsonde (or balloon) can be seen with the naked eye to obtain better wind data (the rawinsonde cannot be visually seen when it goes into clouds or to the sun). In 1955, the JMA introduced the RS II-53 rawinsonde using the automatic-tracking parabolic antenna system with the 1.6 GHz band which was obtained from the US Air Force. The RS II-53 rawinsonde was upgraded to the RS II-56 rawinsonde with a standardized aneroid barometer, and introduced in the JMA's operational observations in 1956 (Figure 1.5). In 1981, the RS2-80 rawinsonde was introduced, which used the frequency modulation method for the data transmission and was equipped with a thermistor thermometer and carbon hygrometer (Figure 1.6). In 1992, the RS2-91 rawinsonde was introduced, which used an Integrated Circuit (IC). This rawinsonde has been changed to the electrostatic capacitance type barometer and hygrometer (Figure 1.7).

After the mid-1990s, the Global Positioning System (GPS) technology started to be applied to the radiosondes from various companies to provide the horizontal wind and geopotential height measurements. Such radiosondes are called the GPSsondes, which gradually replaced the rawinsondes at various operational sites in the world. Meisei developed the RS-01G GPSsonde, which is equipped with a capacitive humidity sensor instead of a carbon hygrometer. The JMA introduced the RS-01G GPSsonde in 2002 at Minamitorishima, the Vaisala RS80-15GA GPSsonde in 2003 at Hachijojima, and the LMS MK2-A GPSsonde in 2003 at Chichijima. (All of the JMA sites switched to GPSsondes at 2010). In 2010, JMA replaced RS-01G with the Meisei RS-06G GPSsonde. The RS-06G GPSsonde has a thermistor of smaller size, which resulted in reduced evaporative cooling (wet-bulb-effect)/solar heating errors.

Based on the technologies developed through the history described above, a light-weight, compact, and high-accuracy GPSsonde, the RS-11G radiosonde was developed in 2013. In addition, a lightweight smaller version of RS-11G, the iMS-100 radiosonde was developed in 2014. Table 1.1 describes the history of radiosondes used at the JMA Tateno station based on the information provided by *Abe* (2015).

Figure 1.1: Photograph of the Central Meteorological Observatory Type No.1 radiosonde (also called as S38 type radiosonde). This radiosonde is composed of a pressure instrument part, temperature instrument part and humidity instrument part. Each part is composed of a sensor and transmitter. This photograph shows a later version (1942-) of the S38 type radiosonde, for the paulownia wood was used for the radiosonde housing.

Table 1.1: History of radiosondes used at Tateno since 1944. Rawin and special radiosondes are excluded. Excerpt for Tateno from *Abe* (2015); *JMA* (1975).

			sensor					
Year	Radiosonde Type	Measurement range	Pressure	Temperature	Humidity	Carrier frequency (MHz)	Weight (with batttery)	Remarks
1944-1945	(Sonde) Central Meteorological Observatory No. 1	T: –80 - +20°C P: 760 - 100 hPa U: 0 - 100 %RH	Aneroid barometer	Bimetallic thermometer	Hair hygrometer	T: 10 - 12 P: 6.2 - 7.4 U: 7.5 - 10	400 g (for the type with paulownia wood housing)	PTU data are transmitted separately with different carrier frequencies. Three Hartley oscillators are used. Commonly known as 38 type.
1944-1947	(Sonde) 3-SHIKI ON-SHITSU HASSHINKI	T: –60 - +40°C P: 674 - 90 hPa U: 20 - 100 %RH	Aneroid barometer	Mercury thermometer	Hair hygrometer	T: 9.5 - 11.5 P:– U: 7.5 - 8.5	550 g	TU data are transmitted separately with different carrier frequencies. P data are sent with an altitude switch which has 12 contact points. Commonly known as 43 type.
1947-1949	(Sonde) S43K	T: <–60 - +40°C P: 674 - 90 hPa U: 20 - 100 %RH	Aneroid barometer	Bimetallic thermometer	Hair hygrometer	T: 9.5 - 11.5 P: – U: 7.5 - 8.5	550 g	TU data are transmitted separately with different carrier frequencies. T sensor has been changed from the S43 type, and is able to measure also below –60°.

Continued on next page

Table 1.1 – continued from previous page

Year	Radiosonde Type	Measurement range	Pressure	Temperature	Humidity	Carrier frequency (MHz)	Weight (with batttery)	Remarks
1949-1950	(Sonde) S48	T: –80 - +40°C P: 1040 - 5 hPa U: 0 - 100 %RH	Aneroid barometer	Bimetallic thermometer	Hair hygrometer	27.7	1250 g	Data are transmitted with the Morse code method
1950-1950	(Sonde) S49A S49B	T: –80 - +40°C P: 1040 - 5 hPa U: 0 - 100 %RH	Two connected aneroid barometers (53 mm dia.) Type A: Made of nickel silver Type B: Made of phosphorus bronze	Bimetallic thermometer with nickel plating on both sides Type A: Length: 37 mm, Width: 41 mm, Thickness: 0.31-0.37 mm Type B: Length: 38 mm, Width: 35 mm, Thickness: 0.21-0.27 mm	Hair hygrometer Length: 80 mm, # hairs: 18	402	1400 g	Changed to the frequency assigned by the International Telecommunication Convention. Data are transmitted with the Morse code method.
1950-1952	(Sonde) S50L S50M	T: –80 - +40°C P: 1040 - 5 hPa U: 0 - 100 %RH	Type L: Two connected aneroid barometers (43 mm dia.), made of phosphorus bronze Type M: Two connected aneroid barometers (42 mm dia.), "no wave" type, made of nickel silver	Bimetallic thermometer with nickel plating on both sides. Type L: Length: 50 mm, Width: 42 mm, Thickness: 0.23-0.28 mm Type M: Length: 37 mm, Width: 27 mm, Thickness: 0.25 mm Two cutting-type (at –30°C and –50°C) mercury thermometers are also installed for in-flight calibration and for termination of humidity data transmission.	Hair hygrometer Type L: Length: 60 mm, # hairs: 16 Type M: Length: 55 mm, # hairs: 24	402	850 g	Data are transmitted with the Morse code method. Length of the main string is 7 m.
1952-1954	(Sonde) S52M (Rawinsonde) RS52M, RS52L	ditto	ditto	ditto	ditto	ditto	1300 g	ditto (The Morse code board has been improved)
1954-1956	(Rawinsonde) RS53K, RS53M	T: –80 - +40°C P: 1040 - 5 hPa U: 0 - 100 %RH	Type K: Two connected aneroid barometers (42 mm dia.), "no wave" type, made of nickel silver Type M: Two connected aneroid barometers (44 mm dia.), made of phosphorus bronze	Bimetallic thermometer with nickel plating. Length: 50 mm, Width: 42 mm, Thickness: 0.25 mm Two cutting-type (at –30°C and –50°C) mercury thermometers are also installed for in-flight calibration and for termination of humidity data transmission.	Hair hygrometer, with rolling processing. Length: 60 mm, # hairs: 20	408	970 g	Data are transmitted with the Morse code method. Length of the main string is 7 m.
1956-1957	(Rawinsonde) RS56	T: –85 - +40°C P: 1040 - 5 hPa U: 1 - 100 %RH	Two connected aneroid barometers (44 mm dia.), "no wave" type, made of phosphorus bronze	ditto	Hair hygrometer, with rolling processing. Length: 60 mm, # hairs: 20 until Dec. 1956, 10 from Jan. 1957	408	950 g	Data are transmitted with the Morse code method.
1957-1981	(Rawinsonde) RS II-56	ditto	ditto	ditto	ditto	1680	1275 g	Data are transmitted with the Morse code method. Transistors are used for the modulation and transmitter parts. Length of the main string was changed from 7 m to 15 m in June 1968.
1981-1992	(Rawinsonde) RS2-80	T: –90 - +45°C P: 1040 - 5 hPa U: 0 - 100 %RH	Aneroid barometer (60 mm dia.), made of iron-nickel alloy, with 78 contact points	Diode type thermistor thermometer, with white-painted	Carbon-film hygrometer (an acrylic substrate coated with carbon particles)	1680	600 g	Data are transmitted with the frequency modulation method. Period of element change is 3 sec for analog recording and 1 sec for automated processing. 1 cycle is P-T-P-U-P-T-P-Ref (8 or 24 sec).

Continued on next page

Table 1.1 – continued from previous page

Year	Radiosonde Type	Measurement range	Pressure	Temperature	Humidity	Carrier frequency (MHz)	Weight (with batttery)	Remarks
1992-2009	(Rawinsonde) RS2-91	T: –85 - +40°C P: 1040 - 5 hPa U: 1 - 100 %RH	Aneroid barometer (46 mm dia.), made of iron-nickel alloy. Continuous type capacitive barometer.	Bead type thermistor, coated with silicon and treated with aluminum vapor.	High-polymer electronic capacitive hygrometer	1680	300 g	Data are transmitted with the frequency modulation method. Period of element change is 1 sec. 1 cycle is P-T-U-Ref (4 sec).
2009-2013	(GPSsonde) Vaisala RS92-SGPJ (SGP"J" is a special model for Japan, with a 15-m main string, 404.5 MHz carrier freq., and a switch for dry-cell battery)	T: –90 - +60°C P: 1080 - 3 hPa U: 0 - 100 %RH	Silicon-based capacitive barometer	Capacitive wire thermometer	Thin-film capacitive hygrometer. Heated twin sensor (Two sensors are alternately heated, and non-heated one is used for the measurement.)	404 - 405	290 g	Data are transmitted with the frequency modulation method. Data values are obtained every 2 sec.
2013 - present	(GPSsonde) Meisei RS-11G	T: –90 - +50°C P: 1050 - 3 hPa U: 1 - 100 %RH	Non (calculated from temperature, humidity, and GPS height)	Bead type thermistor, coated with silicon and treated with aluminum vapor.	High-polymer electronic capacitive hygrometer	404.6 - 405.7	85 g	Data are transmitted with the frequency modulation method. Data values are obtained every 1 sec. Length of the main string has been 10 m from July 2013.

1.3 JMA's contributions to the GRUAN

The Tateno station (36.0576°N, 140.1257°E) is the Aerological Observatory of JMA and plays the leading role of all the 17 JMA's radiosonde stations including the Syowa station (Antarctica). Tateno is the leading station which carries out the development of aerological instruments, analyzes all the obtained radiosonde data, and is responsible for managing the quality of the aerological data in Japan. On-site, there is also a Meteorological Research Institute and a wind tunnel facility, also the RIC TSUKUBA reside in the main building of Tateno. Therefore, Tateno is able to perform various radiosonde-related laboratory and field experiments. Tateno became a potential GRUAN site in 2009 and will be in the certification process in 2016. The JMA established the requirements for the verification of meteorological instruments (*JMA*, 2002) which should be applied to all official meteorological instruments (except for education or research purpose) in Japan. The quality of the radiosonde data has been maintained by this JMA rule. However, different types of radiosondes have different accuracy and precision in practice, and thus the changes in the radiosonde type may introduce inhomogeneities in radiosonde climate records. Therefore, campaigns of several multiple-payload comparison flights using new and old radiosondes have been made at Tateno when changing the radiosonde type in 1981 (*JMA*, 1983), in 1993-1994 (*Sakoda et al.*, 1999), in 2009-2010 (*Tateno Aerological Observatory*, 2011; *Kobayashi et al.*, 2012a; *Kobayashi*, 2014), and in 2013 (see Chapter 6 of this document). Based on these intercomparison results, data from the older types of radiosonde were corrected in reference to the latest radiosonde type (i.e., Meisei RS-11G), and a climate diagram was created (Figure 1.8; (updated Figure 2 of *Uesato et al.*, 2008)). Figure 1.8 shows that temperature has increased in the troposphere and has decreased in the lower stratosphere in recent five decades and that these tendencies are stronger for the corrected dataset. Thus, in order to maximize the value of the radiosonde data for climate monitoring, continuous efforts are needed to evaluate the quality and uncertainty of data from each radiosonde type, to characterize the differences among different radiosonde types, and to verify the evaluation and the characterization by several intercomparison flights. In particular, intercomparison campaigns for, e.g., one year are necessary at the radiosonde type change.

The rest of this technical document is structured as follows: Chapter 2 describes the overview of the

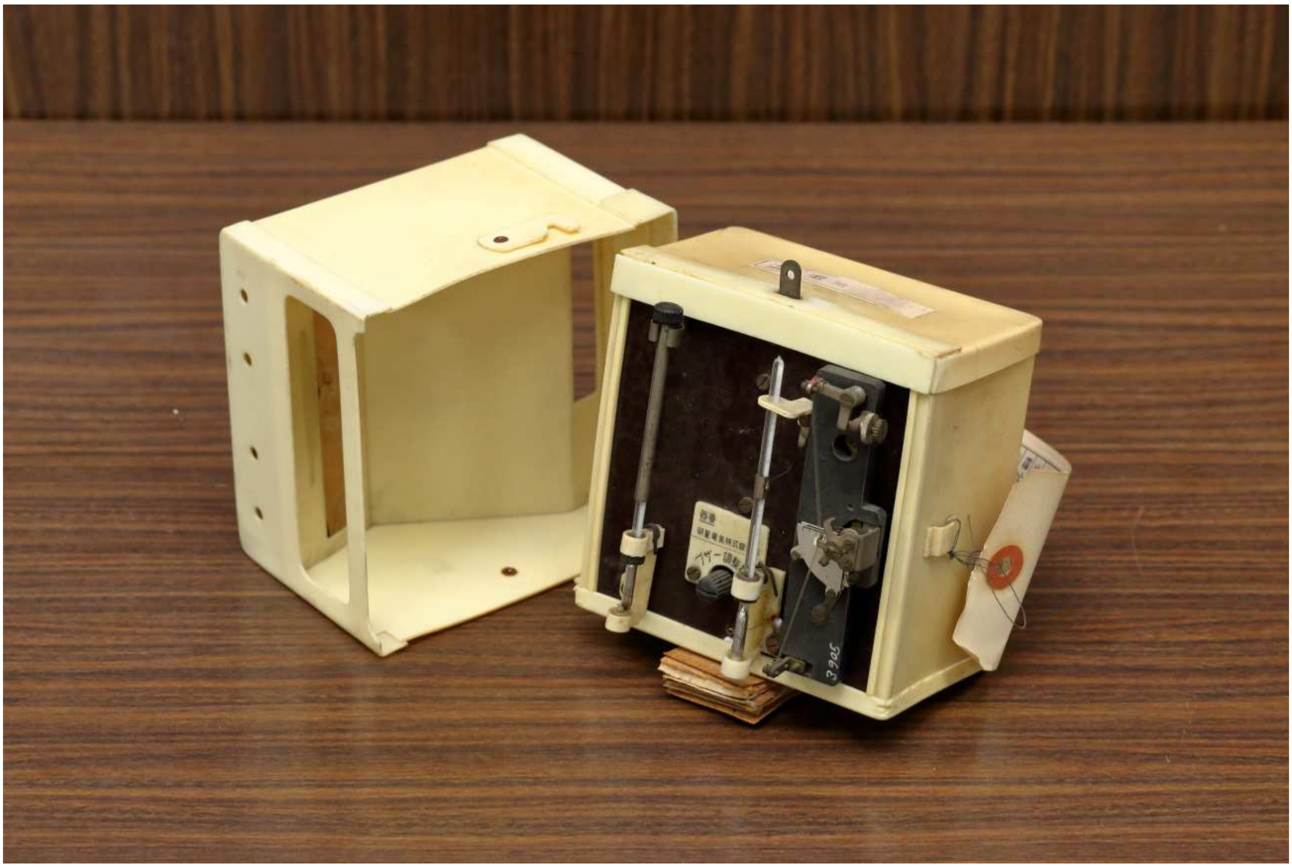

Figure 1.2: Photograph of the 3-SHIKI ON-SHITSU HASSHINKI (also called as S43 type radiosonde). This radiosonde was manufactured by the Meisei Electric Co., LTD for the Imperial Japanese Army. The Japan Meteorological Agency (JMA) employed this radiosonde from the Imperial Japanese Army after the World War II, and used it until the new S48 type radiosonde was developed in 1949.

RS-11G and iMS-100 radiosondes, Chapter 3 gives the data processing algorithms and the uncertainty evaluations, Chapter 4 gives the GRUAN processing procedures of the RS-11G and iMS-100 data, and Chapter 5 gives the tractability chain of the RS-11G and iMS-100 data. The verification of the uncertainty evaluations based on some test fights are discussed in Chapter 6. Finally, Chapter 7 presents a summary.

Figure 1.3: Photograph of the S48 type radiosonde. Data were converted to the Morse coded data, and sent by the fixed 27.7 MHz carrier frequency.

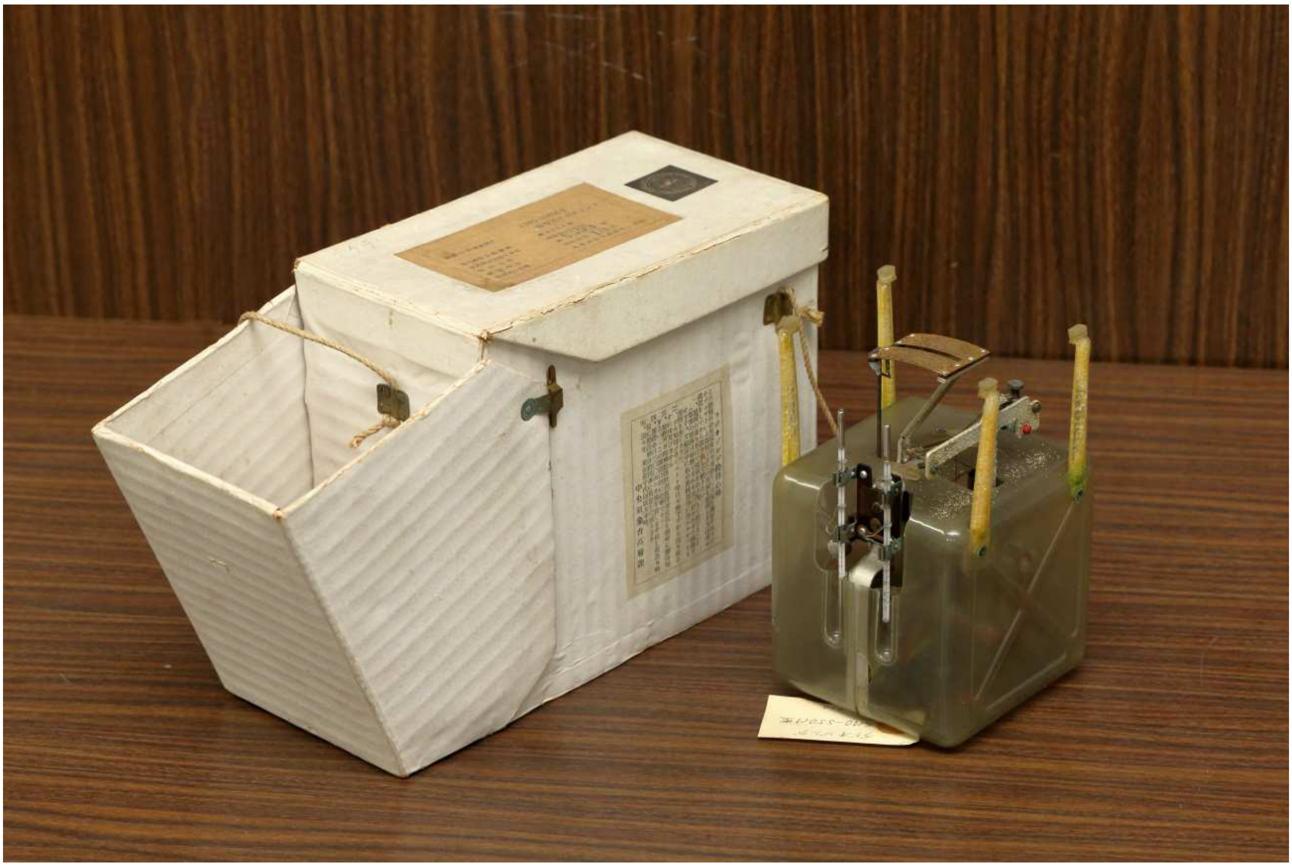

Figure 1.4: Photograph of the S50 type radiosonde. This radiosonde weight was changed to 850g from 1400g of previous type (S49 type).

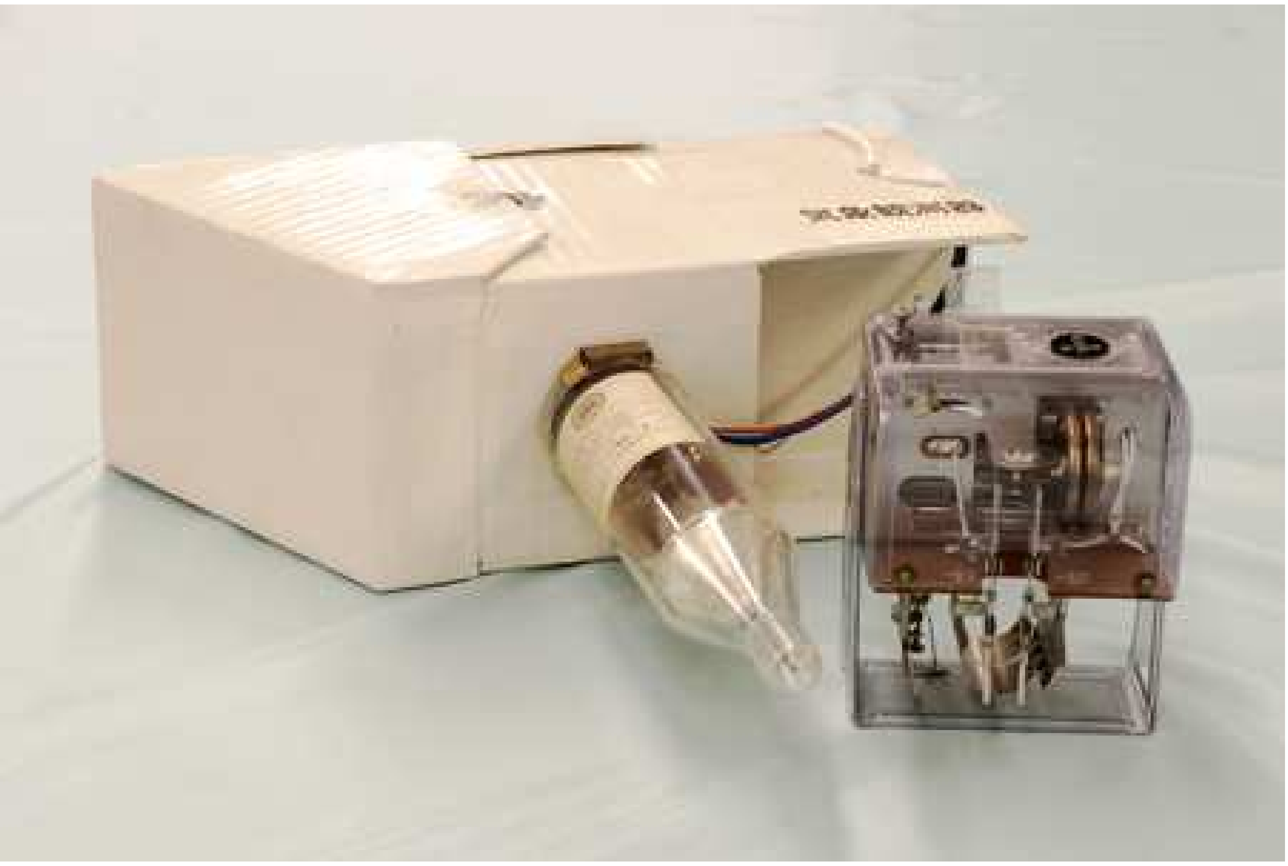

Figure 1.5: Photograph of the RS II-56 type rawinsonde. Before introduction of this type, different radiosonde manufacturers provided their own aneroid barometers. With this model, a unified aneroid barometer was introduced.

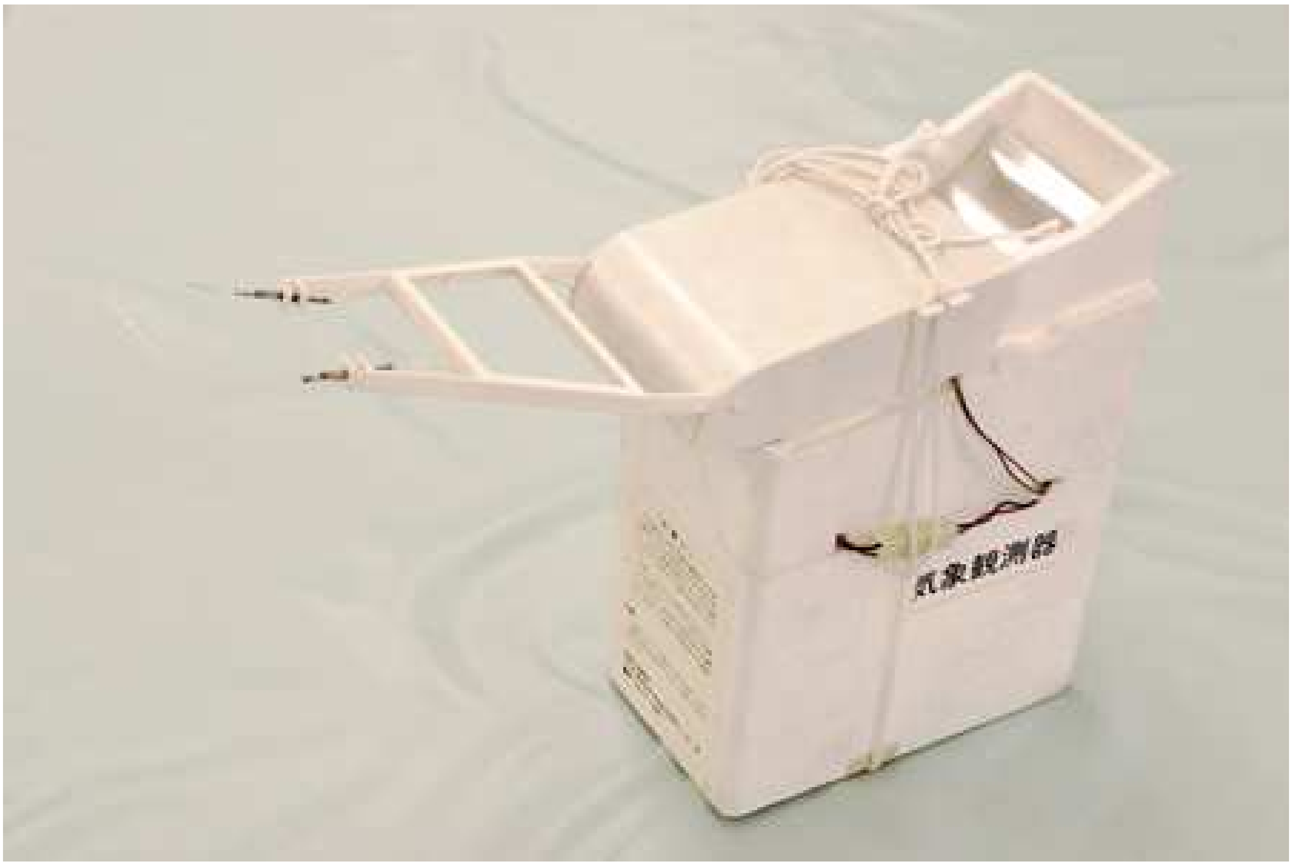

Figure 1.6: Photograph of the RS2-80 type rawinsonde. This type uses the frequency modulation method for the data transmission, and is equipped with a thermistor thermometer and carbon hygrometer.

Figure 1.7: Photograph of the RS2-91 type rawinsonde. This type uses an Integrated Circuit in place of transistors.

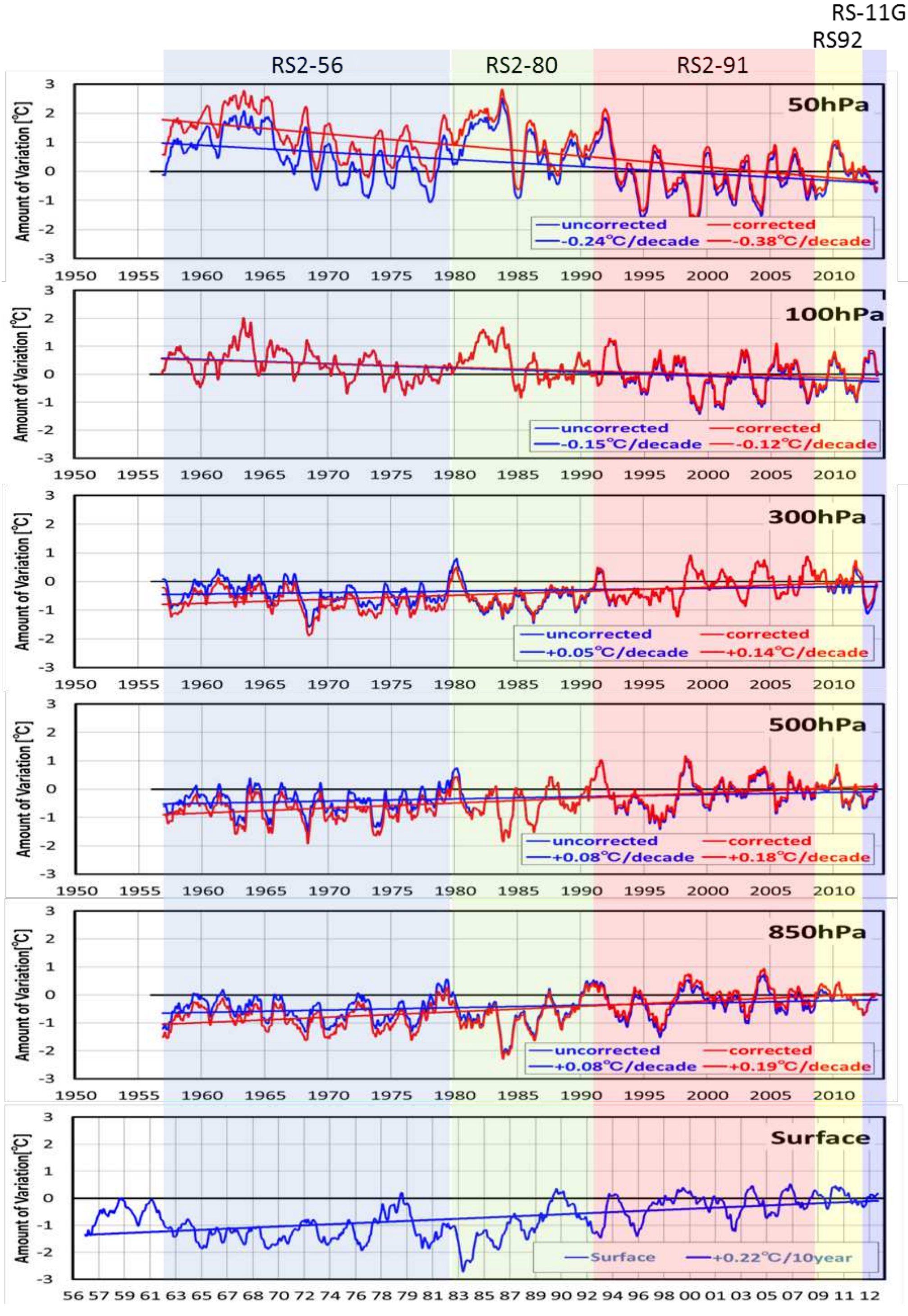

Figure 1.8: Time series of monthly mean temperature at Tateno at six levels. Blue curves are for uncorrected data, while red curves for corrected data using the intercomparison results at the instrument changes. Adopted and updated from Figure 2 of *Uesato et al.* (2008).

2 Overview of the RS-11G and iMS-100 radiosondes

2.1 RS-11G radiosonde

The RS-11G radiosonde is equipped with a thermistor temperature sensor, capacitive relative humidity (RH) sensor, a GPS receiver for geopotential height, pressure, and horizontal wind measurements, and a 400 MHz transmitter. Compared with the previous version, i.e., the RS-06G radiosonde (whose performance was evaluated in the 2010 WMO radiosonde intercomparison campaign (*Nash et al.*, 2011)), the mass has become smaller (from 160 g to 85 g, including the battery) and the temperature and RH measurement performance has been improved both by hardware and software. (It is noted here that the thermistor, i.e., its material and dimension, and the solar radiation correction method are exactly the same between the RS-06G and RS-11G.) Geopotential height is calculated from the GPS-based height, and pressure is calculated from temperature, RH, and GPS-based geopotential height data.

The RS-11G radiosonde was released in 2012, and has been used at many of the JMA stations, other meteorological services outside Japan, and several research institutes and universities. It should be noted that the open interfacing protocol (Meisei's original protocol or the XDATA protocol) has been adapted to facilitate connectivity of external sensors such as the electrochemical concentration cell (ECC) ozone sensor, various cloud particle sensors (e.g., the Hydrometeor Videosonde (HYVIS) and Cloud Particle Sensor (CPS)), and other sensors (see Section 2.3.2). The XDATA format is the digital interface developed by researchers at the National Oceanic and Atmospheric Administration (NOAA). The external view of the RS-11G radiosonde is shown in Figure 2.1 and Figure 2.2, and the specifications are listed in Table 2.1.

Table 2.1: Specifications of the RS-11G radiosonde.

Model	RS-11G
Dimensions	86 (W) 67 (D) 154 (H) mm^3
Volume	893 cm^3
Weight	85 g (with battery)
Impact force (terminal speed) w/o parachute	544 N (at 7-8 m s^{-1})
Telecommunications standard	ETSI EN 302054
Consumption current	300 mA or less
Radio wave modulation	F1D
Transmission power	100 mW or less
Battery	CR-123A 3 V (one piece)
Material of case unit	EPS (Expanded polystyrene)
Released in 2012	

2.2 iMS-100 radiosonde

The iMS-100 radiosonde is equipped with the same temperature and RH sensors as those of the RS-11G radiosonde. The data processing algorithm in the sounding software is also the same as for the RS-11G. The latest miniature electronic components have been applied to the iMS-100 to substantially reduce the mass of the radiosonde package (from 85 g for RS-11G to 38 g, including

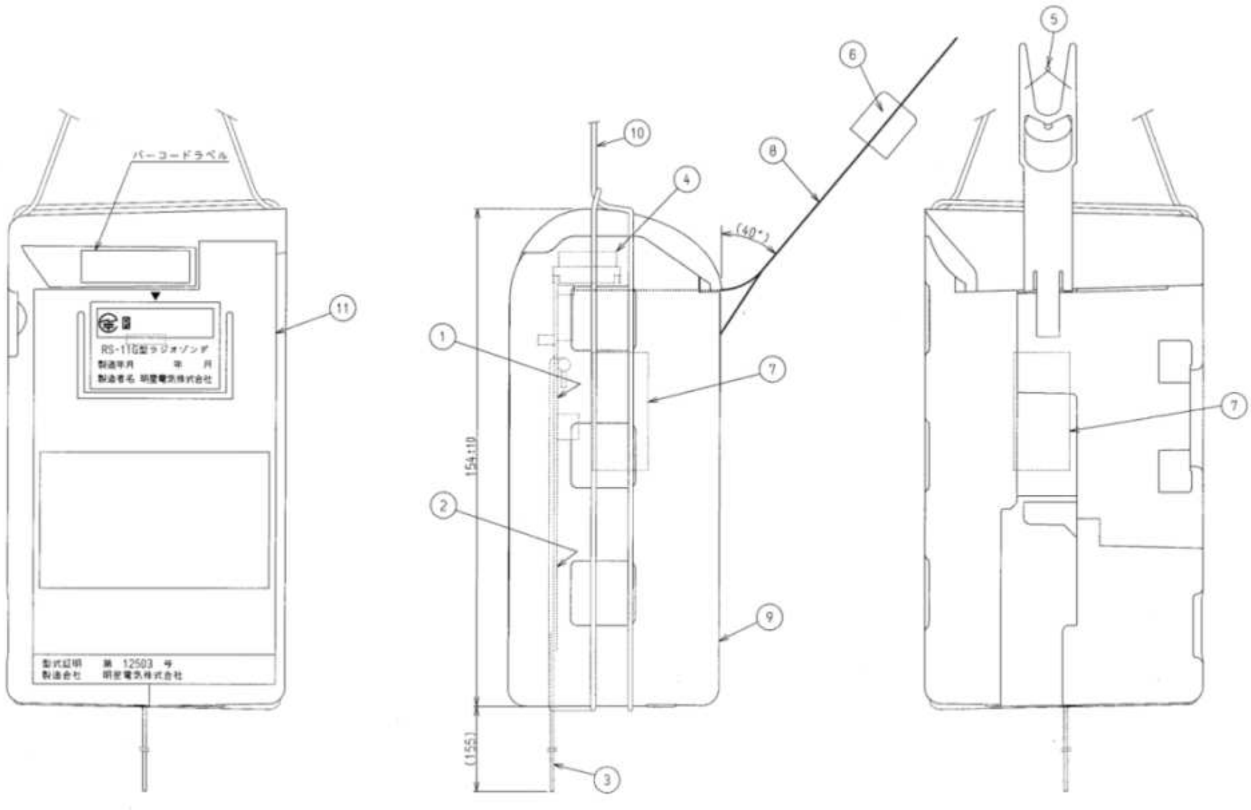

Figure 2.1: External view of the Meisei RS-11G radiosonde (unit: mm). 1: Processing unit and signal converting unit; 2: Transmitter; 3: Antenna; 4: GPS module; 5: Temperature sensor; 6: Relative humidity sensor with a cap; 7: Battery; 8: Sensor boom; 9: Styrofoam (EPS) case; 10: Rope; 11: Label; and 12: Interface.

battery). This leads to a substantial reduction of the impact force when falling down to the ground, ensuring much safer operation. Besides, the downsizing has led to smaller pendulum motions, and improved the horizontal wind measurements (see Section 3.4.3). The iMS-100 was released in late 2014. The external view of the iMS-100 radiosonde is shown in Figure 2.3 and Figure 2.4, and specifications are listed in Tables2.1 and 2.2.

2.3 Specifications of the RS-11G and iMS-100 radiosondes

This section describes the major parts used in the RS-11G and iMS-100 radiosondes, the connectivity of external sensors, and the production of these radiosondes.

2.3.1 The configuration of the RS-11G and iMS-100 radiosondes

(1) The components of the RS-11G and iMS-100 radiosondes
Figure 2.5 shows the system diagram of the RS-11G and iMS-100 radiosondes. All modules are basically common. The operation and specifications of each module are discussed below.

a) Sensor boom

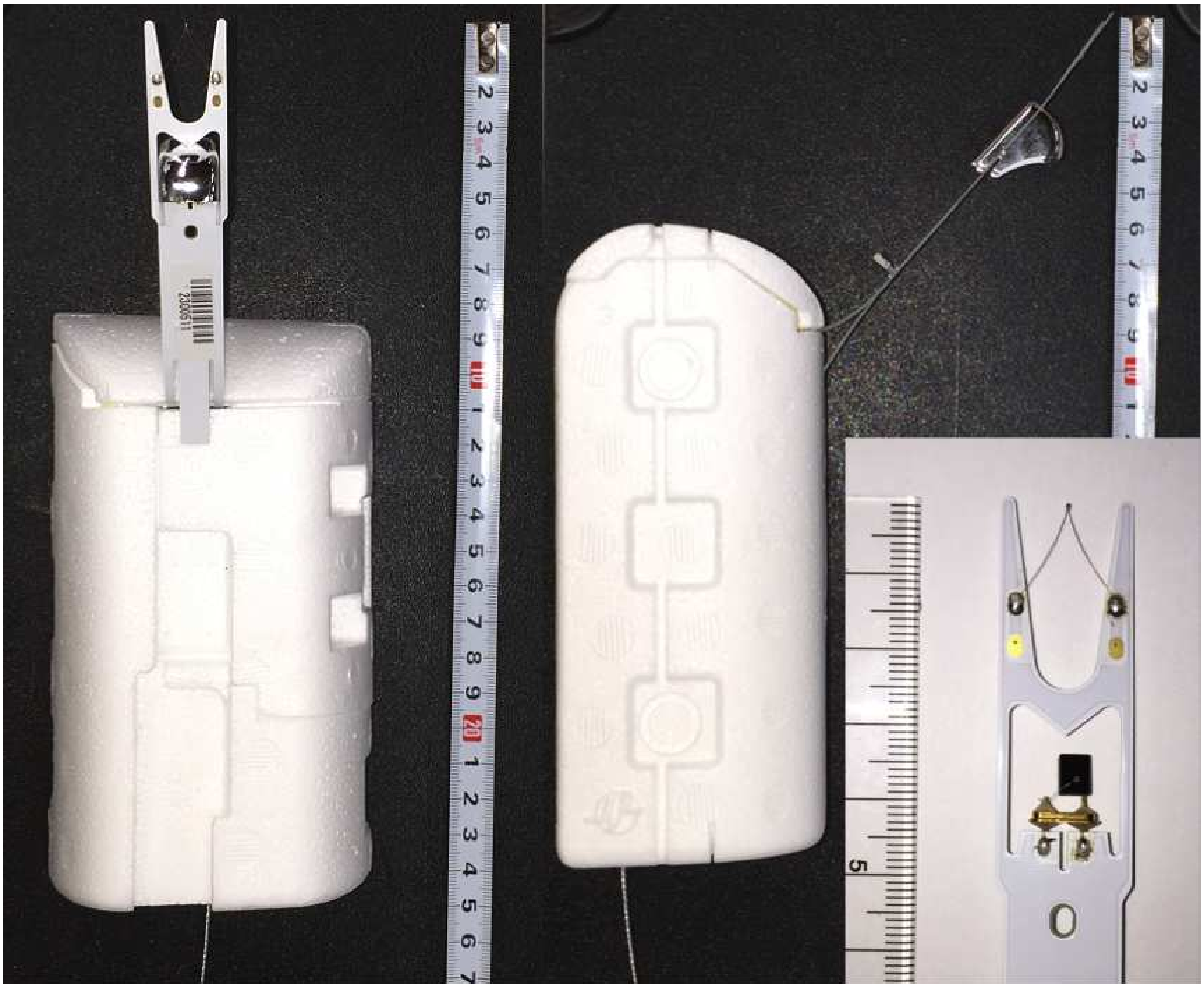

Figure 2.2: Photographs of the RS-11G radiosonde. The inset in lower right shows a magnified photograph of the sensor boom including the thermistor sensor and thin-film capacitive relative humidity sensor. The unit of the scales is cm.

The sensor boom consists of a temperature sensor and a RH sensor. The sensor boom is flexible and tilted up as shown in Figures 2.1 and 2.3 to prevent water droplets from sticking to the sensors and to prevent heat contamination from the radiosonde package. Also, the surface of the boom is coated with white solder resist to minimize solar radiative heating. The temperature sensor is a thermistor, which is mounted to the tip of the sensor boom; this minimizes the heat flux from the radiosonde package. The RH sensor is a thin-film capacitive sensor, with a plastic cap coated with aluminum vapor deposition to reduce the errors due to solar and infrared radiation and to prevent water condensation on the sensor surface. The details of the temperature and relative humidity sensor are discussed in Section 3.1 and Section 3.2.

b) GPS module

The GPS modules mounted on the RS-11G and iMS-100 (Table 2.3) are customized for Meisei radiosondes, and not commercially available for general use. The GPS module calculates the position

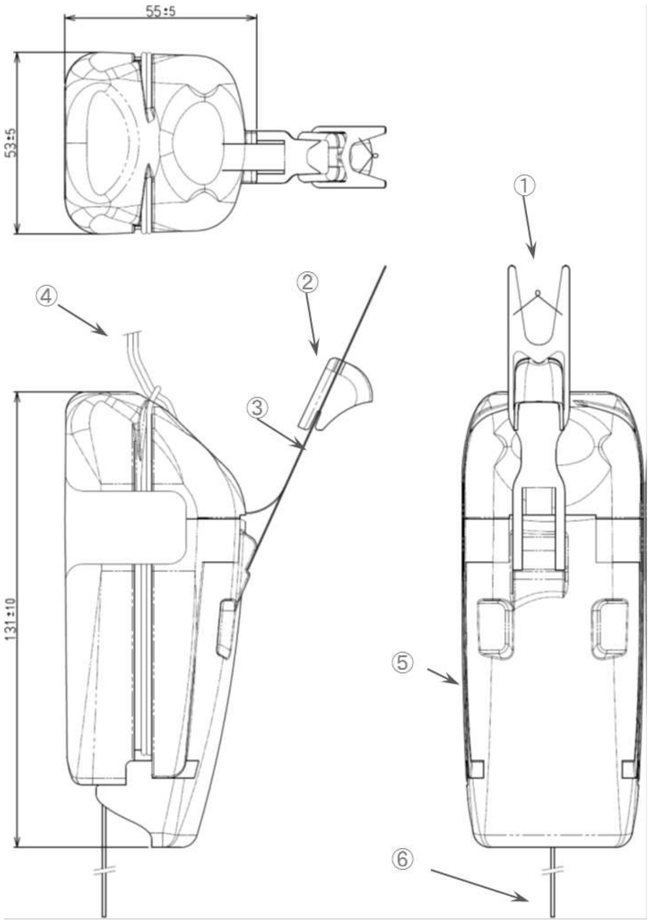

Figure 2.3: External view of the Meisei iMS-100 radiosonde (unit: mm). 1: Temperature sensor; 2: Relative humidity sensor with a cap; 3: Sensor boom; 4: Rope; 5: Styrofoam (EPS) case; and 6: Antenna.

and velocity of the radiosonde. The GPS module consists of the GPS antenna with a preamplifier and the GPS receiver supporting the Satellite-Based Augmentation System (SBAS). It should be noted that the SBAS is a method of improving the navigation system's attributes, such as accuracy, reliability, and availability, through the external information from satellite and that the positioning accuracy of the SBAS is at the same level as the Ground-based Augmentation System (GBAS). The receiving frequency is 1575.42 MHz. The module provides data with the National Marine Electronics Association (NMEA) format, including the GPS status (e.g., number of GPS satellites whose signals are received), latitude, longitude, altitude, Doppler velocity, azimuth direction, GPS time, and the Dilution of Precision (DOP) value. These data are sent to the Central Processing Unit (CPU) on the processing unit every second, and edited into the transmitted format.

c) Signal converting unit
The signal converting circuit works for the temperature and RH measurements. It consists of a resistor-capacitor (CR) oscillating circuit including the thermistor and the thin-film capacitive sensors with a Schmitt circuit and an analog switch. The temperature and RH signals are converted into frequency data, which are switched by the analog switch with switching signals from the CPU in the

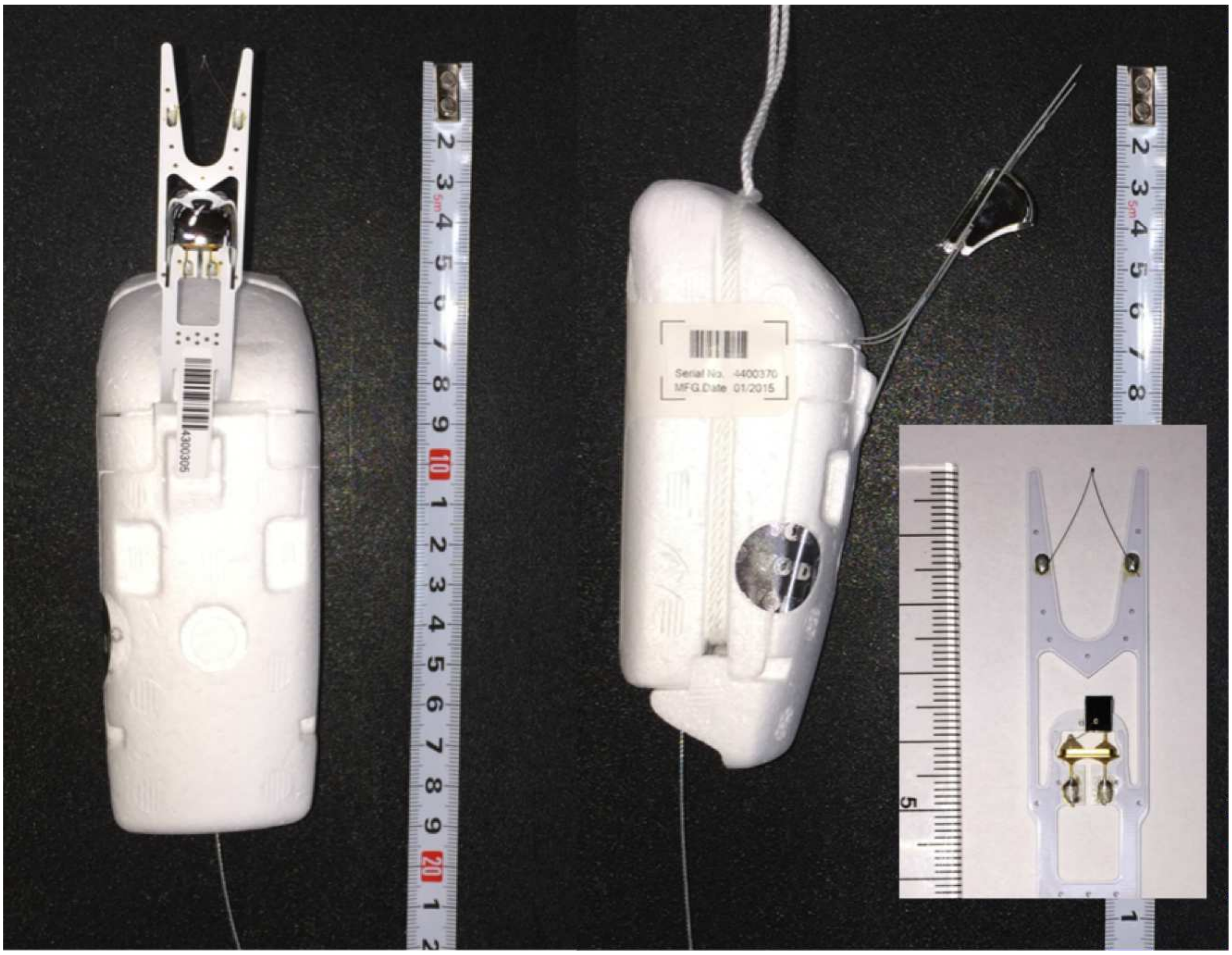

Figure 2.4: Photographs of the iMS-100 radiosonde. The inset at lower right shows a magnified photograph of the sensor boom with the heat type thermistor sensor and thin-film capacitive humidity sensor. The unit of the scales is in cm.

processing unit and are output via the CR oscillating circuit. Each oscillating frequency is determined by the following parts: Reference frequency (FR): A fixed resistor and a fixed capacitor Frequency of temperature (FT): The resistance of the thermistor and a fixed capacitor Frequency of humidity (FU): A fixed resistor, capacity of the humidity sensor, and a fixed capacity arranged in line with the humidity sensor The calculation procedures from the oscillating frequencies to the values of meteorological variables are explained in Chapter 3.

d) Processing unit
The processing unit controls the switching signals for the signal converting unit and the processing of the temperature and RH signals. Also, the signals from the GPS receiver are input to the processing unit. These data are edited and converted to the digital signals, which are output to the transmitter as modulated signals. In addition, the processing unit edits the physical conversion parameters stored in the unit and transmitted together with the measurement signals. The conversion parameters are determined by the factory calibration procedures and stored in the radiosonde (see Chapter 3), and

Table 2.2: Specifications of the iMS-100 radiosonde.

Model	iMS-100
Dimensions	55 (W) 53 (D) 131 (H) mm^3
Volume	262 cm^3
Mass	38 g (with battery)
Impact force (terminal speed) w/o parachute	330 N (at 7-8 m s^{-1})
Telecommunications standard	ETSI EN 302054
Consumption current	200 mA or less
Radio wave modulation	F1D
Transmission power	100 mW or less
Battery	CR-123A 3 V (one piece)
Material of case unit	EPS (Expanded polystyrene)
Released in 2014	

Table 2.3: Specifications of the GPS module.

	RS-11G	iMS-100
Type	MES-39525-01	EAU00002539
Received channels	12	66
Received frequency	1575.42 MHz ±1 MHz C/A code	
DGPS method	SBAS	
Dimensions (excluding protrusion)	20.8mm(W)x20.8mm(D)x9.2mm(H)	10.8mm(W)x10.0mm(D)x2.05mm(H)

are used in the ground processing system when the physical values of the meteorological variables are calculated.

e) Transmitter
A dedicated Integrated Circuit (IC) is used, which contains a transmitter with a frequency synthesizer controlled by the crystal oscillator. The transmitting frequency can be changed at a 100 kHz step within the range of 400.1 – 406.0 MHz. (Note that the frequency actually used depends on the national radio law for frequency in each country).

f) Battery
A Direct Current (DC) 3 V lithium battery, CR-123A, is used, which is small, light, and tolerant to low temperatures, to supply the power to the radiosonde for more than 4 hours.

g) Power control unit
The power control unit supplies a stable power to each part of the radiosonde by making a constant voltage from the battery power.

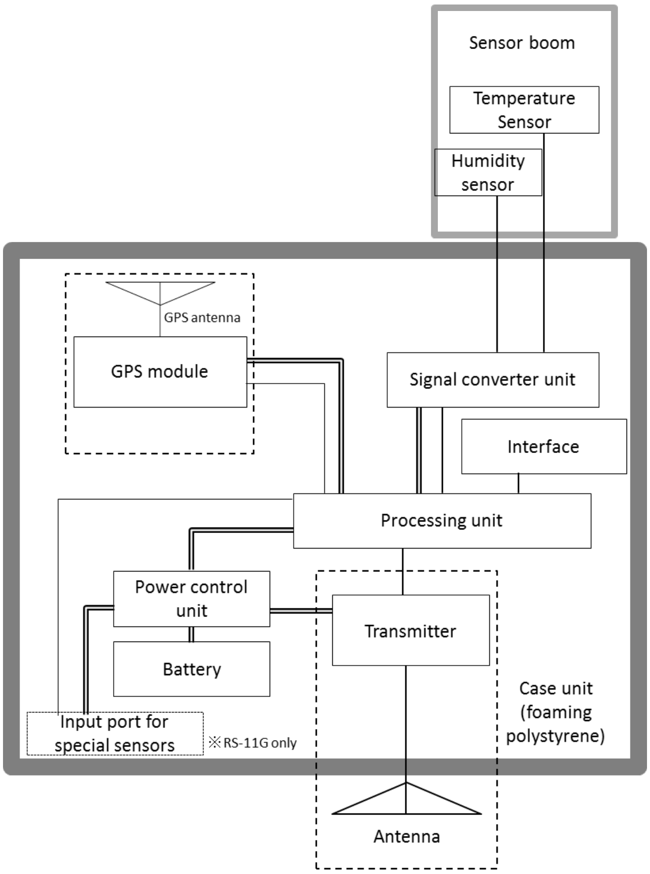

Figure 2.5: System diagram of the Meisei RS-11G and iMS-100 radiosondes. The input port for external sensors is available only for the RS-11G radiosonde. Single lines indicate those for signals, and double lines indicate the power lines.

h) Interface with the sounding software on a PC
The RS-11G radiosonde is operated with the sounding software (named MGPS2) on a personal computer (PC) in the ground receiving system through an associated connector and cable when the radiosonde power is turned on. The iMS-100 radiosonde has an infra-red module and uses the Infra-Red (IrDA) communication with the dedicated processing unit (baseline checker) that is connected to a PC in the ground receiving system when the radiosonde is activated.

i) Input port for external sensors (with both analog and digital channels)
The RS-11G radiosonde has an interface for external sensors. Both analog and digital connections are supported. More details are explained in Section 2.3.2.

j) Package box (Radiosonde housing)
White colored EPS (expanded polystyrene) is used for the radiosonde housing to prevent the radiosonde circuit board from cold temperatures, to minimize the solar heating, and to reduce the falling impact at the ground.

(2) Special features of the iMS-100 radiosonde

The basic configuration is the same as that of the RS-11G radiosonde. The major differences from the RS-11G radiosonde is summarized as follows.

- The iMS-100 radiosonde does not have the input port (both digital and analog) for external sensors.
- The connection between the radiosonde and the MGPS2 software in the PC during turning radiosonde power on is performed through the wireless infrared communication (IrDA).
- All the hardware of the iMS-100 radiosonde is smaller in size and in mass by adopting state-of-the-art and downsized electronic parts.
- A different GPS module is used (Section 2.3.1 and Table 2.3).

2.3.2 Information on the connectivity of external sensors for the RS-11G radiosonde

There are two interfaces (i.e., analog and digital) in the RS-11G radiosonde for external sensors. Note that there is no interface in the iMS-100 radiosonde for external sensors.

2.3.2.1 Analog interface

This is a 1 Hz sampling, 16-bit A/D converter.
Available sensor:

- The Electrochemical Concentration Cell (ECC) ozonesonde sensor (*Komhyr et al.*, 1995).

2.3.2.2 Digital interface

The data downlink is at 25 byte per second (including 1 byte for header, and 2 byte for delimiter).
Available sensors:

- The Cryogenic Frostpoint Hygrometer (CFH) (*Vömel et al.*, 2007)
- The Fluorescence Lyman-Alpha Stratospheric Hygrometer for balloons (FLASH-B) hygrometer (*Yushkov et al.*, 1998)
- The Optical Particle Counter (OPC) developed by *Hayashi* (2001)
- The Meisei Temperature Reference (MTR) tungsten temperature sensor (*Shimizu and Hasebe*, 2010)
- The CO2 sensor (produced by Meisei)
- The Radiation (beta-rays, gamma-rays) sensor (produced by Meisei)
- The Cloud Particle Sensor (CPS) sensor (produced by Meisei; *Fujiwara et al.*, 2016)
- Other sensors whose output data format is the XDATA format up to 22 byte s^{-1}

The communication between the RS-11G radiosonde and an external sensor is synchronized using the 1 Hz pulse sent from the RS-11G radiosonde. The external sensor is to send the 25-byte data every second according to the ”1 Hz demand pulse” rule. The checksum is included in the 25-byte data, and detecting errors which may have been introduced during its transmission every second. The external sensor needs to send a full 25-byte data between the sequential 1 Hz demand pulses; otherwise all data become missing at this particular 1-second time window.). When a sensor with the XDATA format is used, a special communication interface board provided by Meisei is attached between the sensor and the RS-11G radiosonde, which converts the XDATA-formatted data into the RS-11G 25-byte data format. The detailed communication protocol for external sensors is described in Appendix A.

2.3.3 Manufacturer-provided measurement specifications

The list of measurement specifications of the RS-11G and iMS-100 radiosondes are shown in Table 2.4. The values in this table are provided by the manufacturer.

2.3.4 Production of the radiosondes

As of 2015, the RS-11G radiosonde is being used operationally at 8 of the JMA upper-air stations (Wakkanai, Sapporo, Akita, Tateno, Fukuoka, Kagoshima, Chichijima, Minamitorishima), some stations in other countries, and is also used for research purposes by universities, research institutes, and private weather companies. The annual production is approximately 50,000 units of radiosondes for the case of year 2014. It takes about 2.5 months between the order and the delivery of the RS-11G and iMS-100 radiosondes. Meisei has a production system that can produce 100,000 units of radiosondes per year.

2.4 Ground checks

The ground check is conducted on-site before the launch to confirm that the sensors calibrated at the factory are not damaged nor deteriorated during the delivery and storage. The results of the ground check are used to judge whether the radiosonde can be flown.
The ground check is made by using both the manufacturer’s instrument called Ground Checker (GC) and the Standard Humidity Chamber (SHC) which is independent of the manufacturer and has been developed by the JMA. The manufacturer’s GC checks the temperature and RH measurements under room conditions just before the launch. On the other hand, the SHC checks the RH measurements at 100 %RH using distilled water and at 0 %RH using desiccant (molecular sieve), which are carried out more than one day before the launch. The manufacturer-independent ground check is required by the GRUAN (GCOS, 2013). The RH deviations obtained at 0 %RH, RH under a room condition, and 100 %RH are used for the recalibration of the obtained data to produce the GRUAN data product.
First, the ground check procedure using Meisei’s GC under room condition is carried out. The radiosondes that have passed the GC check precede to 0 %RH check using the SHC system. The sensor boom is placed in the SHC (0 %RH). Then, the sensor boom is placed in the SHC (100 %RH). The radiosondes are then stored in a low humidity environment for more than one day, and are subject to the room environment GC check again right before the launch.

2.4.1 Ground check (baseline check) using the manufacturer’s Baseline Checker

The manufacturer’s ”GC” equipment (baseline checker) has reference temperature and RH sensors. The radiosonde sensors are placed in a small chamber, and the readings are recorded with the software

Table 2.4: Measurement specifications information of the RS-11G and iMS-100 radiosondes provided by the manufacturer.

S/N	Description	Specifications		Remarks
1	Usage environment	Pressure: Temperature: RH:	1050 hPa to 3 hPa -90°C to +60°C 0 %RH to 100 %RH	
2	Measurement range	Pressure: Geopotential height: Temperature: Humidity: Wind direction: Wind speed:	1050.0 hPa to 3.0 hPa -500.0 m to 40000.0 m -90.0°C to +60.0°C 0 %RH to 100 %RH 0.01° to 360.00° 0.00 m/s to 200.00 m/s	
3	Transmitter	Type of radio wave: Carrier frequency: Occupied bandwidth: Transmission power: Modulation method: Transmission rate: Transmission interval:	F1D 403.3 MHz to 405.7 MHz $\leq$ 15 kHz $\leq$ 100 mW Frequency shift keying 1200 bps 1 s	The carrier wave frequency can be changed in 100 kHz steps
4	Resolution	Pressure: Geopotential height: Temperature: Humidity Wind direction: Wind speed:	0.1 hPa 0.1 m 0.1°C 0.1 %RH 0.01° 0.01 m/s	
5	Uncertainty (k=2)	Pressure: Temperature RH: Wind direction: Wind speeds:	3 hPa (1-10 km) 2 hPa (16 km) 1 hPa (24 km) 0.4 hPa (32 km) 1 K (0-16 km) 2 K (Above 16 km) 15 %RH (0-12 km) 30 %RH (12-17 km) 10° $<$ 10 m/s (0-16 km) 4° at higher speeds 20° $<$ 10 m/s (16 km -) 8° at higher speeds 2 m/s $<$ 10 m/s (0-16 km) 4 m/s (16 km -)	According to the manufacturer's catalog The uncertainty is evaluated in Chapter 3.

MGPS2. If the difference between the radiosonde and the reference sensors is within a certain range, normally $\Delta U < \pm 7$ %RH and $\Delta T < \pm 0.5$ °C, the radiosonde can be used for the observation. For the RS-11G radiosonde, the reference temperature and RH instrument is the Rotronic Hygro Parm HP22-A (hereinafter referred to as HP22). The reference data are imported to the software MGPS2 through a dedicated cable or manual operation, and the data of both the RS-11G and HP22 are compared. A plastic container (110 mm in length 75 mm in width 73 mm in height) is used as a chamber, which is ventilated with a fan.
For the iMS-100 radiosonde, the reference instruments are the MES-39535 (produced by Meisei) for temperature and the TU-CONV (produced by Meisei) for RH. The reference instruments that are different from those for the RS-11G radiosonde were chosen because the iMS-100 radiosonde has a special feature to communicate with the software through the IrDA (see Section 2.3.1 (2)). The reference data are imported to the software MGPS2 through the IrDA. The inside of baseline checker is ventilated by a fan. See Appendix F for more details.

2.4.2 Ground check with the 0 %RH and 100 %RH Standard Humidity Chamber

The manufacturer-independent SHC has a reference RH instrument and provides 0 %RH and 100 %RH under room temperature conditions. 0 %RH is provided using about 170 g of molecular sieve, and 100 %RH is provided using a sponge saturated with distilled water. A plastic airtight containers (150 mm in length 100 mm in width 98 mm in height) is used for both 0 %RH chamber and 100 %RH chamber. These chambers are ventilated with a fan to ensure that the RH in each chamber is spatially homogeneous.
The reference instrument for both temperature and RH is the "Rotronic HygroClip 2 /HC2-S" (hereinafter referred to as HC2). (See Appendix F for the specifications of the reference instruments.) A data logger Rotronic Hygrolog HL-NT and the software HW4 are used for collecting the reference data. The corresponding ground check data of the RS-11G radiosonde is collected using the MGPS2 software through radio wave transmission in the same way as the upper-air observation.
Every month, the reference instrument HC2 is compared against the HMP155 instrument (produced by the Vaisala) in a GC chamber under room conditions to monitor the temporal variability. The RH sensors of all the reference instruments (i.e., the HC2, TU-CONV, and HMP155) are also checked every year in conformity to the ISO/IEC 17025 at the Regional Instrument Centre (RIC) Tsukuba. There, these RH instruments are compared with the reference standard hygrometer (a chilled mirror hygrometer D-2-SR manufactured by GE Sensing EMEA) under the environment of 20 %RH, 40 %RH, 60 %RH, 80 %RH and 95 %RH. The temperature sensors of all the reference instruments (i.e., the HC2, MES-39535, and HMP155) are also calibrated at 15°C, 20°C, 25°C and 30°C conditions by comparing with the reference standard thermometer TS81A (manufactured by CHINO).
The RS-11G radiosonde that has passed a room-environment ground check (manufacturer's GC) is moved on to the 0 %RH SHC ground check. The sensor boom of the RS-11G radiosonde is placed in the 0 %RH chamber of the SHC for 10 minutes to obtain RH and temperature data of the RS-11G and HC2. Then, the sensor boom of the RS-11G radiosonde is placed in the 100 %RH chamber of the SHC for 10 minutes to obtain the data. The radiosonde and HC2 measurement data for 3 minutes between the 6th minute and the 9th minute are averaged, and the radiosonde bias relative to the HC2 is obtained. The same procedure will be taken for the iMS-100 radiosonde. More details of the ground check using the SHC are described in Appendix F.
The RS-11G radiosonde that has passed the SHC ground checks is stored in a desiccator which kept approximately 40 %RH environment. On the day of flight, the ground check under the room conditions using the manufacturer's GC is made with the ±0.5 K and ±7 %RH criteria. The results of

all these ground checks are reported to the GRUAN Lead Centre via the GRUAN RsLaunchClient. Regarding these transmission data by GRUAN RsLaunchClient, it is described in "User Guide of GRUAN RsLaunchClient" (*Sommer*, 2014).

2.5 Launching method

The prelaunch procedures are explained in Figure 2.6. The flight configurations are shown in Figure 2.7. When the surface wind is strong (typically more than 10 m/s), an unwinder is used at Tateno (Figure 2.6, Case (b)).

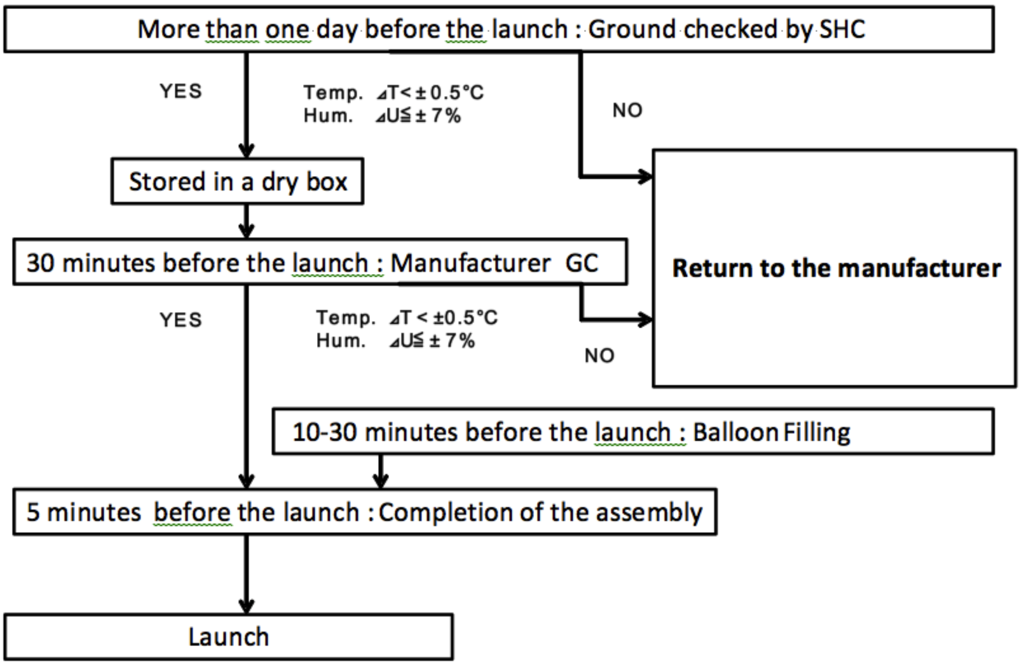

Figure 2.6: Prelaunch procedures for the RS-11G or iMS-100 radiosonde at Tateno.

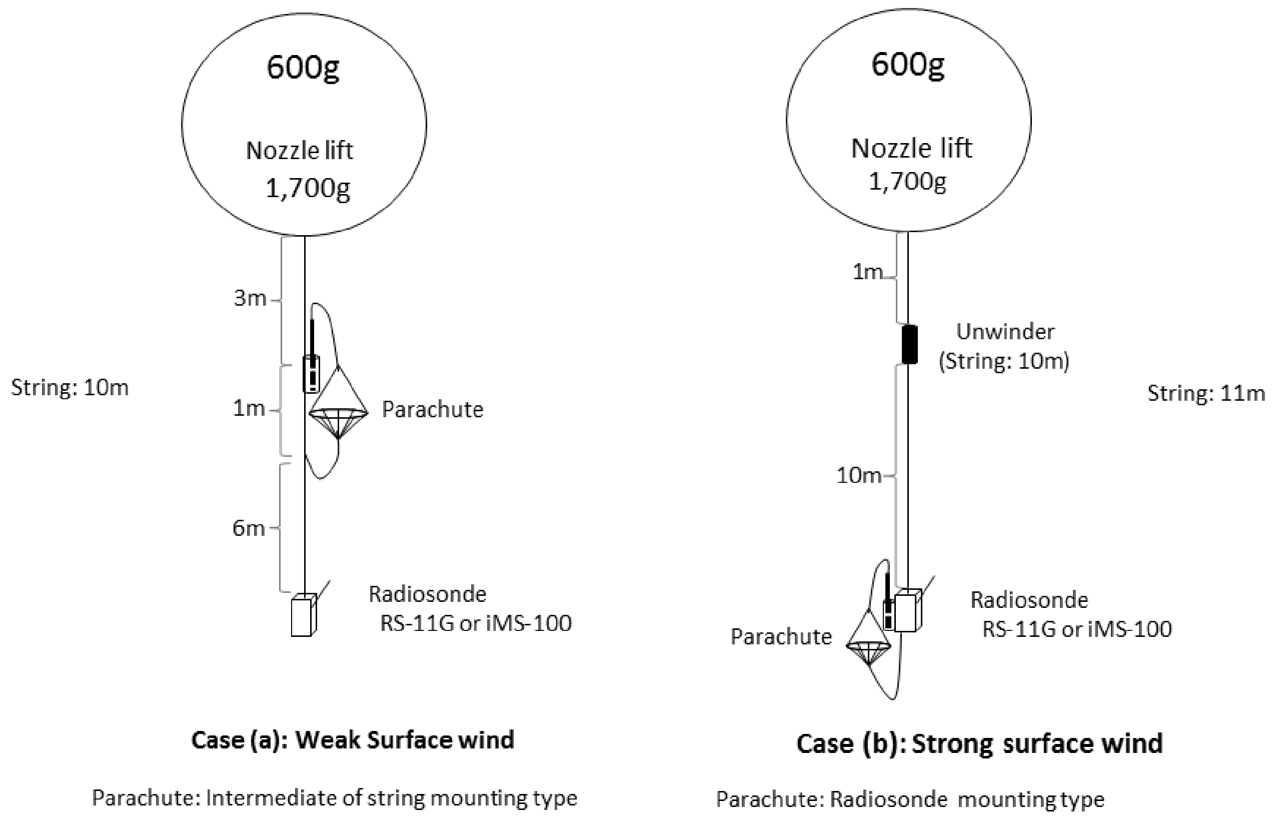

Figure 2.7: Flight configurations for (a) weak surface wind conditions and for (b) strong surface wind conditions (typically, $>5\,\mathrm{m\,s^{-1}}$) at Tateno.

3 Measurements from the RS-11G and iMS-100 radiosondes

In this chapter, we describe the calculation procedures of temperature, RH, geopotential height, pressure, and horizontal wind data from the RS-11G and iMS-100 radiosondes, and discuss the measurement uncertainty evaluations. We follow the approach outlined in the Guide to the expression of uncertainty in measurement by the working group 1 of the Joint Committee for Guide in Metrology (*JCGM/WG 1*, 2008) (see also *Immler et al.*, 2010; *Dirksen et al.*, 2014). There are two types of measurement error quantities, that is, systematic and random errors. A systematic error (or a measurement bias) is associated with the fact that a measured quantity value contains an offset. A random error, on the other hand, is associated with the fact that when a measurement is repeated, it will generally provide a measured quantity value that is different from the previous value; it can be reduced by increasing the number of measurements. For the radiosonde measurements, there are many factors that introduce systematic biases such as the radiation error for the temperature measurement. If systematic biases are properly characterized, they can be removed with confidence by correction procedures, which reduces the uncertainty of the measurement. The corrections described in the following are applied to the original data to compensate for some known systematic effects that significantly influence the measurement results. However, because the systematic errors are in general not completely characterized, all corrections involve uncertainty. We attempt to identify the likely sources of uncertainty and to estimate the total uncertainty.

3.1 Temperature measurements

3.1.1 Sensor material

The temperature sensor of the RS-11G and iMS-100 radiosondes is a thermistor. Figure 3.1 shows the external view of the sensor. The thermistor is coated with aluminum and silica dioxide to reduce the solar heating, and to minimize the correction amount for the solar heating. The reflectively is about 89% at 500 nm wavelength. The thermistor has a spherical shape (the maximum diameter is $\sim$0.43 mm) for its cross section with length of $\sim$0.8 mm. This smallness in size leads to a small heat capacity, and thus fast response even under low-air-pressure conditions.

3.1.2 Sensor calibration

The thermistor is calibrated during the manufacturing process. The thermistors are immersed in liquid solution in the calibration chamber together with a platinum resistance thermometer and are calibrated at 20 temperature points between -85°C to +40°C. From the 20 measurement points, 11 points including +40°C and -85°C are selected and used as the calibration points. The other 9 points are used to check the accuracy of the obtained calibration curve, by calculating the deviation. If the difference between the maximum deviation (positive) and minimum deviation (negative) is more than 0.3 K, the thermistor is rejected. Figure 3.2 shows an example of the relationship between the temperature and the resistance for a particular thermistor used in the RS-11G and iMS-100 radiosondes.
For the RS-11G and iMS-100 radiosondes, the resistance of the thermistor is detected as the frequency of temperature through the CR oscillating circuit on the radiosonde board. The relationship between the resistance and the frequency of temperature is obtained by the calibration using reference resistances. Figure 3.2 (right panel) shows an example of relationship between the frequency of temperature and the resistance for a particular thermistor – CR oscillating circuit system used in the RS-11G radiosonde.

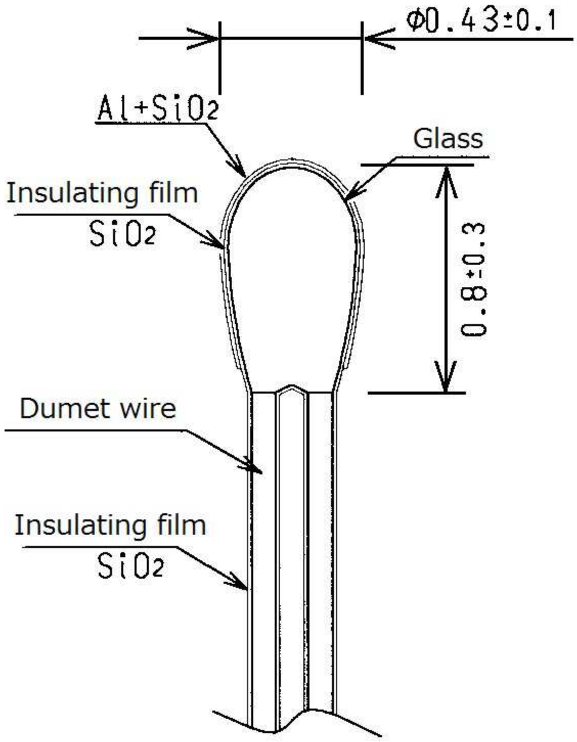

Figure 3.1: Appearance and dimensions of the temperature sensor of the RS-11G and iMS-100 radiosondes (unit: mm).

3.1.3 Calculation and correction procedures

The algorithm for the temperature calculation is shown in Figure 3.3. First, the resistance of the thermistor is obtained from the received frequency data for temperature. In the sounding software (MGPS2), the frequency of temperature is converted into the resistance, which is then converted to temperature (T_0) by using spline interpolation with factory calibration coefficients. More details are described in Appendix B.
The raw temperature data (T_0) may include the following errors.

1. Heat spike error due to, e.g., the balloon wake;
2. Solar radiation error;
3. Infrared radiation error;
4. Evaporative cooling error after passing through a cloud layer of supercooled droplets; and
5. Time-lag error due to a finite sensor time response.

Although the RS-11G and iMS-100 radiosondes were designed to minimize these errors as described in the following sections, there still exist some bias errors. The heat spike error and solar radiation error are considered to be the dominant errors for the radiosonde temperature measurements. Therefore, two correction processes, one for heat spike error and the other for solar radiation error, are applied to

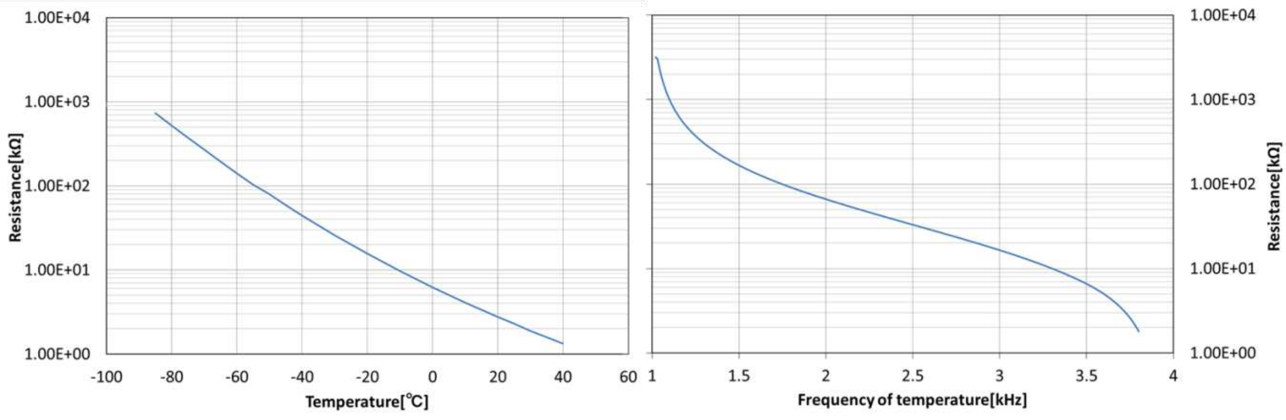

Figure 3.2: An example of the characteristics of the temperature sensor used for the RS-11G radiosonde. (Left) Relationship between the temperature and the resistance of the thermistor. (Right) Relationship between the frequency of temperature and the resistance. The obtained frequency is converted to the resistance, and the resistance is converted to temperature with these relationships.

obtain the final temperature data. Note that the heat spike filtering is applied depending on the flight configuration.
The evaporative cooling of the wetted sensor under cloudy conditions (e.g. *Immler et al.*, 2010) may result in a systematic error, but is not corrected because no appropriate correction algorithm is currently available. Also, the time-lag error and infrared radiation error are not corrected because these effects are considered negligible.

3.1.3.1 Heat spike filtering

Heat spikes affect daytime measurements of air temperature. The heat spikes result from air being heated by the sensor frame and radiosonde package, and possibly also result from passing through the warm wake of the balloon in association of the pendulum motion of the payload (*Shimizu and Hasebe*, 2010). Some of the recent radiosonde thermometers have become much more sensitive to small temperature fluctuations, and accordingly have started to show the effects of such heat spikes. The RS-06G radiosonde, the preceding model of the RS-11G, has a sensor frame that surrounds the thermistor (e.g. *Nash et al.*, 2011, Figure 3.4), which may be the main source of heat spikes. For the RS-11G and iMS-100 radiosondes, the top part of the frame enclosing the thermistor has been removed (Figure 3.4), keeping the thermistor open to the ambient air as much as possible. As a result, heat spikes are considerably reduced as shown in Figure 3.4. (Note that the thermistor, i.e., its material and dimension, and the solar radiation correction method are exactly the same between the RS-06G and RS-11G/iMS-100.) Therefore, the correction of removing heat spikes is not applied when the length of the string between the balloon and the radiosonde is long enough (e.g., 15 m with a 350 g balloon). However, when the length of the string is relatively short and the size of the balloon is relatively large (e.g., ∼10 m with a 600 g balloon) or a multiple-payload is launched, the heat spike filtering may be necessary. The heat spike filtering takes the following two steps. First, a minima-pass filtering with a certain time window (e.g., 3 sec) is applied, which picks up only minimum values within the time window. Second, the selected data are smoothed by a moving average procedure with

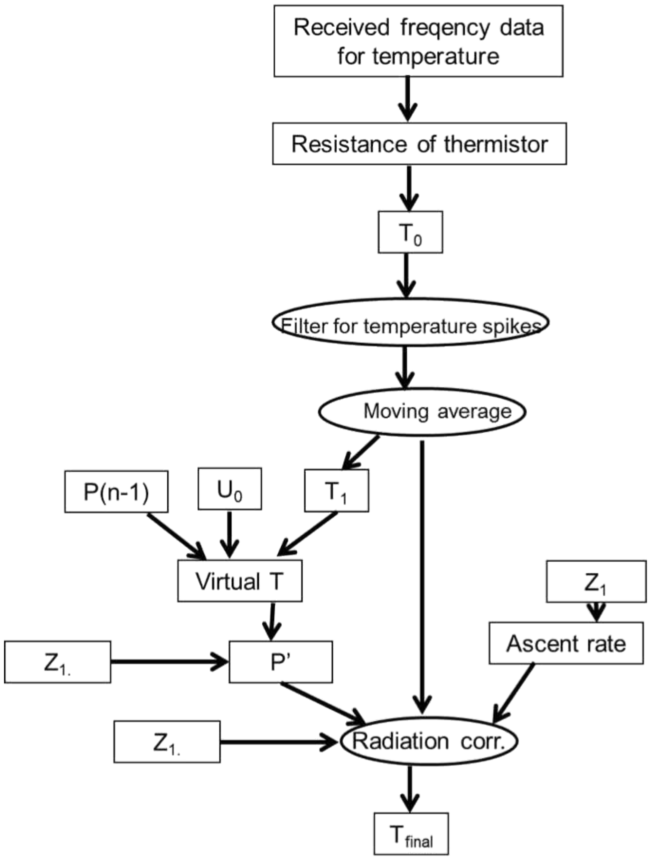

Figure 3.3: Schematic diagram of the processing steps and correction algorithms for the RS-11G and iMS-100 temperature measurements in the sounding software MGPS2. T_0 is the uncorrected temperature, U_0 is the uncorrected RH, P(n-1) is pressure one step before, P is preliminary pressure for radiation correction, Z_1 is the smoothed geopotential height, and T_{final} is the corrected, final temperature data.

the same time window.

Heat spikes generally become larger in magnitude at higher altitudes. Also, larger balloons and shorter strings tend to cause larger heat spikes. To evaluate the effects of heat spikes for the temperature measurements quantitatively, two comparison flights together with the Meisei Temperature Reference (MTR) sonde were conducted at Tateno, Japan. The MTR sonde is an upper-air temperature sensor of very fast response using a 10-μm-diameter tungsten wire (*Shimizu and Hasebe*, 2010; *Nash et al.*, 2011). The MTR can detect fine structures and small fluctuations in temperature profile with a response time of about 40 ms at 10 hPa at the typical balloon ascending rate of 5 m/s. Therefore, the MTR can detect the heat contamination from the balloon. Two sets of the RS-11G and MTR, with different lengths of the strings (i.e., 10 m and 15 m), were launched at the same time at Tateno at 14:30 LT on 6 February 2014. Figure 3.5 shows the obtained four temperature profiles (uncorrected values, i.e., T_0 in Figure 3.3). The solar radiation error of the MTR sonde is 0.4 K in the stratosphere and is much smaller than that of the RS-11G thermistor; see subsection 3.1.3.2 below. This is the reason why the raw-temperature difference of the RS-11G with respect to the MTR generally increases with altitude for both cases, and reaches $\sim$ 1.5 K in the stratosphere. Furthermore, we can see that high-frequency spiky oscillations exist for the shorter string flight (i.e., the 10 m case in comparison with the 15 m case) particularly in the stratosphere. A closer look of the MTR results around 25 km – 28 km (Figure 3.5, the right-hand-side panels) confirms warm (thus heating) spikes of up to ∼1K existing in the 10 m string flight. These irregular spikes are due to heat contamination from the balloon (*Shimizu and Hasebe*, 2010). This phenomenon increasingly occurs above 23 km altitude. The RS-11G results for the 10 m string case show high-frequency oscillations which, most probably, correspond to the heat spikes measured with the MTR. Therefore, we decided that we apply the heat spike filter with the window width of 3 sec above the 30-hPa level when a 10 m string and 600 g balloon are used during the daytime flights.

If a longer string and/or a smaller balloon is used, the parameters of the filter (i.e., the window width and the pressure level) should be changed. When using a 15 m string or longer with a 600 g balloon, no filtering is recommended. The filter settings can be determined by the user according to the sounding conditions such as string length and balloon size. (For the details, see the user's manual of the software MGPS2).

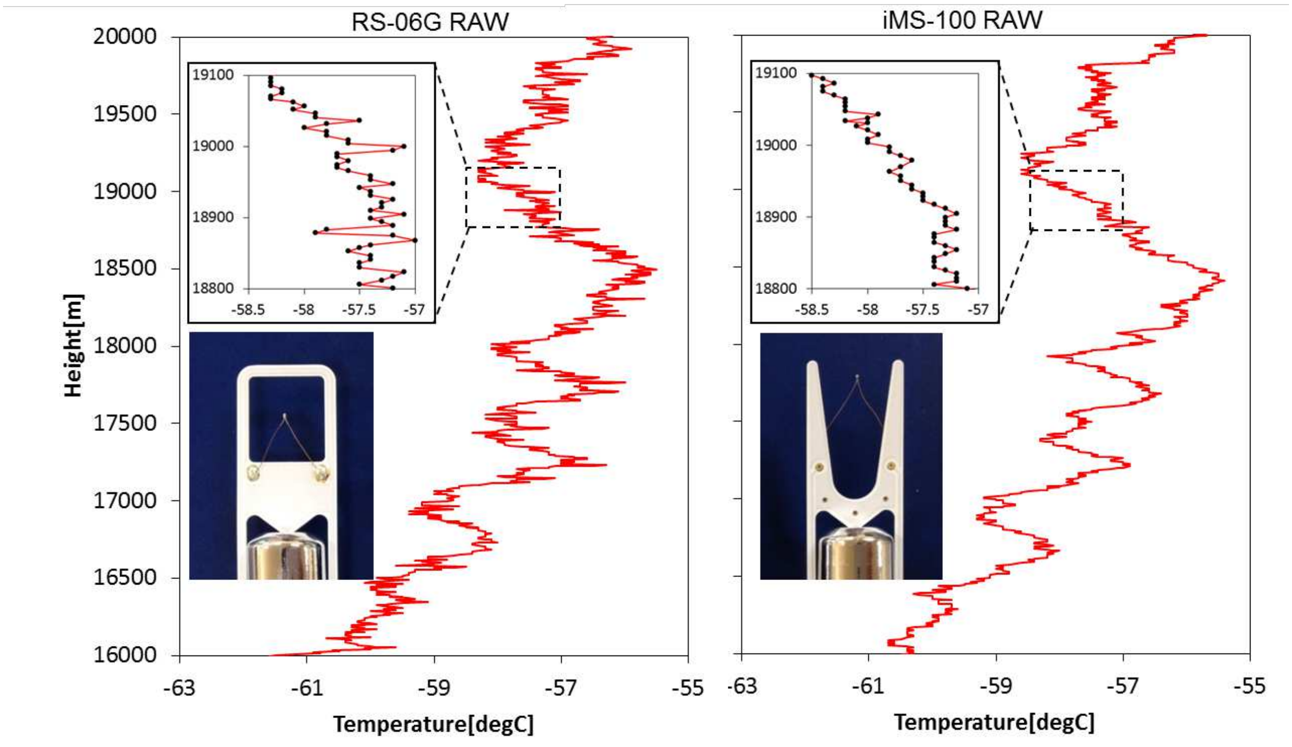

Figure 3.4: Characteristics of the heat spikes (the small fluctuations, which are superimposed on a-few-hundred-meter oscillations due to atmospheric gravity waves) between the RS-06G radiosonde (the previous model; left) and the iMS-100 radiosonde (right). In each panel, an enlargement of temperature profile between 18880 m and 19200 m is also shown (black dots are data at every second). The data were taken from a multiple-payload launch of the RS-06G and iMS-100 radiosonde at Moriya (35.9°N, 140.0°E), Japan, at daytime. The temperature sensor of the RS-06G radiosonde is surrounded by the supporting structure, while that of the iMS-100 radiosonde is more open to the ambient air, as shown in the photographs within the panels. But, the thermistor itself is the same in terms of material and dimension. The data sampling frequency is 1 s for both radiosondes.

3.1.3.2 Solar radiation correction

Daytime radiosonde temperature measurements are affected by solar radiative heating particularly at higher altitudes (e.g. *Nash et al.*, 2011; *Dirksen et al.*, 2014). The amount of solar radiative heating depends on the amount of absorbed radiation into the sensor, heat transfer with the ambient air, and the thermal conduction of the thermistor and lead wire. (Note that Meisei's thermistor is quasi-spherical, and thus sensor orientation is not a significant issue compared with other thermistors with different shapes.) The amount of solar radiative heating can theoretically be estimated by solving the heat-balance equation including these three factors (*JMA*, 1995, Appendix C), and the final solution becomes as follows:

$$\Delta t = \frac{(K(P_{st} + Q_2))}{Q_1} \tag{3.1}$$

where Δt is the amount of temperature correction, P_{st} [kcal s^{-1} or J s^{-1}] is the directly absorbed solar radiative energy, Q_2 [kcal s^{-1} or J s^{-1}] is the heat conduction of radiation energy through the lead wire, Q_1 [kcal s^{-1} K^{-1} or J s^{-1} K^{-1}] is the heat conduction to the ambient air through the thermistor surface, and K is a parameter representing attenuation of solar radiation by clouds. Q_1 and Q_2 are determined according to the characteristics of the temperature sensor. More details of the solar radiation correction are explained in Appendix C. To apply the solar radiation correction, the pressure, temperature, ventilation speed (estimated from the balloon ascent rate and pendulum motion speed), and solar elevation angle at the time of measurement are needed. As shown in Figure 3.3, uncorrected temperature and RH values and tentative pressure and geopotential height values are used for this purpose. The correction model explained above (and in Appendix C) is called the JMA solar radiation correction model hereafter.

Figure 3.6 shows the correction amount calculated based on the JMA solar radiation correction model which considers the effects of absorption of solar radiation, heat transfer between the ambient air and the temperature sensor, and thermal conduction of the lead wire, with the assumed balloon ascent rate of 6 m/s. Figure 3.6 shows that the correction amount becomes ∼2.0 K at 10 hPa at all solar elevation angles during the daytime.

3.1.3.3 Infrared radiation error

For the RS-11G and iMS-100 radiosondes, the solar radiation error is naturally corrected for daytime only. This section discusses the infrared radiation error of the two radiosondes and shows that it is negligible and not necessary to be corrected.

The budget of the infrared radiative energy for the case of a radiosonde temperature sensor is given by the following equations (*Nakamura et al.*, 1983).

$$P_{lt} = A_t \varepsilon_1 \left[\frac{1}{2}(\sigma\theta_{e_1}^4 + \sigma\theta_{e_2}^4) - \sigma\theta_t^4 \right] \tag{3.2}$$

$$\Delta T_l = \frac{P_{lt}}{Q_1} \tag{3.3}$$

where $P_l t$ [kcal s^{-1} or J s^{-1}] is infrared radiation energy, A_t [m^2] is surface area of the thermistor, ε_1 is the emissivity, σ is the Stefan-Boltzmann's constant, θ_{e_1} is the radiative effective temperature of downward longwave emission from the atmosphere, θ_{e_2} is the radiative effective temperature of upward longwave emission from the atmosphere and ground, θ_t is thermistor temperature, ΔT_l is the infrared radiation error in temperature, and Q_1 [kcal s^{-1} K^{-1} or J s^{-1} K^{-1}] is the heat conduction from the thermistor to the ambient air. For simplicity, the radiative effective temperature is treated as $\frac{1}{2}\sqrt[4]{\theta_{e_1}^4 + \theta_{e_2}^4} = \theta_e$. The value of θ_e varies significantly depending on atmospheric conditions. With the assumption that $\theta_e - \theta_t$ = 10 K (*Kobayashi et al.*, 2012b), the infrared error is estimated to be ΔT_l = 0.002 K. If the emissivity changes from 0.1 to 0.8 due to icing on the thermistor, the infrared error can become as large as ~0.02 K, which is still substantially small compared to, e.g., the solar radiation error. Therefore, the infrared radiation error is negligible and needs not to be corrected.

3.1.3.4 Evaporative cooling error

During the flights through liquid cloud layers, the thermistor may be coated with water or ice; this would introduce errors in the temperature measurement above those cloud layers due to evaporative cooling until water or ice completely evaporates. This effect may cause erroneous super-adiabatic lapse rates (e.g. *Hodge*, 1956; *Dirksen et al.*, 2014; *JMA*, 1995). Note that, while the radiosonde is flying inside those cloud layers, the condensate on the thermistor would be close to the equilibrium with the ambient air, so that it is unlikely that the temperature measurement is substantially affected.
It is difficult to quantitatively estimate the evaporative cooling error because the error depends on the unknown condensate amount attached to the thermistor, and the evaporating speed, temperature and RH above the cloud layer. Thus, currently, correction for the evaporating cooling is not applied for the Meisei RS-11G and iMS-100 GRUAN data product.
For the TEMP message data sent through the GTS from the JMA stations, however, the process that removes super-adiabatic lapse rates is applied according to the JMA guideline (*JMA*, 1995).

3.1.3.5 Sensor response time

The response time of the temperature sensor is evaluated in the manufacturer's laboratory as 0.374 s at 1000 hPa with 5 m s^{-1} airflow. The response time depends on the air density and air flow (ventilation speed) around the sensor, and becomes slower at lower pressure conditions. The response time t of temperature sensors is calculated from the following equation,

$$t = t_0(\rho \cdot v)^n \tag{3.4}$$

where t_0 is the response time at 1000 hPa, ρ is air density, v is ventilation speed, and n is a constant ranging from 0.4 and 0.8 depending on the shape of the sensor and on the nature of air flow (laminar or turbulent) (*WMO*, 2008). According to Eq. 3.4, typical response times are 0.94 s at 100 hPa and 2.36 s at 10 hPa. The response of the temperature sensor is thus fast enough for balloon soundings so that the correction is not applied for the Meisei RS-11G and iMS-100 GRUAN data product.

3.1.4 Uncertainty budget of the temperature measurements

Following *JCGM/WG 1* (2008) and *Dirksen et al.* (2014), the uncertainties for the Meisei RS-11G and iMS-100 temperature measurement have been estimated and are listed in Table 3.1. See below for the uncertainty calculation for each factor.

(1) Calibration error

Table 3.1: The uncertainty sources and values for the Meisei RS-11G and iMS-100 temperature measurement. The values are described as k=1.

Components	Value [K]	Reference	Corrected	Error classification
Thermistor calibration	$0.3/\sqrt{3}$	Fig. 3.7	–	systematic
Variability in the calibration chamber	$0.13/\sqrt{3}$	Fig. 3.8	–	systematic
Solar radiation (albedo)	$\|I_{clear} - I_{cloudy}\|/(2\sqrt{3})$	Fig. 3.9	Corrected	systematic
Solar radiation (ventilation)	ΔT (Ascent rate +3 m/s)/$\sqrt{3}$	Fig. 3.9	Corrected	systematic
Heat spike	0	Fig. 3.4	Uncorrected	systematic, random
Evaporative cooling	–		Uncorrected	systematic

Figure 3.7 shows the variability of temperature sensors at the factory calibration process for temperatures, +35°C, 0°C, -40°C, and -80°C for one year. It is confirmed that the variability is within ±0.3 K at 0°C and smaller at other temperatures throughout the year. These data are always monitored at the factory calibration process by the manufacturer.

In addition to the uncertainty derived from the calibration procedure, the spatial variability in the calibration chamber is a possible source of uncertainty. This is because the calibration procedure is conducted for 10 sensors at one time as shown in Figure 3.8. The spatial variability is investigated using the calibration data from 43638 temperature sensors. As shown in Figure 3.8, the spatial variability in the calibration chamber is well within 0.13 K between -85°C and +40°C.

(2) Heat spike filtering

The uncertainty from the heat spike filtering is determined by using the standard deviation of the correction amount, following *Dirksen et al.* (2014). The typical uncertainty values of the heat spike filtering is 0.1∼0.2 K for a 10 m string and a 600 g balloon. As the uncertainty from this factor depends on the flight configuration and actual flight conditions, it is not included in the total uncertainty budget (Table 3.1.)

(3) Solar radiation correction

The solar radiation correction is the largest source of uncertainty in the temperature measurement particularly in the stratosphere. There are two major factors for the uncertainty of this correction: (a) Uncertainty of the assumed surface and cloud albedo; and (b) uncertainty of the assumed ventilation speed around the sensor. Also, there is a potential factor which is the uncertainty of the JMA solar radiation correction model itself.

The JMA solar radiation correction model assumes that the surface/cloud albedo is constant at 20%. However, the actual albedo during the balloon flight depends on the surface and cloud conditions. The surface albedo ranges from less than 10% for dark ocean surface up to 90% for fresh snow cover, whereas cloud albedo typically ranges from 40% to 80% (*Dirksen et al.*, 2014). Figure 3.9 shows the correction amount at 100 hPa and 10h Pa for albedo values of 10%, 20%, and 60%. The results indicate that the correction amount is too small when highly reflective clouds are present, and the final temperature might have a warm bias of ∼0.5 K in the stratosphere. The other major uncertainty source of the solar radiation correction is the ventilation effect that depends on the balloon ascent rate. The solar radiation correction uses the ascent rate as the ventilation speed in Eq. C.12-C.14 in Appendix C. In fact, the ventilation may be stronger than the ascent rate because of the pendulum motions of the payload. Figure 3.9 shows the correction amount for the ventilation speed as the ascent rate (e.g., 6 m/s) plus 3.0 m/s. The possible bias by this effect is ∼0.2 K. Because the ventilation speed is always larger than the ascent rate, this additional ventilation always results in cooling effect.

The final major uncertainty source is the JMA solar radiation correction model itself. We also evaluated the solar radiation error using the results from the simultaneous MTR flights shown in Figure 3.5. Figure 3.10 shows the correction amount and temperature difference between RS-11G and MTR. The MTR sonde is known to have much smaller effects of solar radiative heating, and the heating error has been estimated as less than 0.5 K even at 30 km altitude (*Shimizu and Hasebe*, 2010). As shown in Figure 3.10, the temperature difference between the RS-11G and the MTR results and the RS-11G correction amount agree within ±0.4 K. Exactly speaking, the correction amount becomes greater than the RS-11G-to-MTR difference around 30 km because the MTR actually has a small effect of solar radiation heating around this altitude region. We conclude that the JMA solar radiation correction model is reasonable, and will not consider it in the uncertainty budget in Table 3.1.

To validate the above uncertainty estimate for the solar radiation correction, we also made an experiment in a vacuum chamber with a quartz glass window which is situated outside and lit by the sun at the Meisei factory in Isesaki (36.26°N, 139.20°E), Japan, as shown in Figure 3.11. In the chamber, two thermistors are situated. One of the thermistors directly receives the solar radiation, and the other is not illuminated by the sun by using a shade. The vacuum chamber is oriented perpendicular to the incoming solar radiation. There is a shutter in front of the chamber's window so that the warming of the chamber can be prevented until the experiment starts. To ensure a proper airflow of ∼6 m/s, the base holding the two thermistors is rotated at a constant speed of 800 – 900 rpm (revolution per minute). The air pressure in the chamber is decreased by a vacuum pump. The open-and-close cycle of the shutter is repeated at each pressure condition. The test conditions are as follows:

- Pressure [hPa]: 1017, 509, 254, 128, 60.6, 21.9, and 10.2
- Solar radiation flux [W m^{-2}]: 1070 (±19) (measured with the illuminometer)
- Ventilation [m s^{-1}]: 6.01 (±0.35)

It should be noted that the uncertainty of ventilation (±0.35 m/s) is obtained from the variations among several measurements, i.e., assuming that the air in the chamber is at rest, and does not include the effect of potential stirring of the air in the chamber due to the rotating object. The actual ventilation speed at the sensor may be smaller than that calculated from the rotation speed, and thus its uncertainty may be greater, in particular, to the negative direction.

Figure 3.12 shows an example of the experimental results. When the shutter is opened (after 23 minutes), both thermistors is warmed up. But, the opened thermistor reading becomes warmer than the shaded thermistor reading because of the solar radiation heating. The shaded thermistor measures the air temperature in the chamber, and the temperature difference indicates the amount of solar radiation heating. Figure 3.13 summarizes the results for all the pressure conditions, together with the JMA solar radiation correction curve which was derived using the same measurement conditions of this experiment (i.e., solar radiation flux = 1070 W m^{-2}, ventilation speed = 6.01 m s^{-1}, and temperature = 25°C). We can see that the JMA solar radiation correction curve agrees with the experimental results within the measurement uncertainty.

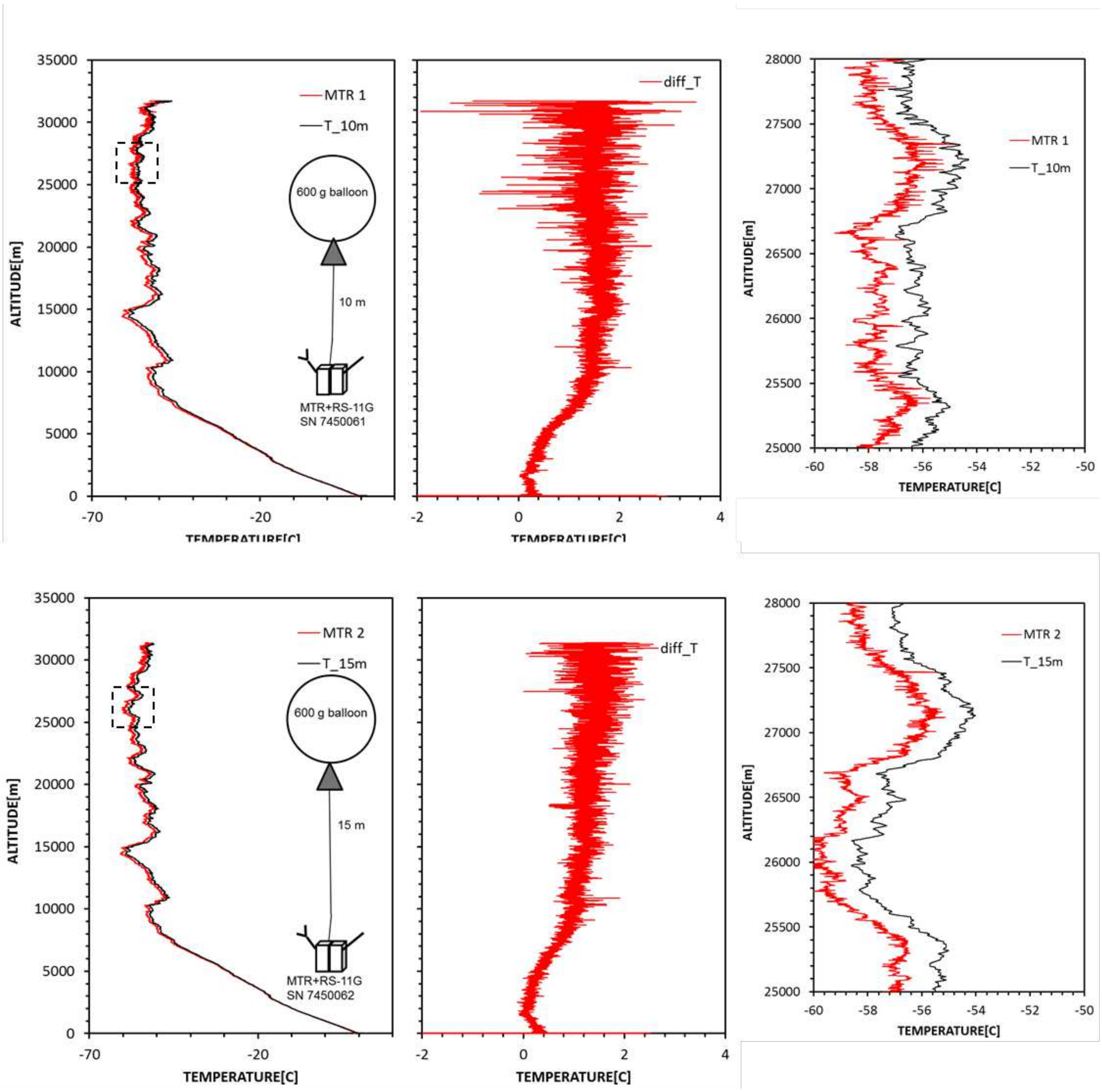

Figure 3.5: Temperature profiles obtained from two sets of MTR and RS-11G multiple payloads simultaneously launched at Tateno at 14:30 LT on 6 February 2014. One MTR-RS-11G payload is connected to a 600 g balloon with a 10 m string (top), and the other is with a 15 m string (bottom). (Left panels) Black lines indicate the RS-11G raw temperature profiles, and red lines indicate the MTR temperature. Note that the RS-11G temperature data is raw meaning that the heat spike filter and the solar radiation correction are not applied. (Center panels) Temperature difference of the RS-11G results with respect to the MTR results. (Right panels) A closer look at the region between 25 km and 28 km.

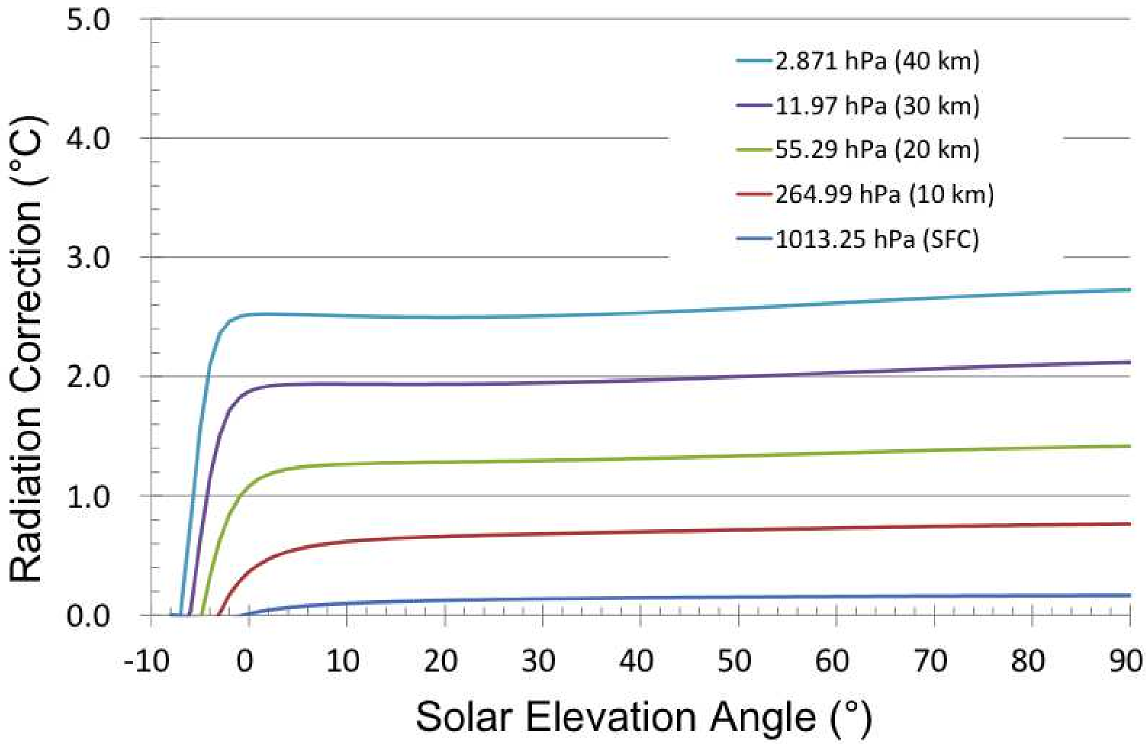

Figure 3.6: Amount of the solar radiation correction for the RS-11G and iMS-100 temperature measurements at different pressure levels. The correction amount is calculated with the JMA correction model (JMA 1995) which considers the effects of absorption of solar radiation, heat transfer between the ambient air and the temperature sensor, and thermal conduction of the lead wire. The balloon ascent rate is assumed to be $6\,\mathrm{m\,s^{-1}}$.

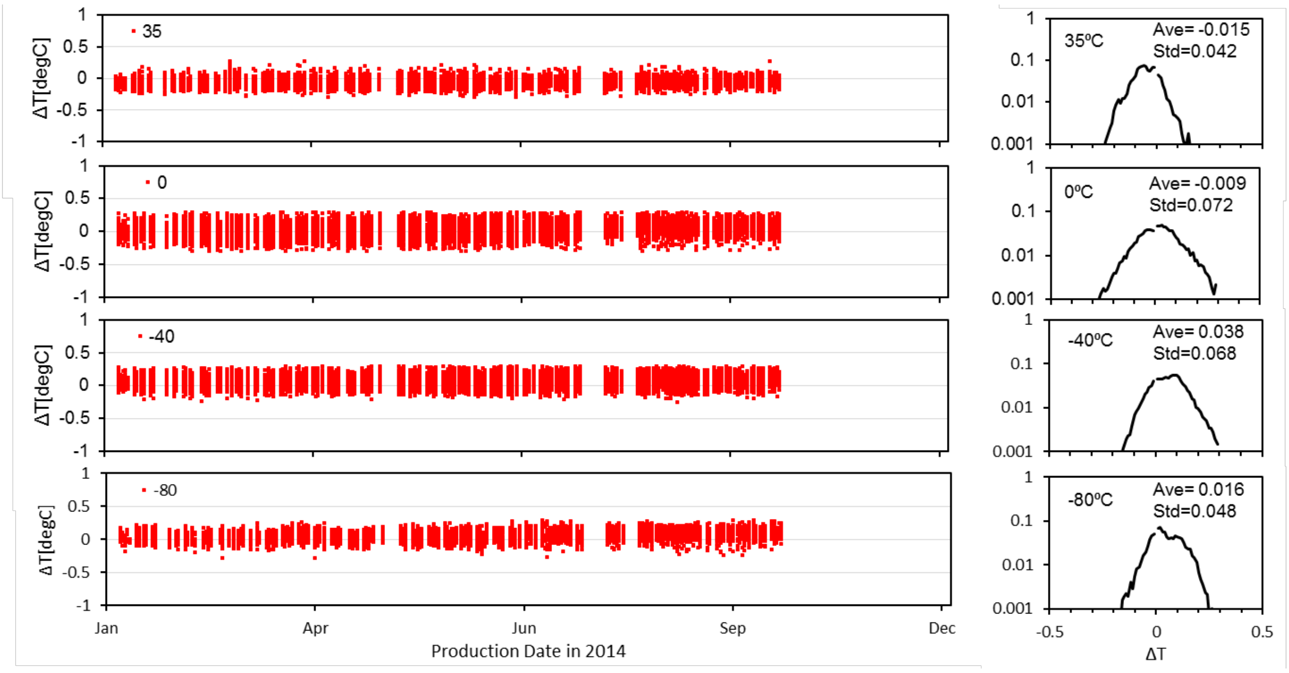

Figure 3.7: Variability of the temperature sensors at the factory calibration process, from top to bottom, +35°C, 0°C, -40°C, and -80°C. (Left) Time series of difference of the temperature measurement of individual radiosonde sensors with respect to the simultaneous measurement of a reference instrument (see Section 5 and Figure 5.1 for the details) during 2014.These data were obtained at the actual production process. All calibration data produced during this period were plotted. (Right) The frequency distribution of the temperature difference.

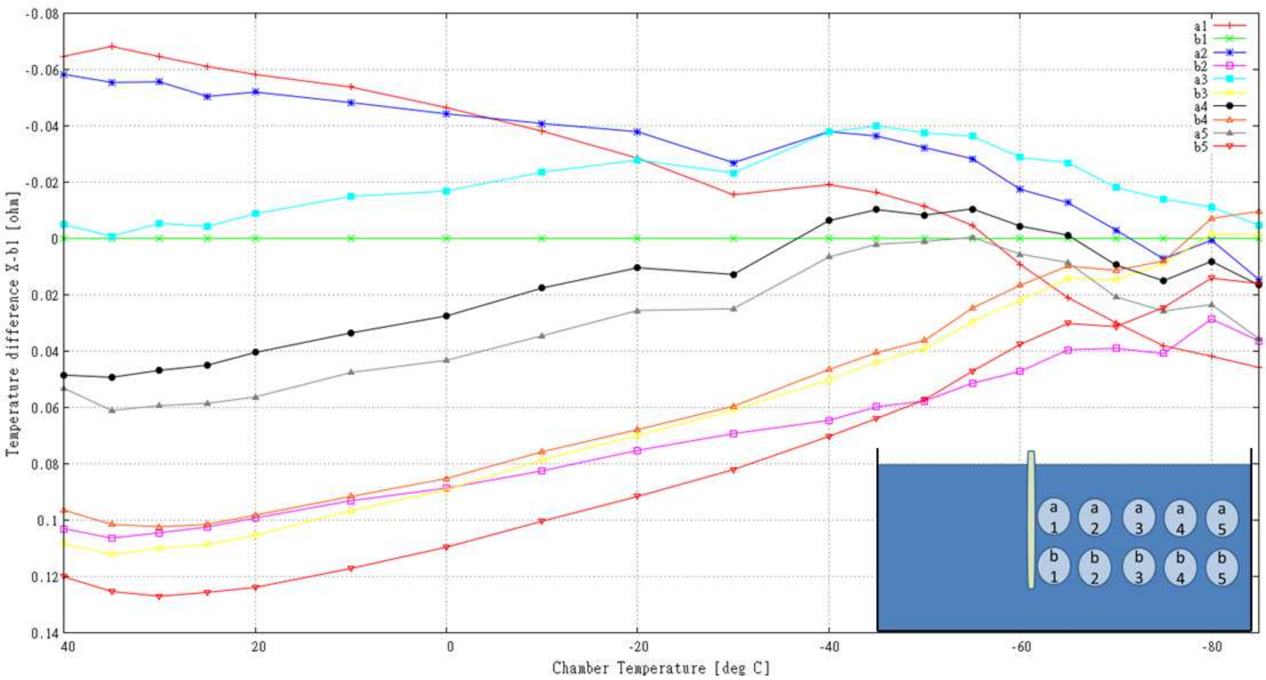

Figure 3.8: Spatial variability in the calibration chamber. The measurement points in the calibration chamber are distributed to 10 areas (a-1 to a-5, and b-1 to b-5) as shown in the schematic. The bar at center indicates the reference thermometer. The thermistors at positions a-1 and b-1 were closest to the reference sensor. Shown are the differences between the measurement at point b-1 and the measurement at the other points in the calibration chamber at various temperatures between +40°C and -85°C.

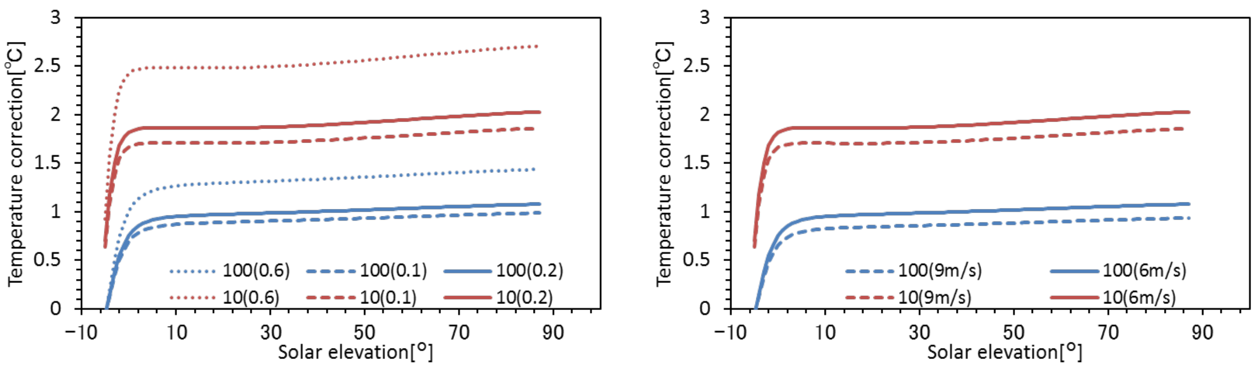

Figure 3.9: Dependence of the solar radiation correction on the assumed albedo and ascent rate (ventilation affect). (Left) The correction amount for albedo of 0.1 (e.g., for sea surface), 0.2 (assumed in the actual correction algorithm), and 0.6 (e.g., under cloudy condition) at pressures of 100 hPa and 10 hPa (see the legends in the panel). (Right) The correction amount for ventilation speeds of 6 m s^{-1} and 9 m s^{-1} at pressures 100 hPa and 10 hPa, respectively.

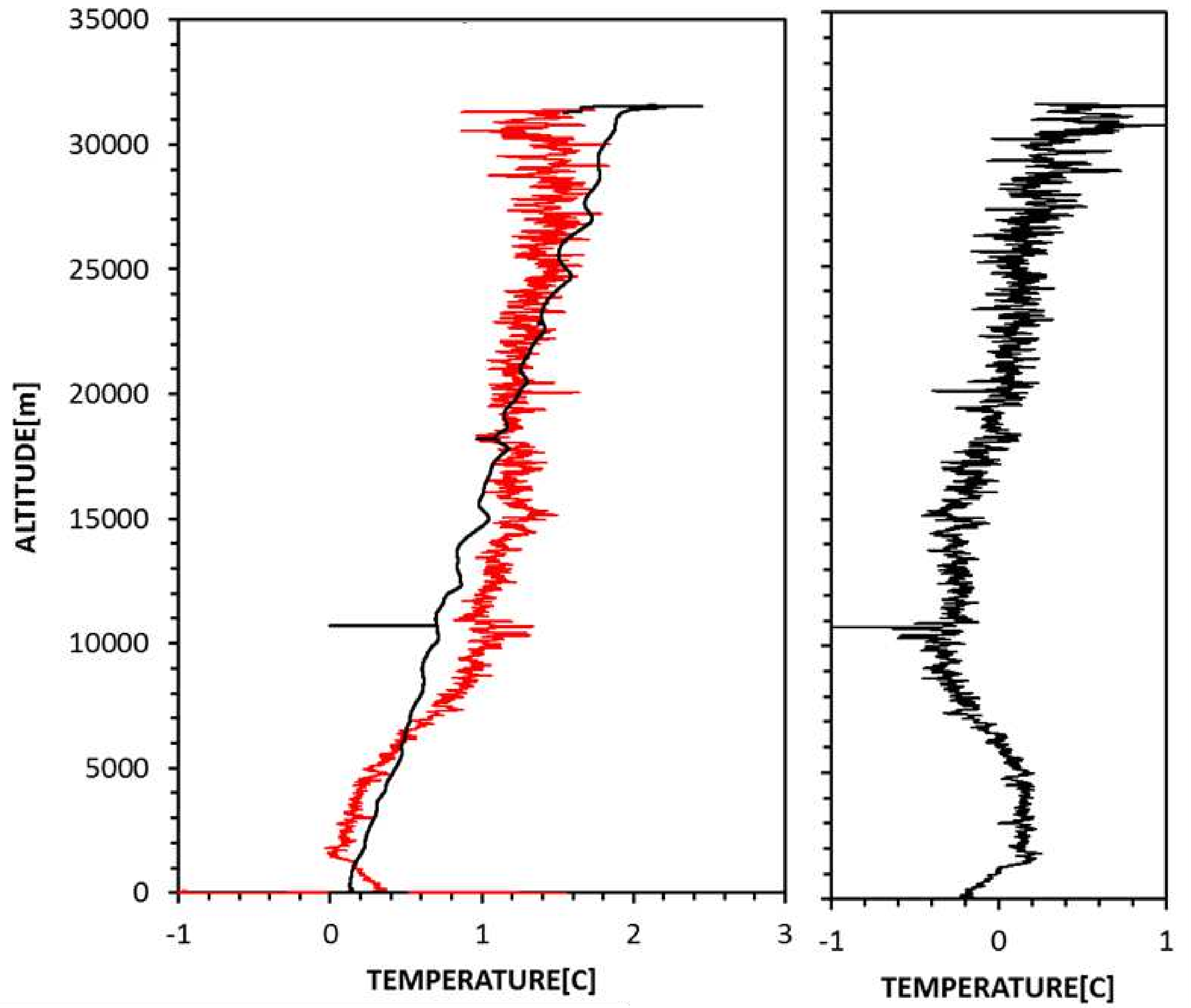

Figure 3.10: (Left) Correction amount for the RS-11G data by the JMA solar radiation correction model (black) and the temperature difference between the MTR and RS-11G results (red) for the multiple-payload flight shown in Figure 3.5 with a 15 m string. (Right) Difference between the two curves in the left panel.

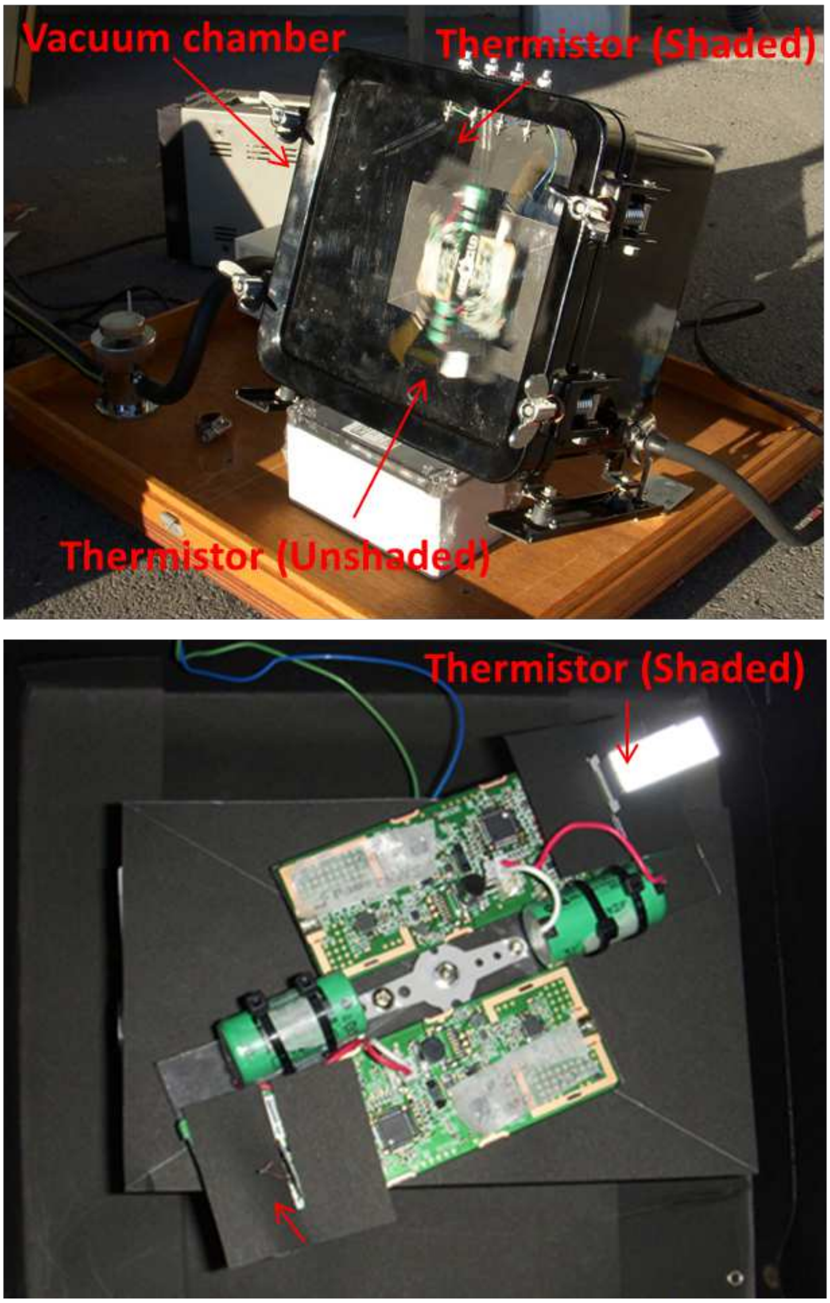

Figure 3.11: The experimental setup to evaluate the solar radiation correction model. See text for the details. Black-colored sheet with very low reflectivity is placed under the sensors and on the inner walls of the chamber to prevent solar light reflection to the sensors.

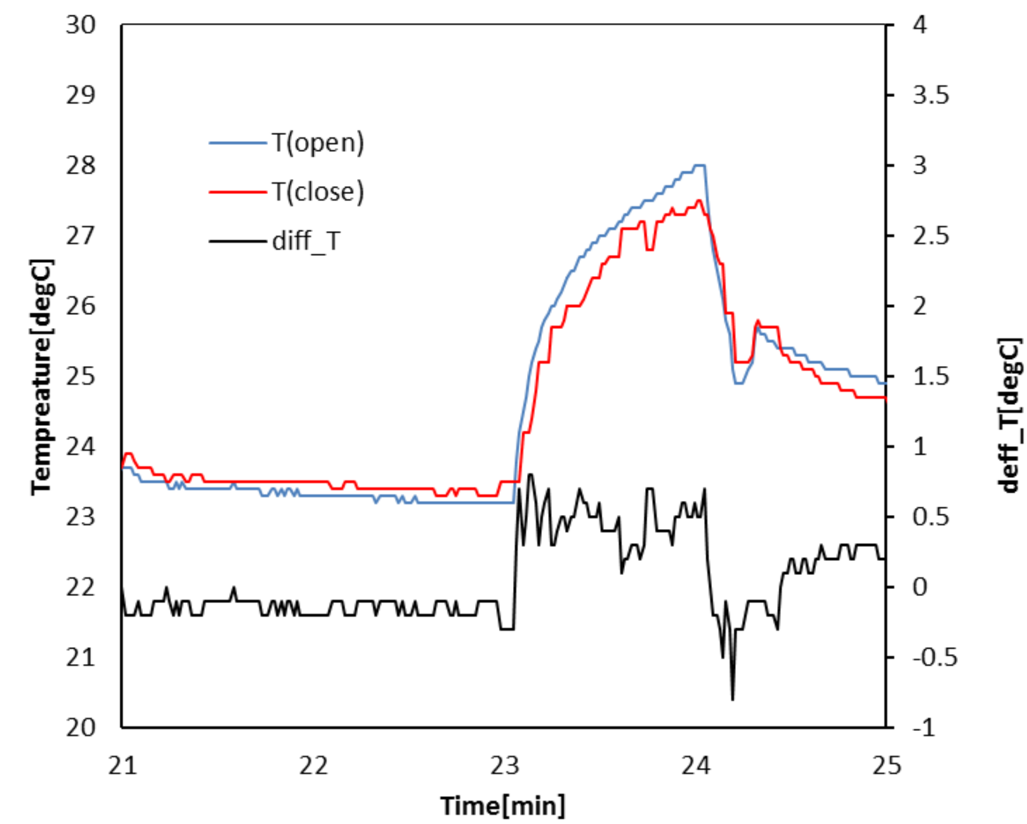

Figure 3.12: Example of the experimental radiation-chamber results at a pressure of 100 hPa. Red, blue, and black curves indicate the temperature from the opened thermistor, that from the shaded thermistor, and their difference, respectively. The difference corresponds to the amount of solar radiation heating.

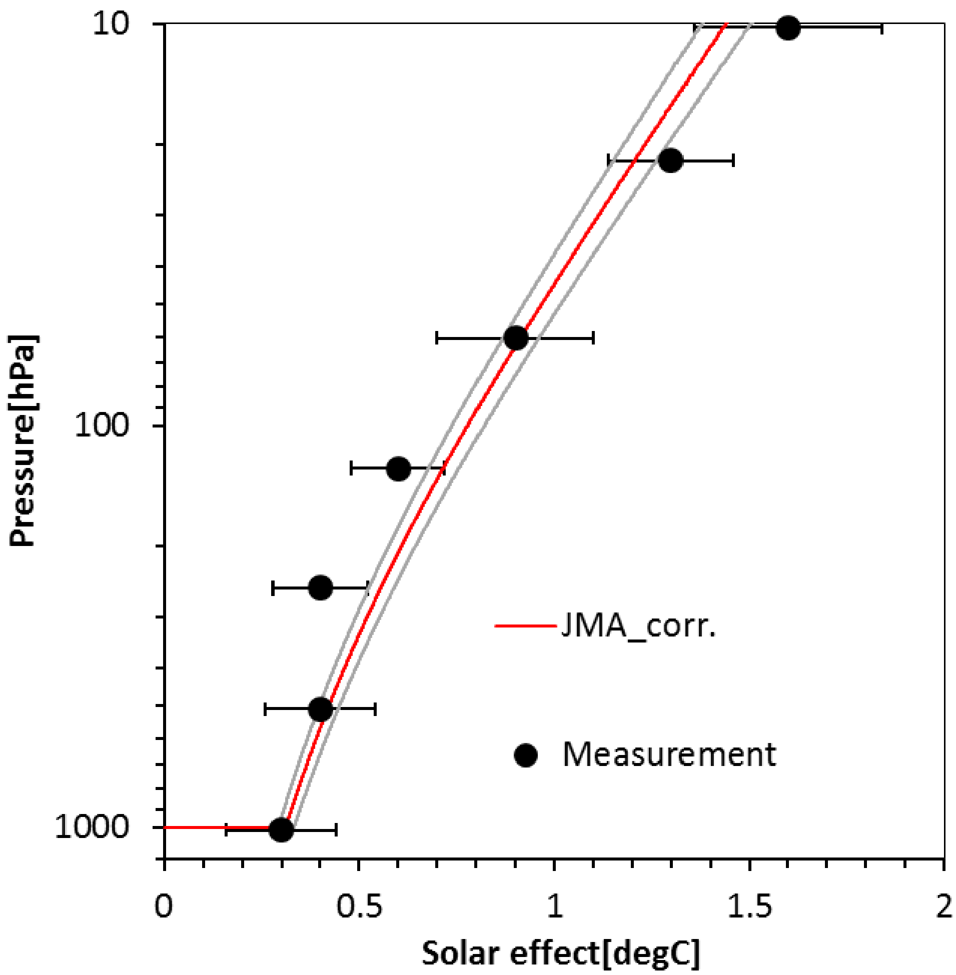

Figure 3.13: Pressure dependence of the solar radiation error for the RS-11G (and iMS-100) thermistor. Black dots indicate the experimental results, and the attached error bars are twice of the standard deviation of temperature measurement differences between the irradiated and shaded sensors. The red curve indicates the amount of solar radiation correction by the JMA model using this experimental condition, solar radiation = 1070 W m^{-2} and ventilation = 6.01 m s^{-1}. Gray curve indicates the uncertainty (k=2) of the solar radiation correction which is derived from the uncertainty of air speed measurement ($\pm$0.70 m s^{-1}) and radiation measurement ($\pm$19 W m^{-2}).

(4) Total uncertainty of the RS-11G and iMS-100 temperature measurement
The total uncertainty depends on altitude and observation conditions, and its amount generally increases with altitude. Figure 3.14 shows an example of the measurement uncertainty profile of temperature for a daytime observation, launched at 14:00 LT on 07 October 2014 14:00 LT, at Lindenberg (52.21°N, 14.12°E), Germany. The uncertainty increases with altitude and reaches 0.8 K at 30 km. Up to ∼15 km, the uncertainty is dominated by the calibration uncertainty. In the stratosphere, the uncertainty from the solar radiation correction is the main source of uncertainty. Note that the surface/cloud albedo is assumed to be constant at 20%, which is not the case for actual surface and cloud conditions during the flight, and that the ventilation speed around the sensor is assumed to be equal to the ascent rate, i.e., not including the additional ventilation by the pendulum motions of the payload. It is considered that these uncertain parameters, the albedo and the ventilation speed, cause large uncertainty in temperature measurements. It is noted that the uncertainty from the infrared radiation error and time-lag error is negligible and not considered here. Also, the uncertainty from heat spikes is not considered because this flight was conducted with a long string of 30 m. If the payload configuration is different, e.g., with a much shorter string and/or with multiple payload with a rig, additional uncertainty would arise.

3.2 Relative humidity measurements

3.2.1 Sensor material

The RS-11G and iMS-100 radiosondes are equipped with the same thin-film capacitive RH sensor. Figure 3.15 shows the external view of the RH sensor. This thin-film capacitive sensor consists of a thin hydrophilic polymer layer on a glass substrate, which acts as the dielectric of a capacitor. The capacitance changes in response to the number of water molecules permeating from the ambient air into the polymer layer. The capacitive sensor on the RS-11G and iMS-100 radiosondes measures the change of capacitance as electric frequency signals (frequency of humidity) by the CR oscillation circuit described in Section 2.3. The relationship between the frequency of humidity and the RH of the ambient air is determined by factory calibration procedures. The RH sensor of the RS-11G and iMS-100 radiosondes has a protective cap coated with aluminum vapor deposition to prevent the sensor from icing of supercooled droplets and heating by solar radiation (see Figures 2.1-2.4). Potential negative effects of having a protective cap include trapping of water droplets, whose impacts are reduced by applying a contamination removal filter (see Section 3.2.3). In addition, the iMS-100 radiosonde is equipped with a dedicated thermistor on the RH sensor for the temperature correction of the RH data.

3.2.2 Sensor calibration

The relationship between the frequency of humidity and the value of RH is approximated with a cubic function. A set of four sensor-specific calibration coefficients of the cubic function is obtained for each sensor by a calibration procedure, which is conducted in the factory at 15 %RH, 30 %RH, 50 %RH, 70 %RH, 90 %RH, and 95 %RH at a constant air temperature of +25°C. Figure 3.16 shows an example of the relationship between the frequency of humidity and the value of RH for a particular sensor. In this calibration process, the reference RH values are obtained from a reference platinum resistance thermometer (R900-F25 by CHINO) and a reference chilled mirror hygrometer (D-2-SR by General Eastem for the RS-11G, or DewStar S-2 by SHINYEI for the iMS-100). For the D-2-SR (for RS-11G), the water vapor pressure equation by *Buck* (1981) is used, while for the DewStar S-2 (for

iMS-100), the equation by *Hyland and Wexler* (1983) is used. For both equations, the enhancement factor "f" is set to be unity. Because the calibration is made only at 25°C, the difference due to the use of different water vapor pressure equations is negligible (the difference among different water vapor pressure equations is non-negligible only at very low temperatures; see e.g., *Nash et al.* (2011), their section 8.2.5, and *Murphy and Koop* (2005)). As described later, for both RS-11G and iMS-100, the Hyland-Wexler equation is only used for all the data processing, i.e., for the Temperature-Humidity Dependence correction (Section 3.2.3 (3)), for the sensor versus air temperature correction (Section 3.2.3 (4)), for the pressure calculation (Section 3.3.2), and for creating the GRUAN data product (Appendix H).
According to the WMO Commission for Instruments and Methods of Observation (CIMO) guide (*WMO*, 2008), by convention, RH should be calculated with respect to liquid water even at air temperatures below 0°C. In addition to normal manufacturer's calibration as described above, at Tateno site, new calibration coefficients are determined by using the data for 0 %RH and 100 %RH during the SHC checks. This process enables to improve the measurement accuracy around 0 % RH and 100 %RH because these points are the extrapolated values for the original manufacture's calibration. Note that all calibrations are conducted at +25°C or room temperatures. The temperature dependence correction procedure will be described in Section 3.2.3 (3).

3.2.3 Calculation and correction procedures

The algorithm to obtain the RH data is shown in Figure 3.17. The received frequency data for humidity is converted to the capacitance values and then to the raw RH values (U_0) by using the sensor-specific factory calibration coefficients. More details to obtain the raw RH values are described in Appendix D. In general, thin-film capacitive RH sensors on radiosondes are subject to several sources of errors, including slow responses at low temperatures, contamination errors caused by supercooled cloud droplets, bias errors related to non-water molecules being absorbed into the hydrophilic polymer layer, and bias errors due to the temperature difference between the RH sensor and ambient air (e.g. *Dirksen et al.*, 2014). Thus the raw radiosonde RH data (U_0) may need the following corrections or filtering.

1. Contamination removal filter for rain and cloud droplets (Contami_corr)

2. Time-lag correction (TL_corr.)

3. Temperature-Humidity Dependence correction (TUD_corr.)

4. Sensor versus air temperature correction (Ts/Ta _corr.)

5. Hysteresis consideration

6. Sensor aging consideration

For the RS-11G and iMS-100 radiosondes, the corrections (1), (2), (3), and (4) are considered necessary and thus are applied to obtain the final RH data. Note that for the former models of the Meisei radiosonde, these corrections are not necessarily considered. For example, the RS-06G radiosonde applies correction (3) only (e.g. *Sugidachi and Fujiwara*, 2013).

3.2.3.1 Contamination removal filter for rain and cloud droplets (Contami_corr)

During soundings under rainy conditions, water droplets or ice may attach to the RH-sensor cap and/or the sensor arm. After the radiosonde passes through the cloud layer and enters a drier region, the RH sensor may quasi-periodically be affected by the air flow directly capturing additional water vapor from the wet structures surrounding the sensor, resulting in wet biases in its measurements. The RH profile affected by this wet contamination error shows spiky structures or small-vertical-scale oscillations, similar to the heat spikes in contaminated temperature measurements. Therefore, the following procedure is applied to remove contaminated RH measurements.

1. The raw humidity profile is separated into the high-frequency and low-frequency components by using the time response of RH sensor as the cut-off frequency with a window width of 60 s.

2. The time-lag correction (explained below) is applied to both the high-frequency and low-frequency components.

3. The RH offset by the contamination is determined by applying a minimum filter, which is similar to heat spike filter for temperature measurements, with a window width of pendulum frequency (depending on the string length: 6.3 s for the string of 10 m, 7.8 s for the string of 15 m) to the high-frequency component.

4. The filtered high-frequency component is added to the low-frequency component to obtain the contamination-corrected RH (U_1).

3.2.3.2 Time-lag correction

Thin-film polymer RH sensors show slower responses at lower temperatures, which result in smoothing of the RH profile and a major error component in the upper troposphere and above (*Miloshevich et al.*, 2004). The response time of the RS-11G and iMS-100 RH sensor, defined as the time required to respond by 63% to a sudden change, has been evaluated by laboratory experiments at some temperature points in a thermostatic chamber. Figure 3.18 shows the response time measured at -60°C, -40°C, -20°C, and 0°C. The response time increases exponentially at lower temperatures. The obtained relationship for the stepwise change from dry to wet condition can be expressed as

$$\tau(T) = 0.1537e^{-0.087T} \tag{3.5}$$

where T is the sensor temperature. Although the response time is different by the condition (the response time from wet to dry is slower than that from dry to wet), we use the values from dry to wet condition in any case to prevent from over correction (over-shooting). Also, the dashed lines in Figure 3.18 indicate the uncertainty derived from the standard deviation from the 69 measurements at each temperature points, which can be approximately expressed as

$$u(\tau) = 0.25\tau \tag{3.6}$$

Using the response time values, the time-lag error is corrected with the following equation (*Miloshevich et al.*, 2004).

$$U_1(t) = \frac{U_0(t) - U_0(t - \Delta t)e^{-\Delta t/\tau(T)}}{1 - e^{-\Delta t/(\tau(T)}} \tag{3.7}$$

where $U_1(t)$ is the RH value after the time-lag correction, $U_0(t)$ is the RH value before the time-lag correction, Δt is the time interval (sampling rate). 1 s for both RS-11G and iMS-100, and $\tau(T)$ is the e-folding (63%) response time of the RH sensor as a function of temperature.
Eq. 3.7 not only retrieves the actual large gradients in the RH profile but also tends to amplify noises in the original U_0. Therefore, a low-pass digital filter using the Kaiser window (Appendix E), with the cutoff period of the RH sensor's response time in Eq. 3.5, is applied to the original U_0 before the time-lag correction Eq. 3.7 is applied.

3.2.3.3 Temperature-Humidity Dependence correction (TUD_corr.)

A thin-film polymer RH sensor has temperature dependence at lower temperatures, while the factory calibration of the RS-11G and iMS-100 radiosondes is conducted at a constant temperature at 25°C. Therefore, the RH biases at lower temperatures need to be corrected during the correction procedure. The temperature dependence of the RS-11G and iMS-100 RH sensor was evaluated by comparison with the reference dew/frost-point by a chilled mirror hygrometer (FDW10, manufactured by the Azbil; with the water vapor pressure equation by *Hyland and Wexler* (1983) and temperature by PT100 instruments (RF-100, manufactured by the ETI) under various chamber conditions, at air temperatures from -80°C to +40°C. The experimental setup was the same as that described in *Sugidachi and Fujiwara* (2013).
Figure 3.19 shows the measured biases of the RS-11G RH sensor with respect to the reference measurements under various chamber conditions. Results from these chamber experiments showed wet biases between -60°C and 40°C, and dry biases below -60°C (down to -75°C). Also, these biases have a RH dependence, being larger at higher RH conditions. To correct these biases, the following correction curve for the temperature-RH dependence is developed by least squares method based on the experiment results.

$$\Delta U = (K_0 + K_1 T_s + K_2 T_s^2 + K_3 T_s^3)(K_4 + K_5 U_1 + K_6 U_1^2) \tag{3.8}$$

$$U_2 = U_1 - \Delta U \tag{3.9}$$

where ΔU (%) is the correction, U_1 is the uncorrected RH, U_2 is the corrected RH, K_0 to K_6 are constant coefficients, and T_s is the sensor temperature. T_s is measured with a dedicated thermistor attached to the RH sensor for the case of iMS-100, while it is estimated from air temperature measurements by considering the effect of solar heating and thermal lag for the case of RS-11G. Figure 3.19 also shows the correction curves at selected RH values.

3.2.3.4 Sensor versus air temperature correction (Ts/Ta _corr)

During the sounding, temperature of the RH sensor does not necessarily equal to the ambient air temperature because of the solar heating and the thermal lag of the RH sensor. Measurements with an RH sensor warmer (colder) than the ambient air would result in dry (wet) biases. Therefore, the RH values obtained from Eq. 3.8 need to be translated to the RH with respect to the saturation vapor pressure of the air temperature by using the following equation.

$$U_3 = U_2 \times \frac{e(T_s)}{e(T_a)} \tag{3.10}$$

where U_3 is the corrected RH, U_2 is the uncorrected RH, T_s is the temperature of the RH sensor, and T_a

is the temperature of the ambient air. The water vapor pressure equation $e(T)$ by *Hyland and Wexler* (1983) is used.
For the iMS-100 radiosonde, T_s is measured with a dedicated thermistor attached to the surface of the RH sensor. On the other hand, the RS-11G radiosonde does not have the dedicated thermistor for the RH sensor. Therefore, the temperature of the RH sensor is estimated on the assumption that the sensor becomes warmer (or colder) than the ambient air due to the thermal lag and solar radiation heating, using the following equation.

$$T_s = T_a + \Delta T_{s\_SR} + \Delta T_{s\_TL} \tag{3.11}$$

where ΔT_{s_SR} is the heating amount by solar radiation (see Appendices D and C for details), ΔT_{s_TL} is the warming by thermal lag (in the troposphere). The time constant of the thermal lag (the 63% response time) is estimated to be 22 s at surface pressure level from chamber experiments. The thermal lag used in this correction was determined by considering the measurement results of the RH sensor temperature in some flight tests.
The RH sensor temperature becomes generally warmer at higher altitudes (upper-troposphere and stratosphere). The difference between T_s and T_a reaches above 5 K in the upper troposphere, and above 10 K in the stratosphere. In the lower troposphere, on the other hand, T_s is generally very close to T_a because solar radiation is weak and air density is large. Therefore, T_s/T_a correction is applied above the 600 hPa level. More details of this correction is explained in Appendix D.

3.2.3.5 Hysteresis consideration

The RH sensor of the RS-11G and iMS-100 has a small hysteresis property, which causes small wet biases when the sensor goes from a wetter condition to a drier condition. This wet bias of the hysteresis affects longer times than that of time-lag error. Note that this hysteresis error does not appear when measuring in a constant RH condition for a long period of time (such as in the calibration procedure).
The hysteresis property was investigated by chamber experiments at the GRUAN Lead Center, Lindenberg, Germany (Figure 3.20). Five chambers with different RH values are prepared by using saturated salt solutions, LiCl for 11 %RH, $MgCl_2$ for 33 %RH, NaCl for 75 %RH, and pure water for 100 %RH. RH was then measured with six RS-11G sensors for 3 minutes at each condition in the following order, 0 %RH, 11 %RH, 33 %RH, 75 %RH, 100 %RH, 75 %RH, 33 %RH, 11 %RH, and 0 %RH. The results (Figure 3.20) show that wet biases of ∼1.8 %RH appear when the RH conditions were changed from 100 %RH to 0 %RH, while biases are much smaller when the RH conditions were changed from 0 %RH to 100 %RH. The wet biases found here are considered to be due to the hysteresis. Additional experiments using the thermostatic chamber and a chilled-mirror hygrometer at Meisei showed the following characteristics. These biases are always observed when the RH sensor is exposed to wet conditions (e.g. ∼80 %RH) as well as to the saturated (100 %RH) condition. These biases do not disappear quickly and are only very slowly reduced at the rate of ∼0.5 %RH/hour. It is difficult to create a correction procedure for this hysteresis error because the effect is considered to be determined by the combination of the wet and dry RH values and the elapsed time from the RH-condition change. Therefore, the correction is not applied, and instead, this error (maximum 1.8 %RH) will be considered as an uncertainty source in the uncertainty budget calculation.

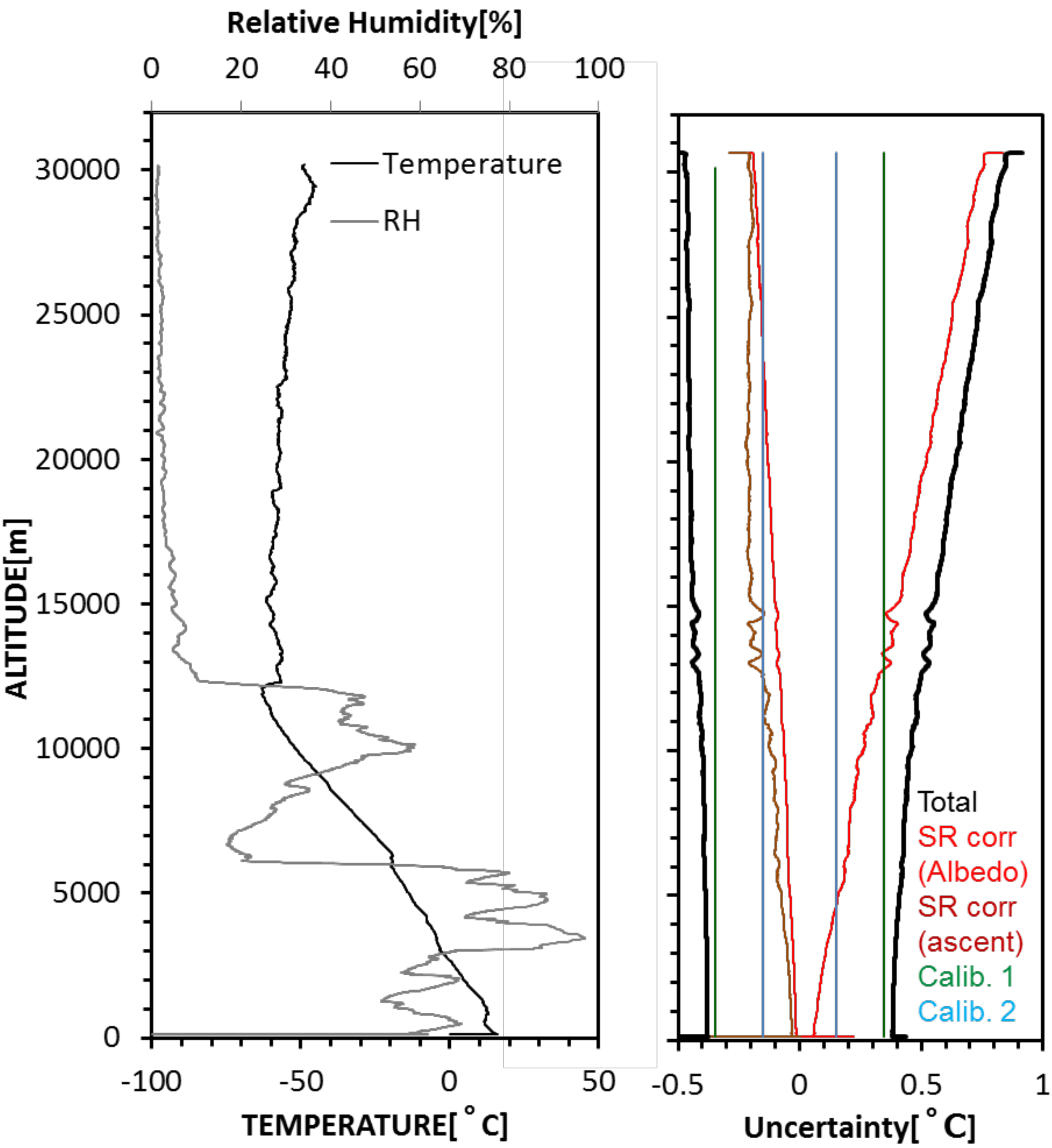

Figure 3.14: Example of the temperature uncertainty profile for the RS-11G radiosonde launched at 14:00 LT on 7 October 2014 at Lindenberg (52.21°N, 14.12°E), Germany. (Left) Profiles of temperature and RH. (Right) Uncertainty of temperature measurement (k=2). Calib. 1 corresponds to the thermistor calibration error, while Calib. 2 corresponds to the component of variability in the calibration chamber in Table 3.1. As shown in Figure 3.9, the uncertainty has different positive and negative values for both SR corr (Albedo) and SR corr (Ascent). Therefore, the total uncertainty is also different for different signs. Also, the SR corr (ascent) only has the negative component because horizontal, pendulum motion is not considered, which would act to further cool the temperature sensor.

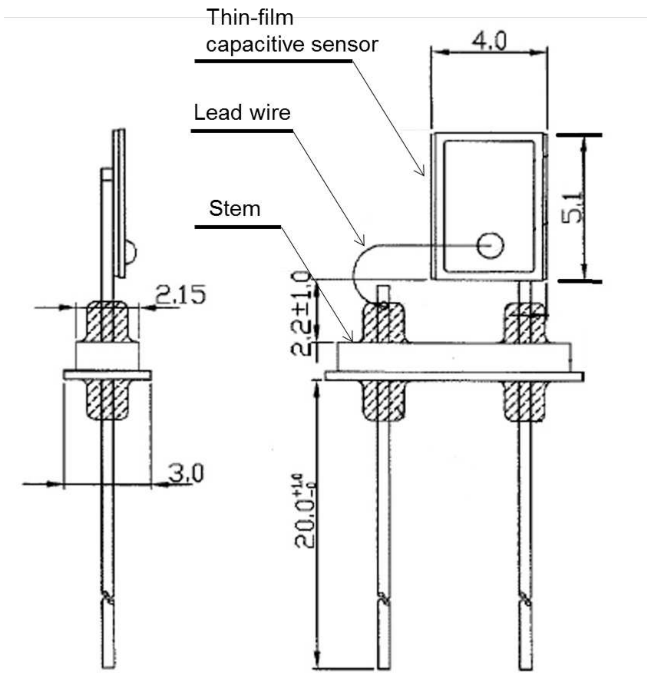

Figure 3.15: Appearance and dimensions of the RH sensor of the RS-11G and iMS-100 radiosondes (unit: mm).

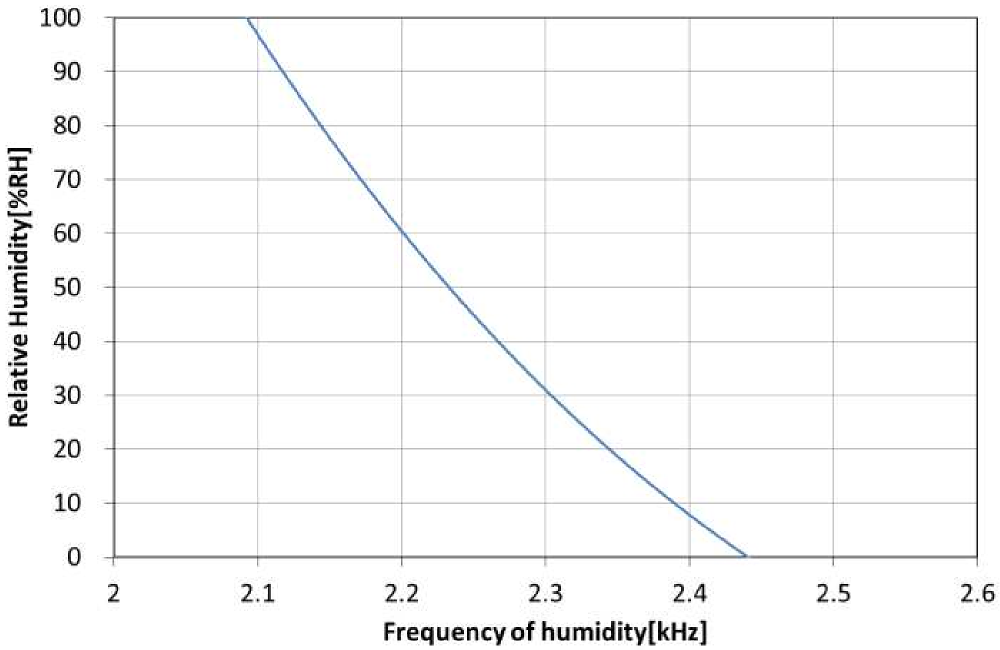

Figure 3.16: Example of the characteristics of a RH sensor used for the RS-11G radiosonde. Shown is the relationship between the frequency and RH at 25°C. The fitted curve is a cubic function.

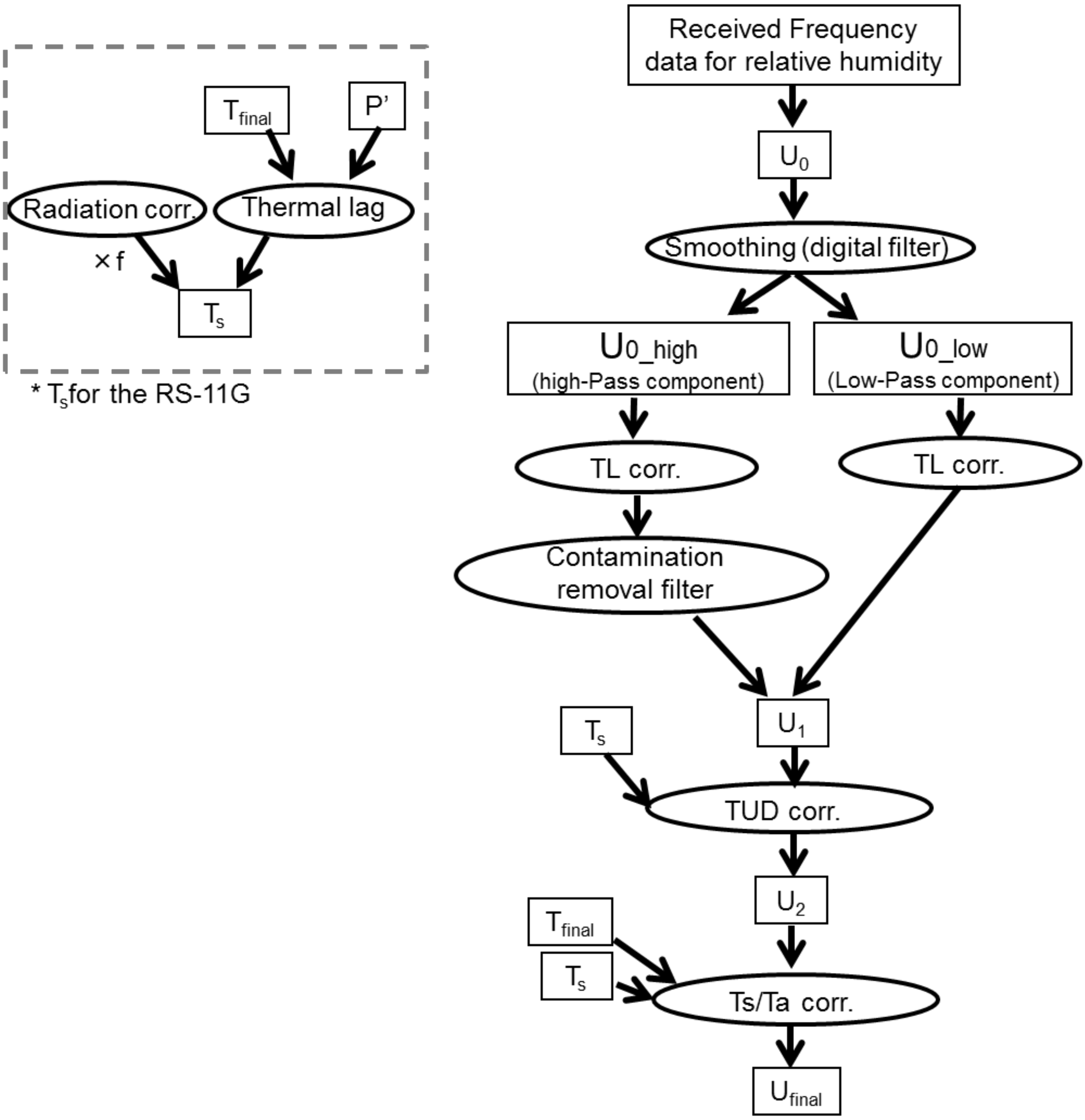

Figure 3.17: Schematic diagram of the processing steps and correction algorithms for the RS-11G and iMS-100 RH measurements in the sounding software MGPS2. The circles indicate processing, and the boxes indicate variables. Shown in the top left dotted box is the process to obtain the RH sensor temperature Ts, only applicable for the RS-11G radiosonde. For the iMS-100 radiosonde, Ts is directly measured with the dedicated thermistor. U_0 is uncorrected RH, P is tentative pressure, T_{final} is the corrected, final temperature, and U_{final} is the corrected, final RH data. U_0 is separated into the high-pass component, U_{0_high}, and the low-pass component, U_{0_low}. U_1 is the RH value after the TL correction and contamination removal filter applied. U_2 is the RH value after the TUD correction applied.

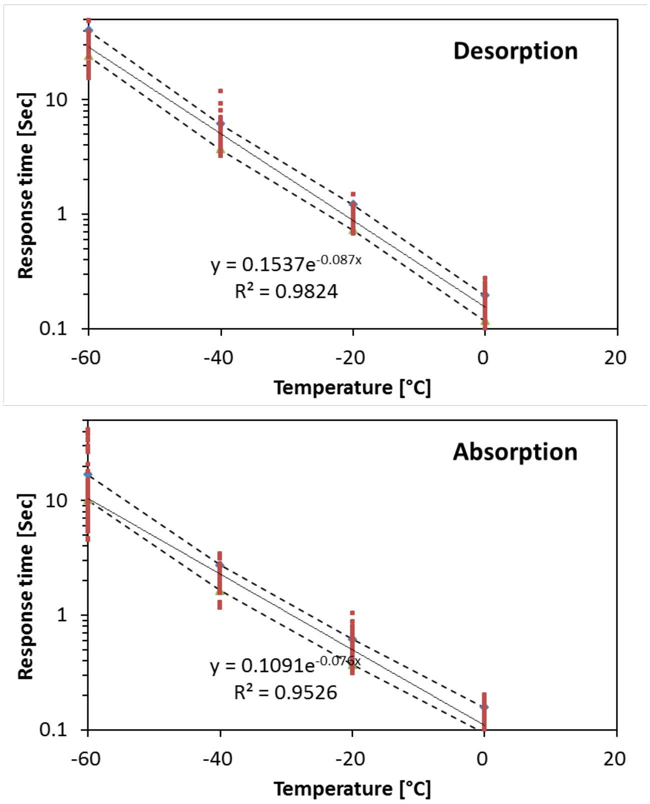

Figure 3.18: Results from laboratory experiments to determine the response time of the RS-11G and iMS-100 RH sensor at four temperatures (red dots). The ventilation speed in the thermostatic chamber was set to $5\,\mathrm{m\,s^{-1}}$. (Top) The response time for desorption conditions (i.e., for a stepwise change from wet to dry condition). (Bottom) The response time for absorption conditions (i.e., for a stepwise change from dry to wet condition). Solid lines indicate the averages of 69 measurement results at each temperature levels, and dotted lines indicate the deviation (2σ).

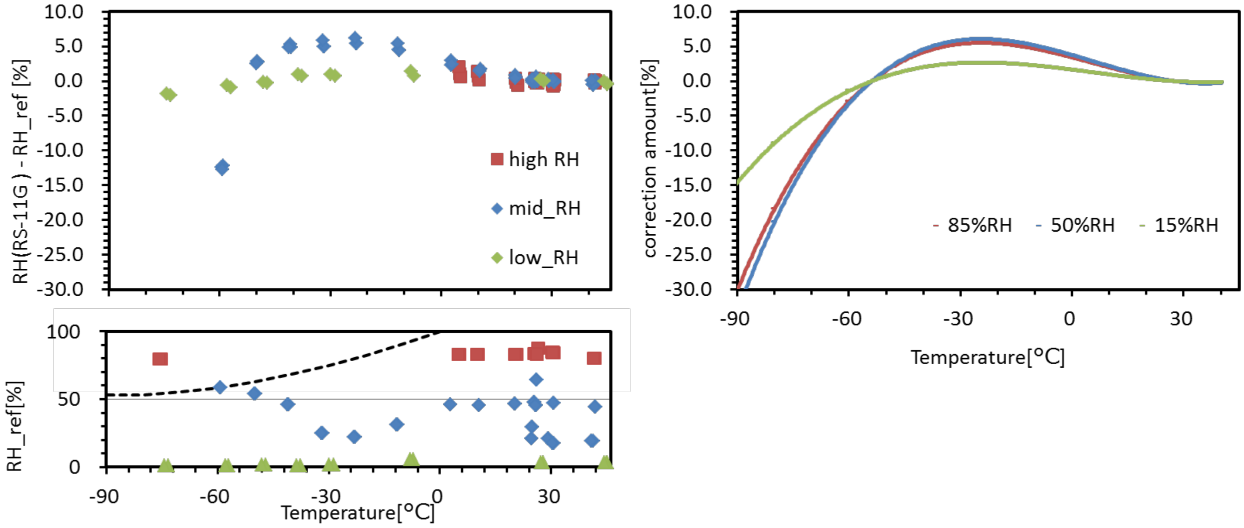

Figure 3.19: (Left) Temperature-Humidity dependence of the RS-11G RH sensor obtained under different temperature and RH conditions shown in the left-bottom panel. (Right) The correction curves obtained by fitting the experimental results as a function of temperature at 85%RH (red), 50(green), and 15%RH (blue).

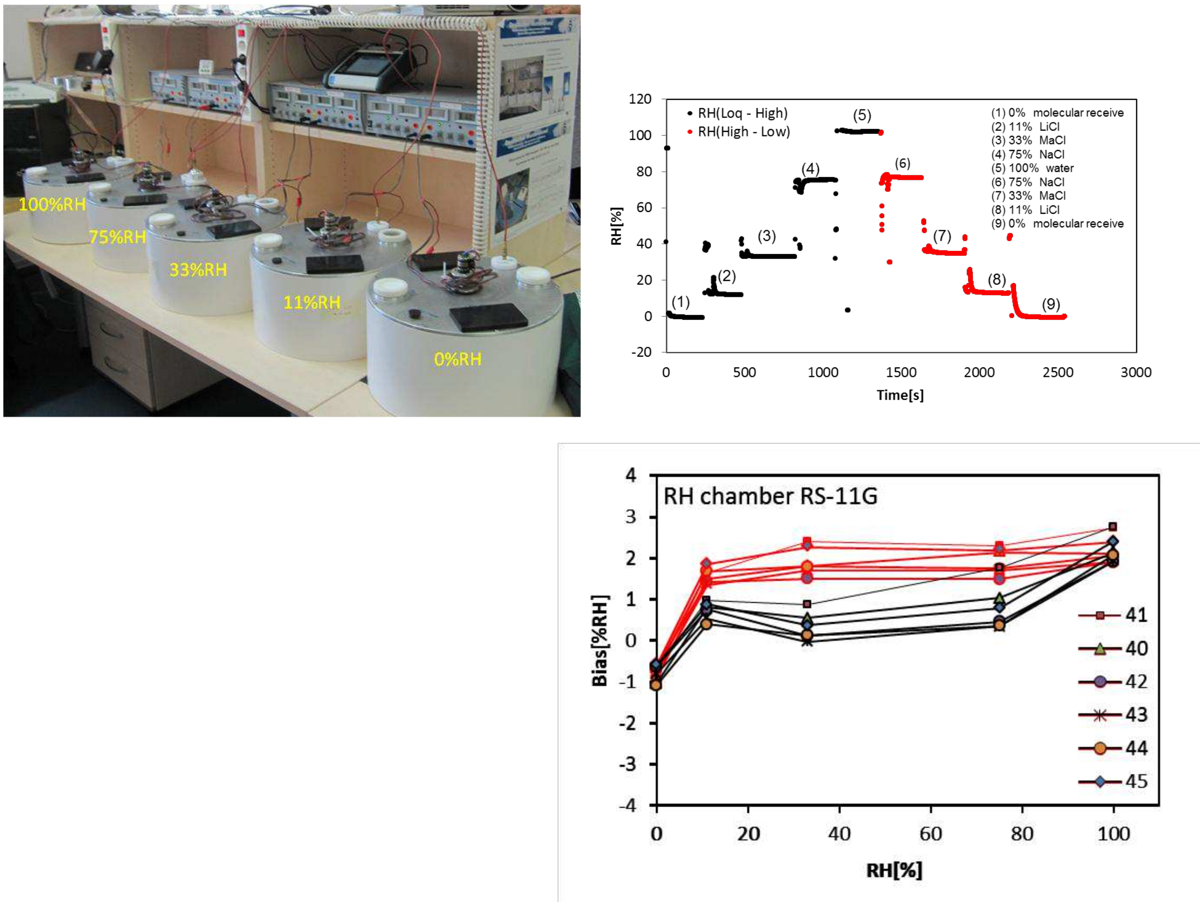

Figure 3.20: (Top left) The experimental setup to investigate the hysteresis of the RS-11G RH sensor. Five chambers of different RH values are prepared by using various saturated salt solutions and pure water. The RH sensor is placed in each chamber for 3 minutes in a dry-to-wet or wet-to-dry order. Six RS-11G RH sensors were investigated. (Top right) An example of a series of experiments using a particular RH sensor. (Bottom right) Summary of the experimental results for all six RS-11G RH sensors (#40 to #45). Black (red) lines indicate the results for dry-to-wet (wet-to-dry) experiments.

3.2.3.6 Sensor aging consideration

To prevent the sensor from any contamination during storage, the aluminized polyethylene was introduced as the radiosonde packaging material (*Shimizu et al.*, 2008). We investigated the effect of any contamination with an acceleration-testing chamber at +40°C and 93 %RH condition (JIS C60068). Figure 3.21 shows the measured biases by contamination during the storage for one and two years for the radiosonde with the previous polyvinyl package and the one with the aluminized package. With the aluminized package the sensor aging effect could substantially be reduced to within 1 %RH. Therefore, we will not consider the sensor aging in the uncertainty budget estimation below. (Note that the manufacturer-specified maximum allowable storage time for unopened one is 2 years for the aluminized package.)

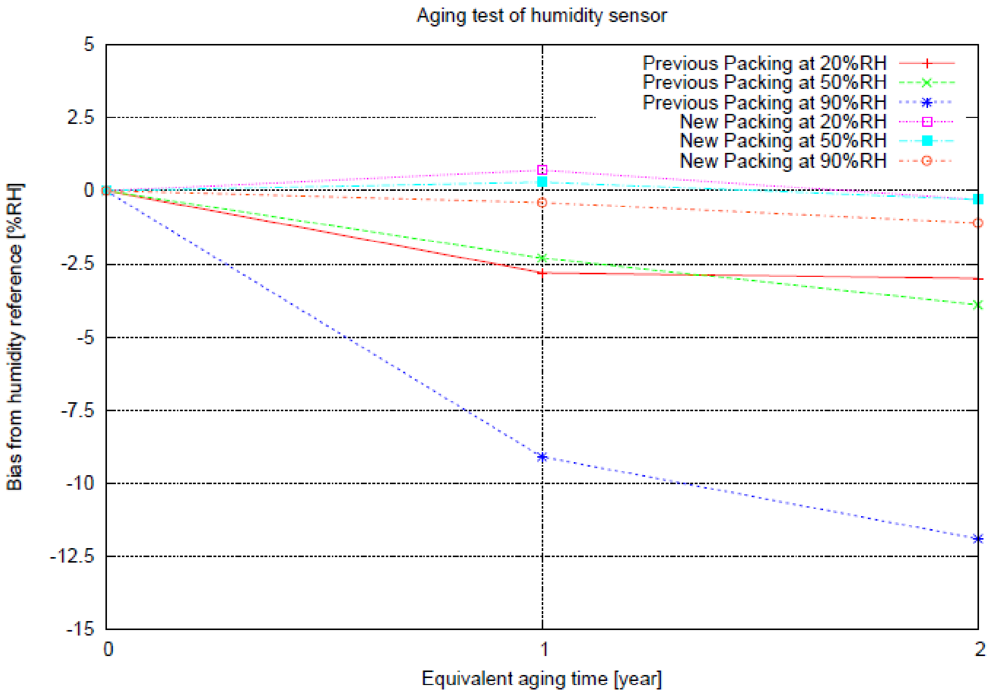

Figure 3.21: RH sensor changes during the storage from the accelerated aging test in a heated thermostatic chamber. Solid (dashed) lines are for the sensor with the new aluminized package (the previous polyvinyl package) at three different RH conditions (see the legends in the figure). Pink, light blue, and orange lines are for the aluminized package at three different RH conditions (see the legends in the figure). Red solid, green dashed, and blue dashed lines are for non-aluminized packing (vinyl package)

3.2.4 Uncertainty budget of the relative humidity measurements

The uncertainties in the RH measurements are listed in Table 3.2. The uncertainty from each process is described below.
(1) Calibration error
The RS-11G and iMS-100 RH sensor is calibrated at 15 %RH, 30 %RH, 50 %RH, 70 %RH, 90 %RH, and 95 %RH at 25°C. The uncertainty from this process does not exceed ±2 %RH because sensors that have biases exceeding ±2 %RH are rejected. Figure 3.22 shows the variability of the RS-11G

Table 3.2: The uncertainty sources and values for the Meisei RS-11G and iMS-100 RH measurement. The values are described as k=1.

Parameter		Value[%RH]	Reference	Corrected	Error classification
Sensor calibration		$2/\sqrt{3}$	Fig. 3.22	–	systematic
SHC 100 %RH check	Uncertainty of the calibration of the reference instruments	0.95			
	Uncertainty from repeatability of the measurements for a particular radiosonde	0.72			
	Uncertainty from inhomogeneity in the chambers	0.14			
	Uncertainty from the dispersion of measurement between individual radiosondes	0.26			
	Total	1.23	Table F.12		
GC check		–		–	
Time-lag correction		$U(u_\tau)$ $u_\tau = \tau \times 0.25$	Fig. 3.18	Corrected	systematic
Contamination	Correction amount itself (depending on weather conditions)	Corrected	systematic		
TUD correction		1.2	Fig. 3.19	Corrected	systematic
Ts/Ta correction		$U(\Delta T)$ where $\Delta T 0.3K/\sqrt{3}$	Fig. 3.23	Corrected	systematic
Hysteresis		1.8 (only for transition from wet to dry)	Fig. 3.20	uncorrected	systematic

RH sensor performance at the actual factory calibration process at 95 %RH, 70 %RH, 50 %RH, and 15 %RH for about one year. It is confirmed that the difference is centered around zero (i.e., no bias on average) with the deviation of well within ± 2 %RH. Therefore, we take $2/\sqrt{3}$ %RH as the uncertainty from the factory calibration procedure (Table 3.2). Note that in the current version, the uncertainty component from the SHC check is not included. Its inclusion is a future work.

(2) Time-lag correction

The uncertainty of the time-lag correction mainly comes from the uncertainty of the response time determination. As shown in Figure 3.18, the relative standard deviation of the response time is $\sim$25%. This value is used for the estimation of the uncertainty from the time-lag correction.

(3) Contamination correction

The contamination error, which causes wet biases only under rainy (or cloudy) conditions, should be considered. Because its quantification is difficult, the correction amount itself is taken as the uncertainty from this correction.

(4) Correction for the Temperature Humidity Dependence (TUD correction)

The uncertainty of the TUD correction mainly comes from the fitting error of the measurement values shown in Figure 3.19. The fitting error (variability, 1σ) is 1.2 %RH.

(5) Correction for the difference between RH sensor temperature and air temperature

The measurement uncertainty of the dedicated thermistor for the iMS-100 RH sensor is ± 0.30 K. Figure 3.23 shows the uncertainty from the RH sensor temperature correction using this value. The uncertainty becomes larger at lower temperatures and wetter conditions. The same uncertainty is assumed for the RS-11G RH measurements. Although this correction is applied above 600 hPa, the sensor temperature is not always equal to the ambient air temperature even below 600 hPa. Therefore, the uncertainty from this correction is attached at the entire range.

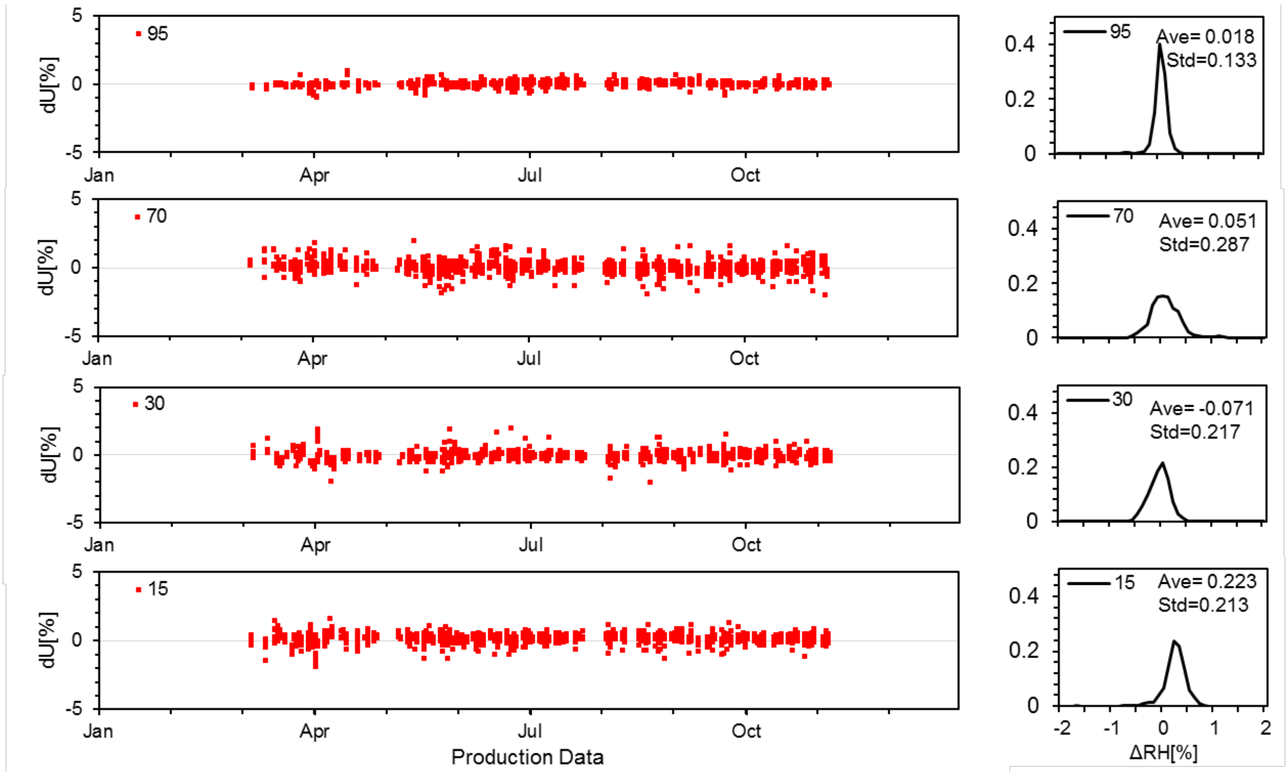

Figure 3.22: Variability of the RS-11G RH sensor at the factory calibration process at (from top to bottom) 95 %RH, 70 %RH, 50 %RH, and 15 %RH. (Left) Time series of the RH difference with respect to the reference instruments (shown in Figure 5.2) during 2014. These data were obtained at the actual production process. All calibration data produced during this period were plotted. (Right) The frequency distribution of the RH difference, with the average and standard deviation values.

(6) Total uncertainty of the RS-11G and iMS-100 RH measurement
The total uncertainty depends on altitude and observation conditions. Figure 3.24 shows the RS-11G RH measurement uncertainty profile for a daytime flight at Lindenberg, Germany, launched at 14:00 LT on 7 October 2014. The total uncertainty is maximal around the tropopause because of the time-lag correction component. This is due to the large drop in the actual RH profile with altitude, with large response time uncertainty, around this region. The uncertainty derived from the T_s/T_a correction tends to be larger at higher RH conditions where its correction amount is large. The uncertainty from contamination error is not large at this sounding because this uncertainty becomes large under rainy conditions. Note that the uncertainty from the hysteresis is considered only when the condition changes from wet to dry.

3.3 Geopotential height and pressure measurements

3.3.1 Geopotential height

The GPS receivers on the RS-11G and iMS-100 radiosondes provide the geometric altitude above the geoid surface. To be precise, the GPS receiver measures the position above the WGS-84 reference ellipsoid and converts it to the geometric altitude above the geoid surface in the GPS module according

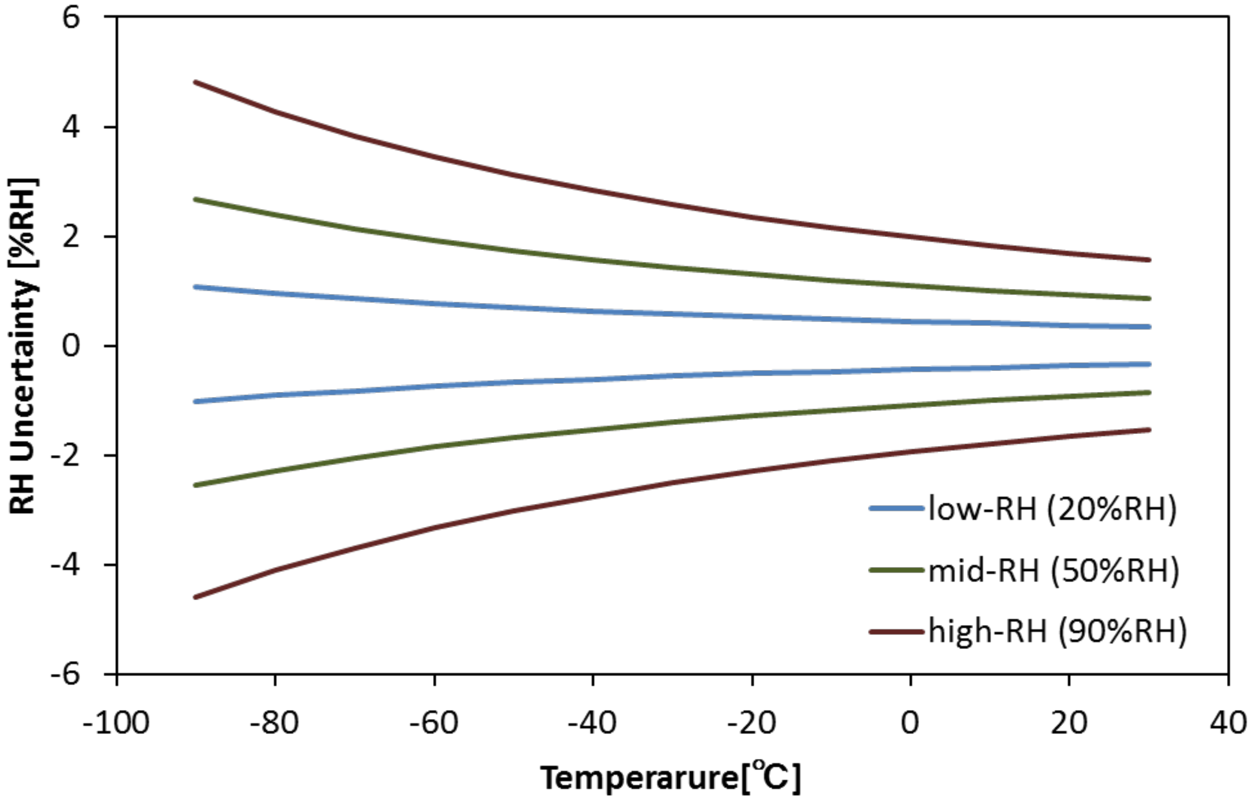

Figure 3.23: Uncertainty from the RH sensor temperature correction, assuming that the uncertainty of the RH sensor temperature measurement is ± 0.3 K.

to the difference between the geoid surface and the WGS-84 reference ellipsoid. For the radiosonde soundings, the vertical coordinate is usually expressed as geopotential height. The calculation of the geopotential height from GPS geometric altitude is given by the following equation (e.g. *JMA*, 1995).

$$H = \frac{g_\phi}{g_0} \frac{R \times z_{GPS_1}}{R + z_{GPS_1}} \tag{3.12}$$

where H is the geopotential height, R is the radius of the earth (6378136.0 m), g_0 is the standard gravity acceleration (9.80665 m s^{-2}), g_ϕ is the gravity acceleration at the observation latitude [m s^{-2}], z_{GPS_1} is the GPS-based geometric altitude above the geoid surface [m]

Here, z_{GPS_1} is different from the raw data from the GPS receivers, z_{GPS_0}. The altitude transmitted from the GPS module is converted to the corrected altitude, z_{GPS_1}, by considering the offset between the balloon release altitude, z_0, and z_{GPS_0} at the release time.

$$\begin{aligned} \Delta H &= z_{GPS_0} - z_0 && \text{at release time} \\ z_{GPS_1} &= z_{GPS_0} - \Delta H && \text{at each altitude} \end{aligned} \tag{3.13}$$

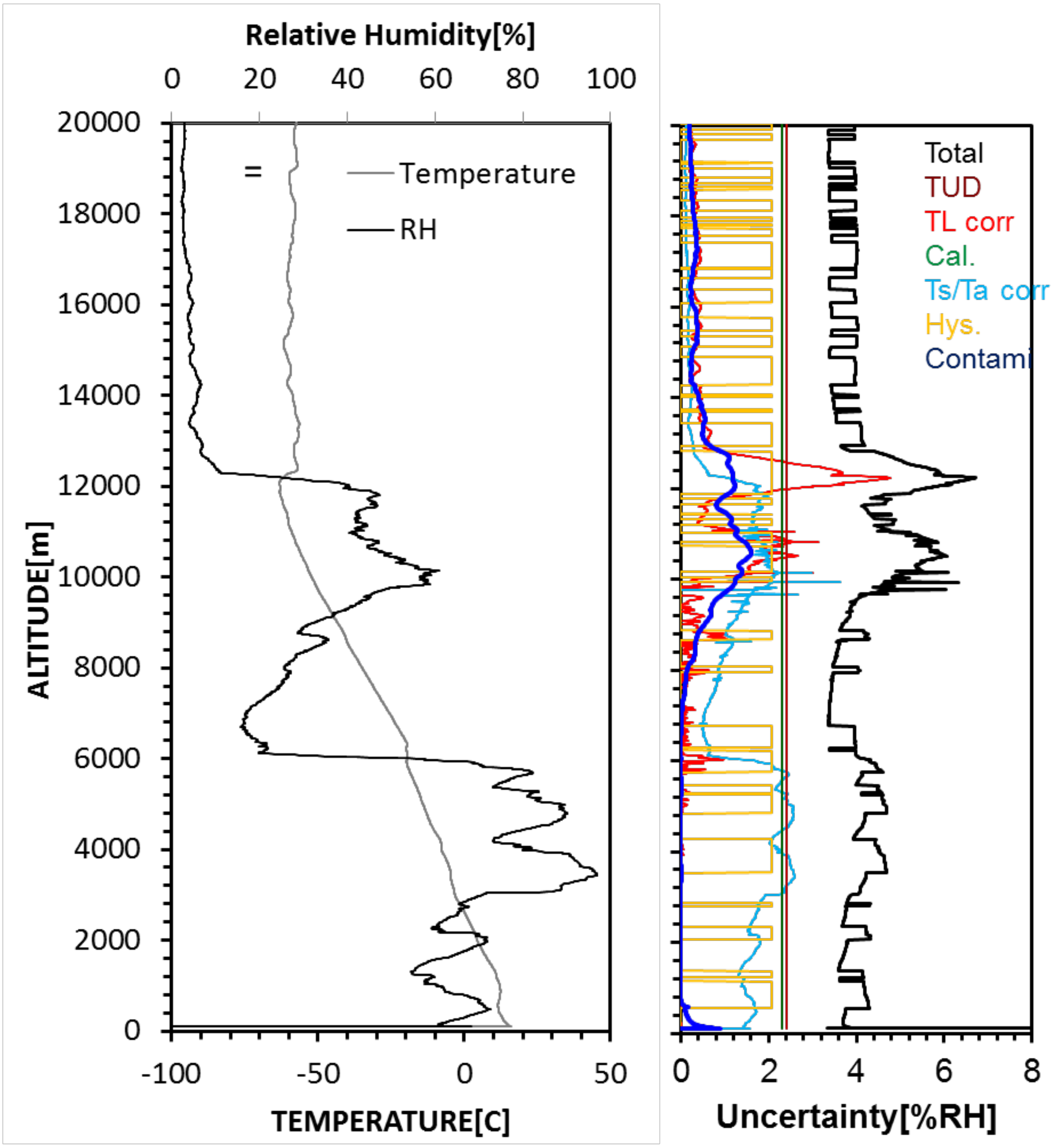

Figure 3.24: An example of the RS-11G RH measurement uncertainty profile at Lindenberg, Germany, launched at 14:00 LT on 7 October 2014. (Left) Obtained profiles of temperature and RH. (Right) Profiles of total uncertainty and individual components.

The offset is caused by the GPS positioning error. The offset would be zero if the position measurement of the GPS module is perfect. Note that the balloon release altitude is decided to the ground level plus 1 m at the release point (e.g., for Tateno, 24.8 m is the ground level above sea level, and 25.8 m is the balloon release altitude), and is expressed as geometric altitude instead of geopotential height. The difference between the geopotential height and geopotential height at the release point causes negligible error.

Also, the GPS-based height data include noise (i.e., random error), which is caused by the pendulum motions. Therefore, the height data are further smoothed using the moving average with a 61 point wide window ($\sim$1 minute). The algorithm for geopotential height is shown in Figure 3.25. The detection error of the GPS receiver and its contribution to the uncertainty of the height measurements will be described in Section 3.3.3.

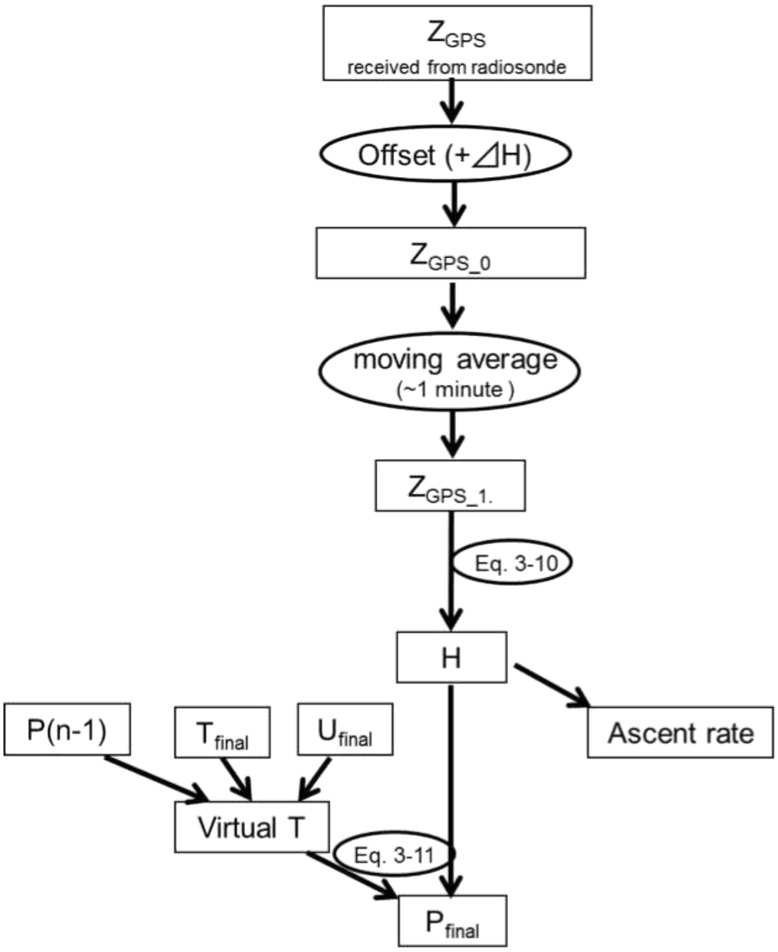

Figure 3.25: Processing steps and correction algorithms for the geopotential-height and pressure measurements. Each symbol denotes the following variable: GPS geometric altitude (Z_{GPS}), geopotential height ($Z_{\mathrm{geopot\_0}}$), smoothed geopotential height ($Z_{\mathrm{geopot\_1}}$), pressure at previous time (1 second before) (P(n-1)), corrected final temperature (T_{final}), corrected final RH (U_{final}), and the pressure (P_{final}).

3.3.2 Pressure

The RS-11G and iMS-100 radiosondes are not equipped with a pressure sensor. The pressure is calculated from the GPS geopotential height using the hydrostatic equation.

$$P_i = P_{i-1} \exp\left[-\frac{g_0}{T_{vm}R_d}(H_i - H_{i-1})\right] \tag{3.14}$$

where P_i is the calculated pressure (hPa) at geopotential height = $H_i(m), P_{i-1}$ is the pressure (hPa) at previous level (1 s before) at geopotential height= $H_{i-1}(m), g_0$ is the standard gravity acceleration (9.80665m s^{-2}), T_{vm} is the averaged virtual temperature between P_i and P_{i-1} (K) (see below), and R_d is the specific gas constant of dry air (287 J kg^{-1} K). Note that g_0 and R_d are used by following the JMA's convention (*JMA*, 1995). The virtual temperature is calculated with the following equations.

$$T_v = T\frac{(1+r_v/\varepsilon)}{1+r_v} \tag{3.15}$$

$$r_v = \frac{\varepsilon e}{P-e} \tag{3.16}$$

where T_v is the virtual temperature (K), r_v is the mixing ratio of water vapor (kg kg^{-1}), ε is the ratio of molecular weight between water vapor and dry air (0.622), P is the pressure (hPa), e is the water vapor pressure (hPa) which is calculated from temperature and RH using the *Hyland and Wexler* (1983) water vapor pressure equation. The pressure value used in Eq. 3.15 is the one at previous time (1 s before).

The surface pressure at the release point is measured with an independent pressure sensor at the observation station. The balloon release altitude is not necessarily equal to the altitude where the surface pressure sensor is located. Thus, the surface pressure at the release point is obtained from the pressure sensor reading and the altitude difference between the pressure sensor and release point using Eqs. 3.14-3.16.

3.3.3 Uncertainty budget of the geopotential height and pressure measurements

(a) Geopotential height

The uncertainty of the geopotential height depends strongly on the detection error of the GPS receiver. In this document, the GPS dimensional error is treated as the standard uncertainty. The sources of the GPS measurement error include the delay of radio propagation in the ionosphere and troposphere, multipath by the reflection from mountains and buildings, and noise of the receiver. The variability of the GPS position is indicated as the value of PDOP (Position Dilution of Position) which depends on the GPS signal receiving conditions (i.e., the geometric layout of between the radiosonde and the GPS satellites) and is outputted from the module every second. The 3-dimensional errors of GPS (1σ) e_{GPS} are estimated with PDOP and UERE (User Equivalent Range Error). The UERE is the distance error between the GPS receiver and the GPS satellite. The value of UERE (1σ) is 5.3 m for the C/A (Coarse/Acquisition) code which is used in the GPS module of the RS-11G and iMS-100 radiosondes. The 3-dimensional errors of GPS (1σ) e_{GPS} are calculated by the following equation (*Kobayashi*, 2006).

$$e_{GPS} = \mathrm{PDOP} \times UERE \tag{3.17}$$

The GPS modules of the RS-11G and iMS-100 radiosondes use the Satellite-Based Augmentation System (SBAS) to improve the accuracy of position detection (i.e., making PDOP smaller). However, at high latitudes, SBAS is not used for the radiosonde observation because the SBAS uses the stationary satellites which are not available at high latitudes. For example, SBAS is not available at Syowa, a Japanese Antarctic station (69.01°S, 39.59°E). Figure 3.26 shows the vertical profile of GPS

3-dimensional error (Eq. 3.17) in Japan and in Antarctica. The value of e_{GPS} is typically less than 10 m at high-latitudes even without SBAS as well as at mid-latitudes.

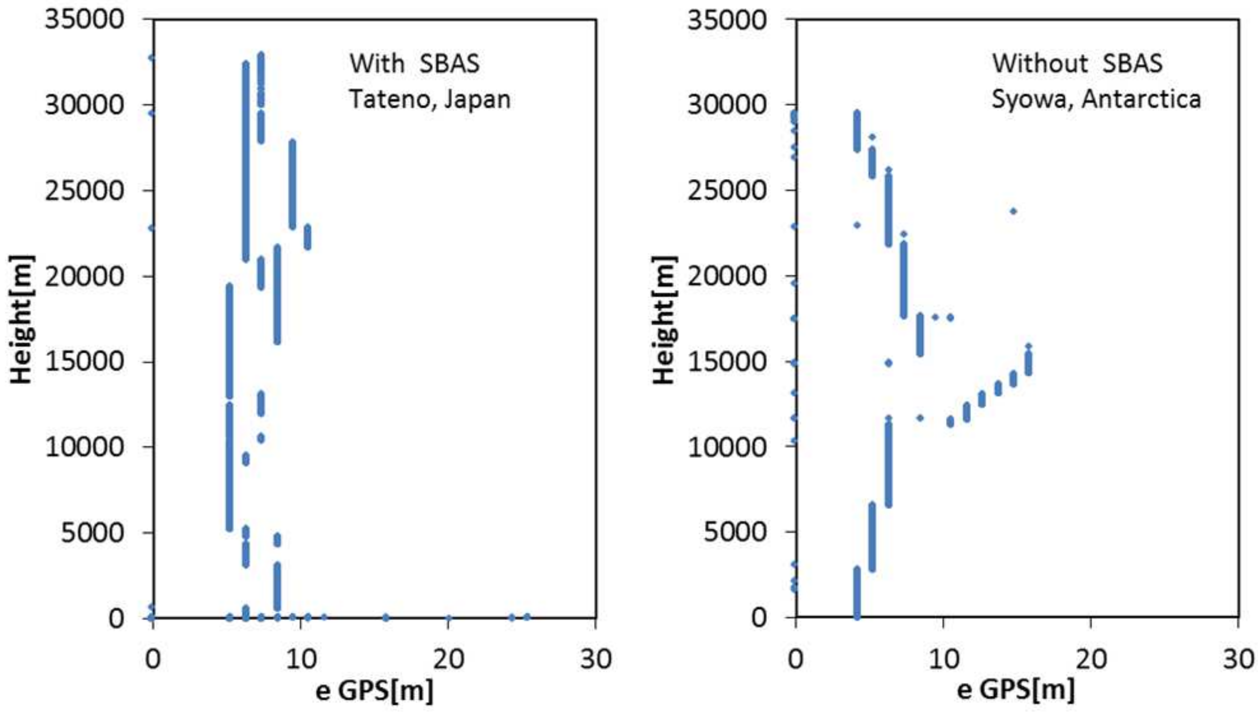

Figure 3.26: Vertical profiles of the 3 dimensional error of GPS geometric height (e GPS). (Left) For sounding with the SBAS at Tateno, Japan (36.06°N, 140.13°E) launched at 8:30 LT on 28 May 2014, and (right) for sounding without the SBAS at Syowa, Antarctica (69.01°S, 39.59°E) at 14:30LT on 5 September 2015.

(2) Pressure

Because pressure is calculated using geopotential height, temperature, and RH, the uncertainties of these measurements propagate to the uncertainty of the pressure measurement. In addition, the uncertainty of surface pressure measurements contribute to the pressure uncertainty. Table 3.3 summarizes the uncertainties in the GPS geopotential height and pressure measurements. Figure 3.27 shows the measurement uncertainty profile of pressure. For this example, PDOP is assumed to be 1 (i.e., e_{GPS}=5.3 m). Figure 3.27 indicates that the GPS-based geopotential height measurement is the main uncertainty source at lower altitudes, while the temperature measurement is the main source at higher altitudes. The RH and surface pressure measurements only have small contributions.

3.4 GPS-based wind measurements

3.4.1 Procedures to obtain the wind information

Zonal and meridional winds, U and V, respectively, are calculated from the GPS Doppler speed data obtained in the GPS receiver. In the ground software, the GPS Doppler speed data (i.e., wind speed and direction) is divided into the components U and V. The vector U and V includes the pendulum

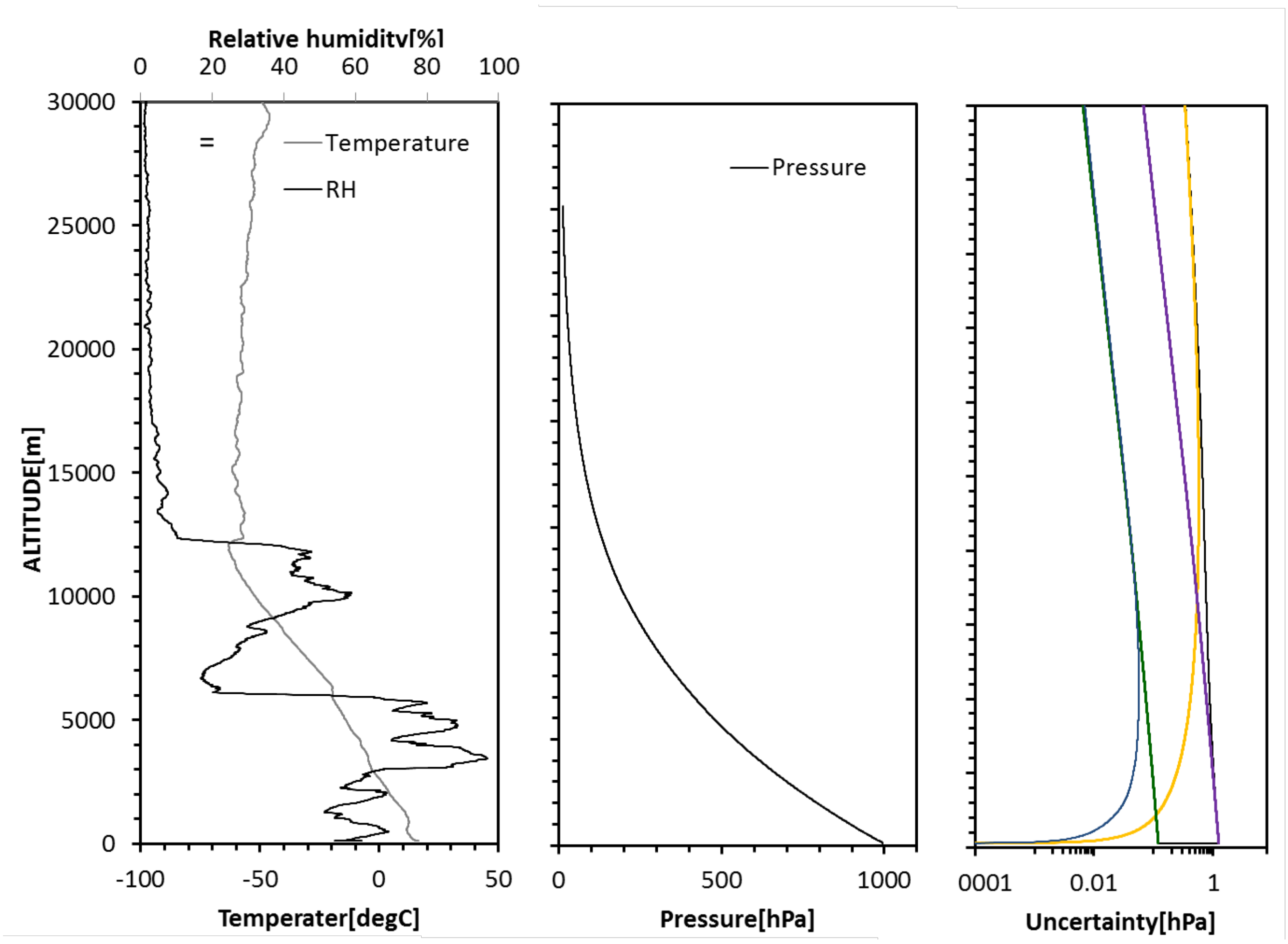

Figure 3.27: Example of the pressure uncertainty profile. (Left) Profiles of temperature and RH. (Middle) Profile of pressure. (Right) Profiles of total and individual uncertainty values (k=2). Purple, blue, and yellow lines indicate the uncertainties from GPS-based geometric height (PDOP is assumed to be 1 throughout the profile), RH, and temperature measurements (taken from the profiles in Figure 3.14 and Figure 3.24), respectively. Green line indicates the surface pressure uncertainty. Black line indicates the total uncertainty.

motion (random noises) similar to the GPS altitude. Therefore, U and V are smoothed by the digital filter with the Kaiser window (Appendix E). Figure 3.28 shows the processing steps in the wind measurements. During the ascent of the radiosonde, the GPS-based wind data includes the oscillations by pendulum motion. For operational radiosonde soundings, such oscillations must be removed by low-pass filtering. For research purposes, this filtering function can be turned off by the users. The period of the pendulum motion is estimated by the length of the string between the radiosonde and balloon. Normally, the string of 15 m (10 m) length would cause oscillations of 7.8 s (6.3 s) period.

3.4.2 Uncertainty budget of the wind measurements

The uncertainty sources of the wind measurement include the stability of the GPS Doppler speed data and the low-pass filtering process to remove the pendulum-motion and noise components. The stability of the GPS Doppler speed data is investigated using a RS-11G radiosonde. Figure 3.29

Table 3.3: The uncertainty sources and values of the GPS geopotential height and pressure measurements. The values are described as k=1.

Parameter	Value	Error classification
(GPS Altitude)		
detection accuracy of GPS	PDOP $\times$ UERE (UERE is set to be 5.3)	random
(Geopotential Height)		
Uncertainty derived from GPS altitude	Based on the hydrostatic equilibrium	–
Difference between the geopotential height and geometric height at surface	$< \sim 0.6\%$ below 30,000 m	systematic
(Pressure)		
Uncertainty of the surface pressure gauge	As shown in Fig. 3.27 0.06 (hPa) @surface 0.01 (hPa) @100 hPa 0.001 (hPa) @10 hPa	systematic
Uncertainty from temperature measurements	As shown in Fig. 3.27 0 (hPa) @surface 0.5 (hPa) @100 hPa 0.12 (hPa) @10 hPa	systematic
Uncertainty from RH measurements	As shown in Fig. 3.27 0 (hPa) @surface 0.01 (hPa) @100 hPa 0.002 (hPa) @10 hPa	systematic

shows the variability of the GPS Doppler speed data at a static condition when the radiosonde is situated at surface at Moriya, Japan (35.9°N, 140.0°E) for more than 1000 s. We see that the variability (1σ) is less than 0.01 m s^{-1}, being negligible for the wind measurement uncertainty.

The low-pass filtering to remove the pendulum motions is the main source of uncertainty in the horizontal wind measurements. The uncertainty from the filtering is calculated based on the method by *Dirksen et al.* (2014). First, the uncertainties of U and V components are calculated individually. Then, the uncertainties of wind speed and direction are derived. See Appendix E for the details. Figure 3.30 shows the profiles U and V components before and after the low-pass filtering, and the estimated uncertainty profiles for the low-pass filtered U and V. The raw wind profiles clearly show oscillations due to the pendulum motions. The uncertainty due to these oscillations are $1 \sim 3$ m s^{-1}, being larger at higher altitudes. This means that the magnitude of the pendulum motions became larger at higher altitudes for this sounding. Figure 3.31 shows the profiles of wind speed and direction and their uncertainties of the same sounding. The uncertainty values are 2 – 4 m s^{-1} for wind speed and mostly $< 2°$ for wind direction except for the region 25 – 30 km. When wind speed is small (i.e., at 25–30 km), the relative magnitude of pendulum motions becomes large so that the uncertainty of

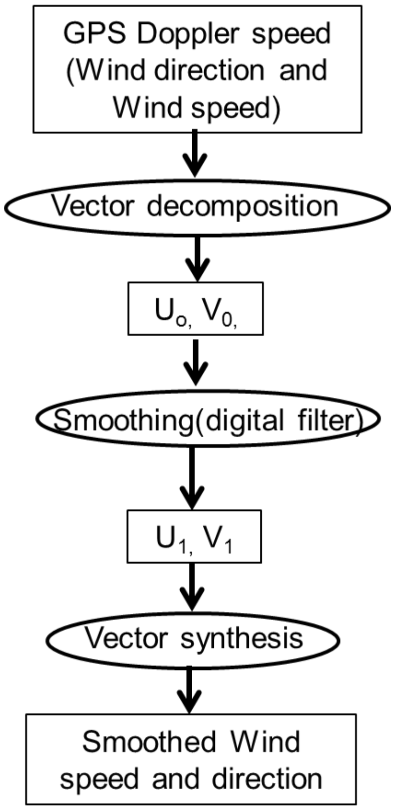

Figure 3.28: Processing steps and correction algorithms for the horizontal wind measurements. Each symbol denotes the following variable: U_0 for the uncorrected zonal wind; V_0 for the uncorrected meridional wind; U_1 for the smoothed zonal wind; and V_1 for the smoothed meridional wind.

wind direction becomes much larger.
Figure 3.32 shows an example of the power spectra of raw and filtered meridional wind data. The filter removes the power around the pendulum periodicity (6-8 s) effectively. Because of the pendulum motions, the ordinary radiosonde wind measurements cannot detect atmospheric variabilities with scales shorter than the pendulum period.

3.4.3 Better wind measurements with a lighter radiosonde

The iMS-100 radiosonde provides less noisy wind data thanks to much smaller pendulum motions. This is because of the small mass (38 g) of the iMS-100 radiosonde together with a relatively larger resistance to the ambient air, which results in damping of the pendulum motions initiated by wind shear. Figure 3.33 shows the zonal wind data from a single iMS-100 radiosonde with a 600 g balloon and a 30 m string and from another, simultaneously launched iMS-100 radiosonde with a 200 g weight (∼250 g weight) with the same size of balloon and string. We can observe that the variability of the iMS-100 radiosonde (σ=1.42) is smaller than that of the 250 g radiosonde (σ=1.74). This result indicates that the uncertainty of the wind measurements becomes smaller for the radiosondes which have larger resistance to the ambient air. Furthermore, the iMS-100 radiosonde has captured fine structures better, compared with the 250 g radiosonde, such as the ones between the surface to 2 km

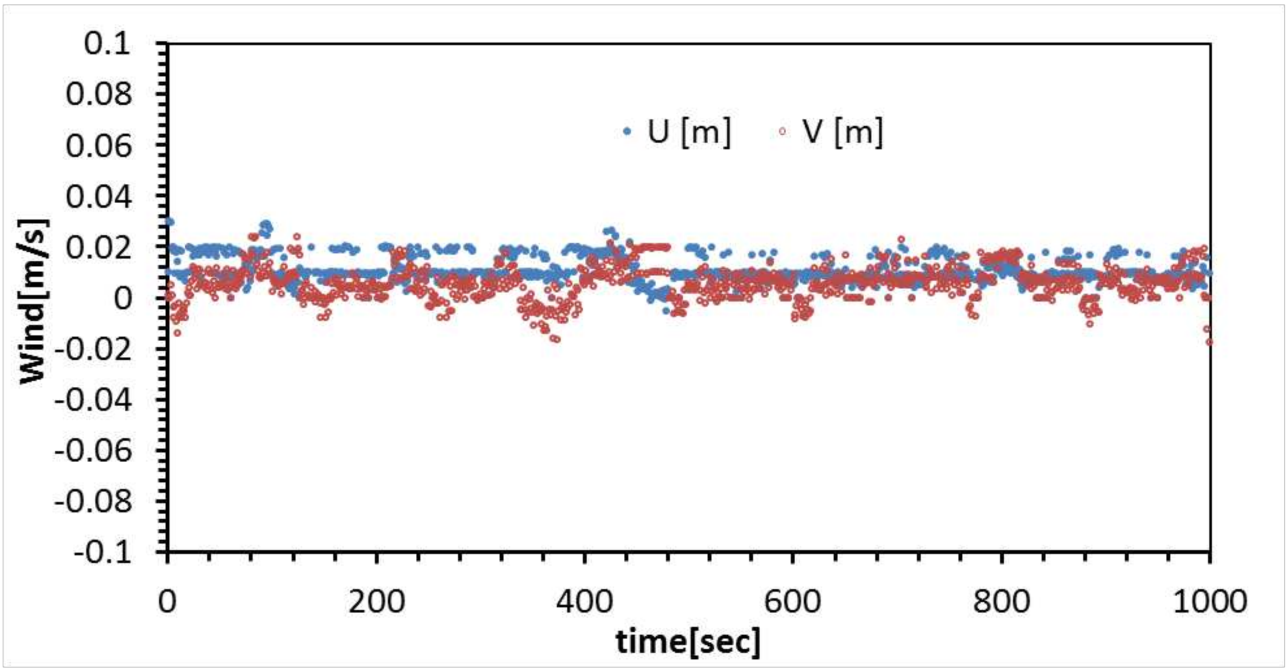

Figure 3.29: Variability of the GPS doppler speed data (i.e., U_0 and V_0 in Figure 3.28) under a static condition. The RS-11G radiosonde was placed on the ground at Moriya, Japan (35°N, 140°E) on 22 December 2014.

and the sharp changes at 3 km and at 4.5 km. In the lower stratosphere, we found no clear difference in capturing fine structures.

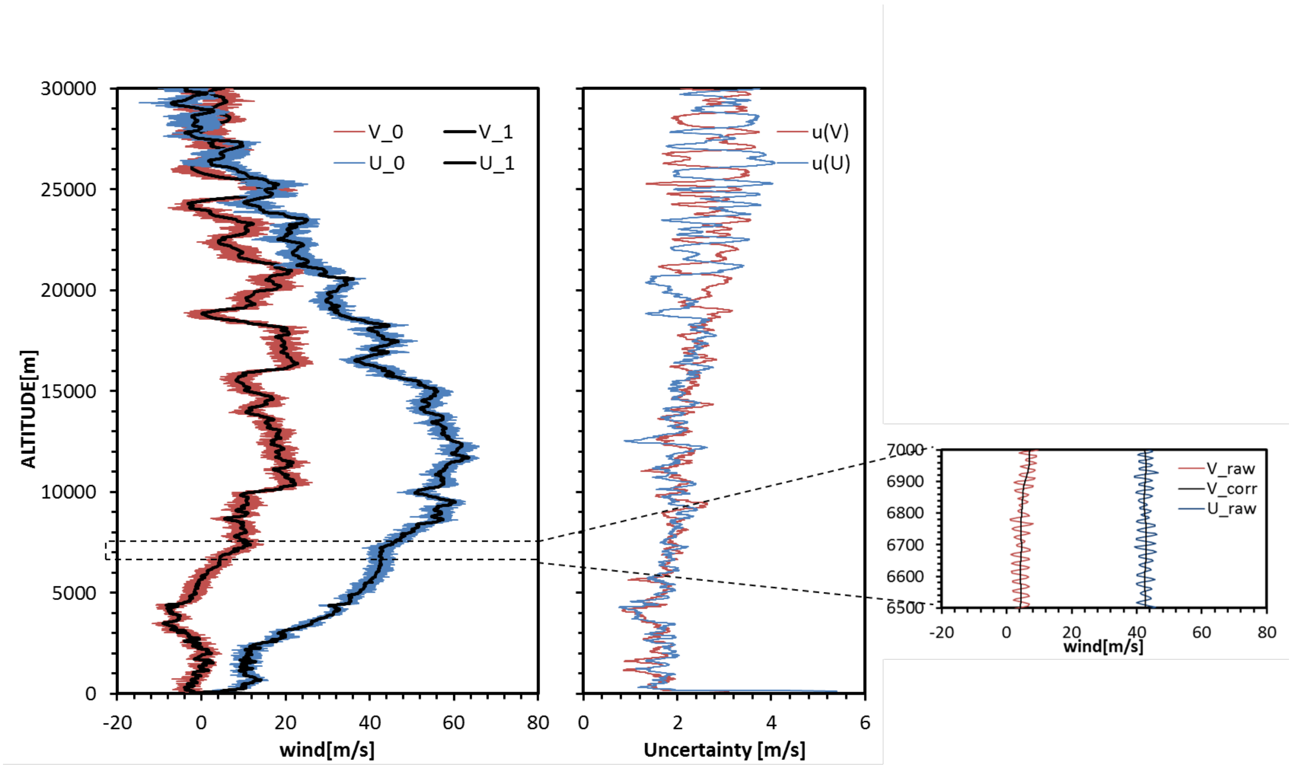

Figure 3.30: Vertical profiles of the horizontal winds and their uncertainty taken at Moriya, Japan launched at 17:30 LT on 22 December 2014. (Left) Colored lines and black lines indicate the wind profiles before and after the low-pass filtering, respectively. (Center) Red and blue lines indicate the uncertainty of U and V components, respectively. (Right) A closer look at 6.5-7.0 km of the left panel.

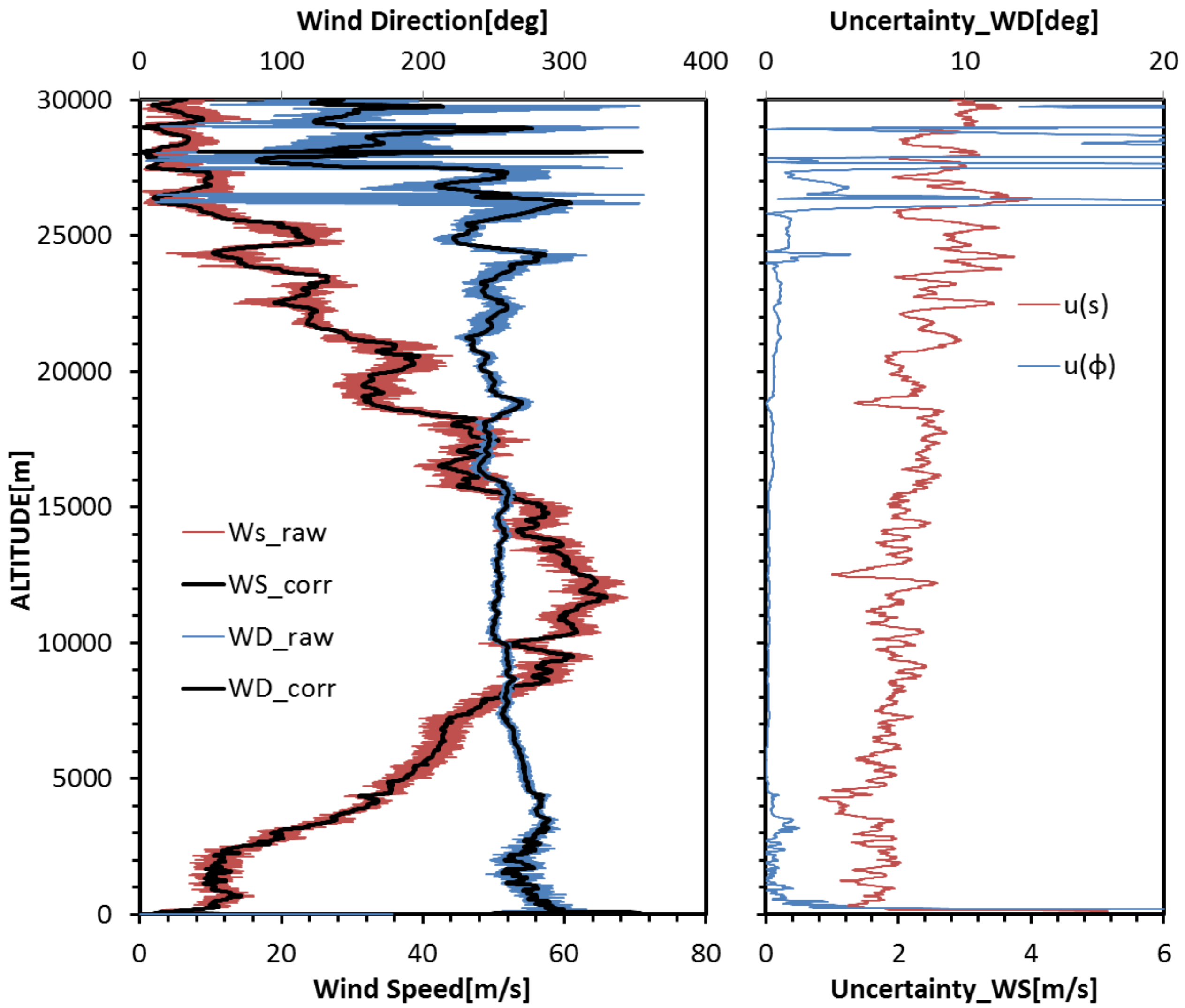

Figure 3.31: Vertical profiles of (left) wind speed and direction and (right) their uncertainties for the same sounding as shown in Figure 3.30.

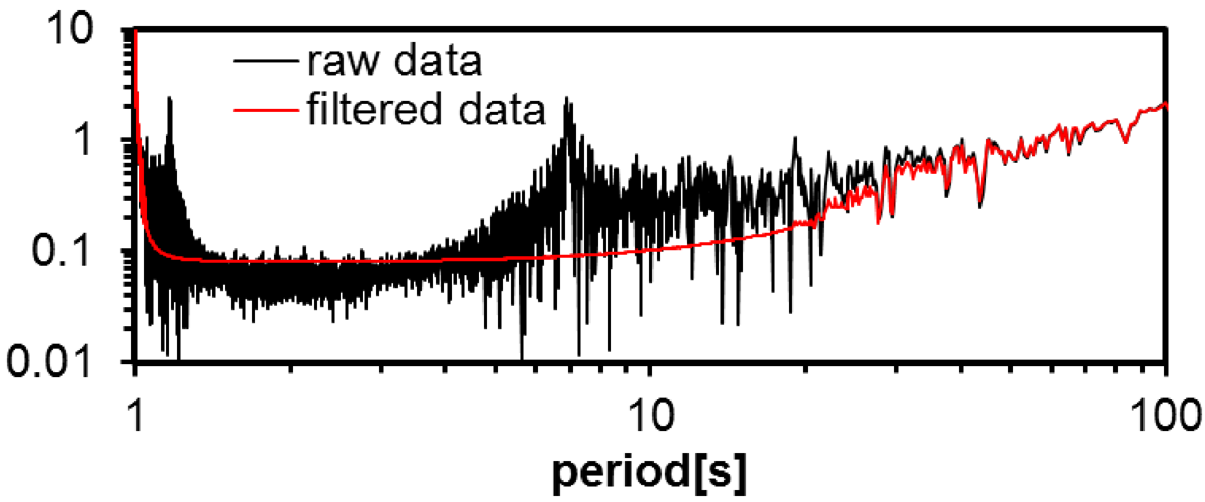

Figure 3.32: Power spectra of the meridional wind between surface and ∼15 km shown in Figure 3.30. The black line indicates the spectrum for raw data, and the red line indicates the one for filtered data.

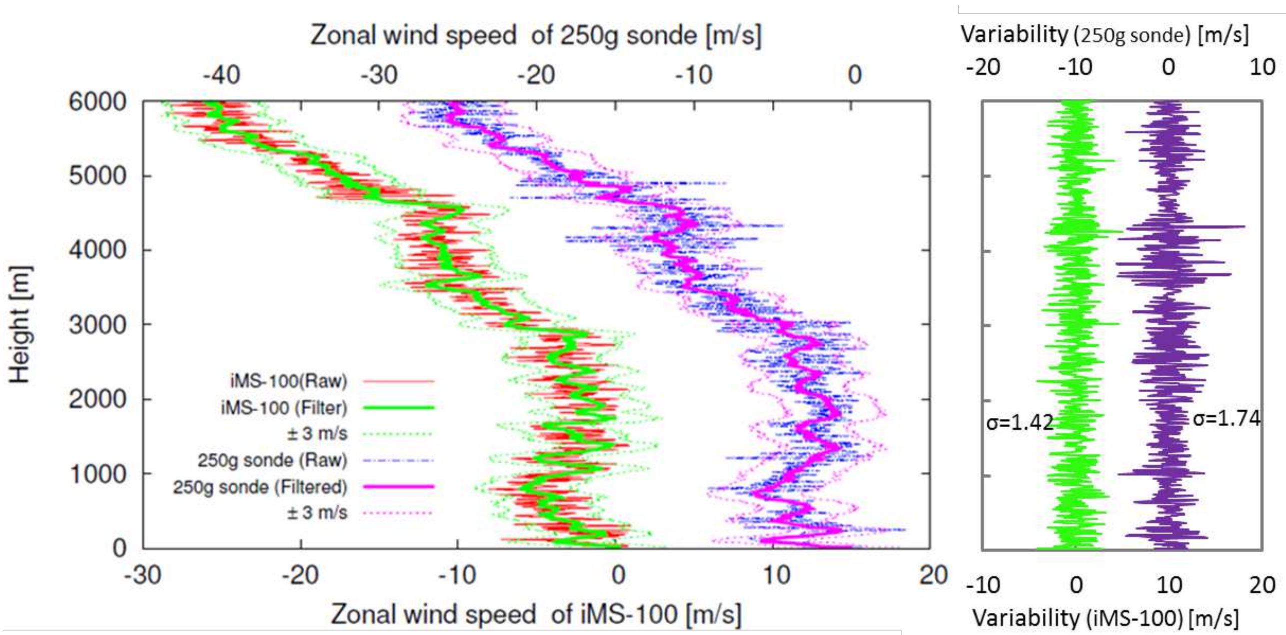

Figure 3.33: (Left) Comparison of zonal wind measurements with the iMS-100 (green line, reference to lower axis) and a 250-g radiosonde (another iMS-100 with a 200-g weight) (purple line, reference to upper axis). Both were launched at Moriya, Japan. The horizontal axes are displaced by 15 m s^{-1}. (Right) Corresponding profiles of high frequency component for the iMS-100 (green) and the 250-g radiosonde (purple). The horizontal axes are displaced by 10 m s^{-1}.

4 Data product

4.1 Data processing software prepared by Meisei

Sounding data for the RS-11G and iMS-100 radiosondes are obtained by the manufacturer's sounding software named MGPS2. The MGPS2 software has various functions, including the operation of the ground receiver (RD-08 or RD-06), preparations of the radiosonde (e.g., radiosonde frequency setting), ground check before the sounding, real-time monitoring of the observation data, and file output. The data processing flow is shown in Figure 4.1. At each process, transferring of raw data and applying several correction procedures, as explained in Sections 3.1-3.4, are conducted and the data at each step are stored in the database files.

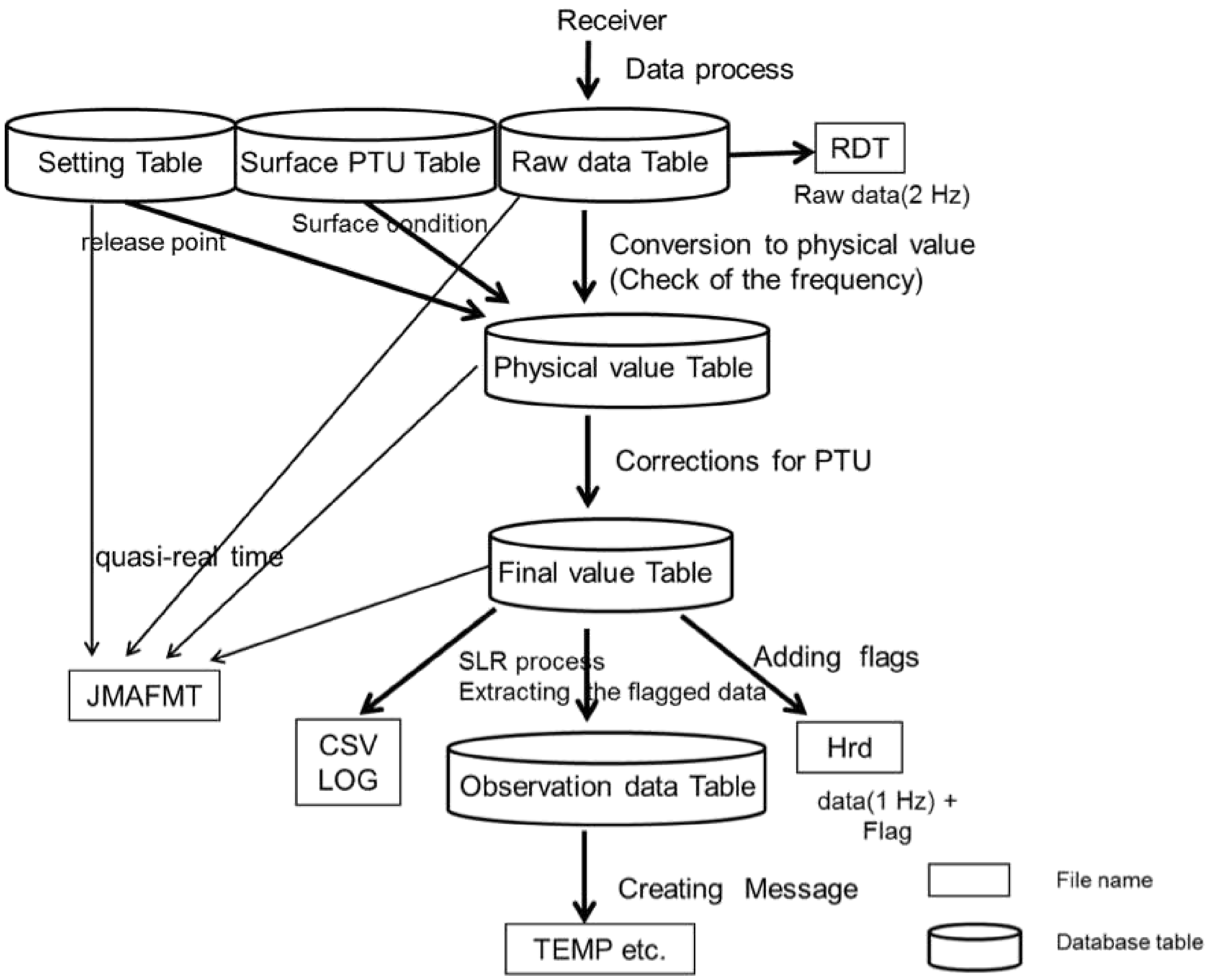

Figure 4.1: Data processing flow in the MGPS2 software in the ground system. Boxes show the types of files for the output data. The RDT file contains all the raw data. The JMAFMT file contains the uncorrected data sent to and archived at the GRUAN Lead Centre. The CSV file contains the corrected data at 1 Hz.

4.1.1 JMAFMT/GRUAN files

The JMAFMT/GRUAN files are in the format for the GRUAN data product, including various raw data such as frequency data from temperature and RH sensors and GPS data before being converted to the physical quantities. See Appendix G for the details. The Meisei MGPS2 software can output the JMAFMT/GRUAN files as an option.

4.1.2 Algorithm for the GRUAN data product for the RS-11G and iMS-100 radiosondes

Radiosonde data taken at the GRUAN sites are archived at the GRUAN database (*Dirksen et al.*, 2014). Figure 4.2 shows the data flow and storage of the GRUAN data product (GDP) for the RS-11G and iMS-100 radiosondes. See Appendix H for the details. For all the sites where the Meisei radiosondes are used, the JMAFMT/GRUAN files and metadata files are uploaded to the GRUAN database at Lindenberg. The Tateno site then downloads these data, and creates the GDP. The GDP includes all the key information, namely, metadata, raw data, instrument parameters (e.g., payload configuration, balloon type and weight), and the results of the pre-launch ground checks. The data processing algorithms described in Sections 3.1 to 3.4 are all applied to the GDP. The GDP created at Tateno are uploaded to the GRUAN database. Finally, the GDP that has passed the quality control at the Lead Centre is disseminated through the File Transfer Protocol (FTP) server of the NOAA's National Centers for Environmental Information (NCEI) (www.gruan.org/data).

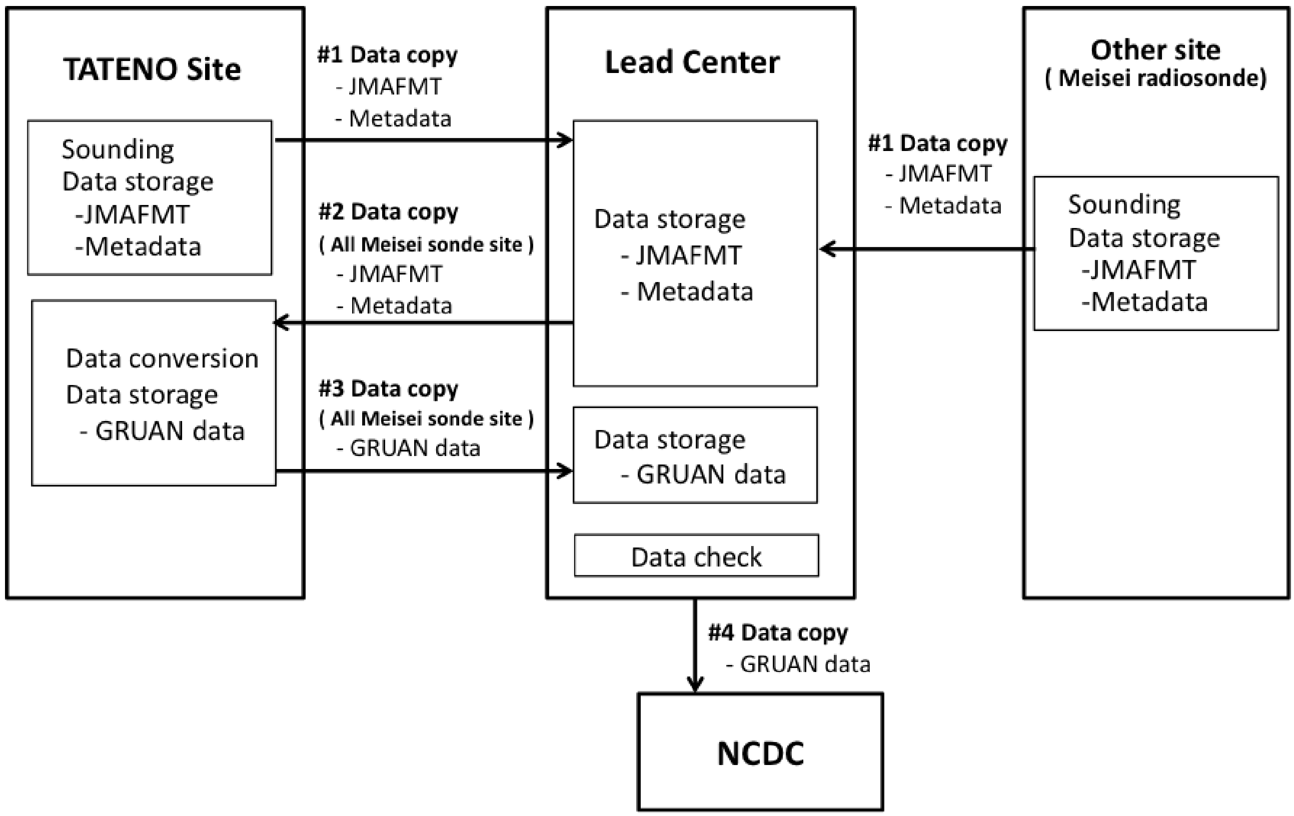

Figure 4.2: The data flow and storage of the GRUAN data product (GDP) for the Meisei RS-11G and iMS-100 radiosondes among Tateno site, GRUAN Lead Centre, other potential sites, and National Centers for Environmental Information (NCEI) of the US National Oceanic and Atmospheric Administration (NOAA).

5 Traceability

In this Chapter we describe the traceability chain for the RS-11G and iMS-100 measurements.

5.1 RIC Tsukuba

Globally uniform, high-quality meteorological data are required to enable accurate weather forecasting and appropriate monitoring of global climate. To maintain the meteorological instruments of individual countries to a high standard of accuracy and train instrument specialists, the World Meteorological Organization (WMO) recommended the establishment of Regional Instrument Centres (RICs) for each of its six regions worldwide in 1986. Sixteen countries in these six regions now actively operate RICs. At the eleventh session of WMO Regional Association II (RA II) in 1996, Japan and China were designated as the Regional Instrument Centres (RICs) of RA II, which consists of 35 countries and areas. Following the designation, the JMA established the RIC Tsukuba at Tateno site. The RIC Tsukuba maintains standard meteorological instruments and testing equipments for barometers, thermometers, hygrometers, and anemometers. It also maintains traveling standards (except for anemometers) that are traceable to Japanese national standards. Using its instruments and equipments, the RIC Tsukuba calibrates standard instruments of member countries and the working standard instruments of manufacturers. For the details about the RIC Tsukuba, see http://www.jma.go.jp/jma/jma-eng/jma-center/ric/RIC_HP.html.

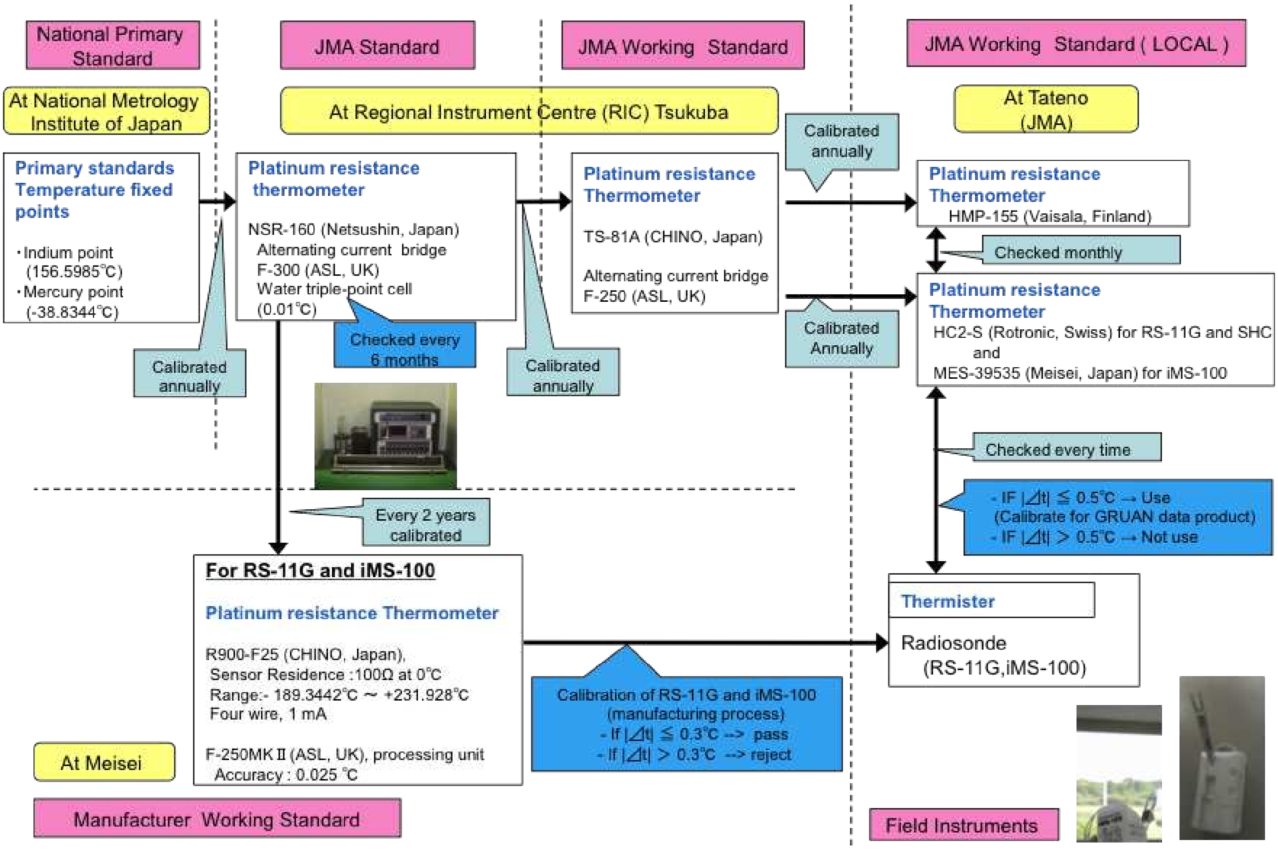

Figure 5.1: Traceability of the temperature sensors on the RS-11G and iMS-100 radiosondes.

5.2 Traceability chain for the RS-11G and iMS-100 radiosondes

Metrological traceability is a property of the result of a measurement or the value of a standard whereby it can be related to stated references, usually national or international standards, through an unbroken chain of comparisons all having stated uncertainties. The temperature and RH measurements from the RS-11G and iMS-100 radiosondes are traceable to standards of the international system of units (SI). Figure 5.1 shows the traceability chain for the RS-11G and iMS-100 temperature measurements, indicating the steps required to link the measurement to the fundamental SI units. The national primary standards are traceable to international standards (SI units) or WMO standards. JMA standard is annually calibrated with the national primary standard. The RS-11G and iMS-100 temperature sensors are calibrated by working standard instruments of the Meisei which are directly traceable to JMA standard through regular calibration once every 2 years. On the other hand, radiosonde operators (i.e., JMA's staff at Tateno radiosonde site) check and calibrate the radiosonde with another working standard instrument (which is also regularly calibrated at the RIC Tsukuba) before launch. Figure 5.2 shows the traceability chain for the RS-11G and iMS-100 RH measurements. The traceability for the RH measurements is similar to that of the temperature measurements. Note that the RS-11G and iMS-100 RH sensors give RH values, while RH and temperature instruments are used to ensure the traceability to JMA standards. (As in Figs. 5.1 and 5.2 and, the accuracy of the JMA standards is 0.01 K for the thermometer and is 0.2 K for the dew point hygrometer. See also Appendix F.)

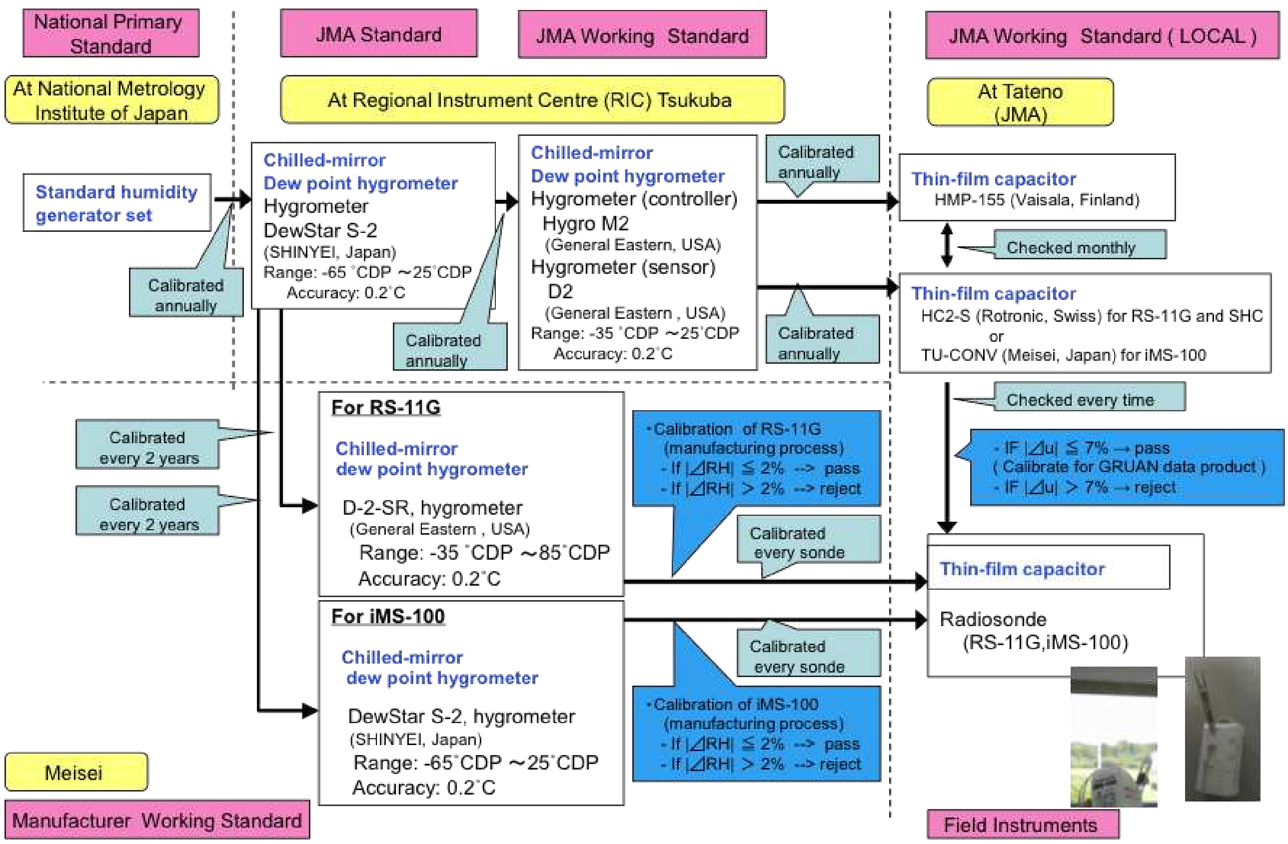

Figure 5.2: Traceability of the RH sensors on the RS-11G and iMS-100 radiosondes.

6 Verification

6.1 Results from the pre-launch checks

In this section, we investigate the pre-launch ground check results taken from 1 January to 30 June 2015 in order to confirm the performance of the RS-11G radiosonde. Two pre-launch checks are conducted at Tateno (see Section 2.4). The first one uses the Standard Humidity Chamber (SHC; 0 %RH and 100 %RH chambers) being carried out up to 24 hours before the launch. This is a manufacturer independent pre-launch check. The second one uses the manufacturer's Ground Checker (GC) being carried out ∼30 minutes before the launch. The former only checks the RH sensor, while the latter checks both the temperature and RH sensors. The number of radiosondes used during the investigation period is 351 which came from 8 production lots. (All sensors in each production lot have been calibrated at the same time and with the same calibrator.) Here, the production lot means the set of radiosondes calibrated at the same time. Among these 8 lots, we will mainly discuss the results for 5 lots because for the rest 3 lots, the sample number was too small (i.e., less than 10 radiosondes; see Table 6.1). Table 6.1 summarizes, for each lot, the number of radiosondes and the pre-launch RH check statistics.

Table 6.1: Summary of the pre-launch checks for relative humidity conducted from 1 January 2015 to 30 June 2015. The lot number indicates the year, month, day, and hour (PM2 means 2:00 pm local time) of the production. The mean and standard deviation (SD) values shown are calculated from the radiosonde measurement minus the reference sensor measurement for each radiosonde sensor.

	Number of	SHC (100 %RH)		SHC (0 %RH)		GC (Room condition)	
Lot Number	radiosondes	Mean (%)	SD	Mean (%)	SD	Mean (%)	SD
◯ Lot (20141030PM2)	39	0.3	0.96	-1.2	0.18	0.1	0.35
◯ Lot (20141031PM1)	107	1.6	0.92	0.2	0.40	0.5	0.37
◯ Lot (20141104PM3)	48	1.8	0.61	-1.4	0.55	0.9	0.44
□ Lot (20141107PM1)	3	0.8	0.71	0.6	0.50	0.5	0.25
◯ Lot (20150126PM3)	83	-1.6	0.74	0.5	0.24	-1.0	0.86
◯ Lot (20150205PM1)	63	-1.9	0.83	-0.5	0.22	-0.2	1.17
□ Lot (20150209PM1)	4	-0.8	0.42	-3.2	0.14	0.2	0.13
△ Lot (20150209PM5)	4	1.1	0.77	-0.8	1.76	0.3	0.36
Total/average	351	0.1	1.73	-0.2	0.85	0.0	0.96

6.1.1 Temperature sensor checks using the Baseline Checker

Under room conditions (22-27°C, Fig. 6.1), temperature comparisons between the radiosonde and the standard instrument (Rotronic HC2) have been carried out ∼30 minutes before the launch using the manufacturer's GC. JMA has a criterion that the radiosondes which show more than 0.5 K difference during this pre-launch check are not used for the soundings. During this investigation period, there is no radiosonde rejected by this criterion. From the results shown in Figure 6.1, the mean biases were 0.04 K on average. Some lots showed much larger biases, but this is due to the small number of samples (less than 10). Also, the standard deviation was 0.14 K on average during this period.

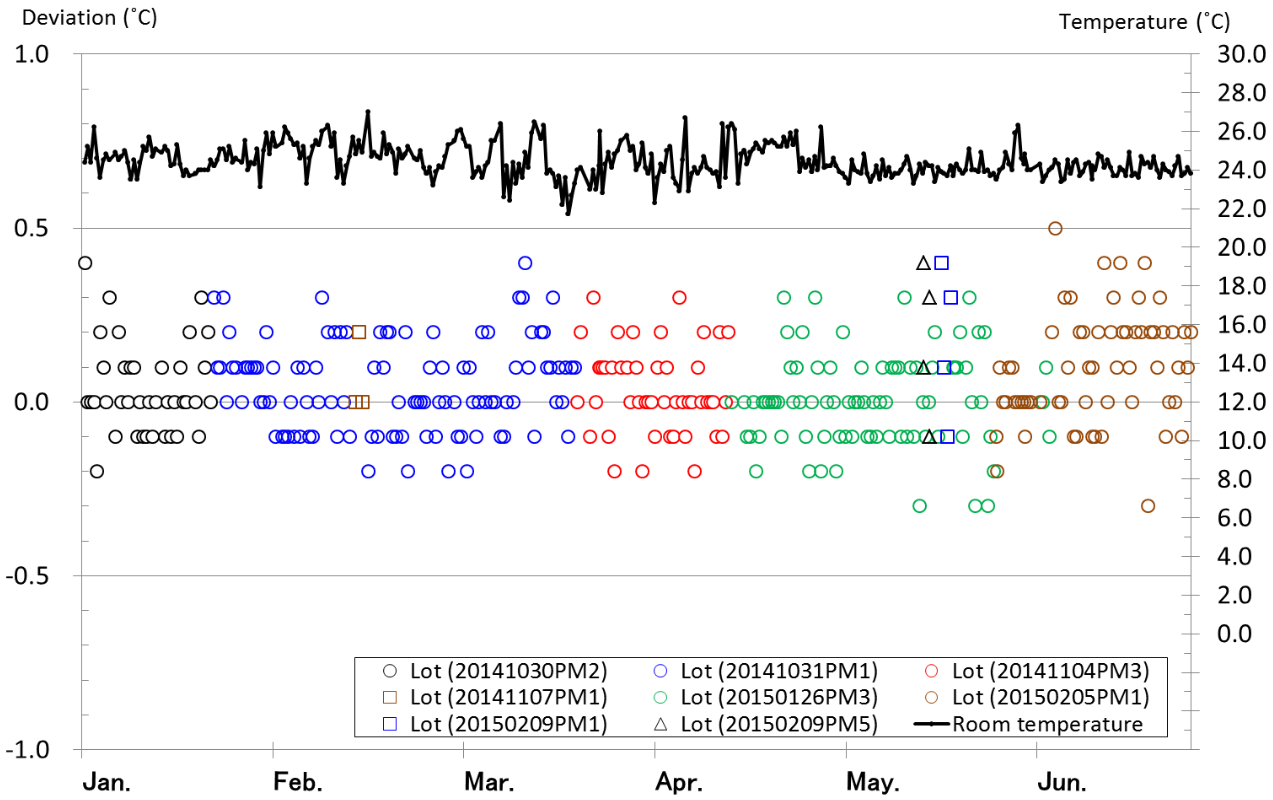

Figure 6.1: Time series of the temperature deviation of radiosonde reading with respect to the standard instrument reading under room temperature conditions (22–27°C, black line) using the manufacturer's Ground Checker. Different marks indicate radiosondes from different lots.

6.1.2 Relative humidity sensor checks using the Baseline Checker

The RH comparison was also carried out with the standard instrument (Rotronic HC2) during the manufacturer's GC under room conditions (10 %RH-70 %RH, Fig. 6.2). JMA has a criterion that the radiosondes which show more than 7 %RH difference during this pre-launch check are not used for the soundings. During this investigation period, there is no radiosonde rejected by this criterion. Table 6.1 and Figure 6.2 show that the mean biases were 0.04 %RH on average, with the standard deviation of 0.96 %RH on average. There is a large seasonal evolution in room RH conditions from dry in winter to wet in summer. In the following we make the analysis with water vapor pressure rather than RH. Figure 6.3 shows the water vapor pressure deviation (%) reading relative to the standard-instrument reading under room RH conditions. In this figure, there are no seasonal changes in each radiosonde. At this moment, there is no clear explanation why there is an apparent seasonality in Figure 6.2. Thus, the GC readings are currently not used to scale/correct the RH profiles.

6.1.3 Relative humidity sensor checks using the Standard Humidity Chamber

The RH comparison is carried out using the two types of manufacturer independent Standard Humidity Chamber (SHC) up to 24 hours before the launch. The SHC has the reference instrument Rotronic HC2, and the near 100% RH condition is provided with a sponge saturated with distilled

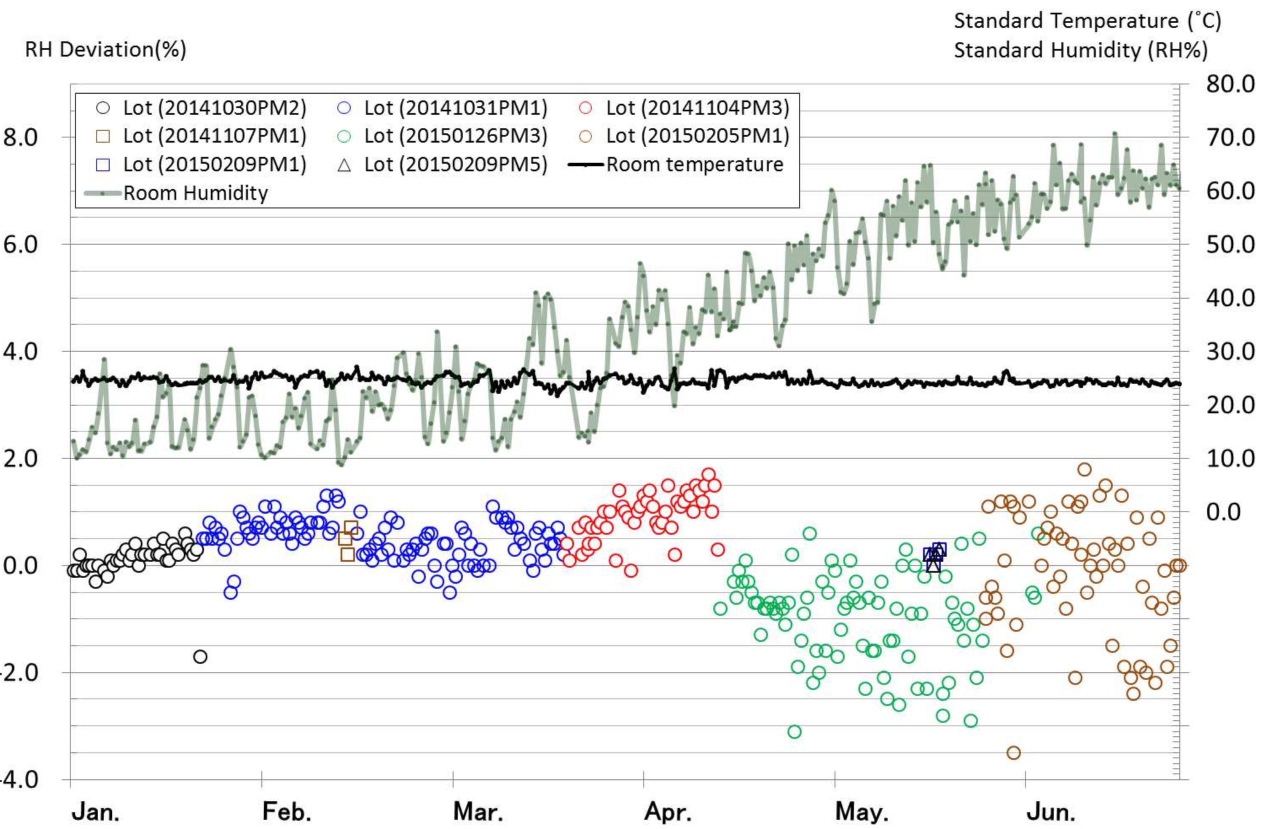

Figure 6.2: Time series of the RH deviation of radiosonde readings from the standard-instrument readings under room RH conditions (10%RH-70%RH, gray line) using the manufacturer's Ground Checker. Different marks indicate radiosondes from different lots.

water, while 0% RH condition is provided with molecular sieves (Appendix F). These comparison data are used when creating the GDP. At the same time, checks under the room conditions using the manufacturer's GC are also carried out. JMA has a criterion that the radiosondes which show more than 10 %RH difference during this pre-launch check are not used for the soundings. During this investigation period, there was no radiosonde rejected by this criterion. The RH differences between the radiosonde and standard instruments measured in the two SHCs are shown in Figure 6.4. According to the two graphs in Figure 6.4, the RH deviation of approximately 100 %RH and 0 %RH SHC shows small deviations between the radiosonde humidity and standard instrument. Especially, each lot of radiosonde has individual difference for RH deviation. The differences among different lots are most probably due to the fact that the factory calibration is conducted at 15%-95% RH and not at 0 %RH and at 100 %RH. Therefore, the GDP for RS-11G and iMS-100 is recalculated by adding Tateno SHC (0 %RH and 100 %RH) calibration data to manufacturer's calibration data.

6.2 Results from the multiple-payload soundings

6.2.1 Comparison of two RS-11G radiosondes

To investigate the production variability, i.e., differences between two RS-11G or two iMS-100 radiosondes, two sets of multiple-payload soundings of two RS-11G radiosondes and another two sets of

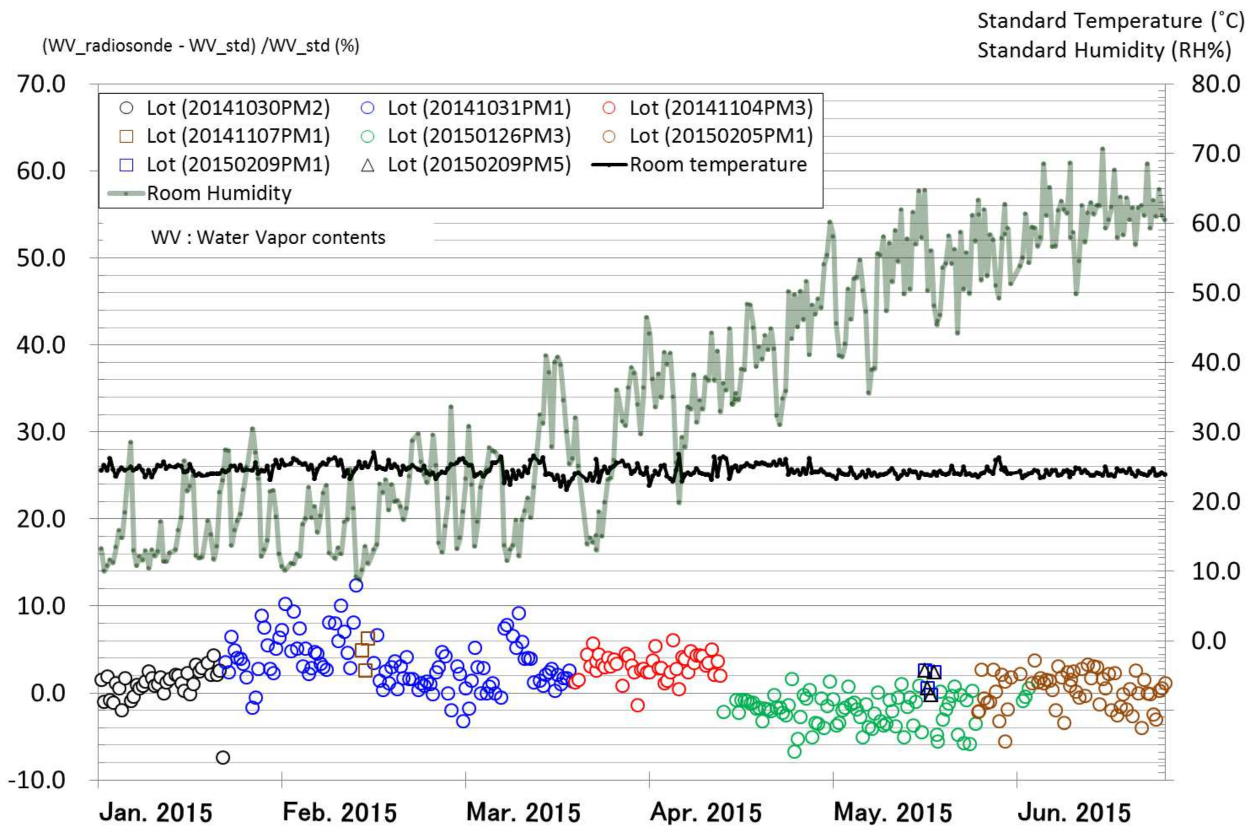

Figure 6.3: As for Figure 6.2 but for water vapor pressure difference (in percent) relative to the standard-instrument reading (colored circles).

two iMS-100 soundings were conducted with a single balloon for each set at Moriya, Japan (Figs 6.5-6.8). For both RS-11G and iMS-100 investigations, one daytime sounding and one nighttime sounding were conducted. *Dirksen et al.* (2014) recommended to make this type of soundings also for verification of the uncertainty evaluation of the GDP.

Figure 6.5 shows the profiles of differences in the temperature, RH, geopotential height, and pressure measurements for the daytime sounding. For this sounding, the heat pulse filter was applied above ∼24 km (∼30 hPa). The temperature difference is 0.10 K on average, and its variability is 0.16 K (1σ) throughout the profile. This value is much smaller than the estimated uncertainty. The variability becomes larger at higher altitudes, probably due to additional heat contamination arising from the multiple-payload configuration. The RH difference is mostly less than 2 %RH from surface to 30 km. Because sensors withRH biases exceeding 2 %RH are rejected at the factory calibration, this result is reasonable. The geopotential height difference is 7.5 m on average. The PDOP for this soundings was typically less than 1.4, and therefore, the variability (1σ) expected from Eq. 3.17 is less than 7.4 m. Also, we can see the large difference immediately after the balloon release (i.e. below a few hundred meter in this case). This is probably because of the effect of multi-path signal. The pressure difference is strongly affected by the geopotential height difference.

Figure 6.6 shows the profiles of differences for the nighttime sounding. The temperature difference is 0.22 K on average, and its variability is 0.09 K (1σ) throughout the profile. The variability is much smaller during the nighttime sounding than that during the daytime because the nighttime measure-

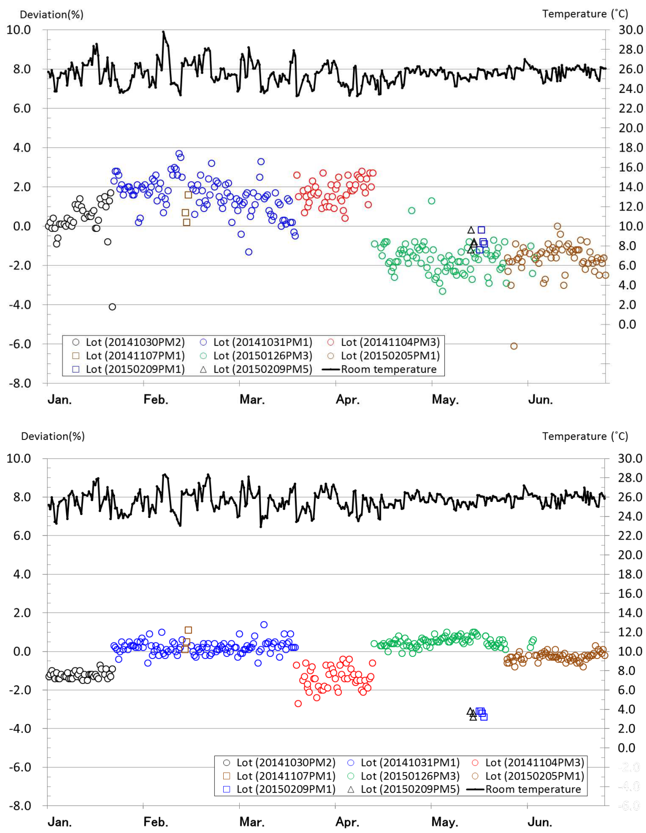

Figure 6.4: Time series of the RH deviation of radiosonde reading with respect to (top) 100 %RH and (bottom) 0 %RH created in the SHC (left axis) and the temperature conditions for the SHC check (right axis). Different marks indicate radiosondes from different lots.

ments do not suffer from the contamination from solar heated balloon and package. The major source of nighttime temperature differences is the calibration uncertainty. The RH difference is less than 1 %RH. This is also smaller than for the daytime sounding because of the absence of solar heating on the RH sensor. The geopotential height difference is 3.5 m on average, but sometimes reaches ∼20 m. The pressure difference is within 1 hPa except the region below 1 km.

Figure 6.7 shows the daytime comparison of two iMS-100 radiosondes. The results are similar to those of the RS-11G radiosondes. Figure 6.8 shows two sets of nighttime comparison of two iMS-100 radiosondes. For a cloudy condition case (Figure 6.8, top), the results are similar to those of the RS-11G radiosondes, except for RH in the stratosphere. The large differences in the stratospheric RH for this case are due to wet contamination of the RH sensor while going through very wet/cloudy troposphere. This sounding indicates that in such a situation, the uncertainty of the RH measurements becomes large. Figure 6.8 (bottom) shows another nighttime comparison case, where the wet contamination issue did not occur and the two radiosondes show quite similar results.

These multiple-payload comparisons of the RS-11G and iMS-100 radiosondes show that the production variability is in general smaller than the uncertainty evaluated in Chapter 3. This supports the notion that the production of the RS-11G and iMS-100 radiosondes are stable.

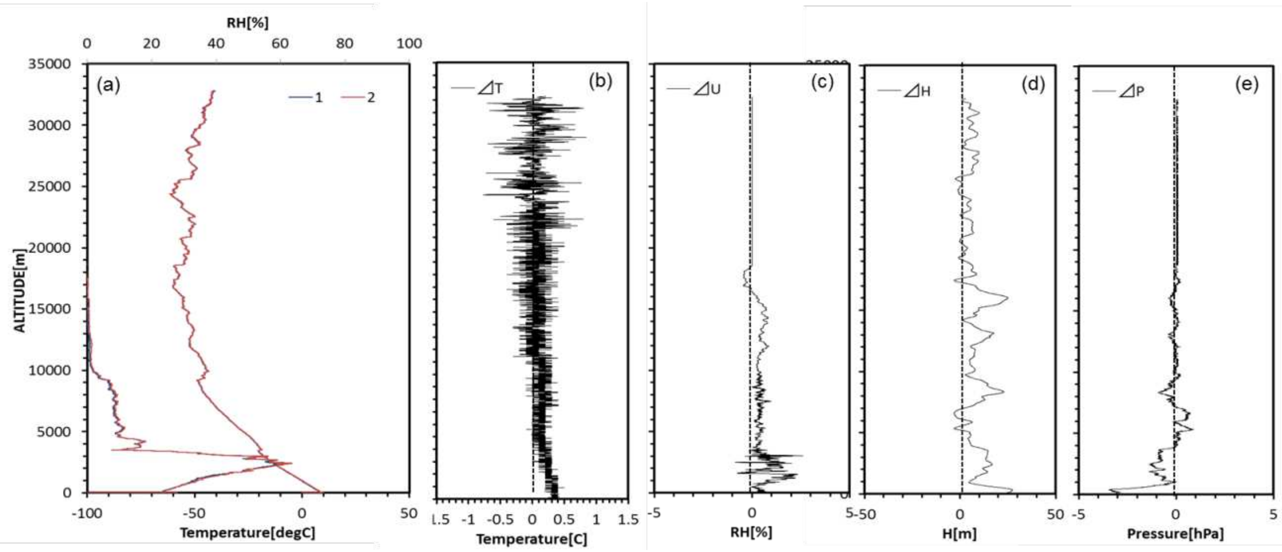

Figure 6.5: (a) Vertical profiles of temperature and RH obtained from a daytime multiple-payload sounding of two RS-11G radiosondes with a single balloon launched at Moriya (35.94°N, 140.00°E), Japan at 14:30 LT on 22 December 2014. Note the two curves are mostly overlapping for both temperature and RH. The profiles of differences in (b) temperature, (c) RH, (d) geopotential height, and (e) pressure.

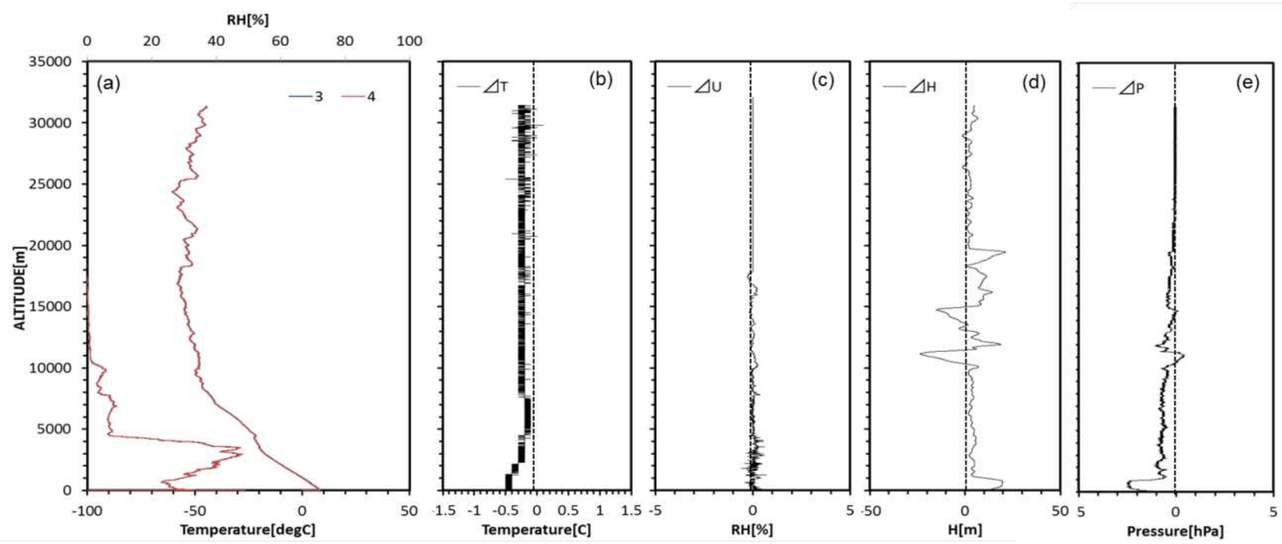

Figure 6.6: As for Figure 6.5, but for a nighttime multiple-payload sounding of two RS-11G radiosondes launched at 17:30 LT on 22 December 2014.

6.2.2 Comparison with the Vaisala RS92 radiosonde

JMA has conducted weekly comparison flights of the RS-11G radiosonde with the Vaisala RS92 radiosonde since July, 2015. It is important to compare the GDP-RS-11G with the GDP-RS92 because the RS92 radiosondes are in operational use at 13 out of the 22 GRUAN (certified/potential; as of January 2017) sites on December 2015. Figures 6.9 and 6.10 show two examples of the comparison

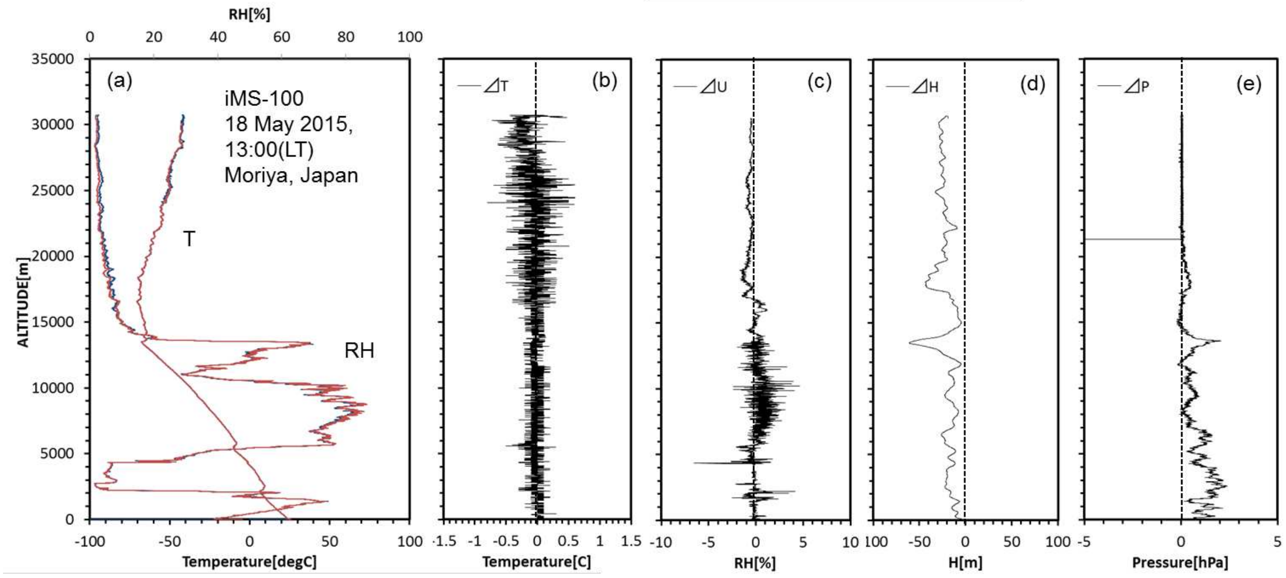

Figure 6.7: As for Figure 6.5, but for a daytime multiple-payload sounding of two iMS-100 radiosondes launched at 13:00 LT on 18 May 2015.

between the GDP-RS-11G (red) and the GDP-RS92 (blue) at Tateno. For these examples, the temperature and RH measurements show good agreement within the estimated uncertainties (red shade for GDP-RS-11G and blue shade for GDP-RS92) throughout the profile. The statistical analysis of all the comparison flight results will be reported elsewhere in the future.

6.2.3 Comparison with the Cryogenic Frostpoint Hygrometer

Several comparison flights with the Cryogenic Frostpoint Hygrometer (CFH) (*Vömel et al.*, 2007, 2016) were conducted at two midlatitude sites, Tateno (36.06°N, 140.13°E), Japan and Lindenberg (52.21°N, 14.12°E), Germany, and at a tropical site, Biak (1.1°S, 136.1°E), Indonesia. The RS-11G RH data were processed according to Section 3.2.3 (i.e., GDP). CFH measures the dew/frost point temperature of the ambient air with the uncertainty of ∼0.5 K. The CFH RH data were calculated with the CFH dew/frost point temperature and the RS-11G temperature using the water vapor pressure equation by *Hyland and Wexler* (1983).

Figure 6.11 shows a daytime comparison with the CFH at Lindenberg. The RH profiles from the CFH and RS-11G show good agreement with differences of less than 10 %RH mostly from the surface to the stratosphere. This result is roughly consistent with the uncertainty estimation of the RS-11G RH measurements with the exception of upper troposphere (around 10 km). Figure 6.12 shows the comparison results taken at Biak. The RH profiles show good agreement (<10 %RH) from the surface to 14 km. However, in the upper troposphere (∼15 km), the RS-11G RH shows dry biases, or the CFH shows wet biases. The CPS sonde (*Fujiwara et al.*, 2016), which was launched simultaneously with the CFH, indicates that there were cloud layer between 5 km and 16 km. This cloud layer may have caused contamination after passing through clouds and unstable behavior (oscillation) of dew/frostpoint profile by the CFH feedback controller in clouds. The measurement from the RS-11G is also affected by cloud contamination error, and the measurement uncertainty may become larger after passing cloud layer. Because there is a possibility that the uncertainty for the RH profile under

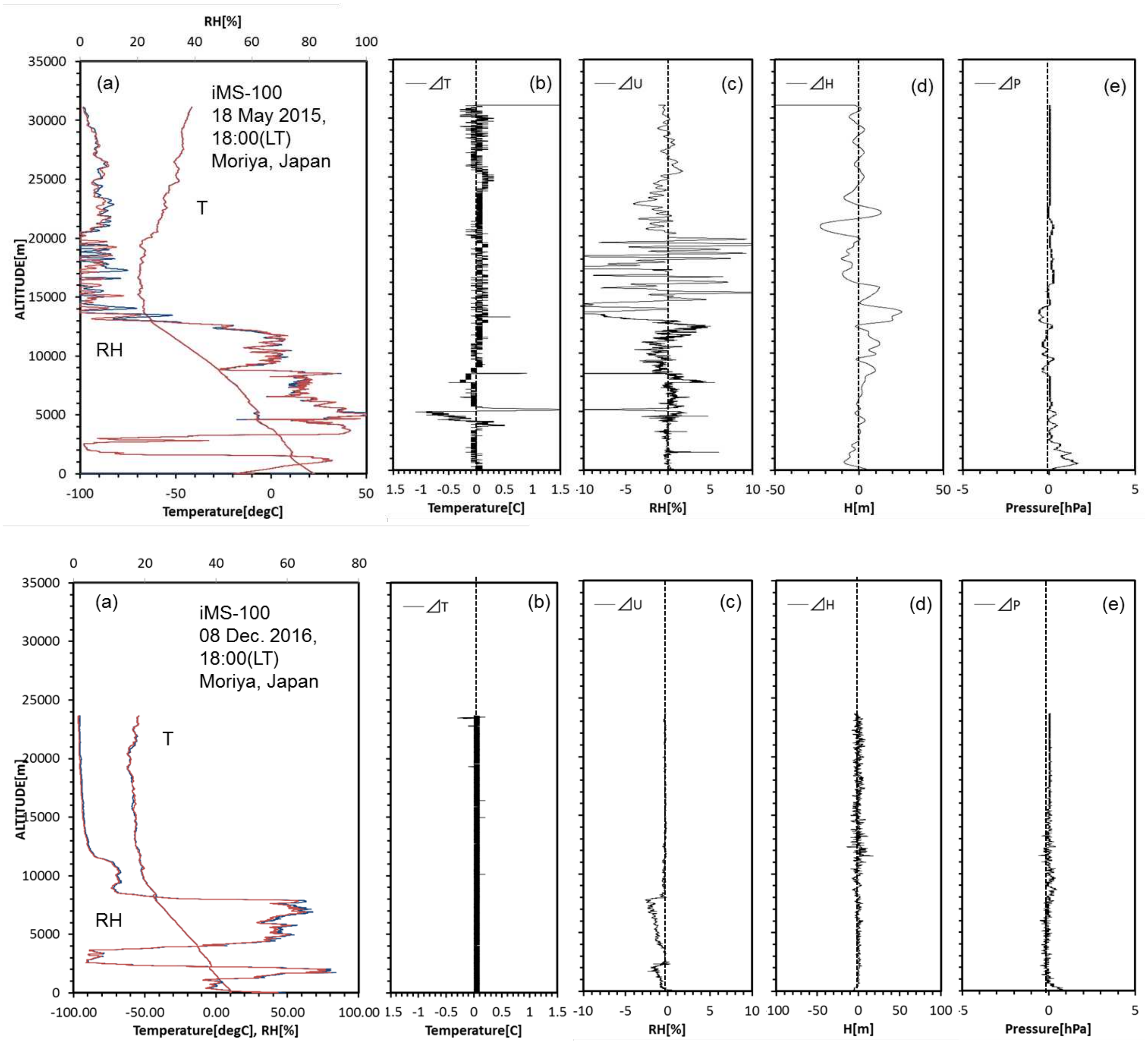

Figure 6.8: As for Figure 6.5, but for a nighttime multiple-payload sounding of two iMS-100 radiosondes. (Top) the sounding under cloudy conditions, launched at 18:00 LT on 18 May 2015, and (bottom) the sounding at 18:00 LT on 8 December 2016.

cloudy/rainy conditions is larger than that in clear sky, we estimate the uncertainty from contamination error in a large as described in Section 3.2.4.

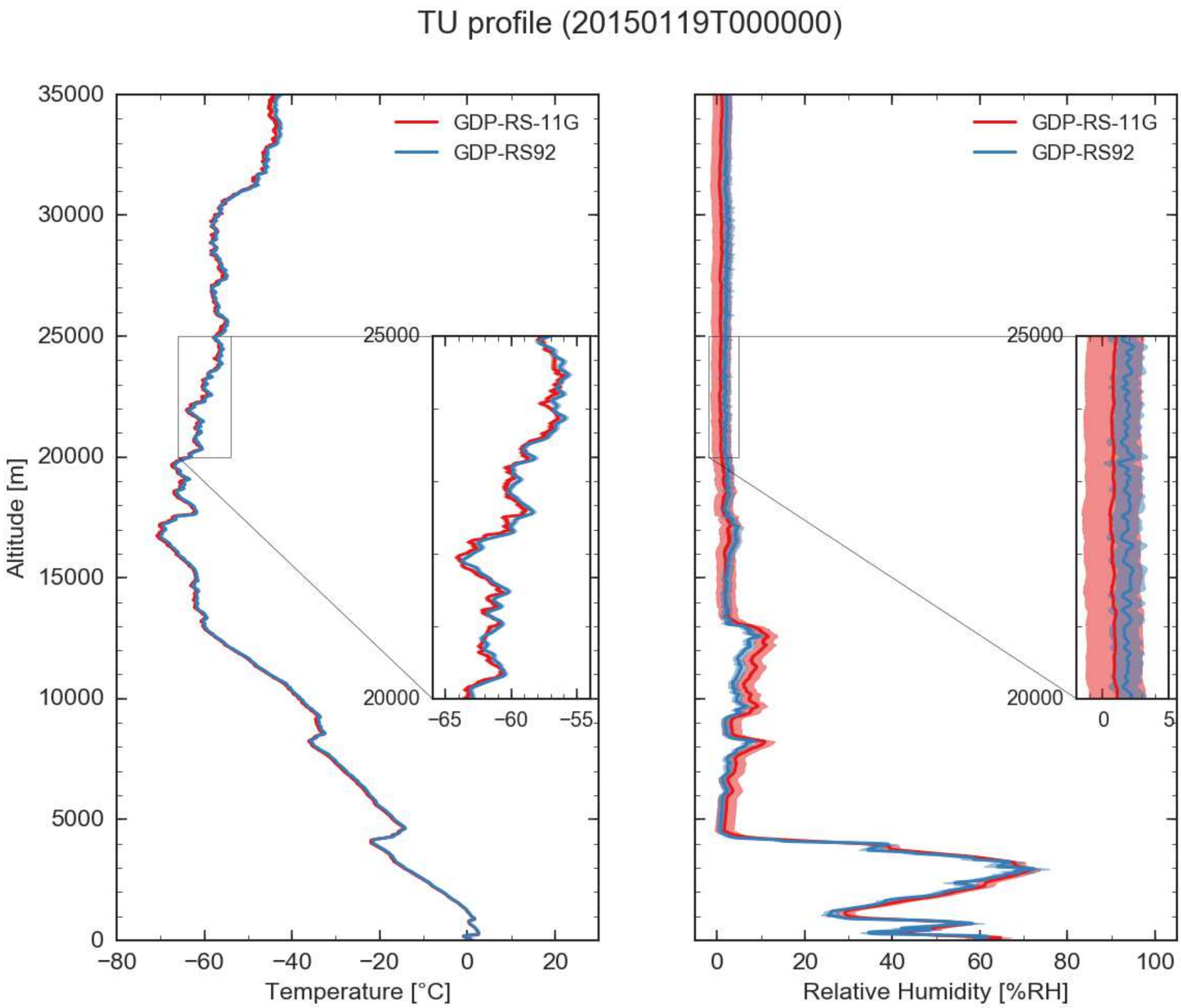

Figure 6.9: Comparison of temperature (left) and RH (right), with uncertainty range, between the RS-11G GDP (red) and RS92 GDP (blue) at Tateno, both launched at 00:00 UTC on 19 January 2015.

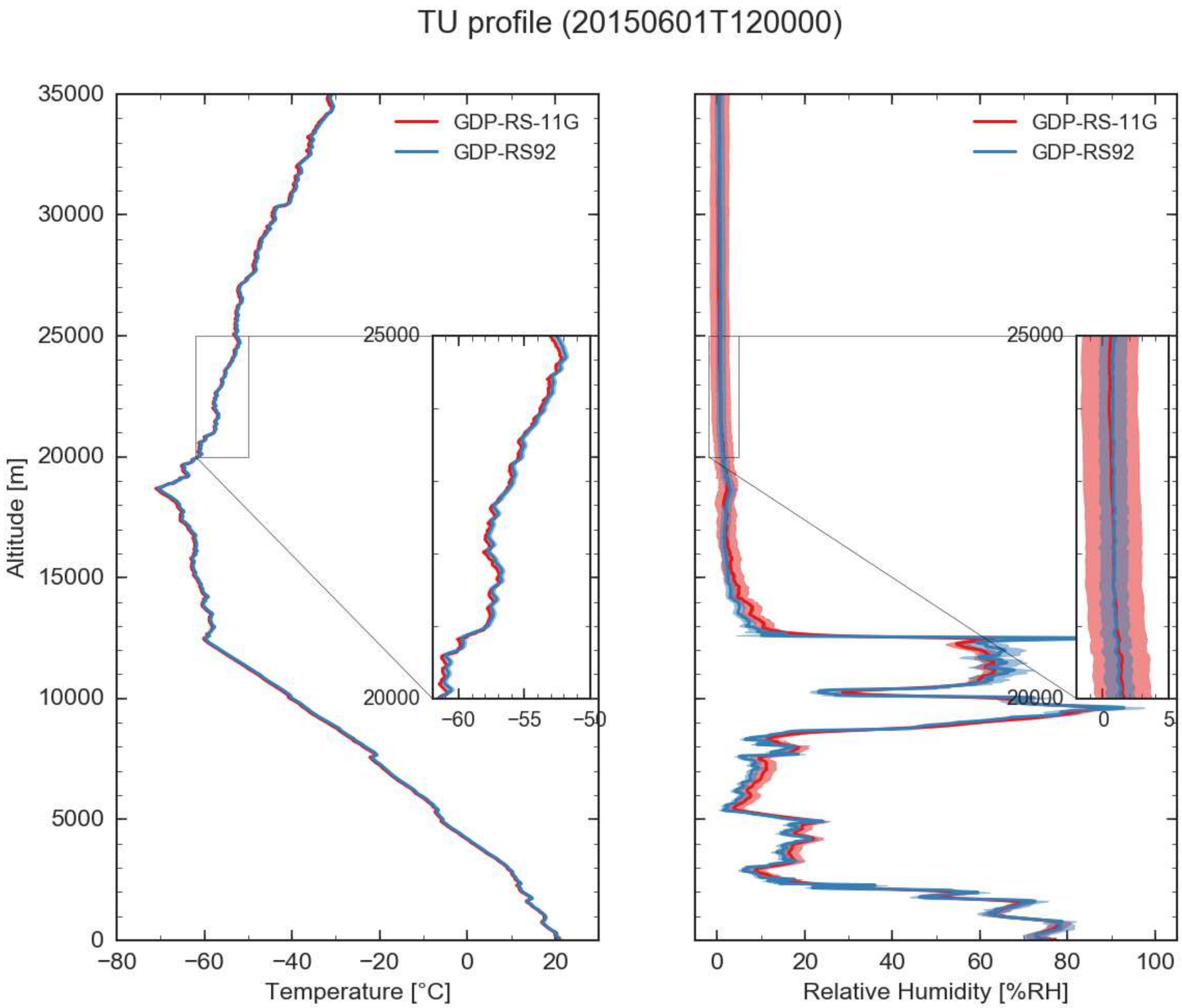

Figure 6.10: As for Figure 6.9, but for the sounding at 12:00 UTC on 1 June 2015.

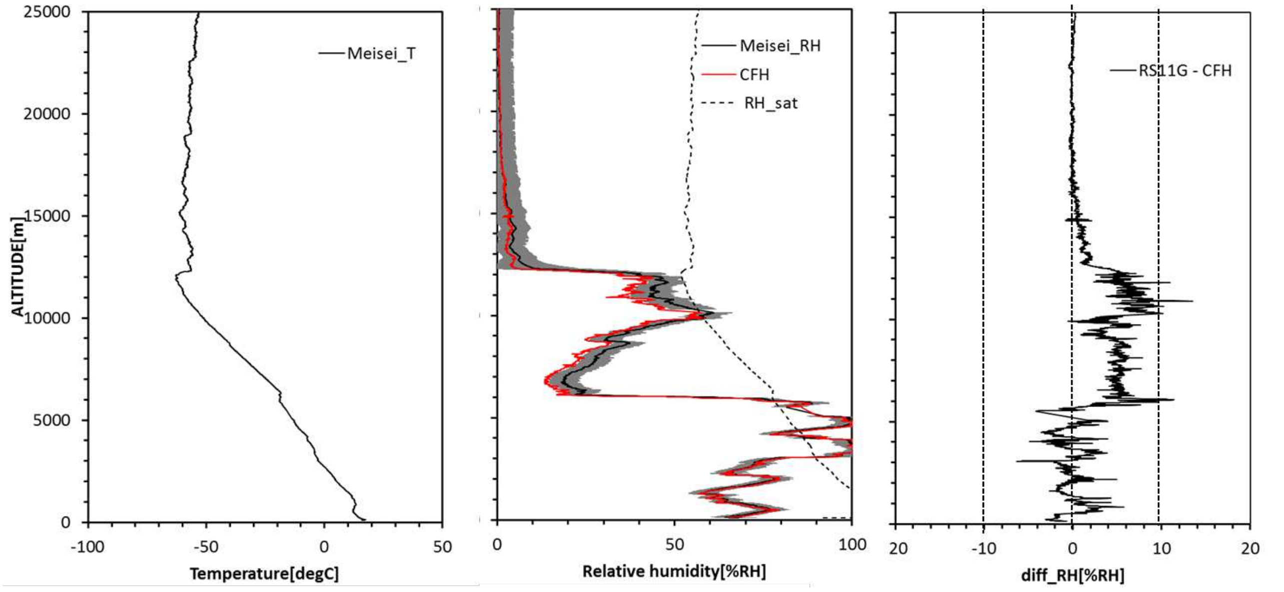

Figure 6.11: Profiles of (left) temperature, (center) RH, and (right) RH difference obtained from a daytime simultaneous sounding of the RS-11G and CFH at Lindenberg (52.21°N, 14.12°E), Germany at 14:00 LT on 7 October 2014. In the center panel, red curve is for CFH RH, black for RS-11G RH, and dotted for saturation RH. Gray shade is the measurement uncertainty calculated according to Section 3.2.4. In the right panel, the RH difference is calculated as RS-11G RH minus CFH RH.

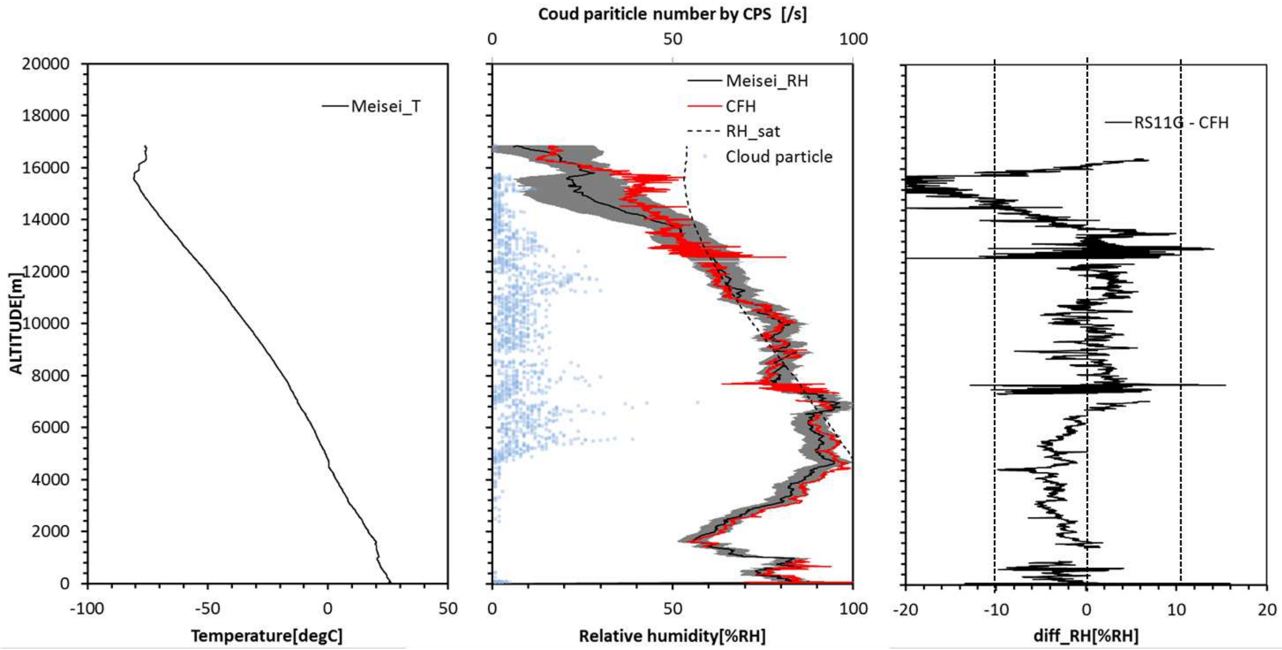

Figure 6.12: As for Figure 6.11, but for a nighttime simultaneous sounding of the RS-11G and CFH at Biak (1.1°S, 136.1°E), Indonesia at 18:00 LT on 23 February 2015. Blue dots in the center panel indicate the cloud particle number by the CPS sonde. This indicates that there are cloud layer between 5 km and 16 km. For this sounding, the balloon burst at ∼17 km, around tropopause.

7 Summary

The Meisei RS-11G radiosondes have been launched operationally at the Aerological Observatory of Japan Meteorological Agency, Tateno (36.0576°N, 140.1257°E), Japan since July 2009. Also, the Meisei iMS-100 radiosonde, which is equipped with the same sensors as the RS-11G radiosonde, will be used in the future at Tateno. The technical details including the calculation and correction algorithms and the measurement uncertainty evaluation of the RS-11G and iMS-100 radiosondes were fully described. The corrections for the RS-11G and iMS-100 measurements compensate for all the major systematic biases. For temperature, the dominant contributions to its total uncertainty come from the solar radiation heating error and heat spike error. For RH, the dominant contributions come from the solar heating dry bias error, time-lag error, and temperature-humidity dependence error. For geopotential height and pressure, no correction is applied. Finally, for horizontal winds, the fluctuation by the pendulum motion are removed by filtering. Each component of the measurement uncertainties was estimated by laboratory experiments and theoretical considerations. The estimated total uncertainties were verified in part by various comparison flights (two same model flights, flights with Vaisala RS92 radiosonde, and flights with the CFH).
Table 7.1 summarizes the uncertainty estimates of the temperature, RH, geopotential height, pressure and horizontal wind measurements of the two radiosonde types. The dominant uncertainty for the temperature measurement arises from the solar radiation correction and the factory calibration error. The total uncertainty increases with altitude, and reaches 0.8 K at 30 km. Up to ∼15 km the uncertainty is dominated by the calibration error. In the stratosphere, the uncertainty by the radiation correction is the main factor. Because the actual sounding condition is in general different from the assumed condition (e.g., surface/cloud albedo), it is evident that additional information such as the surface and cloud conditions is needed to reduce the uncertainty. Also, the uncertainty due to heat spikes is added depending on the flight configuration (e.g., with a shorter string of 15 m with a 600 g balloon). A large payload and a rig for multiple-payload soundings may introduce additional heat spikes.

Table 7.1: Summary of the uncertainty estimates for the RS-11G and iMS-100 radiosondes (k=2; typical uncertainty values at mid-latitudes).

Parameter	Uncertainty estimated in this paper	Reference
Temperature (night)	< 0.4 K	Table 3.1
Temperature (day)	< 0.5 K troposphere, < 0.8 K stratosphere	Table 3.1, Fig. 3.14
Relative humidity	< 5%RH, except around tropopause	Table 3.2, Fig. 3.24
Geopotential height	$< \sim 42$ m (PDOP < 4)	Table 3.3
Pressure	< 1 hPa	Table 3.3, Fig. 3.27
Wind u- v component	$< 1 – 3\,\mathrm{m\,s^{-1}}$	Fig. 3.30

The uncertainty of the RH measurements maximizes at the tropopause because of the time-lag correction component. Also, the uncertainty from the Temperature-hUmidity Dependence (TUD) correction is relatively large at low temperatures. The large uncertainty of the T_s/T_a correction arises from the sensor temperature measurement uncertainty, which is a major uncertainty source for the RH measurement. The hysteresis bias arises only when RH changes from wet to dry. Also, wet biases due to contamination could occur under rainy conditions, though the uncertainty quantification is difficult due to a lack of reference measurements under such conditions.

The uncertainty of the geopotential height measurement is mainly determined by the GPS signal accuracy. Pressure data from the RS-11G and iMS-100 radiosondes are calculated from GPS geopotential height using the hydrostatic equation. Therefore, the uncertainties of the temperature, RH, and geopotential height measurements propagate to the pressure uncertainty. In addition, the uncertainty of the surface pressure measurement at the launch affects the pressure uncertainty. The GPS-based geopotential height is the main uncertainty source for pressure at lower altitudes, while temperature is the main source at high altitudes.
GPS-based horizontal wind data include oscillations by pendulum motions of the radiosonde. Such oscillations must be removed by a low-pass filter. This is the main source of the uncertainty of the wind measurements.

A Connection to external sensors for the RS-11G radiosonde

A.1 Meisei's original protocol interfacing with external sensors

The RS-11G radiosonde and an external sensor are synchronized by using 1 Hz demand pulse from the RS-11G radiosonde. The external sensor should send 25-byte data per second between the two 1 Hz pulses. The format of the output data is as follows:

- 1 byte: header;
- 21 byte: data;
- 1 byte: Block Check Code (BCC); and
- 2 byte: delimiters.

As the header, an identification code is assigned for each external sensor. The external sensor is usually connected by using three cables, which are for the data reception from the RS-11G radiosonde (Pin #1), for the data transmission to the RS-11G radiosonde (Pin #2), and for the ground (GND) (Pin #3). Some sensors (e.g., CO_2 sensor) need another cable in addition to three cables. For example, for the CPS sonde, the header code is the American Standard Code for Information Interchange (ASCII) code C (0x43). The BCC is calculated as the eXclusive OR (XOR) from header to data. The delimiters are CR (0x0D) and LF (0x0A).
If a GRUAN sensor such as CFH is used as an external sensor, an I/F board is needed between GRUAN sensor and RS-11G (see section A.2).

Table A.1: An example of the ASCII data format of the CFH sensor, for the case xdata=0802E21FFD85C8CE078A0193 as 1-second data.

offset	bytes	description
0	1	Instrument_type = 08 (=CFH)
1	1	Instrument_number = 02 (Second instrument in the daisy chain)
2	3	Mirror temperature = E21FFD
5	3	Optics voltage = 85C8CE
8	2	Optics temperature = 078A
10	2	CFH Battery = 0193

Table A.2: An example of the CFH data translated in the I/F board.

	1	2	3	4	5	6	7	8	9	10
0	0x58	0x08	0x02	0xE2	0x1F	0xFD	0x85	0xC8	0xCE	0x07
1	0x8A	0x01	0x93	0x00	0x00	0x00	0x00	0x00	0x00	0x00
2	0x00	0x00	0x31	0x0D	0x0A					

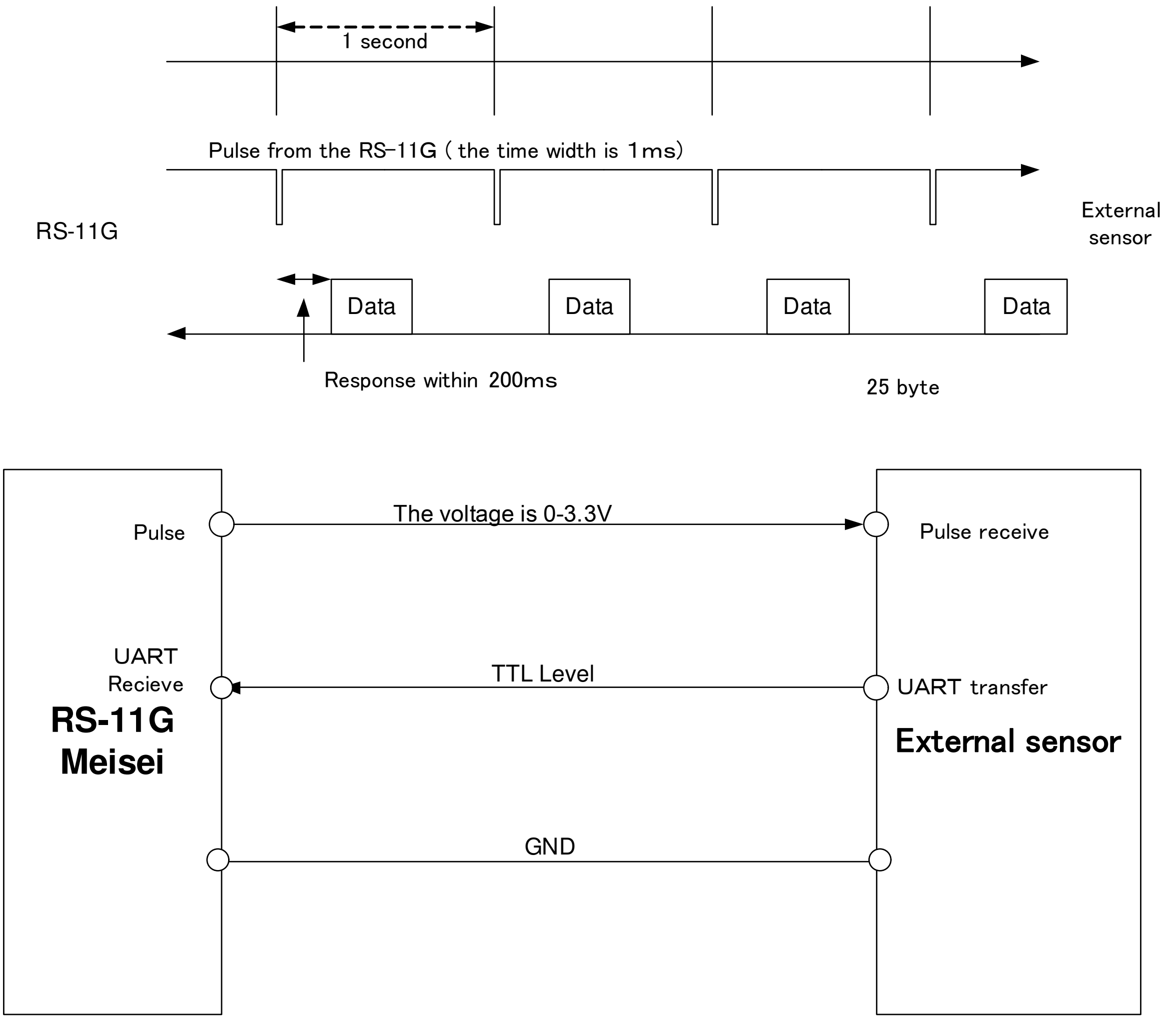

Figure A.1: Connection between the RS-11G radiosonde and an external sensor. The timing chart in the top side indicates the signal transferred between the RS-11G and the external sensor.

A.2 Sensors with the GRUAN standard generic interface (the GRUAN sensors)

The GRUAN standard generic interface is proposed by Dr. Holger Vömel then at the GRUAN Lead Centre. The sensors with this interface protocol are called the GRUAN sensors. For example, the Cryogenic Frostpoint Hygrometer (CFH) is one of the GRUAN sensors. An I/F communication board provided by Meisei is necessary to establish the communication between a GRUAN sensor and the RS-11G radiosonde. The serial interface port of the GRUAN sensor is used as shown in Fig. A.2. The communication between the I/F board and the GRUAN sensor is asynchronous communication, whereas that between the I/F board and the RS-11G radiosonde is synchronous communication as described in A.1. The GRUAN sensor is connected to the I/F broad with four wires: Pin #1 for Common (GND), Pin #2 for the instrument serial output, Pin #3 for the instrument serial input, and Pin #4 for Common (GND). The data format of the GRUAN sensor needs to be adjusted for the Meisei I/F communication board. It should be written in the ASCII code, and is defined for each sensor. It should start from xdata=, being followed by the actual data. Table A.1 shows an example for the case of CFH sensor. The data processing in the Meisei I/F board is as follows:

- Step 1: I/F board receives the data, ”xdata=. . . ” from the GRUAN sensor.
- Step 2: I/F board deletes the portion, ”xdata=”.
- Step 3: I/F board converts the ASCII data into binary data.
- Step 4: Header code ”X (0x58)”, which is the header for GRUAN sensors, is added to the 1st field. The data are added to the 2nd to 21st field. If the data length is less than 20 byte, the ”0x00” codes are added. The 23nd field is used as a block check code, i.e., XOR from the 1st byte to 22nd byte. The delimiters are added to the 24th and 25th field.

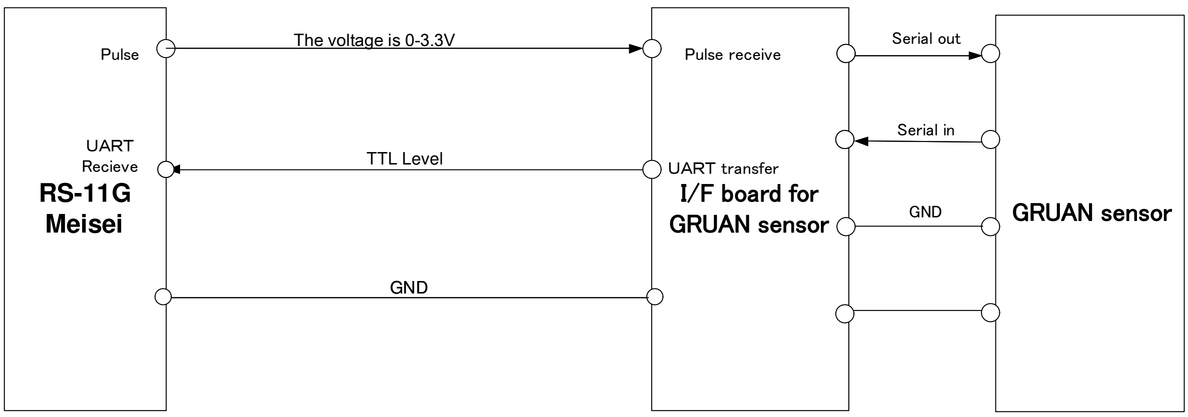

Figure A.2: Connection between the RS-11G radiosonde and a GRUAN sensor. An I/F board is needed between RS-11G and the GRUAN sensor.

B Temperature calculation for the RS-11G and iMS-100 radiosondes

This section describes the method of temperature calculation from the raw data, i.e., the temperature frequency data and the reference frequency data, by using the coefficients determined at the factory. The frequency of temperature received by the ground system is converted to the resistance value of the thermistor. The relationship between the frequency and resistance is given by

$$rt = FT/FR \times 4, \tag{B.1}$$

$$R_t = A_0 + A_1 \times (1/(rt-1)) + A_2 \times (1/(rt-1))^2 + A_3 \times (1/(rt-1))^3 \tag{B.2}$$

where FT is the frequency of temperature, FR is the reference frequency, rt is converted frequency of temperature, R_t is the resistance of the thermistor [$k\Omega$]; and A_0, A_1, A_2, and A_3 are the set of calibration coefficients for each radiosonde. The set of calibration coefficients, A_0 to A_3, is determined for each radiosonde during the manufacturing and calibration process.
The resistance value is converted into temperature by the following processes. When the resistance value is between the minimum and maximum calibration resistances, CR_0 and CR_{10}, respectively (i.e., between -85°C and +40°C), temperature is calculated with the Cspline function refereeing to the GNU Scientific Library (GSL), using the 11 calibration temperatures and the corresponding natural logarithm of calibration resistances:

$$T(Rt) = CSpline[CT_0 \ldots CT_{10}, CR_0 \ldots CR_{10}] \tag{B.3}$$

where T is temperature [°C], CT_0 to CT_{10} are 11 calibration temperature values, and CR_0 to CR_{10} are corresponding 11 calibration resistance values. When the resistance is smaller than CR_0 (i.e., above $\sim$+40°C), temperature is calculated via the following B_1 coefficient,

$$B_1 = (ln(CR_0) - ln(CR_1))/(1/(CT_0 + 273.15) - 1/(CT_1 + 273.15)) \tag{B.4}$$

$$T(Rt) = 1/((ln(Rt) - ln(CR_0))/B_1 + 1/(CT_0 + 273.15)) - 273.15 \tag{B.5}$$

If the calculated temperature becomes greater than +60°C, the measurement is judged as being in error. When the resistance is greater than CR_{10} (i.e., below $\sim$-85°C), temperature is calculated via the following B_2 coefficient,

$$B_2 = (ln(CR_9) - ln(CR_{10}))/(1/(CT_9 + 273.15) - 1/(CT_{10} + 273.15)) \tag{B.6}$$

$$T(Rt) = 1/((ln(Rt) - ln(CR_{10}))/(BB_2) + 1/(CT_{10} + 273.15)) - 273.15 \tag{B.7}$$

C Radiation correction for the RS-11G and iMS-100 temperature measurements

C.1 Equation of radiation correction

Figure C.1 shows the schematic illustration of the RS-11G and iMS-100 temperature sensor, which consists of thermistor, rod, and lead wires. The relationship among the corrected air temperature, t_0 [K], the thermistor reading, t [K], and the amount of the solar radiation correction, Δt [K] is given as

$$t_0 = t - \Delta t \tag{C.1}$$

By following the Guidelines of radiosonde soundings in Japan (JMA,1995), The amount of the solar radiation correction is given as

$$\Delta t = \frac{K(P_{st} + Q_2)}{Q_1} \tag{C.2}$$

where P_{st} [kcal s^{-1}] (note that JMA (1995) uses kcal instead of J, so that we use kcal in this appendix) is the solar radiation energy which is directly absorbed by the thermistor part, Q_2 [kcal s^{-1}] is the radiation energy absorbed by the rod lead-wire parts and conducted to the thermistor part, Q_1 [kcal s^{-1} K^{-1}] is the heat conduction from the thermistor part to the ambient air, and K is a parameter for cloud effects. Q_1 and Q_2 are given by

$$Q_1 = h_t S_t + k_r A_r \delta_r \frac{1 + C_{rl} \tanh(L_r \delta_r) \tanh(L_1 \delta_1)}{\tanh(L_r \delta_r) + C_r l \tanh(L_1 \delta_1)} \tag{C.3}$$

$$Q_2 = \frac{Q_{21}}{\tanh(L_r \delta_r) + C_{rl} \tanh(L_1 \delta_1)} \tag{C.4}$$

where,

$$\begin{aligned} Q_{21} \quad = \quad & \left(\frac{P_{sr}}{L_r \delta_r}\right) \{1 + C_{rl} \tanh(L_r \delta_r) \tanh(L_l \delta_l) - \operatorname{sech}(L_r \delta_r)\} + \\ + \quad & \left(\frac{2 C_{rl} P_{sl}}{L_l \delta_l}\right) \{1 - \operatorname{sech}(L_l \delta_l)\} \operatorname{sech}(L_r \delta_r) \end{aligned} \tag{C.5}$$

$$\delta_r = \sqrt{\frac{h_r S_r}{k_r A_r L_r}} \tag{C.6}$$

$$\delta_l = \sqrt{\frac{h_l S_l}{k_l A_l L_l}} \tag{C.7}$$

$$C_r l = \frac{k_r A_r \delta_r}{2 k_l A_l \delta_l} \tag{C.8}$$

The symbols used in Equations C.3–C.8 are explained in Table C.1.

C.2 Thermal conductivity

The coefficients of the thermal conductivity between the sensor parts and the air (i.e., h_t, h_r, h_l) are the function of ascending speed, air density, air temperature, observation position (i.e., height), and

Table C.1: Symbols used in EquationsC.3–C.8.

Symbol	Explanation	Unit
P_{sr}	Solar energy absorbed by the rod part	kcal s^{-1}
P_{sl}	Solar energy absorbed by one of the two wires	kcal s^{-1}
k_r	Thermal conductivity of the rod part	kcal m^{-1} s^{-1} K^{-1}
k_l	Thermal conductivity of the lead wire part	kcal m^{-1} s^{-1} K^{-1}
S_t	Surface area of the thermistor part	m^2
S_r	Surface area of the rod part	m^2
S_l	Surface area of one of the lead wires	m^2
A_r	Cross-sectional area of the rod part perpendicular to the axis	m^2
A_l	Cross-sectional area of the lead wire perpendicular to the axis	m^2
L_r	Length of the rod part	m
L_l	Length of the lead wire	m
h_t	Thermal conductivity coefficient between the air and the thermistor part	kcal m^{-2} s^{-1} K^{-1}
h_r	Thermal conductivity r coefficient between the air and the rod part	kcal m^{-2} s^{-1} K^{-1}
h_l	Thermal conductivity coefficient between the air and the lead wire	kcal m^{-2} s^{-1} K^{-1}

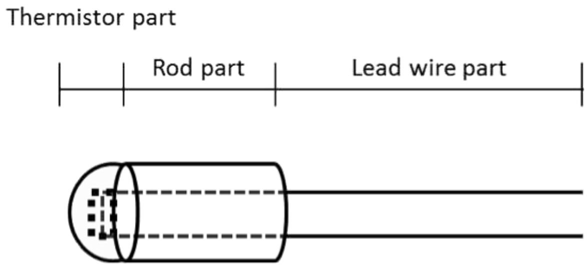

Figure C.1: Structural drawing of the temperature sensor.

temperature sensor's property (size and shape) (e.g. JSME, 1975). First, the kinematic viscosity of air at the observation position (height), ν [$\mathrm{m^2\,s^{-1}}$] is written as

$$\nu = \frac{\mu}{\rho} \tag{C.9}$$

where, μ [$\mathrm{kg\,m^{-1}\,s^{-1}}$] and ρ [$\mathrm{kg\,m^{-3}}$] are dynamic viscosity coefficient and air density, respectively, and given by

$$\mu = \frac{1.458\times 10^{-6} T^{3/2}}{T + 110.4} \tag{C.10}$$

$$\rho = \frac{MP}{R^* T} \tag{C.11}$$

where T is air temperature [K], R^* is the universal gas constant [= 8314 $\mathrm{kcal\,K^{-1}\,kmol^{-1}}$], and P is air pressure [hPa]. Eq. C.10 is taken from JSME, 1975.
Second, the Reynolds numbers of the thermistor part (Re_t), rod part (Re_r) and lead wire part (Re_l) are expressed as

$$Re_t = \frac{D_t V}{\nu} \quad \text{(C.12)}$$
$$Re_r = \frac{V D_r / \cos(50°)}{\nu} \quad \text{(C.13)}$$
$$Re_l = \frac{V D_l / \cos(33°)}{\nu} \quad \text{(C.14)}$$

where D_t is the diameter of the thermistor part [m], D_r is the diameter of the rod part [m], D_l is the diameter of the lead wire part [m], V is the ascent rate of the radiosonde at observation position [m s^{-1}]. The factor of cos(50°) in Eq. C.13 is considered because the rod part is tilted, on average, by 50° with respect to the horizontal plane during the flight. The factor of cos(33°) in Eq. C.14 is considered because the lead part is tilted by 33° with respect to the horizontal plane.

Third, the Nusselt number, Nu is a dimensionless number related to the thermal conductivity in a fluid, which is related with the Reynolds number as

$$Nu_t = 2 + 0.50 Re_t^{0.5} \quad \text{(C.15)}$$
$$Nu_r = 0.445 + 0.499(Re_r - 0.189)^{0.492} \quad \text{(C.16)}$$
$$Nu_l = 0.445 + 0.499(Re_l - 0.189)^{0.492} \quad \text{(C.17)}$$

(*Nakamura et al.*, 1983)

Assuming the thermistor part, rod part and lead wire part as columnar forms, the thermal conductivity for each part can be expressed using the Nusselt number as

$$h_t = \frac{Nu_t \lambda}{D_t} \quad \text{(C.18)}$$
$$h_r = \frac{Nu_r \lambda}{D_r / \cos(50°)} \quad \text{(C.19)}$$
$$h_l = \frac{Nu_l \lambda}{D_l / \cos(33°)} \quad \text{(C.20)}$$

where, λ [kcal m^{-1} s^{-1} K^{-1}] is the thermal conductivity of air at the radiosonde position, which is expressed as a function of temperature as

$$\lambda = \frac{6.325 \times 10^{-7} T^{3/2}}{T + 245.4 \times 10^{-(12/T)}} \quad \text{(C.21)}$$

C.3 Solar radiation energy absorbed by sensor parts

The amounts of solar radiation energy absorbed by the sensor parts, i.e., P_{st}, $P_t extrmsr$, and P_{sl} in Equations C.2 and C.5 are given as in *Nakamura et al.* (1983) as

$$
\begin{aligned}
P_{st} &= \varepsilon_{st} S_{st} (1+\alpha) I && \text{(C.22)} \\
P_{sr} &= \varepsilon_s r S_{sr} (1+\alpha) I && \text{(C.23)} \\
P_{sl} &= \varepsilon_{sl} S_{sl} (1+\alpha) I && \text{(C.24)}
\end{aligned}
$$

where ε_{st}, ε_{sr}, and ε_{sl} are the solar radiation absorption rate of the thermistor part (0.20), rod part (0.20), and lead wire part (0.70), respectively, S_{st}, S_{sr}, and S_{sl} are the effective cross-sectional area [m^2] of the thermistor, rod, and one lead wire, respectively, to the direct solar radiation, α is a co-efficient representing the contribution of reflected light from the surface or scattered light from the atmosphere (0.20), and I is the direct solar radiation energy at the observation position [$\mathrm{kcal\,m^{-2}\,s^{-1}}$]. Radiosondes are generally ascending while rotating around the vertical axis as shown in Figure C.2. With this in mind, S_{st}, S_{sr}, and S_{sl} can be expressed as

$$
\begin{aligned}
S_{st} &= \frac{\pi D_t^2}{4} F_{st}(Z) && \text{(C.25)} \\
S_{sr} &= D_r L_r F_{sr}(Z) && \text{(C.26)} \\
S_{sl} &= D_l L_l F_{sl}(Z) && \text{(C.27)}
\end{aligned}
$$

where Z is the solar elevation angle, and F_{st} (Z), F_{sr} (Z), F_{sl} (Z) represent the angle between the solar energy transfer and the sensor parts, being expressed as

$$
\begin{aligned}
F_{st}(Z) &= 0.5(1+\cos\beta \sin Z) && \text{(C.28)} \\
F_{sr}(Z) &= 1/\pi \int_0^{\pi} \sqrt{1-(\cos\beta \sin Z + \sin\beta \cos Z \cos\phi)^2} d\phi && \text{(C.29)} \\
F_{sl}(Z) &= 1/\pi \int_0^{\pi} \sqrt{1-(\cos\beta' \sin Z + \sin\beta' \cos Z \cos\phi)^2} d\phi && \text{(C.30)}
\end{aligned}
$$

where ϕ is azimuth angle of the sun as seen from the radiosonde, β is the angle of the rod part with respect to the vertical axis, and β' is the angle of the lead wire part with respect to the vertical axis. The integration in Equations C.29 and C.30 cannot be obtained analytically. Therefore, F_{sr} (Z) and F_{sl} (Z) are approximated by a cubic equation of Z as

$$
\begin{aligned}
F_{sr}(Z) &= a_3 Z^3 + a_2 Z^2 + a_1 Z + a_0 && \text{(C.31)} \\
F_{sl}(Z) &= b_3 Z^3 + b_2 Z^2 + b_1 Z + b_0 && \text{(C.32)}
\end{aligned}
$$

The eight constant coefficients, a_0 to a_3 and b_0 to b_3 are obtained from a numerical integration and given in Table C.2.

C.4 Equation of radiation energy

The direct solar radiation energy (I) at the observation position is expressed as

$$
I = I_0 (T_r - A_w) \qquad \text{(C.33)}
$$

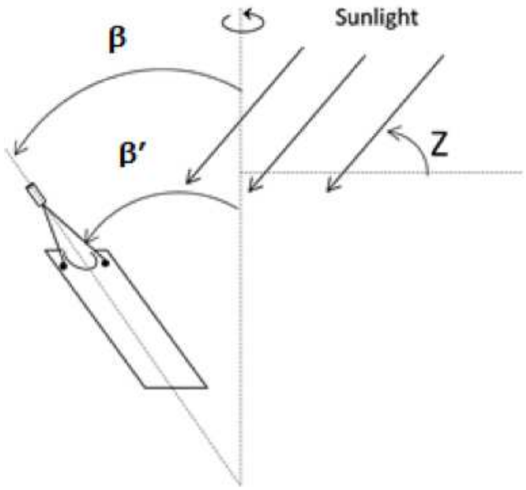

Figure C.2: Schematic illustration of the rotational motions of the radiosonde temperature sensor around the vertical axis.

Table C.2: Values of the coefficients in Equations C.29 and C.30.

Symbol	constant coefficients	Symbol	constant coefficients
a_0	8.92377922e-01	b_0	7.97858532e-01
a_1	-6.61143216e-04	b_1	-2.78070889e-03
a_2	-1.09735342e-04	b_2	7.35237209e-05
a_3	9.75528911e-07	b_3	-4.10272477e-07

where I_0 is the solar constant (1381.644 W m^{-2}), T_r is the transmittance of the atmosphere (considering the scattering by air molecules), and A_w represents the absorption by water vapor. T_r can be expressed using the atmospheric path length [m] at the observation position (Figure C.3) as

$$T_r = \exp\left(am + \frac{bm}{m-c}\right) \tag{C.34}$$

where a, b, and c are constant coefficients, a = -0.0165248, b = -0.664412, and c = -7.12379. The atmospheric path length m is a function of pressure p [hPa] and solar altitude Z, and given by

$$m = \exp\left(f(p) + g(Z)\right) \tag{C.35}$$

where

$$f(p) = A(\ln p)^4 + B(\ln p)^3 + C(\ln p)^2 + D(\ln p) + E \tag{C.36}$$
$$g(Z) = a(SZ)^6 + b(SZ)^5 + c(SZ)^4 + d(SZ)^3 + e(SZ)^2 + f(SZ) \tag{C.37}$$
$$SZ = \sin Z/(\sin Z + 0.1848469) \tag{C.38}$$

The constant coefficients A to E and a to f are given in Table C.3.
The absorption by water vapor is a function of water vapor column amount u [g cm^{-2}] along the

Table C.3: Values of the coefficients in Equations C.34 and C.35

Symbol constant	coefficients	Symbol constant	coefficients	Symbol constant	coefficients
A	0.001521491	B	-0.01631784	C	0.04158605
D	0.9578739	E	-3.066776	–	–
a	-0.1263798	b	-0.6810729	c	-0.9013728
d	0.5597896	e	1.047277	f	-4.465039

atmospheric path and is giving by

$$A_w = 0.0938 \exp\left(0.7990 \log u - 0.1289 (\log u)^2 - 0.01382 (\log u)^3\right) \tag{C.39}$$

and

$$u = w_0 \left(\frac{p}{p_0}\right)^4 \frac{m(p,Z)}{m(p,Z=90)} \tag{C.40}$$

where w_0 is the water vapor column amount averaged for January and July at 30°N (2.55 g cm^{-2} (*Miller*, 1977), p is air pressure at the observation position, and p_0 is surface pressure. With these equations, the maximum contribution of the solar radiation correction amount by the water vapor column amount (W_0) is estimated. For this estimate, a tropical water vapor condition (W_0 = 10 g cm^{-2}), with a low solar elevation angle (10°) and low GPSsonde altitude (1 km), is assumed. The result is that the contribution of the solar radiation to the amount of correction of the W_0 is 0.06 K. Thus, it is concluded that variations in W_0 would not significantly affect the solar radiation correction amount.

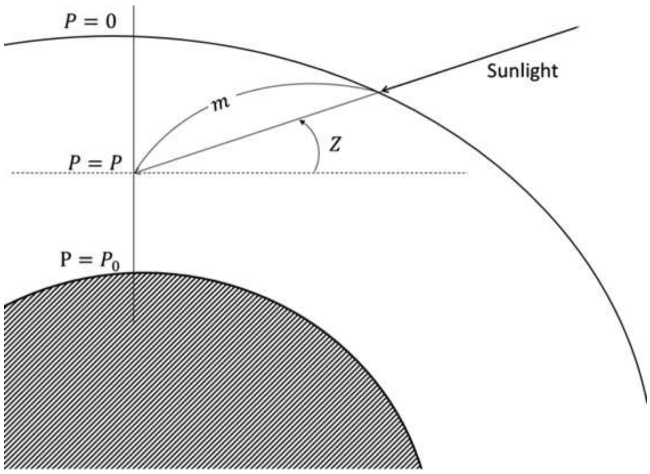

Figure C.3: Atmospheric path length for the solar radiation for a radiosonde located at pressure P.

C.5 Effect of clouds

Existence of clouds complicates the radiative transfer. Here, the reduction of direct solar radiation by clouds is only considered by setting the factor K in Eq. C.2 appropriately. As there is no measurement of cloud radiative property on the radiosonde, an average situation is assumed for all the soundings. Specifically, K is set as follows:

$$K = \begin{bmatrix} 1 & (0 \leq p \leq p_1) \\ 1-(1-K_0)\frac{\ln p - \ln p_1}{\ln p_0 - \ln p_1} & (p_1 \leq p \leq p_0) \end{bmatrix} \tag{C.41}$$

where p is the pressure of the observation position, p_0 is the surface pressure, K_0 equals 0.5, and p_1 equals 500 hPa.

C.6 Amount of the radiation correction

Figure C.4 shows an example of the amount of solar radiation correction as a function of solar elevation angle for different altitudes. The atmospheric pressure and temperature profiles are based on the U.S. Standard Atmosphere (1976), and the ascent rate is assumed to be 6 m s^{-1}. Table C.4 summarizes the parameters used to determine the solar radiation correction amount of the RS-11G and iMS-100 temperature measurements.

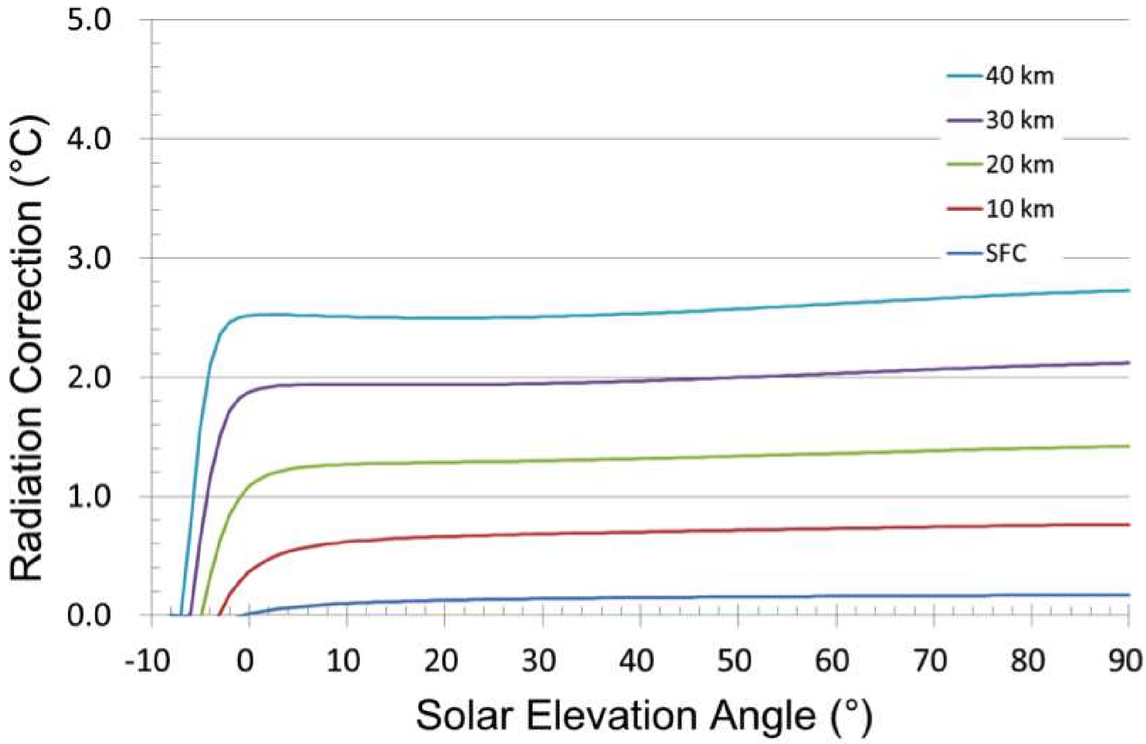

Figure C.4: Example of the amount of solar radiation correction for RS-11G and iMS-100 temperature measurements as a function of solar elevation angle for five different altitudes.

Table C.4: Summary of the parameters used to determine the solar radiation correction amount of the RS-11G and iMS-100 temperature measurements.

Solar absorptance	Thermistor part (ε_{st})	Rod part (ε_{sr})	Lead part (ε_{sr})
	0.2	0.2	0.7
Solar constant	I_0[W m^{-2}]		
	1381		
Reflection / scattering coefficient from the surface or clouds	α		
	0.2		
Diameter of the sensor unit	Diameter of thermistor part D_t [m]	Diameter of Rod part D_r [m]	Diameter of Lead part D_l [m]
	8.00×10^{-4}	8.00×10^{-4}	1.50×10^{-4}
Surface area of the sensor unit	Surface area of Thermistor part S_t [m^2]	Surface area of Rod part S_r [m^2]	Surface area of Lead part S_l [m^2]
	1.01×10^{-6}	1.51×10^{-6}	5.18×10^{-6}
Thermal conductivity of sensor unit		Thermal conductivity of Rod part K_r [kcal m^{-1} K^{-1}]	Thermal conductivity of Lead part K_l [kcal m^{-1} K^{-1}]
		2.36×10^{-3}	4.00×10^{-2}
Cross-sectional area of the sensor unit		Cross-sectional area of rod part A_r [m^2]	Cross-sectional area of Lead part A_l [m^2]
		5.02×10^{-7}	8.83×10^{-9}
Length of the sensor unit		Length of Rod part L_r [m]	Length of Lead part L_l [m]
		6.00×10^{-4}	1.10×10^{-2}
PWV at the surface (average of January and July at 30°N) W_0 [g cm^{-2}]			2.55
Highest point of clouds P_1 [hPa]			500
The cloud correction coefficient at the ground K_0)			0.5

D RH calculation of the RS-11G and iMS-100 radiosondes

This section describes the method of relative humidity (RH) calculation from the raw data, i.e., the RH frequency data and the reference frequency data, by using the coefficients determined at the factory.

D.1 Calculation of the raw RH values

The frequency of humidity received by the ground system is converted to the capacitance of the RH sensor. The relationship between the frequency and capacitance is given by

$$ru = \frac{FU}{FR} \times 4 \tag{D.1}$$

$$U_0 = B_0 + B_1 \times ru + B_2 \times ru^2 + B_3 \times ru^3 \tag{D.2}$$

where ru is converted frequency of humidity, FU is the frequency of humidity, FR is the reference frequency, U_0 is the raw relative humidity value [%RH], and B_0, B_1, B_2, and B_3 are the set of calibration coefficients for each radiosonde.
The set of calibration coefficients, B_0 to B_3 is normally determined for each radiosonde during the manufacturing and calibration process (at RH levels of 15%, 30%, 50%, 70%, 90%, and 95%, and at a constant air temperature of +25°C). But, for the station where the SHC checks are conducted (e.g., Tateno), the set of coefficients is determined with the frequency data for the levels 0 %RH and 100 %RH in addition to original calibration data in factory.

D.2 Estimation of the RH sensor temperature (applicable only for RS-11G)

The temperature of the RH sensor generally does not equal to the ambient air temperature because of the thermal lag of the RH sensor and the solar heating. During the balloon ascent through the troposphere, the RH sensor temperature would usually become warmer than the ambient air temperature due to the thermal lag. The warmer RH sensor would result in giving RH measurements that are biased dry, so that a correction procedure that considers the difference between the air and sensor temperatures is necessary. Because the RS-11G radiosonde is not equipped with a dedicated temperature sensor for the RH sensor, the temperature of the RS-11G RH sensor needs to be estimated using the air temperature measurement. On the other hand, the solar heating on the RH sensor occurs only during daytime soundings. The amount of heating is estimated by following the same procedure as that for the thermistor, as explained in Appendix C, with some special considerations.

D.2.1 Thermal lag consideration

On the basis of the Newton's law of cooling, the relationship between the RH sensor temperature, T_s and the air temperature, T_a (both in K) can be written as

$$T_s(t) = \frac{T_a \delta t + \tau T_s(t - \delta t)}{\tau + \delta t} \tag{D.3}$$

where τ is the time constant (or the thermal lag) of the sensor, and δt is a finite time step.
The time constant depends on the heat transfer between the ambient air and the surface of the RH sensor and on the sensor property. *Williams and Acheson* (1976) give the time constant of a sensor in

the air theoretically as

$$\tau = \frac{mc}{hA} \tag{D.4}$$

where m is the mass of the sensor, c is the specific heat of the sensor, h is the convective heat-transfer coefficient, and A is the total surface area of the sensor. The convective heat transfer would decrease with height primarily because air density decreases with height. *Morrissey and Brousaides* (1970) proposed that, assuming that the RH sensor is a flat plate with a zero angle of attack to airflow, h can be calculated from

$$h = \frac{1}{L}\int_0^L 0.332kPr^{1/3}\sqrt{\frac{\rho v'}{\mu x}}dx \tag{D.5}$$

where L is the width of the RH sensor, k is the thermal conductivity of air, Pr is the Prandtl number, ρ is the density of air, v' is the flow rate on the RH sensor, and μ is the viscosity coefficient. The values of Pr, k, and μ depend on air temperature. Substituting Eq. D.5 into Eq. D.4, τ can be rewritten as

$$\tau = Ck^{-1}Pr^{-1/3}\sqrt{\frac{\mu}{\rho v}} \tag{D.6}$$

where C is a constant, in theory, determined by the RH sensor property.
The iMS-100 radiosonde has a dedicated temperature sensor for the RH sensor. Therefore, the iMS-100 sounding results can be used to validate Eq. D.6. The results show that the value of C actually has a dependency on pressure. This is because the convective heat-transfer coefficient in Eq. D.5 was assumed to be the one for laminar airflow. In reality, the airflow around the RH sensor during the flight is turbulent, and thus the ventilation depends on pressure particularly in the troposphere below the 200 hPa level. Therefore, C is modified empirically as

$$C = C_{Ts} \times C(P) \qquad C_{Ts} = 150 \tag{D.7}$$

where C_{Ts} is determined based on some RH sensor temperature profiles measured with iMS-100, and C(P) is

$$\begin{cases} C(P) = 1-(1-0.2)\frac{\ln P - \ln 200}{\ln P_0 - \ln 200} & \text{(for } P > 200\,\text{hPa)} \\ C(P) = 1 & \text{(for } P < 200\,\text{hPa)} \end{cases} \tag{D.8}$$

The pressure dependency above the 200 hPa level is negligible.

D.2.2 Solar heating consideration

The amount of the solar heating on the RH sensor is estimated by following the same procedure as that for the thermistor (Appendix C). The surface area of the RH sensor and the sensor cap is much greater than that of the thermistor, and this factor needs to be considered. Also, the factor due to non-laminar airflow (i.e., $C(P)$ in Eq. D.8), which is not considered for the thermistor, needs to be considered. Therefore, the amount of solar heating, ΔT_{s_SR} is estimated as

$$\Delta T_{s\_SR} = C(P) f \Delta T_S R \qquad f = 3.3 \tag{D.9}$$

where f is surface area factor and ΔT_{s_SR} is the solar heating amount for the thermistor at the same time of measurement. The value of f, 3.3 was determined by the comparison with some simultaneous iMS-100 sounding, which are conducted at mid-latitude, Tateno and Moriya, during September–October 2014.

D.2.3 Validation of the estimated RH sensor temperature with iMS-100 radiosonde

The RH sensor temperature for the RS-11G radiosonde is estimated by summation of the thermal lag (D.2.1) and solar heating components to the air temperature value (Section D.2.2). We evaluated the estimation of the RH sensor temperature by the comparison with the iMS-100 radiosonde, which measure the RH sensor temperature directly with dedicated thermistor. Figure D.1 shows the example of the RH sensor temperature profiles measured with iMS-100 radiosonde and the estimated RH sensor temperature profiles. This result shows that the measured and estimated temperature have good agreement in the troposphere. Although the these temperature profiles have difference of $\sim 3°C$, this deference have little effect for the RH profiles because the RH are usually near 0 %RH in the stratosphere.

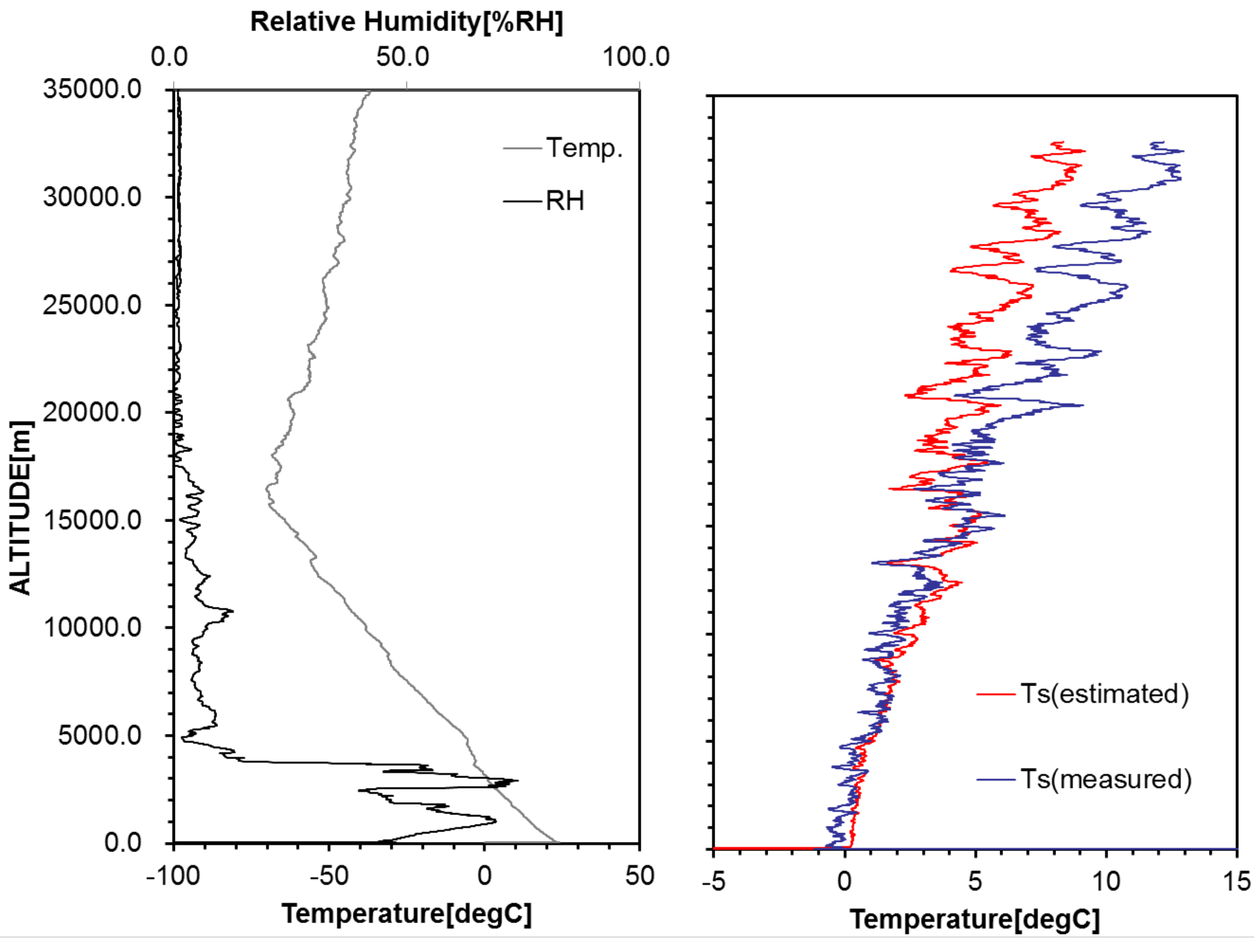

Figure D.1: Temperature profiles of RH sensor for the iMS-100 radiosonde at Moriya, Japan (35.9°N, 140.0°E) launched at 14:30 on 22 September 2014. (Left) temperature and RH profiles from iMS-100 radiosonde, (Right) Blue and red lines indicate the heating amount of the RH sensor measured with dedicated thermistor and that estimated with Equations D.3-D.9.

D.3 Adjustment of the RH sensor temperature for the iMS-100 and RS-11G radiosonde

The iMS-100 has a dedicated temperature sensor (a thermistor) for the RH sensor. Its accuracy is 0.3 K below 0°C, but worse above 0°C. Considering also that in the lower troposphere, the difference between the sensor temperature and the air temperature is very small because of very effective convective heat transfer, it would be reasonable that the iMS-100 RH sensor temperature is calculated in combination with the air temperature and the measured RH sensor temperature by the following equation:

$$T_s = K_{Ta} \times T_{s\_obs} + (1 - K_{Ta}) \times T_a \tag{D.10}$$

where T_{s_obs} is the measured RH sensor temperature, T_a is air temperature, and K_{Ta} is the following weighting parameter:

$$K_{Ta} = \begin{cases} 0 & (\text{for } P > 600\,\text{hPa}) \\ 1 - \frac{\ln P - \ln 400}{\ln 600 - \ln 400} & (\text{for } 400 < P < 600\,\text{hPa}) \\ 1 & (\text{for } P < 400\,\text{hPa}) \end{cases} \tag{D.11}$$

As in Eq. D.11, below the 600 hPa level, air temperature is used as the RH sensor temperature, and above the 400 hPa level, the measured RH sensor temperature is used. Between 400 hPa and 600 hPa, both temperatures are combined according to the weighting parameter K to estimate the RH sensor temperature.

It is noted here that the RH sensor temperature for the RS-11G radiosonde is also calculated with Eq. D.11.

E Low-pass filtering for the wind measurement and RH correction

A low-pass digital filter with the Kaiser window (*Kuo and Kaiser*, 1966) is used to remove noises in the wind and relative humidity (RH) measurements. The same formula are used for the two variables except for the cut-off frequency value. The cut-off frequency for the wind measurements is determined from the period of the pendulum motions, and that for the RH measurements is determined from the response time of the RH sensor. The actual filtering calculations are performed with the following four steps.
(1) Calculation of the Kaiser window
The Kaiser value α is defined as

$$\alpha = \begin{cases} 0 & (\text{for } 21 \text{ dB } \leq A) \\ 0.5842(A-21)^{0.4} + 0.07886(A-21) & (\text{for } 21 \text{ dB } < A < \ 50 \text{ dB}) \\ 0.1102(A-8.7) & (\text{for A } \geq 50 \text{ dB}) \end{cases} \tag{E.1}$$

where A is the rate of decrease of the side lobe. When A is larger, the filter is closer to the step function, being with better selectivity of frequency. The default value is 40 dB.
(2) Calculation of the window function

$$w(n) = \frac{I_0(\beta)}{I_0(\alpha)}, \qquad \beta = \alpha\sqrt{1-\left(\frac{n}{M}\right)^2} \tag{E.2}$$

and

$$I_0(u) = 1 + \Sigma_{r=1}^{\infty}\left[\frac{\left(\frac{u}{2}\right)^r}{r!}\right]^2 \tag{E.3}$$

where M is window length, 30 (i.e., 60 / 2), I_0 is the Bessel function of the first kind with the zeroth order, and r is set to 20 for this filtering.
(3) Calculation of the weighting function
First, the impulse response H(n) is calculated as

$$H(n) = \begin{cases} \frac{\sin \omega_c n}{\pi n} w(n) & \text{for } n \neq 0 \\ \frac{2f_c}{f_s} & \text{for } n = 0 \end{cases} \tag{E.4}$$

and

$$\omega_c = \frac{2\pi f_c}{f_s} \tag{E.5}$$

where f_c is the cut-off frequency and f_s is the sampling frequency (normally 1 Hz).
The cut-off frequency for the wind measurements is determined from the pendulum period, and thus from the length of the string between the balloon and the payload, by the following equation.

$$\begin{aligned} f_c &= \frac{1}{\chi} \times \frac{1}{T_c} \\ &= \frac{1}{\chi} \times \frac{1}{2\pi\sqrt{L/g}} \end{aligned} \tag{E.6}$$

where χ is an empirical coefficient, L is the length of string, and g is gravitational acceleration. The cut-off frequency for the RH measurements is given in Section 3.2.

The standardized impulse response h(n) is obtained by

$$h(n) = \frac{H(n)}{\Sigma_{n=-M}^{M} H(n)} \tag{E.7}$$

(4) Obtaining low-pass filtered data
The filtered data V_{out} is obtained from the original data V_{in} by the following equation.

$$V_{out} = h(0) \times V_{in}(M) + \Sigma_{n=1}^{M}[h(n) \times V_{in}(M-n) + h(n) \times V_{in}(M+n)] \tag{E.8}$$

F Manufacturer-independent ground check for the RS-11G and iMS-100 radiosondes

At Tateno, a manufacturer-independent Standard Humidity Chamber (hereafter referred to as SHC) system has been developed for the relative humidity (RH) sensor of the Meisei RS-11G and iMS-100 radiosondes. This system includes 0 %RH and 100 %RH chambers and a data processing software, and is used for the ground check procedure for the RH sensor in addition to that using the manufacturer's Ground Checker (hereafter referred to as GC) system.

F.1 The manufacturer-independent and manufacturer's ground check systems

F.1.1 The SHC system (0 %RH and 100 %RH) for the RS-11G and iMS-100 radiosondes

Figure F.1 shows a schematic figure of the manufacturer-independent SHC system to create 0 %RH and 100 %RH environment. Figure F.2 shows its appearance. Plastic airtight containers (dimensions: 150 mm length 100 mm width 98 mm height) are used as the chambers. Each chamber is ventilated with a fan to ensure that RH within the chamber is homogeneously 0 %RH or 100 %RH. The 0 %RH chamber (hereafter referred to as SHC(0 %RH)) contains about 170g of molecular sieves, and the 100 %RH chamber (hereafter referred to as SHC(100 %RH)) contains a sponge saturated with distilled water.

The SHC system uses the reference temperature and RH sensor probe "Rotronic HygroClip 2 /HC2-S" (hereafter referred to as HC2), a data logger Rotronic Hygrolog HL-NT, and a data processing software HW4. The specifications of the reference instrument are described in Section F.2. The ground check data of the RS-11G/iMS-100 radiosonde are collected by the Meisei MGPS software through the radiowave transmission in the same way as the upper-air observation.

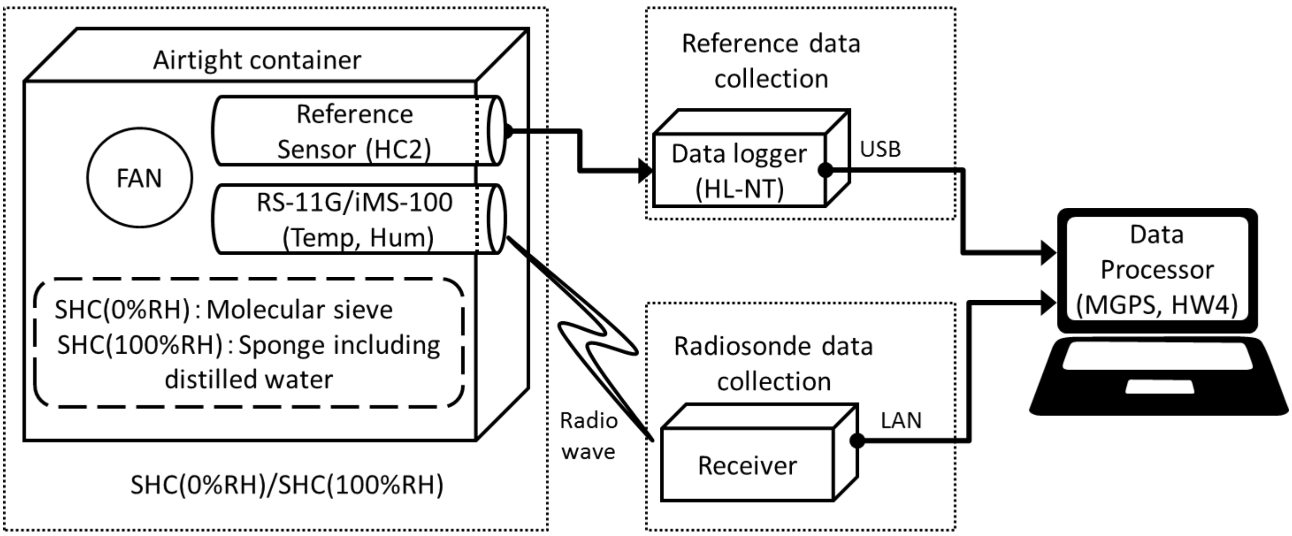

Figure F.1: Schematic diagram of the SHC system used at Tateno.

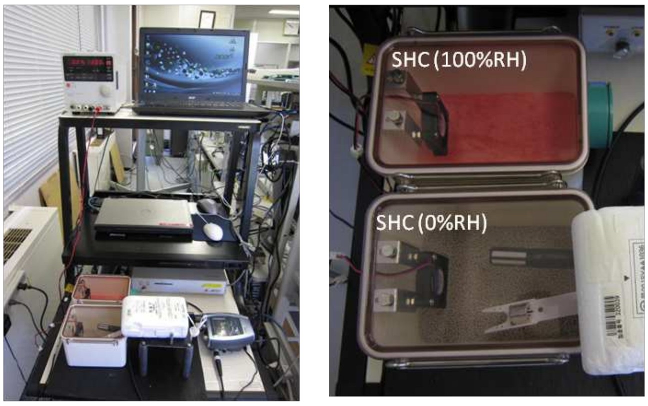

Figure F.2: Photographs of the SHC system. The whole system (left) and the 0 %RH and 100 %RH chambers (right).

F.1.2 The GC system (room environment) for the RS-11G radiosonde

Figure F.3 shows a schematic figure of the manufacturer's GC system for the ground check of the RS-11G radiosonde under a room environment. Figure F.4 shows its appearance. An open plastic container (dimensions: 110 mm length 75 mm width 73 mm height) is used as a chamber which is ventilated with a fan. The inside of the chamber is filled with the room air and is well mixed. The reference temperature and RH instrument is the Rotronic Hygro Parm HP22-A (hereafter referred to as HP22) which is equipped with the HC2 sensor, the same type of sensor used in the SHC system (see Section F.2 for the sensor specifications). The RS-11G data are received by the MGPS software through the radiowave transmission, while the reference HP22 data are sent to the MGPS software with a USB cable or manually. The two datasets are then compared in the MGPS software.

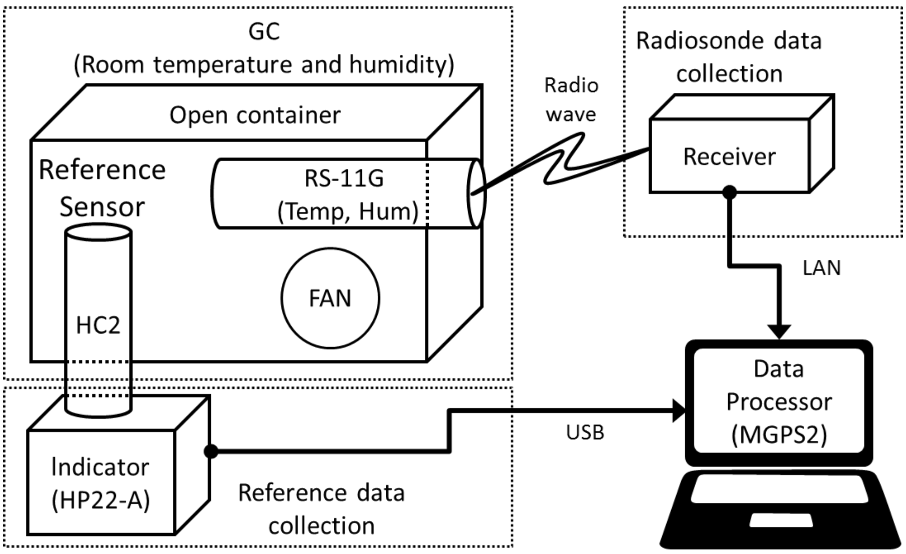

Figure F.3: Schematic diagram of the Meisei's GC system for the RS-11G radiosonde.

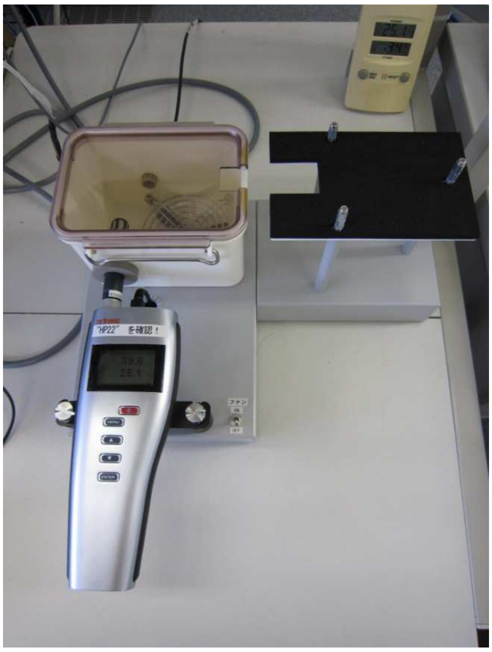

Figure F.4: Photograph of the GC system for the RS-11G radiosonde.

F.1.3 The GC system (room environment) for the iMS-100 radiosonde

Figure F.5 shows a schematic figure of the manufacturer's GC system for the iMS-100 radiosonde, and Figure F.6 shows its appearance. The chamber container is exactly the same as for the RS-11G radiosonde. The reference temperature sensor is MES-39535 (Meisei), and the reference RH sensor is TU-CONV (Meisei). The specifications of these reference sensors are described in Section F.2. The iMS-100 and reference-instrument data are both collected by a synthesizer through infrared communication and sent through a USB cable to the MGPS software, where the two datasets are compared.

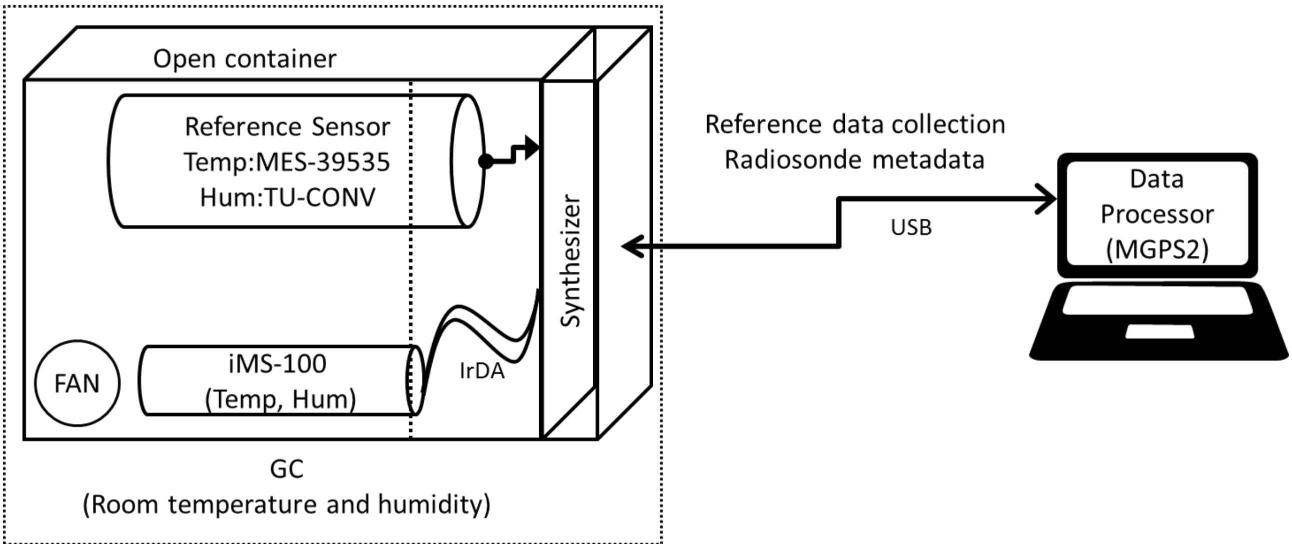

Figure F.5: Schematic diagram of the Meisei's GC system for the iMS-100 radiosonde.

Figure F.6: Photograph of the GC system for the iMS-100 radiosonde.

Table F.1: Specifications of the HC2 instrument.

	HC2-S (HC2)	
	Temperature sensor	RH sensor
Sensor material	Pt100RTD, 1/3 DIN, Class B	Hygromer IN-1
Measurement Range	-50°C to +100°C	0 %RH to 100 %RH
Accuracy	±0.1 °C (at 23°C)	±0.8 %RH(at 23°C)
Response Time	Less than 15 s (at 1 m s^{-1})	Less than 15 s (at 1 m s^{-1}, 23°C)
Filter cartridge	Polyethylene or Teflon	

F.2 Details of the reference sensors in the SHC and GC systems and their calibration

As described above, HC2 is used as the reference instrument in the SHC (for both RS-11G and iMS-100) and in the Meisei's GC for RS-11G. On the other hand, the MES-39535 temperature sensor and the TU-CONV RH sensor are used in the GC for iMS-100. Every month, all the HC2 instruments are compared with Vaisala HMP155 instrument in the GC chamber under a room environment. Every year, the RH sensors in the HC2, TU-CONV, and HMP155 instruments are also checked in conformity to the ISO/IEC 17025 at the Regional Instrument Centre (RIC) Tsukuba, by using the reference standard (a chilled mirror hygrometer D-2-SR) at 20 %RH, 40 %RH, 60 %RH, 80 %RH, and 95 %RH. Also every year, the temperature sensors in the HC2, MES-39535, and HMP155 instruments are calibrated at 15°C, 20°C, 25°C, and 30°C by using the reference standard (a thermometer TS81A). The specifications of the HC2, MES-39535, TU-CONV, and HMP155 instruments are shown in Tables F.1– F.4.

Table F.2: Specifications of the MES-39535 instrument.

Type	MES-39535
Sensor material	Pt100, JIS A class (JISC1604)
Wire	4
specified current	1 mA
Time constant or response time	Less than 1 s
Accuracy	±0.3 K or less
Measurement range	-20°C to +40°C
Operating environment	-20°C to +40°C, 0 %RH to 100 %RH

Table F.3: Specifications of the TU-CONV instrument.

Type	TU-CONV 5
Sensor material	Capacitance Type
Time constant or response time	20 s or less (at 25°C)
Accuracy	±5 %RH
Measurement range	0 %RH to 100 %RH
Operating temperature	-20°C to +40°C, 0 %RH to 100 %RH

Table F.4: Specifications of the HMP155 instrument.

	HMP155	
	Temperature sensor	RH sensor
Sensor material	Pt100RTD Class F0.1 IEC 60751	HUMICAP®180R(c)
Measurement range	-80°C to +60°C	0 %RH to 100 %RH
Accuracy	-80°C to +20°C: ±(0.226 - 0.0028 × temperature) °C +20°C to +60°C: ±(0.055 + 0.0057 × temperature) °C	0 %RH to 90 %RH: ±1 %RH 90 %RH to 100 %RH: ±1.7 %RH (at +15°C to +25°C)
Response Time	Less than 20 s (at 3 m s^{-1})	Less than 20 s (at +20°C in still air with a sintered PTFE filter)
Filter cartridge	Sintered PTFE	

F.3 The 0 %RH and 100 %RH ground check procedures using the SHC system

First, the ground check procedure using Meisei's GC under a room condition is carried out. The requirements for the RS-11G/iMS-100 measurements are within ±0.5 K and ±7 %RH. The radiosondes that do not meet this criteria will not be used for the sounding.

The radiosondes that have passed the GC check proceed to 0 %RH check using the SHC system. The sensor boom is placed in the SHC (0 %RH) for 10 minutes during which time temperature and RH data of the radiosonde and the HC2 are obtained. Then, the sensor boom is placed in the SHC (100 %RH) for 10 minutes to obtain the data. Figure F.7 shows examples of temporal changes in the radiosonde and reference RH data. It can be seen that the changes of sensor readings become smaller in about 5 minutes.

The radiosonde and HC2 measurement data for 3 minutes between the 6th minute and the 9th minute are averaged, and the radiosonde bias relative to the HC2 is obtained. The radiosondes are then stored in a low humidity environment for more than one day, and are subject to the room environment GC check again right before the launch. Again, the radiosondes need to pass the ±0.5 K and ±7 %RH criteria for the use in observation. The results of all the ground checks are reported to the Lead Centre via the GRUAN RsLaunchClient (*Sommer*, 2014).

The molecular sieves in the SHC(0 %RH) chamber are replaced several times a year to ensure that the chamber is always under $<$1 %RH environment. The SHC(100 %RH) chamber is washed and the distilled water in the sponge is replaced every week. The sponge is replaced to a new one every month.

F.4 Results from the SHC checks

Figs. F.8 and F.9 show the results from the SHC 0 %RH and 100 %RH checks conducted during July 2014. The HC2 measurements in Figure F.8 indicate that the RH in the SHC (0 %RH) and SHC (100 %RH) chambers are on average 0.32(±0.12) %RH and 97.89(±0.73) %RH, respectively. The temperature in the SHC (0 %RH) was in the range of 23°C to 27°C. Figure F.9 indicates that the RH differences between RS-11G and HC2 during the 0 %RH, 100 %RH and room-condition ground checks were -2.35(±0.60) %RH, -1.43(±0.99) %RH and -3.50(±0.94) %RH, respectively. Thus, the RS-11G RH sensor has small dry biases with respect to HC2 during this period. Figure F.9 also indicates that the temperature differences during 0 %RH, 100 %RH and room-condition ground checks were +0.17(±0.07) K, +0.12(±0.12) K and 0.00(±0.12) K, respectively.

Figure F.10 shows the results from the ground check of Vaisala RS92-SGP GPS (hereafter referred to as RS92) sondes by using the Vaisala GC25 ground check system during the period between April 2014 and July 2014. From this figure, the RS92 temperature biases are on average +0.1(±0.1) K, and that are approximately same as the RS-11G temperature biases. This figure also indicates that the RS92 RH biases are on average +0.6(±0.5) %RH, and thus the environment in the SHC(0 %RH) chamber for RS-11G is virtually the same as that in the GC25 for RS92 sonde at Tateno during this period, however, the RS-11G RH biases are larger than the RS92 RH biases. It should be noted that the GC25 does not have a reference RH sensor and thus its inside is assumed to be 0 %RH by molecular sieves. According to the results from the GC25 ground checks conducted in daily routine during June 2013, the RS92 RH bias gradually rose from +0.1 %RH to +1.2 %RH within 2 weeks (not shown in the figure), and it seems to be caused by the deterioration of molecular sieves. Therefore, there is additional uncertainty in the RS92 data by this fact.

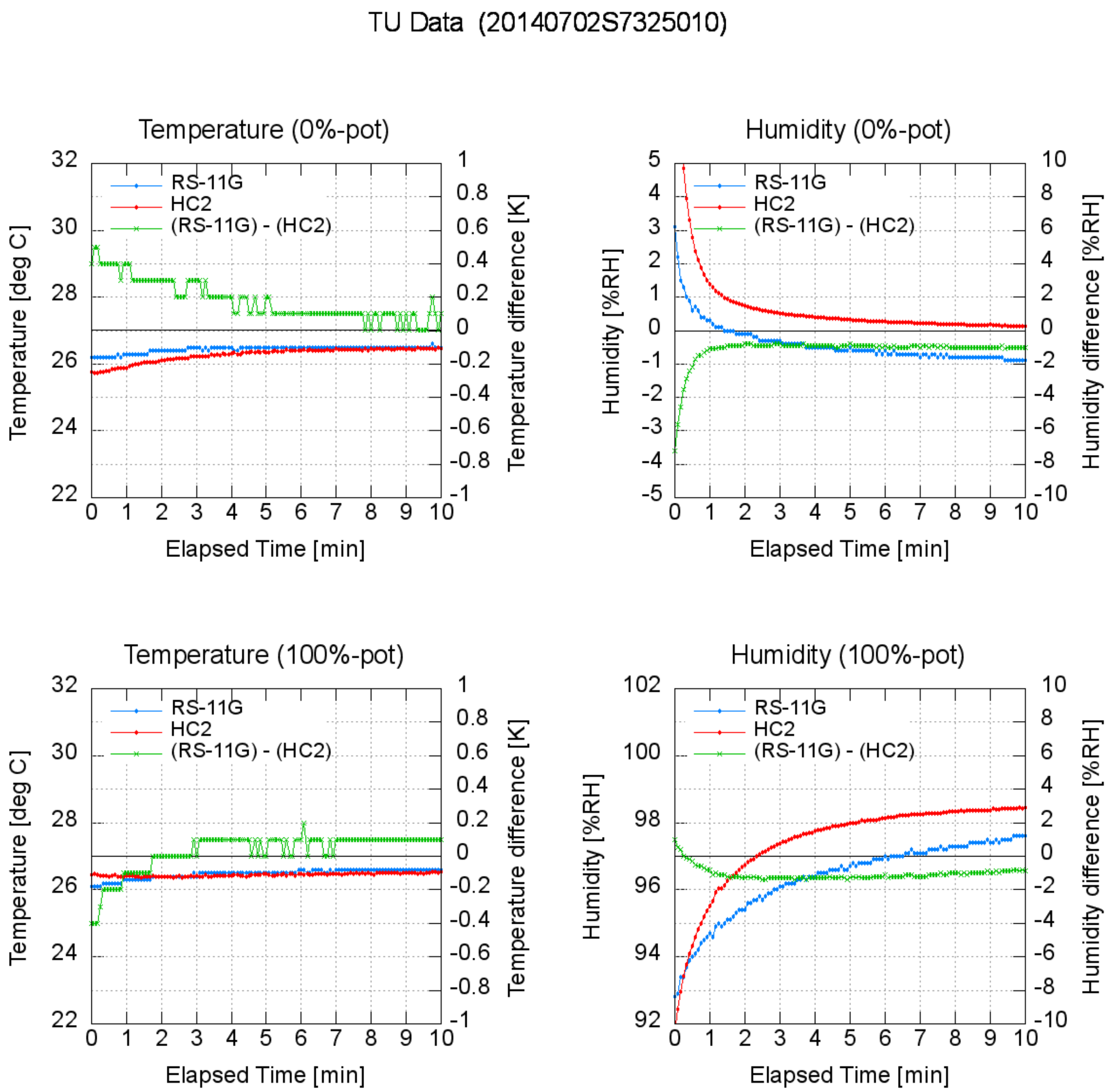

Figure F.7: Examples of temporal changes in RH from the RS-11G radiosonde (blue) and from the HC2 (red) and in the RH difference (green; RS-11G data minus HC2 data) during the 0 %RH check (left) and 100 %RH check (right).

F.5 Uncertainty of the ground check measurements using the SHC system

The total uncertainty of the ground check measurements using the SHC system is composed of the following factors:

1. uncertainty of the calibration of the reference instruments;
2. uncertainty from repeatability of the measurements for a particular radiosonde;

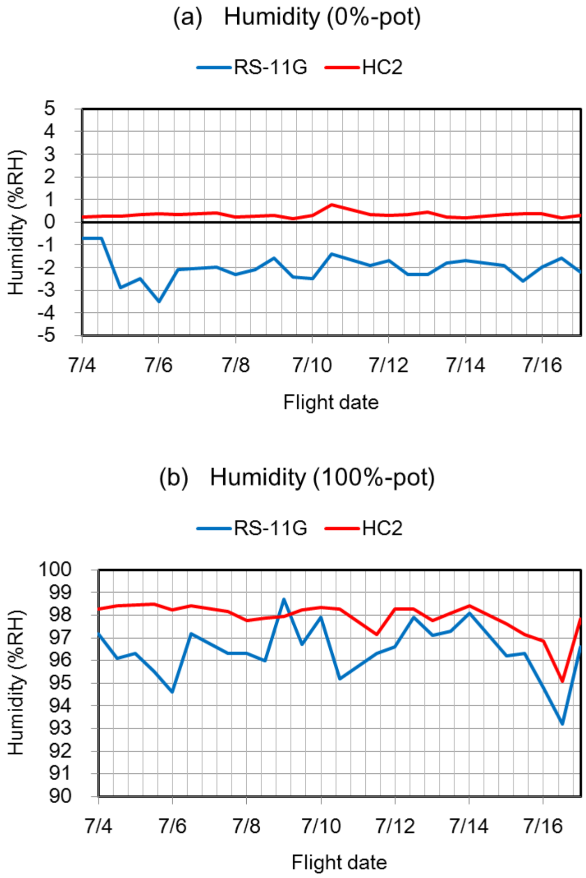

Figure F.8: Ground check RH data from RS-11G (blue) and HC2 (red) for (a) 0 %RH and for (b) 100 %RH. The measurements are plotted at the launch date, not at the date when the SHC check was actually conducted (more than one day before the launch). There were twice daily flights during this period.

3. uncertainty from the dispersion of measurement between individual radiosondes; and

4. uncertainty from inhomogeneity in the chambers.

The following uncertainty estimations are expressed according to the Guide to the Expression of Uncertainty in Measurement (GUM) (*JCGM/WG 1*, 2008).

F.5.1 Uncertainty of the calibration of the reference instruments

The standard uncertainty of the calibration of the reference instruments is estimated from the expanded uncertainty of measurement in the calibration certificate. The reference RH sensors for the ground check procedures are calibrated periodically in conformity to the ISO/IEC 17025 at RIC Tsukuba. The results of the calibration in October-November 2014 are shown in Table F.5. The expanded uncertainty (Table F.5) divided by the coverage factor $k = 2$ gives the standard uncertainty.

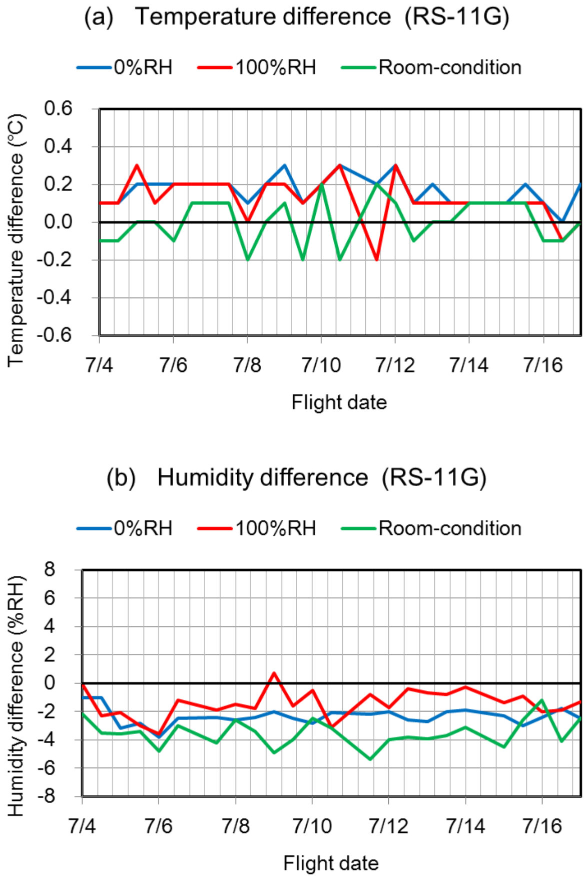

Figure F.9: The differences in (a) temperature and in (b) RH between the RS-11G and HC2 measurements during the 0%RH (blue), 100%RH (red), and room-condition (green) ground checks at Tateno during July 2014.

F.5.2 Uncertainty from repeatability of the measurements for a particular radiosonde

Variations in the results from repeated measurements with the same radiosonde with the same method can be expected due to various causes. To estimate the range of such variations, we made an experiment with repeated ground check measurements. We acquired ground check data 10 times using the same radiosonde under both 0 %RH and 100 %RH environments. The standard deviation of the ground check data (i.e., 3-minute averages of RS-11G values minus HC2 values; see Section F.3) was obtained for each RH environment. The results are shown in Tables F.6 and F.7. The standard deviation of the temperature difference is less than 0.1°C for both environments, and that of the RH difference is 0.32 %RH for the 0 %RH ground check and 0.73 %RH for the 100 %RH ground check.

F.5.3 Uncertainty from the dispersion of measurement between individual radiosondes

Individual radiosondes have different stabilities for measurements. This is one of the sources of the total uncertainty of the SHC ground checks. Therefore, we examined the dispersion of temperature and humidity differences obtained from the SHC ground checks with multiple radiosondes. We calculated the standard deviation of the 3-minute-averaged 0 %RH/100 %RH ground check measurements

Table F.5: The standard uncertainty and the expanded uncertainty (with the coverage factor k=2) of each reference RH sensor at different RH values.

Nominal Humidity (%RH)	Expanded uncertainty (%RH) HC2 (for room-condition check)	Expanded uncertainty (%RH) HC2 (for 0 %RH check)	Expanded uncertainty (%RH) HC2 (for 100 %RH check)	Standard uncertainty (%RH) HC2 (for room-condition check)	Standard uncertainty (%RH) HC2 (for 0 %RH check)	Standard uncertainty (%RH) HC2 (for 100 %RH check)
20	0.9	1.0	0.9	0.45	0.50	0.45
40	1.9	2.0	1.9	0.95	1.00	0.95
60	1.9	2.0	1.9	0.95	1.00	0.95
80	1.9	2.0	1.9	0.95	1.00	0.95
95	1.9	2.0	1.9	0.95	1.00	0.95

Table F.6: Results from the repeated ground check measurements at 0 %RH environment.

Temperature (°C) (3 minutes average)				Relative humidity (%RH) (3 minutes average)			
Number	RS-11G	HC2	Difference	Number	RS-11G	HC2	Difference
1	27.7	27.33	0.37	1	-0.9	0.00	-0.90
2	28.0	27.64	0.36	2	-0.6	0.00	-0.60
3	28.1	27.67	0.43	3	-0.5	0.00	-0.50
4	27.4	27.07	0.33	4	-0.5	0.00	-0.50
5	27.0	26.60	0.40	5	-0.4	0.00	-0.40
6	26.8	26.41	0.39	6	-0.2	0.00	-0.20
7	26.9	26.47	0.43	7	-0.3	0.00	-0.30
8	26.4	25.96	0.44	8	0.3	0.00	0.30
9	26.3	25.93	0.37	9	-0.2	0.00	-0.20
10	26.1	25.72	0.38	10	-0.1	0.00	-0.10
Average	27.1(±0.7)	26.68(±0.72)	0.39(±0.04)	Average	-0.3(±0.3)	0.00(±0.00)	-0.34(±0.32)

Table F.7: Results from the repeated ground check measurements at 100 %RH environment.

Temperature (°C) (3 minutes average)				Relative humidity (%RH) (3 minutes average)			
Number	RS-11G	HC2	Difference	Number	RS-11G	HC2	Difference
1	26.5	26.20	0.30	1	97.1	96.13	0.97
2	26.9	26.57	0.33	2	95.8	95.26	0.54
3	27.2	26.76	0.44	3	95.3	94.79	0.51
4	26.9	26.54	0.36	4	97.3	95.95	1.35
5	26.9	26.50	0.40	5	98.0	96.55	1.45
6	26.7	26.32	0.38	6	98.8	96.99	1.81
7	26.5	26.18	0.32	7	99.1	97.26	1.84
8	26.3	25.98	0.32	8	99.3	97.34	1.96
9	26.3	25.90	0.40	9	99.8	97.44	2.36
10	26.0	25.66	0.34	10	100.0	97.31	2.69
Average	26.6(±0.4)	26.26(±0.34)	0.36(±0.04)	Average	98.1(±1.6)	96.50(±0.94)	1.55(±0.73)

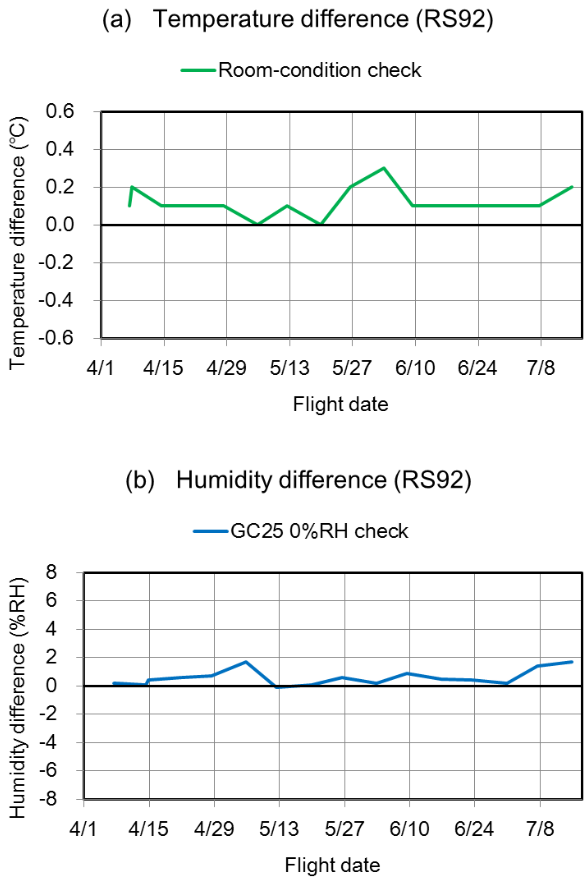

Figure F.10: The differences in (a) temperature under room condition and in (b) RH at the GC25 0 %RH check for Vaisala RS92 radiosondes at Tateno during April to July 2014. The temperature differences are with respect to the reference temperature sensor in the GC25, while the RH differences are with respect to 0 %RH which is assumed in the GC25 chamber. There were weekly flights during this period.

from 20 samples during July 2014. The results are shown Table F.8. The maximum standard deviation of the temperature difference is 0.05 K in both environments. The maximum standard deviation of the RH difference is 0.08 %RH for the 0 %RH environment and 0.26 %RH for the 100 %RH environment.

F.5.4 Uncertainty from inhomogeneity in the chambers

Though a fan is situated in the SHC chambers, there still is a possibility of inhomogeneity in the chambers, which would result in additional uncertainty of the ground check measurements. Therefore, we examined the degree of inhomogeneity by changing the position of the reference sensor. We acquired the reference sensor data at three different positions, depicted as ”A”, ”B”, and ”C” in Figure F.11, both in the 0 %RH and 100 %RH chambers. The measurements were made for about 1 hour continuously. The position of the senor was changed every minute sequentially (i.e., A → B → C → A → . . .).

The results of the RH and temperature measurements are shown in Figure F.12. 1-minute averages at each position are also shown. Though the chamber was placed in the air-conditioned room, the ob-

Table F.8: Average and standard deviation of the 3-minute SHC ground check results for 20 RS-11G radiosondes. The results for temperature and RH are shown for the 0 %RH (left) and 100 %RH (right) environments.

0 %RH environment ground check					100 %RH environment ground check				
	temperature(°C)		humidity(%RH)			temperature(°C)		humidity(%RH)	
Sample number	Difference	Standard deviation	Difference	Standard deviation	Sample number	Difference	Standard deviation	Difference	Standard deviation
1	0.09	0.03	-0.97	0.05	1	0.09	0.04	-1.09	0.09
2	0.27	0.04	-1.00	0.04	2	0.09	0.03	-2.28	0.06
3	0.21	0.03	-3.18	0.05	3	0.34	0.05	-2.12	0.08
4	0.18	0.04	-2.85	0.05	4	0.09	0.03	-3.01	0.13
5	0.23	0.05	-3.83	0.06	5	0.18	0.05	-3.64	0.07
6	0.21	0.04	-2.47	0.05	6	0.24	0.05	-1.19	0.09
7	0.22	0.05	-2.40	0.04	7	0.21	0.04	-1.89	0.09
8	0.08	0.04	-2.58	0.04	8	0.03	0.05	-1.46	0.08
9	0.16	0.05	-2.38	0.06	9	0.17	0.05	-1.86	0.14
10	0.29	0.05	-1.96	0.08	10	0.22	0.04	0.73	0.13
11	0.13	0.05	-2.52	0.05	11	0.15	0.05	-1.58	0.10
12	0.23	0.05	-2.85	0.05	12	0.25	0.05	-0.50	0.26
13	0.30	0.05	-2.16	0.06	13	0.31	0.05	-3.09	0.15
14	0.22	0.05	-2.22	0.06	14	0.15	0.05	-0.84	0.17
15	0.27	0.05	-2.05	0.06	15	0.28	0.04	-1.73	0.12
16	0.12	0.05	-2.65	0.05	16	0.13	0.05	-0.38	0.09
17	0.17	0.05	-2.72	0.05	17	0.09	0.04	-0.68	0.13
18	0.10	0.00	-2.05	0.06	18	0.11	0.03	-0.82	0.13
19	0.13	0.05	-1.92	0.05	19	0.14	0.05	-0.28	0.07
20	0.07	0.05	-2.28	0.04	20	0.08	0.05	-1.41	0.09
Average	0.18	0.04	-2.35	0.05	Average	0.17	0.04	-1.46	0.11
Maximum standard deviation	0.05		0.08		Maximum standard deviation	0.05		0.26	

tained data were found to be influenced slightly by the environmental changes of outside the chamber. Therefore, we estimated the influence of the outside environmental changes by a linear fit for three periods, 1, 2, and 3 in Figure F.12. The anomalies from the linear fit are shown in Figure F.13, and are used for the following discussion. Tables F.9 and F.10 summarize the results of the experiments. Note that the RH measurements in the 0 %RH chamber are 0 %RH regardless of the sensor positions. We assume that the difference due to the different sensor position lies within the interval of the maximum difference in Tables F.9 and F.10 in uniform distribution. The standard uncertainty is defined as the maximum difference divided by $\sqrt{3}$ (*JCGM/WG 1*, 2008). In conclusion, the standard uncertainty of the temperature measurement is 0.05 K and 0.04 K for the 0% and 100% chambers respectively and that of the RH measurement is 0.14 %RH for the 100% chamber.

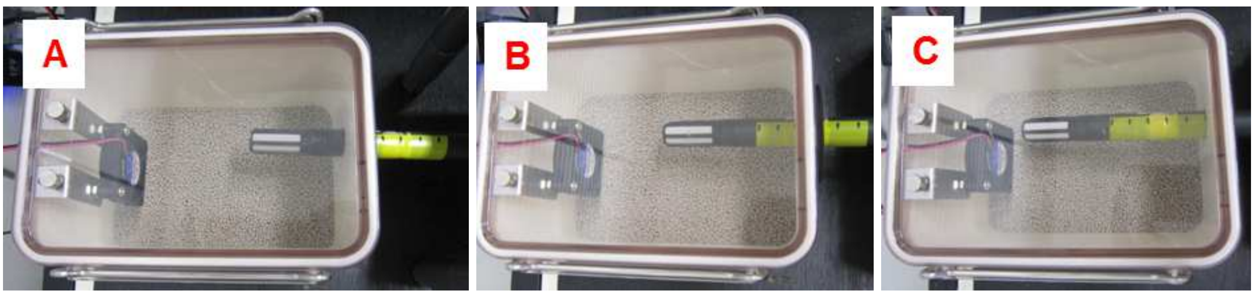

Figure F.11: The three different positions of the reference HC2 sensor in the SHC chamber. (A) The sensor top is located closer to the sensor insertion opening. (B) The sensor top is located around the center of the chamber. (C) The sensor top is located closer to the fan.

Table F.9: Summary of the results for the SHC (0 %RH) chamber experiment (for temperature only).

Period	Sample number (i)	Temperature (°C)						
		A	B	C	$\lvert B_i\text{-}A_i \rvert$	$\lvert C_i\text{-}B_i \rvert$	$\lvert A_{i+1}\text{-}C_i \rvert$	$\lvert C_i\text{-}A_i \rvert$
1	1	25.14	25.17	25.22	0.03	0.05		0.08
	2	25.19	25.24	25.27	0.05	0.03	0.03	0.08
	3	25.21	25.20	25.22	0.01	0.02	0.06	0.01
	4	25.15	25.18	25.20	0.03	0.02	0.07	0.05
	5	25.17	25.20	25.24	0.03	0.04	0.03	0.07
2	6	25.61	25.59	25.58	0.02	0.01		0.03
	7	25.59	25.59	25.61	0.00	0.02	0.01	0.02
3	8	25.71	25.70	25.67	0.01	0.03		0.04
	9	25.70	25.69	25.68	0.01	0.01	0.03	0.02
4	10	25.67	25.67	25.71	0.00	0.04		0.04
	11	25.67	25.69	25.70	0.02	0.01	0.04	0.03
5	12	25.77	25.74	25.73	0.03	0.01		0.04
	13	25.75	25.73	25.75	0.02	0.02	0.02	0.00
		Average			0.02(±0.01)	0.02(±0.01)	0.04(±0.02)	0.04(±0.03)
		Maximum difference			0.05	0.05	0.07	0.08
		Standard uncertainty			0.03	0.03	0.04	0.05

Table F.10: Summary of the results for the SHC (100 %RH) chamber experiment (for both temperature and RH).

Period	Sample number (i)	Temperature (°C)							Relative humidity (%RH)						
		A	B	C	$\lvert B_i\text{-}A_i \rvert$	$\lvert C_i\text{-}B_i \rvert$	$\lvert A_{i+1}\text{-}C_i \rvert$	$\lvert C_i\text{-}A_i \rvert$	A	B	C	$\lvert B_i\text{-}A_i \rvert$	$\lvert C_i\text{-}B_i \rvert$	$\lvert A_{i+1}\text{-}C_i \rvert$	$\lvert C_i\text{-}A_i \rvert$
1	1	25.95	25.99	26.02	0.04	0.03		0.07	95.34	95.32	95.32	0.02	0.00		0.02
	2	25.98	26.01	26.03	0.03	0.02	0.04	0.05	95.26	95.26	95.25	0.00	-0.01	0.06	0.01
	3	25.99	25.99	26.01	0.00	0.02	0.04	0.02	95.22	95.28	95.29	0.06	0.01	0.03	0.07
	4	25.98	25.99	26.00	0.01	0.01	0.03	0.02	95.26	95.31	95.34	0.05	0.03	0.03	0.08
2	5	26.24	26.23	26.23	0.01	0.00		0.01	95.07	95.16	95.21	0.09	0.05		0.14
	6	26.25	26.23	26.22	0.02	0.01	0.02	0.03	95.01	95.12	95.25	0.11	0.13	0.20	0.24
	7	26.26	26.24	26.25	0.02	0.01	0.04	0.01	95.09	95.20	95.27	0.11	0.07	0.16	0.18
	8	26.28	26.26	26.24	0.02	0.02	0.03	0.04	95.04	95.11	95.20	0.07	0.09	0.23	0.16
	9	26.25	26.22	26.21	0.03	0.01	0.01	0.04	95.01	95.13	95.26	0.12	0.13	0.19	0.25
3	10	26.35	26.36	26.39	0.01	0.03		0.04	95.69	95.72	95.72	0.03	0.00		0.03
	11	26.36	26.36	26.39	0.00	0.03	0.03	0.03	95.67	95.71	95.71	0.04	0.00	0.05	0.04
	12	26.36	26.36	26.38	0.00	0.02	0.03	0.02	95.64	95.69	95.71	0.05	0.02	0.07	0.07
	13	26.36	26.36	26.38	0.00	0.02	0.02	0.02	95.66	95.70	95.72	0.04	0.02	0.05	0.06
		Average			0.01(±0.01)	0.02(±0.01)	0.03(±0.01)	0.03(±0.02)	Average			0.06(±0.04)	0.04(±0.05)	0.11(±0.08)	0.10(±0.08)
		Maximum difference			0.04	0.03	0.04	0.07	Maximum difference			0.12	0.13	0.23	0.25
		Standard uncertainty			0.02	0.02	0.02	0.04	Standard uncertainty			0.07	0.08	0.13	0.14

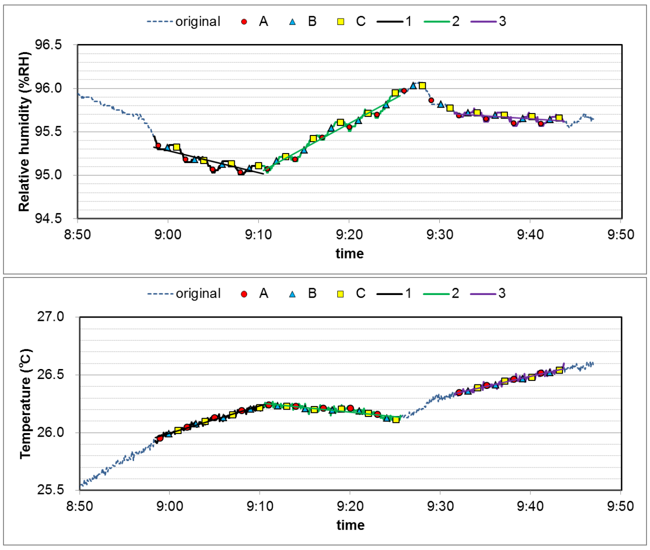

Figure F.12: The HC2 RH (top) and temperature (bottom) data in the SHC(100 %RH) chamber. The measurement data were obtained every 5 seconds (indicated by original). The sensor position was changed sequentially among A, B, and C shown in Figure F.11 every minute. One-minute averages for each position were calculated and shown (indicated by A, B and C). Linear-fit lines are also calculated and shown for three periods, 1, 2, and 3 for both panels.

Table F.11: The uncertainty budget of the RH measurement for the 0 %RH environment ground check. **Note:** The result for the 20 %RH environment is substituted for the uncertainty of the calibration of the reference instrument.

Relative humidity (0 %RH chamber)		
Source of uncertainty	Estimation method	Standard uncertainty (%RH)
Calibration of the reference instrument	Calibration certificate	0.50
Repeatability of the measurements	Standard deviation of 10 repeated experiments	0.32
Dispersion of individual radiosondes	Maximum standard deviation of 20 sample ground checks	0.08
Inhomogeneity in the chamber	Maximum difference for different sensor positions	
Combined standard uncertainty		0.60

F.5.5 Total uncertainty of the ground check measurements using the SHC system

Tables F.11 and F.12 summarize the uncertainty estimations for the RH measurements using the SHC system in Sections F.1 to F.4. The total uncertainty is expressed as combined standard uncertainty in Tables F.11 and F.12 which is equal to the positive square root of a summation of all the terms.

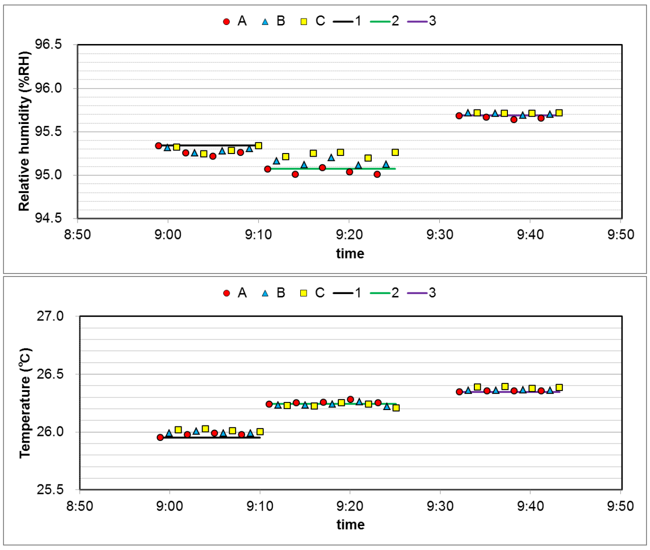

Figure F.13: Same as Figure F.12 but for the anomaly of the one-minute averages with respect to the linear fit (plus the base value) for each period. The first one-minute averages of each period are chosen as the base values for each period.

Table F.12: The uncertainty budget of the RH measurement for the 100 %RH environment ground check. **Note:** The result for the 95 %RH environment is substituted for the uncertainty of the calibration of the reference instrument.

Relative humidity (100 %RH chamber)		
Source of uncertainty	Estimation method	Standard uncertainty (%RH)
Calibration of the reference instrument	Calibration certificate	0.95
Repeatability of the measurements	Standard deviation of 10 repeated experiments	0.72
Dispersion of individual radiosondes	Maximum standard deviation of 20 sample ground checks	0.26
Inhomogeneity in the chamber	Maximum difference for different sensor positions	0.14
Combined standard uncertainty		1.23

G Description of the JMA data format

The Japan Meteorological Agency (JMA) defines the data format of the radiosondes used at JMA upper-air stations as the radiosonde procurement specifications. This format is called JMAFMT. The definition is also applied to the raw data set for the GRUAN data product of Meisei RS-11G and iMS-100 radiosondes. The JMAFMT data consist of raw values, data from the GPS module, and the coefficients of radiosonde sensors, so that the physical quantities can be obtained. Note that the correction and smoothing procedures must be applied separately to obtain the final physical quantities. The JMAFMT data are 976 bit in total (240 bit 4 frames + CRNL (16 bit)) per second. The details of the JMAFMT are described in Tables G.1 to G.6.

The conversion equations for the JMAFMT data to obtain physical quantities are shown below.

(1) Pressure (for the case of a dielectric sensor)

$$F_p = 8S_p/100000 \tag{G.1}$$
$$R_p = 4(F_p/F_r) \tag{G.2}$$
$$P = C_0 + C_1R_p + C_2R_p^2 + C_3R_p^3 + C_4R_p^4 + C_5R_p^5 \tag{G.3}$$

F_p: Pressure Frequency (kHz)
S_p: Element data for the radiowave transmission
R_p: Pressure frequency corrected by the reference frequency (kHz)
F_r: Reference frequency (4 kHz)
C_0 to C_5: Coefficients of the pressure sensor
P: Pressure (hPa)

(2) Temperature (for the case of a thermistor)

$$F_t = 8S_t/100000 \tag{G.4}$$
$$R_t = 4(F_t/F_r) \tag{G.5}$$
$$T_r = A_0 + A_1\left(\frac{1}{R_t - 1}\right) + A_2\left(\frac{1}{R_t - 1}\right)^2 + A_3\left(\frac{1}{R_t - 1}\right)^3 \tag{G.6}$$

$T = Spline(T_r, X_0 to X_{14})$

F_t: Temperature Frequency (kHz)
S_t: Element data for the radiowave transmission
R_t: Temperature frequency corrected by the reference frequency (kHz)
T_r: Thermistor resistance (kHz)
A_0 to A_3: Coefficients of the thermistor (R-F coefficients)
X_0 to X_14: Calibration temperature points (up to 15 points)
T: Temperature (°C) (calculated with a cubic spline with up to 15 calibration points)

Table G.1: GPSsonde Transmission Format (JMA Format) Ver.2.0

Frame 1 (240bit)

Item	Data 0	Data 1	Data 2	Data 3	Data 4	Data 5	Data 6	Data 7	Data 8	Data 9	Data 10	Data 11	Data 12	Data 13	Data 14
Bit Number	16	16	16	16	16	16	16	16	16	16	16	16	16	16	16
Content	SC	DC	Radiosonde serial number 1	Radiosonde serial number 2	Radiosonde version information	Sub-frame NO.	Output Element 1-1	Output Element 1-2	Output Element 2-1	Output Element 2-2	Output Element 3-1	Output Element 3-2	Output Element 4-1	Output Element 4-2	BCC

Frame 2 (240bit)

Item	Data 15	Data 16	Data 17	Data 18	Data 19	Data 20	Data 21	Data 22	Data 23	Data 24	Data 25	Data 26	Data 27	Data 28	Data 29
Bit Number	16	16	16	16	16	16	16	16	16	16	16	16	16	16	16
Content	SC	radiosonde internal state	Radiosonde battery Voltage	Radiosonde frequency	Radiosonde data (pressure)	radiosonde data (temperature)	radiosonde data (humidity)	Reference frequency (Hi-ref)	Output Element 2-1	Radiosonde production date	HDOP	PDOP	Satellite information 1	Satellite information 2	BCC

Frame 3 (240bit)

Item	Data 30	Data 31	Data 32	Data 33	Data 34	Data 35	Data 36	Data 37	Data 38	Data 39	Data 40	Data 41	Data 42	Data 43	Data 44
Bit Number	16	16	16	16	16	16	16	16	16	16	16	16	16	16	16
Content	SC	GPS week number	GPS time of week 1	GPStime of week 2	GPS leap second	Latitude 1	Latitude 2	Longitude 1	Longitude 2	GPS altitude 1	GPS altitude 2	wind direction	wind speed	State of radiosonde external sensor	BCC

Frame 4 (240bit)

Item	Data 45	Data 46	Data 47	Data 48	Data 49	Data 50	Data 51	Data 52	Data 53	Data 54	Data 55	Data 56	Data 57	Data 58	Data 59
Bit Number	16	16	16	16	16	16	16	16	16	16	16	16	16	16	16
Content	SC	Vacancy or Reaction current of ozone	Vacancy or Pump temperature	Vacancy or Pump current	Vacancy or pump voltage	Vacancy	Vacancy	Vacancy	Vacancy	Vacancy	Vacancy	Vacancy	Vacancy	Vacancy	BCC

(3) Relative humidity (for the case of a dielectric sensor)

$$F_u = 8S_u/100000 \tag{G.7}$$
$$R_u = 4(F_u/F_r) \tag{G.8}$$
$$U = B_0 + B_1R_u + B_2R_u^2 + B_3R_u^3 \tag{G.9}$$

F_u: Humidity Frequency (kHz)
S_u: Element data for the radiowave transmission
R_u: Humidity frequency corrected by the reference frequency (kHz)
B_0 to B_3: Coefficients of the relative humidity sensor
U: Relative humidity (%RH)

(4) Temperature for the relative humidity sensor (for the case of a thermistor)

$$F_s = 8S_s/100000 \tag{G.10}$$
$$R_s = 4(F_s/F_r) \tag{G.11}$$
$$R_r = D_0 + D_1\left(\frac{1}{R_s-1}\right) + D_2\left(\frac{1}{R_s-1}\right)^2 + D_3\left(\frac{1}{R_s-1}\right)^3 \tag{G.12}$$
$$T_s = \frac{1}{E_0\log(R_r)^3 + E_1\log(R_r) + E_2} - 273.15 \tag{G.13}$$

F_s: Temperature Frequency (kHz)
S_S: Element data for the radiowave transmission
R_s: Temperature frequency corrected by the reference frequency (kHz)
R_r: Thermistor resistance value (kΩ)
D_0 to D_3, E_0 to E_2: Coefficients of the thermistor (R-F coefficients)
T_s: Temperature of the RH sensor (°C)

Table G.2: Details of each element (Main frame 1)

Frame 1 (240bit)

Data NO.	Bit Number	Content	Detailed description
0	16	SC	Sync code (Frame number) Frame 1 = FFF0, Frame 2 = FFF1, Frame 3 FFF2, Frame 4 FFF3 : Fixation
1	16	DC	Data Counter Data count number from the radiosonde started (0-65535)
2 3	16	Radiosonde serial number	Radiosonde serial number. Last five digits of radiosonde serial number (0-65535)
4	16	Radiosonde version information	Information of radiosonde version. No version is set to FFFF.
5	16	Sub-frame number	Sub-frame number. See Discription(Sub-frame) sheet.
6 7	32	Output element 1 (1-1)+(1-2)	Output element 1, which construct a 32-bit output by data No. 6 plus No. 7. This output element is transmitted repeatedly in order to contents of output element 1 in sub frame. This data is represented in Binary32 format. No transmission data is set to FFFF.
8 9	32	Output element 2 (2-1)+(2-2)	Output element 2, which construct a 32-bit output by data No. 8 plus No. 9. This output element is transmitted repeatedly in order to contents of output element 2 in sub frame. This data is represented in Binary32 format. No transmission data is set to FFFF.
10 11	32	Output element 3 (3-1)+(3-2)	Output element 3, which construct a 32-bit output by data No. 10 plus No. 11. This output element is transmitted repeatedly in order to contents of output element 3 in sub frame. This data is represented in Binary32 format. No transmission data is set to FFFF.
12 13	32	Output element 4 (4-1)+(4-2)	Output element 4, which construct a 32-bit output by data No. 12 plus No. 13. This output element is transmitted repeatedly in order to contents of output element 4 in sub frame. This data is represented in Binary32 format. No transmission data is set to FFFF.
14	16	BCC	Block check character (BCC). From the following data of SC to the front of the BCC, the BCC value is calculated by the horizontal parity (exclusive OR).

Table G.3: Details of each element (Main frame 2)

Frame 2 (240bit)

Data NO.	Bit Number	Content	Detailed description
15	16	SC	Sync code (Frame number) Frame 1 = FFF0, Frame 2 = FFF1, Frame 3 FFF2, Frame 4 FFF3 : Fixation
16	16	Radiosonde internal state	Indicate the status of each function (or sensor) of radiosonde. In order from the MSB, Frequency (0), Battery voltage (1), Pressure (2), Temperature(3), Humidity (4), PDOP(5), GPS week (6), GPS second (7), GPS leap second (8), Number of Satellite (9), Latitude (10), Logitude (11), Altitude(12), Wind direction (13), Wind speed (14), Indicating the SBAS correction (15). The bit '1' denotes normal, and '0' denotes abnormal or no use.
17	16	Radiosonde battery voltage	The numerical value multiplied by 100 to the radiosonde battery voltage. e.g. 12.0 V $\rightarrow$ 12.0 $\times$ 100 = 1200
18	16	Radiosonde frequency	The numerical value multiplied by 100 to the radiosonde frequency. e.g. 404.5 MHz $\rightarrow$ 404.5 $\times$ 100 = 40450
19	16	Radiosonde data (pressure)	Raw data of the pressure sensor (frequency output). This data is represented the Sp value. Refer to the relational equation for pressure and frequency.
20	16	Radiosonde data (temperature)	Raw data of the temperature sensor (frequency output). This data is represented the St value. Refer to the relational equation for temperature and frequency.
21	16	Radiosonde data (humidity)	Raw data of the humidity sensor (frequency output). This data is represented the Su value. Refer to the relational equation for humidity and frequency.
22	16	Reference frequency	The value of reference instrument (resistance or capacitance) convert to a frequency (corresponding to the high reference). The frequency data obtained by 0.01 Hz units, are multiplied by 100. Max 50000. e.g. 499.81 Hz $\rightarrow$ 49981
23	16	Radiosonde data (temperature of humidity sensor)	Raw data of the temperature of humidity sensor (frequency output). This data is represented the Sht value. Refer to the relational equation for temperature of humidity senspor and frequency.
24	16	Radiosonde production date	Radiosonde production date Top two digits is the last two digits of the calendar year, and next 3 digits is the day count from 1 January. e.g.) 2012/Jul/04 $\rightarrow$ 12186 2013/Jan/4 $\rightarrow$ 13004
25	16	HDOP	HDOP measured by the GPSsonde. This measured value is multiplied by 100.
26	16	PDOP	PDOP measured by the GPSsonde. This measured value is multiplied by 100.
27 28	32	Satellite information	GPS PRN number which starting with 1 for the MSB (SVN is not). The Received Satellite is '1', otherwise is '0'.
29	16	BCC	Block check character (BCC) From the following data of SC to the front of the BCC , the BCC value is calculated by the horizontal parity (exclusive OR).

Table G.4: Details of each element (Main frame 3)

Frame 3 (240bit)

Data NO.	Bit Number	Content	Detailed description
30	16	SC	Sync code (Frame number) Frame 1 = FFF0, Frame 2 = FFF1, Frame 3 FFF2, Frame 4 FFF3 : Fixation
31	16	GPS week number	GPS week number obtained from the navigation message of GPS. This week number start from zero week on August 22, 1999.
32	32	GPS time of week	GPS time count obtained from the navigation message of GPS.
33			This time count up from 00m00s UTC on each Sunday.
34	16	GPS leap second	The leap seconds obtained from the navigation message of GPS. If the leap seconds has been included in the "GPS time of week" is 0.
35	32		Latitude is expressed to 7 decimal places, and multiplied by 10^7.
36		Latitude	Positive values: North; negative: South. A negative number is taken as the complement of 2.
37	32		Longitude is expressed to 7 decimal places, and multiplied by 10^7.
38		Longitude	Postive values: East; negative: West. A negative number is taken as the complement of 2.
39	32	GPS altitude	The GPS altitude expressed to 2 decimal places, and multiplied by 100.
40			A negative number is taken as the complement of 2.
41	16	Wind direction	The radiosonde's direction of movement expressed to 2 decimal places, and multiplied by 100. For example, in the case of 360.00 degrees (north) wind, the sonde flows south. This yields 180.00 degrees (=18000).
42	16	Wind speed	The horizontal speed of the radiosonde expressed to 2 decimal places, and multiplied by 100.
43	16	State of Radiosonde external sensor	In order from the MSB, external sensor number 0 (data number 46) ... external sensor number 12 (data number 58). The bit value '1' denotes normal, and '0' denotes abnormal or no use.
44	16	BCC	Block check character (BCC) From the following data of SC to the front of the BCC , the BCC value is calculated by the horizontal parity (exclusive OR).

Table G.5: Details of each element (Main frame 4)

Frame 4 (240bit)

Data NO.	Bit Number	Content	Detailed description
45	16	SC	Sync code (Frame number) Frame 1 = FFF0, Frame 2 = FFF1, Frame 3 FFF2, Frame 4 FFF3 : Fixation
46	16	Vacancy or ECC current	Free channel. When using the Ozone sonde, ECC electric current is represented by values from 0 to 65535. The value represents the number of 0.001μA units multiplied by 100, added with 10000. (For example: 0μA is encoded as 10000. 55.535 μA is encoded as 65535.).
47	16	Vacancy or ECC temperature	Free channel. When using the Ozone sonde, the ECC temperature is represented by values from 0 to 65535. The temperature data are obtained by multiplying this value by 0.01 K.
48	16	Vacancy or Pump current	Free channel. When using the Ozone sonde, pump motor electric current is represented by values from 0 to 65535. The current data are obtained by multiplying this value by 0.01 mA.
49	16	Vacancy or reaction tube temperature	Free channel. When using the Ozone sonde, reaction tube temperature is represented by values from 0 to 65535. The temperature data are obtained by multiplying this value by 0.01 K.
50	16	Vacancy	Unused channel. If necessary, set the data between 0 to 65535.
51	16	Vacancy	Unused channel. If necessary, set the data between 0 to 65535.
52	16	Vacancy	Unused channel. If necessary, set the data between 0 to 65535.
53	16	Vacancy	Unused channel. If necessary, set the data between 0 to 65535.
54	16	Vacancy	Unused channel. If necessary, set the data between 0 to 65535.
55	16	Vacancy	Unused channel. If necessary, set the data between 0 to 65535.
56	16	Vacancy	Unused channel. If necessary, set the data between 0 to 65535.
57	16	Vacancy	Unused channel. If necessary, set the data between 0 to 65535.
58	16	Vacancy	Unused channel. If necessary, set the data between 0 to 65535.
59	16	BCC	Block check character (BCC) From the following data of SC to the front of the BCC , the BCC value is calculated by the horizontal parity (exclusive OR).

Table G.6: Details of Sub-frame element

Sub-frame	Output element 1	Sub-frame	Output element 2	Sub-frame	Output element 3	Sub-frame	Output element 4
	(Data6 + Data7)		(Data8 + Data9)		(Data10 + Data11)		(Data12 + Data13)
0	Sonde type	0	Sonde type	0	Manufacturer's software version	0	JMA format version (=V200)
1	Temp. of calibration point 1	1	Resister of calibration point 1	1	Temperature sensor coefficient (A0)	1	Humidity sensor coefficient (B0)
2	Temp. of calibration point 2	2	Resister of calibration point 2	2	Temperature sensor coefficient (A1)	2	Humidity sensor coefficient (B1)
3	Temp. of calibration point 3	3	Resister of calibration point 3	3	Temperature sensor coefficient (A2)	3	Humidity sensor coefficient (B2)
4	Temp. of calibration point 4	4	Resister of calibration point 4	4	Temperature sensor coefficient (A3)	4	Humidity sensor coefficient (B3)
5	Temp. of calibration point 5	5	Resister of calibration point 5	5	Pressure sensor coefficient (P0)	5	Temperature sensor coefficient of Humidity unit (C0)
6	Temp. of calibration point 6	6	Resister of calibration point 6	6	Pressure sensor coefficient (P1)	6	Temperature sensor coefficient of Humidity unit (C1)
7	Temp. of calibration point 7	7	Resister of calibration point 7	7	Pressure sensor coefficient (P2)	7	Temperature sensor coefficient of Humidity unit (C2)
8	Temp. of calibration point 8	8	Resister of calibration point 8	8	Pressure sensor coefficient (P3)	8	FFFF
9	Temp. of calibration point 9	9	Resister of calibration point 9	9	Pressure sensor coefficient (P4)	9	FFFF
a	Temp. of calibration point 10	a	Resister of calibration point 10	a	Pressure sensor coefficient (P5)	a	FFFF
b	Temp. of calibration point 11	b	Resister of calibration point 11	b	FFFF	b	FFFF
c	Temp. of calibration point 12	c	Resister of calibration point 12	c	FFFF	c	FFFF
d	Temp. of calibration point 13	d	Resister of calibration point 13	d	FFFF	d	FFFF
e	Temp. of calibration point 14	e	Resister of calibration point 14	e	FFFF	e	FFFF
f	Temp. of calibration point 15	f	Resister of calibration point 15	f	FFFF	f	FFFF

H Actual procedures to create the GRUAN data product for the RS-11G and iMS-100 radiosondes

This section describes the workflow for creating the GRUAN data product (GDP). The overview of the workflow is illustrated in Figure H.1.

H.1 The data files

The JMAFMT data file (containing raw data and sensor-coefficient data) and the GRUAN Meta Data file (GMD; containing the meta-data) for each sounding are submitted from a GRUAN site (e.g., Tateno) to the GRAUN Lead Centre. The GRUAN Lead Centre publishes the GRUAN processing ticket (GPT) file for each sounding, which contains the Product ID and Ascent ID of the sounding. Tateno downloads the JMAFMT, GMD, and GPT files that are used to create the GRUAN Data Product (GDP).

H.2 Loading meta data

From the GMD file, the following information is loaded: The date and time of the launch; measuring-system information; serial number of the sonde; list of the instruments; results of the GC checks; results of the SHC check; surface data at the launch; and the site name. The list of the instruments contains the filling weight of the balloon and the length of the unwinder or of the string. The information on latitude, longitude, altitude of the site is loaded from the meta-data file from the RSLaunchClient which is the software for submitting data to the GRUAN Lead Centre.

H.3 Loading raw data

From the JMAFMT file, the following information and data are loaded: The sonde type; version of the JMAFMT file; raw frequency data, GPS time data, GPS position data (latitude, longitude, and altitude), GPS wind data, and the calibration coefficient data to calculate air temperature (A_n), RH (B_n), and the RH sensor temperature (C_n; for the case of iMS-100 radiosondes).

H.4 Re-calibration of the RH coefficients using SHC data

At the factory, the RH sensors were calibrated at 15 %RH, 30 %RH, 50 %RH, 70 %RH, 90 %RH, and 95 %RH, and the original calibration coefficients (B_n) were determined. The frequency data for 0 %RH and 100 %RH during the SHC checks are calculated using the original coefficients, and by adding these SHC calibration information, a set of new calibration coefficients are obtained.

H.5 Obtaining initial ascending data

Raw frequency data are converted to raw air temperature data T_{raw} (Appendix B), raw RH data U_{raw} (Appendix C), and raw RH sensor temperature data Ts_{raw} for the case of iMS-100 (Appendix C). GPS wind (speed and direction) data are converted to zonal and meridional wind data, u_{raw} and v_{raw}, respectively. Raw geopotential height data, geopot_{raw} are calculated using GPS height data, alt_{raw} and GPS latitude data (Section 3.3). GPS latitude data, lat_{raw} and longitude data, lon_{raw} are obtained from GPS position data. Information on the launch time and the burst altitude is also obtained from

GPS data. The time launched the balloon and the burst point are obtained from alt$_{raw}$. The ascending data set, between the launch and the balloon burst, is extracted from the raw data set. Finally, filling measurement-missing fields by linear interpolation using adjacent measurements, the initial data set (T_0, U_0, Ts_0, u_0, v_0, geopot$_0$, alt$_0$, lat$_0$, and lon$_0$) is obtained.

H.6 Calculation of geopotential height and ascending rate

The interpolated GPS altitude alt$_0$ is converted the corrected altitude alt$_1$ in consideration the offset between alt$_0$ at the release time and the release altitude, Δ alt.

$$\mathrm{alt}_1 = \mathrm{alt}_0 - \Delta\mathrm{alt} \tag{H.1}$$

The moving averages of alt$_1$ within ± 30 seconds are calculated to obtain the final GPS altitude data, alt$_{fin}$. The uncertainty of the GPS altitude $u(alt)$ is calculated by the composition with the uncertainty by the raw GPS altitude from PDOP, u_{GPS} (alt), and the uncertainty by the moving average, u_{ma} (alt), (Section 3.3). The estimated standard uncertainty of smoothed (moving averaged or low-pass filtered) data are calculated using the method written in Appendix A of *Dirksen et al.* (2014) as

$$N' = \left(\sum_{j=-M}^{M} h_j^2 \right)^{-1} \tag{H.2}$$

$$u(\bar{s}_i) = \sqrt{\frac{N'}{N'-1} \sum_{j=-M}^{M} h_j^2 (s_{i+j} - \bar{s}_i)^2} \tag{H.3}$$

where M is the half-width of the filter window (30 for the case of ± 30 s moving average of 1-sec-resolution data), h is the normalized weight coefficient, and s is the value before filtering and $\bar{s}$ is the value filtered. N' is the parameter called as the effective sample size.
The final geopotential height data, geopot$_{fin}$ is derived from alt$_{fin}$ and lat$_0$. The ascending rate data, *asc*, are derived from the time difference of geopot$_{fin}$ as

$$asc = \begin{cases} 0 & (t = 0) \\ \mathrm{geopot}_{fin}(t) - \mathrm{geopot}_{fin}(t-1) & (t > 0) \end{cases} \tag{H.4}$$

H.7 Calculation of temperature

If the length of the string or the unwinder is equal to or less than 10 m, the temperature spike filtering is applied when the pressure is below 30 hPa. For this filtering and the radiation correction (will be discussed below), the provisional pressure P_1 are derived using T_0, U_0, surface pressure data, P_{surf}, and geopot$_{fin}$ (Section 3.1). T_1, the temperature after spike filtering, equals to T_0 if the filter is not needed. The uncertainty with this filtering is u$_{spike}$(T).
The moving averages of T_1 within ± 1 second are calculated to obtain the uncorrected temperature data, T_2 and the standard uncertainty of temperature, u_{ma} (T). The amount of the radiation correction, T_{cor} is calculated using T_2, P_1, P_{surf}, asc, GPS time, lat$_0$, and lon$_0$. T_{cor} is subtracted from T_2 to obtain the final temperature data, T_{fin}.
The total uncertainty of the temperature $u(T)$ is also calculated (Section 3.1).

The correlated uncertainty of the temperature u_{cor} (T) is calculated from the uncertainties by albedo u_{albedo} (T), by ventilation $u_{ventilation}$ (T), and by calibration $u_{Tcalib1}$ (T) and $u_{Tcalib2}$ (T).
u_{albedo} (T) is derived from the difference between the radiation correction values with albedo of 0.1 and with albedo of 0.6.

$$u_{albedo}(T) = \frac{1}{2\sqrt{3}} \left| T_{cor}(albedo = 0.6) - T_{cor}(albedo = 0.1) \right| \tag{H.5}$$

$u_{ventilation}$ (T) is derived from the difference between radiation correction values with ventilation of asc + 3.0 m s^{-1} and with ventilation of asc.

$$u_{ventilation}(T) = \frac{1}{\sqrt{3}} \left| T_{cor}(v = asc + 3) - T_{cor}(v = asc) \right| \tag{H.6}$$

The total, correlated uncertainty becomes:

$$u_{cor}(T) = \sqrt{(u^2_{Tcalib1} + u^2_{Tcalib2} + u_{albedo}(T)^2 + u_{ventilation}(T)^2 + u_{spike}(T)^2} \tag{H.7}$$

Finally, the total uncertainty of the temperature $u(T)$ is derived as

$$u(T) = \sqrt{(u_{cor}(T)^2 + u_{std}(T)^2)} \tag{H.8}$$

H.8 Calculation of the temperature of the RH sensor

For the RS-11G radiosonde, the uncorrected RH sensor temperature data, Ts_0 is derived from T_{fin}, P_1, P_{surf}, and asc (Appendix C). The corrected RH sensor temperature data, Ts_{fin} is obtained by considering the thermal lag and solar radiative heating from T_{fin}, P_1, and Ts_0 (Appendix C). Ts_{fin} is used in the corrections of RH.

H.9 Calculation of RH

The response time τ_U is estimated from Ts_{fin} (Section 3.2). U_0 are separated into low and high frequency components, U_{1low} and U_{1high}, respectively, by the digital filter (Appendix E) whose cutoff period is set as four times of T$_{pendulum}$. The statistical uncertainty for this step is written as $u_{std1}(U)$. The time-lag correction is applied to the both components to obtain U_{2low} and U_{2high}. The contamination correction is applied to U_{2high} to obtain U_{3high}, and the statistical uncertainty for this is u_{std3} (U). Moving averages for ±90 seconds are taken for U_{3high} to obtain U_{4high} with the statistical uncertainty, $u_{std4}(U)$. The corrected high frequency component U_{4high} and the low frequency component U_{2low} are composed to obtain U_4. The TUD correction using Ts_{fin} is applied to U_4 to obtain U_5. Finally, the Ts/Ta correction is applied to U_5 to obtain the final RH data, U_{fin}. If U_{fin} is less than 0% or greater than 100% RH, they are replaced with 0 %RH or 100 %RH, respectively.
The statistical uncertainty of RH, u_{std} (U) is calculated as

$$u_{std}(U) = \sqrt{u_{std1}(U)^2 + u_{std3}(U)^2 + u_{std4}(U)^2} \tag{H.9}$$

The correlated uncertainty of RH, u_{cor} (U) is calculated from the uncertainties by the time-lag correction, u_{TL} (U), by TUD correction, u_{TUD} (U), by the Ts/Ta correction, u_{Ts} (U), by the hysteresis of the RH sensor, $u_{hysteresis}$ (U), and by the calibration, u_{Ucalib} (U).

$u_{TL}(U)$ is determined by the uncertainty of the response time, and is written as

$$u_{TL}(U) = \frac{1}{2\sqrt{3}} |U(\tau = \tau_U + u(\tau_U)) - U(\tau = \tau_U - u(\tau_U))| \tag{H.10}$$

$u_{TUD}(U)$ is a fixed value as $u_{TUD}(U) = 1.8$ $u_{Ts}(U)$ is determined by the uncertainty of the Ts_{fin} whose uncertainty is assumed to be ± 0.3 K, and thus is written as

$$u_{Ts}(U) = \frac{1}{2\sqrt{3}} \left| U(Ts = Ts_{fin} + 0.3) - U(Ts = Ts_{fin} - 0.3) \right| \tag{H.11}$$

Significant hysteresis appears only when RH is decreasing, so $u_{hysteresis}(U)$ is given as

$$u_{hystereis}(U) = \begin{cases} 0 & (\text{trend} \geq -0.05\%\text{RH}s^{-1}) \\ \frac{1.8}{\sqrt{3}} & (\text{trend} < -0.05\%\text{RH}s^{-1}) \end{cases} \tag{H.12}$$

where trend is a short-term trend in U_{fin} which is estimated as the slope of the tangent using the Savitzky-Golay method (*Savitzky and Golay*, 1964) with ± 10 s values. The threshold value of -0.05 %RH s^{-1} (i.e., almost constant vertically) is determined empirically.

$u_{cor}(U)$ and the total uncertainty, $u(U)$ are calculated as

$$u_{cor}(U) = \sqrt{(u_{TL}(U)^2 + u_{TUD}(U)^2 + u_{Ts}(U)^2 + u_{hysteresis}(U)^2 + u^2_{Ucalib}} \tag{H.13}$$

and

$$u(U) = \sqrt{u_{cor}(U)^2 + u_{std}(U)^2} \tag{H.14}$$

respectively.

H.10 Calculation of pressure

The final pressure data, P_{fin} are calculated from geopot$_{fin}$, T_{fin}, U_{fin}, and P_{surf} (Section 3.3).

The correlated uncertainty of the pressure is calculated from the uncertainties by the surface pressure, u_{psurf} (P), by GPS altitude, u_{alt} (P), by temperature, u_{temp} (P) and by RH u_{RH} (P).

u_{psurf} (P) is calculated in the consideration of P_{surf} with the error, $u(P_{surf})$.

$u_{alt}(P), u_{temp}(P), u_{RH}(P)$, and the totally uncertainty $u(P)$ as:

$$u_{alt}(P) = \frac{1}{2\sqrt{3}} |P(T_{fin}, U_{fin}, alt - u(alt)) - P(T_{fin}, U_{fin}, alt + u(alt))| \tag{H.15}$$

$$u_{temp}(P) = \frac{1}{2\sqrt{3}} |P(T_{fin} + u(T), U_{fin}, alt) - P(T_{fin} - u(T), U_{fin}, alt)| \tag{H.16}$$

$$u_{RH}(P) = \frac{1}{2\sqrt{3}} |P(T_{fin}, U_{fin} + u(U), alt) - P(T_{fin}, U_{fin} - u(U), alt)| \tag{H.17}$$

$$u(P) = \sqrt{u^2_{psurf}(P) + u^2_{alt}(P) + u^2_{temp}(P) + u^2_{RH}(P)} \tag{H.18}$$

respectively.

H.11 Calculation of horizontal wind

The final zonal wind data, u_{fin} and the final meridional wind data, v_{fin} are derived from u_0 and v_0 using the low-pass filter with the cutoff frequency as 1/T$_{pendulum}$ (Appendix E). The statistical uncertainties, $u_{std}(u)$ and $u_{std}(v)$ are also calculated. The final wind speed data, wspeed$_{fin}$ and the final wind direction data, wdir$_{fin}$ are derived from u_{fin} and v_{fin}. The uncertainty of wind speed, u(wspeed) and the uncertainty of wind direction, u(wdir) are calculated using Equations 27 and 28 in *Dirksen et al.* (2014) as

$$
\begin{aligned}
u(wspeed) &= \sqrt{\frac{(u \cdot u_{std}(u))^2 + (v \cdot u_{std}(v))^2}{u^2+v^2}} && \text{(H.19)}\\
u(wdir) &= \frac{180}{\pi} \frac{\sqrt{(u_{std}(u)^2 + u_{std}(v)^2}}{(1+\frac{u}{v}^2)\,|v|} && \text{(H.20)}
\end{aligned}
$$

H.12 Calculation of other derived data

In the GDP file, dewpoint/frostpoint temperature, FP, water vapor volume mixing ratio, WVMR, and precipitable water vapor (or the column amount of water vapor), PWV are also stored as the derived data. The saturation vapor pressure for air temperature T [K], $e_s(T)$ [hPa], is calculated as (by *Hyland and Wexler* (1983)):

$$
\begin{aligned}
\ln(100e_s(T)) = \; & -0.58002206 \times 10^4/T \\
& +0.13914993 \cdot 10 \\
& -0.48640239 \cdot 10^{-1} \times T \\
& +0.41764768 \cdot 10^{-4} \times T^2 \\
& -0.14452093 \cdot 10^{-7} \times T^3 \\
& +0.65459673 \cdot 10 \times \ln T
\end{aligned} \qquad \text{(H.21)}
$$

FP is derived by solving the equation below:

$$e_s(FP) = e_s(T_{fin}) \times 0.01U_{fin} \qquad \text{(H.22)}$$

WVMR is derived from FP and P_{fin} as

$$WVMR = \frac{e_s(FP)}{P_{fin}} = \frac{e_s(T_{fin}) \times 0.01U_{fin}}{P_{fin}} \qquad \text{(H.23)}$$

The mixing ratio by weight mr is derived from

$$mr = 0.622\frac{e_s(FP)}{P_{fin} - e_s(FP)} = 0.622\frac{e_s(T_{fin}) \times 0.01U_{fin}}{P_{fin} - e_s(T_{fin}) \times 0.01U_{fin}} \qquad \text{(H.24)}$$

PWV is derived from the integration of mr as

$$PWV = \frac{1}{g}\int_{P_{surf}}^{P_{bp}} mrdp \qquad \text{(H.25)}$$

where P_{surf} and P_{bp} are the pressures at the surface and at the burst point, respectively. In practice, PWV is calculated as

$$PWV = \sum_{i=0}^{N-1} \frac{1}{2}(mr_i + mr_{i+1})(P_{fin,i} - P_{fin,i+1}) \tag{H.26}$$

H.13 Output file

The GDP file is in the NetCDF format. The attributes and values of the GDP file are shown in Tables H.1, H.2, and H.3.

H.14 The environments

The calculation program works in the following environments (as of February 2018):

- Python 3.6.4+
- Numpy 1.14.0+
- Scipy 1.0.0+
- bitstring 3.1.3+
- pandas 0.21.1+
- netCDF4 1.3.1+
- pyephem 3.7.6+

Table H.1: Attributes stored in the GDP NetCDF file.

Attribute	Example	Description
Global attributes (.<attribute>)		
Conventions	CF-1.4	The convention followed
title	RS-11G GRUAN Data Product (Version 0.1)	Title of the data product
institution	Tateno, JMA, Japan	Institution where the data file was created
source	RS-11G	Source of measurement data - the instrument
history	–	Sequence of processing steps
references	–	References to publications or documentations, describing the data product.
comment	RS-11G GRUAN Data Product	Description of data product
Category: Product (g.Product.<attribute>)		
		Continued on next page

Table H.1 – continued from previous page

Attribute	Example	Description
ID	160983	Product ID obtained from the GPT file
Code	RS-11G	Code of the data product
Name	RS-11G GRUAN Data Product	Name / title of the data product
Version	1	Version of data product
Level	2	Level of data file
LevelDescription		Description of .Level
History	–	Sequence of processing steps
References	–	References to publications or documentations, describing the data product
Producer	Tateno, JMA, Japan	Institution, where the data file was created
OrgResolution	1 s (time)	
Status	Data_approved	Quality status of data file. Only status Data_approved will be published at NCDC. Possibilities are: Data_approved - best (GRUAN stamp) Data_checked - some small issues Data - several issues Garbage - Do not use this data
StatusDescription	'Data exist, PTU + altitude columns available, all BL tests ok, all uncertainties as expected'	Long description of status
Category: General (g.General.<attribute>)		
FileTypeVersion	0.1	Version of file type definition
Timestamp	2016-01-01T06:00:00	Date and time of file creation
SiteCode	TAT	GRUAN station code
SiteName	Tateno	GRUAN station name
SiteWmoId	47646	WMO number of GRUAN site
SiteInstitution	JMA - Japan Meteorological Agency	Institution of GRUAN site
Category: MeasuringSystem (g. MeasuringSystem.<attribute>)		
ID	TAT-RS-01	Code of measurement system
Latitude	36.06°	Latitude of the measurement system (launch site) [°north]
Longitude	140.13°	Longitude of the measurement system (launch site) [°east]

Continued on next page

Table H.1 – continued from previous page

Attribute	Example	Description
Altitude	27.4 m	Altitude of the measurement system (launch site)
Category: SurfaceObs (g. SurfaceObs.<attribute>)		
Pressure	’1024.20 hPa’	Surface Pressure at launch site
Temperature	10.60°C	Temperature at launch site
RelativeHumidity	73.0 %	Relative Humidity at launch site
Category: Ascent (g. Ascent.<attribute>)		
ID	47989	Ascent ID obtained from GPT file
StandardTime	2015-11-01T00:00:00	Scheduled Time
StartTime	2015-10-31T23:30:15	Launch Time
BalloonNumber	1	Number of balloon (in case several balloons were launched at the same StandardTime)
BalloonType	JMA-B1200	Code of balloon type (codes are defined in the GRUAN meta database -GMDB)
UnwinderType	STRING	Code of unwider type (defined in GMDB)
FillingWeight	2000 g	Weight under the balloon to determine the filling
Payload	85.0 g	Weight of all components attached underneath the balloon
GrossWeight	1285.0 g	Weight of all components (including balloon) to launch
IncludeDescent	no	The descent data included [yes/no]
BurstpointAltitude	’31754.7 m’	Altitude of burstpoint
BurstpointPressure	’9.23 hPa’	Pressure of burstpoint
TropopauseHeight	’12344.3 m’	Altitude of WMO tropopause
TropopauseTemperature	’213.0 K’	Temperature at WMO tropopause
TropopausePressure	’189.9 hPa’	Pressure at WMO tropopause
TropopausePotTemperature	’342.5 K’	Potential temperature at WMO tropopause
PrecipitableWaterColumn	’14.7 kg m^{-2}’	Precipitable water vapor (PWV)
PrecipitableWaterColumnU	1.0 kg m^{-2}	Unit of the precipitable water vapor
Category: Instrument (g. Instrument.<attribute>)		
SerialNumber	’523254’	Serial number of instrument
Type	RS-11G	Identifier of the instrument type (defined in GMDB)
TypeFamily	RS-11G	Identifier of the instrument family (defined in GMDB)
Manufacturer	Meisei	Name of the instrument manufacturer

Continued on next page

Table H.1 – continued from previous page

Attribute	Example	Description
Weight	'85.0 g'	Weight of the instrument
TelemetrySonde	RS-11G	[not relevant] - Code of the instrument family of the used telemetry sonde. This is only relevant for sondes which have no own telemetry (like MTR, CFH)
SoftwareVersion	'2.2.6'	Used version of telemetry/processing software
Comment	'VP_formula: HylandWexler,'	

Table H.2: Variables stored in the GDP NetCDF file. The units of the variables follow the CF-1.4 convention and RS92-GDP described in GRUAN-TD4.

Variable	Unit	Description
time	s	Time in seconds after launch
press	hPa	Air pressure derived from GPS altitude measurement (P_fin)
u_press	hPa	Total uncertainty of the air pressure (u(P))
alt	m	Geometric altitude above sea level calculated from GPS altitude (alt_fin)
u_alt	m	Uncertainty of the geometric altitude (u(alt))
geopot	m	Geopotential height calculated from GPS altitude and latitude (geopot_fin)
lat	deg north	Latitude (lat_0)
lon	deg east	Longitude (lon_0)
temp	K	Air temperature (T_fin)
cor_temp	K	Radiation correction of air temperature (T_cor)
u_temp	K	Total uncertainty of the air temperature composed of both correlated and uncorrelated components (u(T))
u_std_temp	K	Standard uncertainty component of the air temperature (u_std (T))
u_cor_temp	K	Correlated uncertainty component of the air temperature (u_cor (T))
rh	1	Relative humidity over liquid water using Hyland and Wexler formula (U0.01)
cor_rh	1	Correction applied to the relative humidity ((U_fin-U_0)0.01)
u_rh	1	Total absolute uncertainty of the relative humidity composed of both correlated and uncorrelated components (u(U)0.01)
u_std_rh	1	Standard uncertainty component of the relative humidity (u_std (U))
u_cor_rh	1	Correlated uncertainty component of the relative humidity (u_cor (U))
wdir	deg	Wind direction in degrees from north derived from smoothed GPS data (wdir_fin)
u_wdir	deg	Uncertainty of the wind direction (u(wdir))
wspeed	$m\,s^{-1}$	Wind speed derived from smoothed GPS data (wspeed)
u_wspeed	$m\,s^{-1}$	Uncertainty of the wind speed (u(wspeed))
u	$m\,s^{-1}$	Raw zonal wind (u_raw)
v	$m\,s^{-1}$	Raw meridional wind (v_raw)
asc	$m\,s^{-1}$	Ascent rate of radiosonde (asc)
FP	K	Dewpoint/frostpoint temperature (FP)
WVMR	1	Water vapor volume mixing ratio (WVMR)

Table H.3: Variable attributes stored in the GDP NetCDF file. Examples are shown for the case of air temperature (variable name, temp).

Attribute	Example	Description
CF specific variable attributes		
standard_name	air_temperature	Standard name of the field. (compatible with the standard CF-1.4, where applicable)
long_name	Temperature	Name of variable
units	K	SI unit (confirm to CF-1.4)
coordinates	lon lat alt	List of relevant coordinate variables (mostly lon lat alt)
related_columns	'u_cor_temp u_std_temp u_temp'	List of the variables (columns) in this table that is related to this one (e.g. uncertainties)
GRUAN specific variable attributes		
g_column_type	original data	Type of data: original data derived data product total uncertainty standard deviation correlated uncertainty uncorrelated uncertainty resolution correction
g_resolution	3.0s (time)	Cut-off period of smoothing filter
g_format_format	F6.2	[internal use] - Format code (Fortran-like) for output in ASCII files
g_format_type	FLT	[internal use] - Internal code of format type (e.g. FLT for floating-point number)
g_format_nan	nan	[internal use] - Internal format for missing values
g_format_width	6	[internal use] - Width of formatted value
g_processing_flag	raw, spikes removed, individually smoothed, uncertainty calculated, corrected	Description of processing steps that were performed: raw corrected uncertainty calculated individually smoothed GC checks are positive additional GC positive spikes removed
g_source_desc		Unused (variable for compatibility to RS92-GDP)
comment		

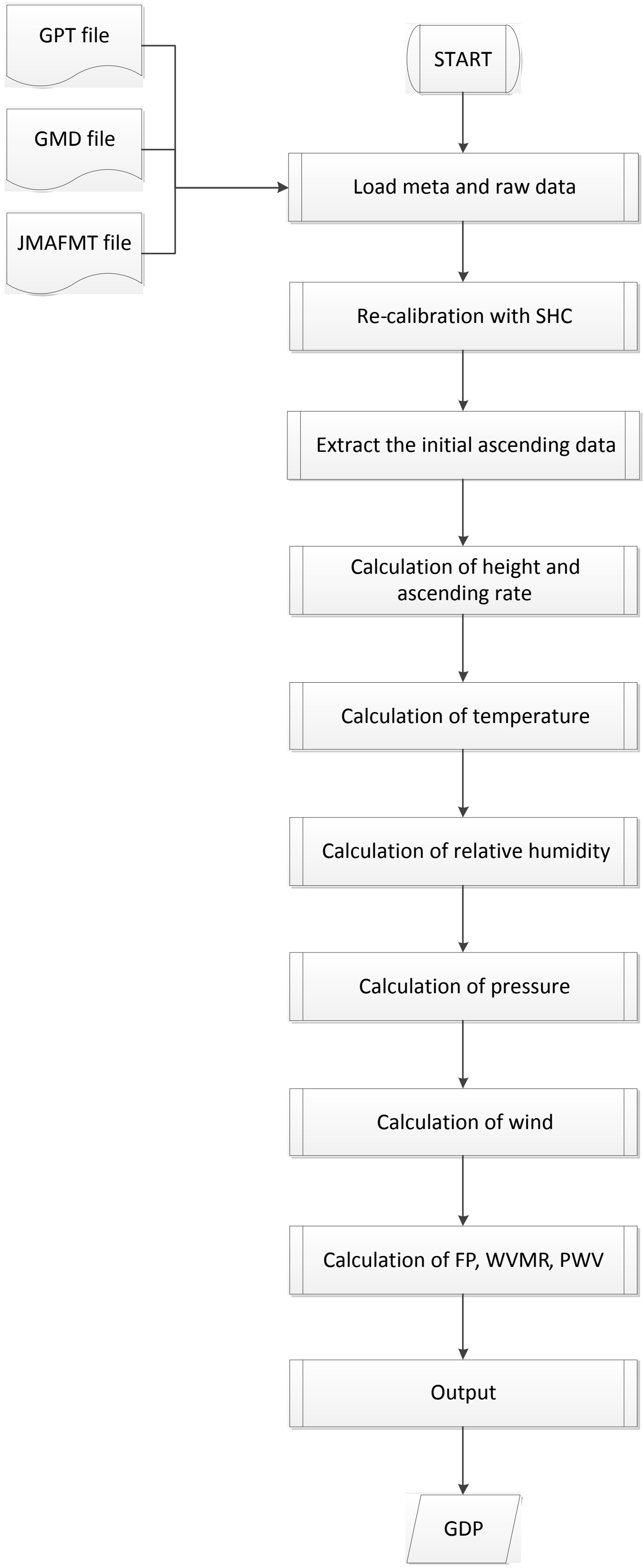

Figure H.1: Overview of the GDP creation workflow.

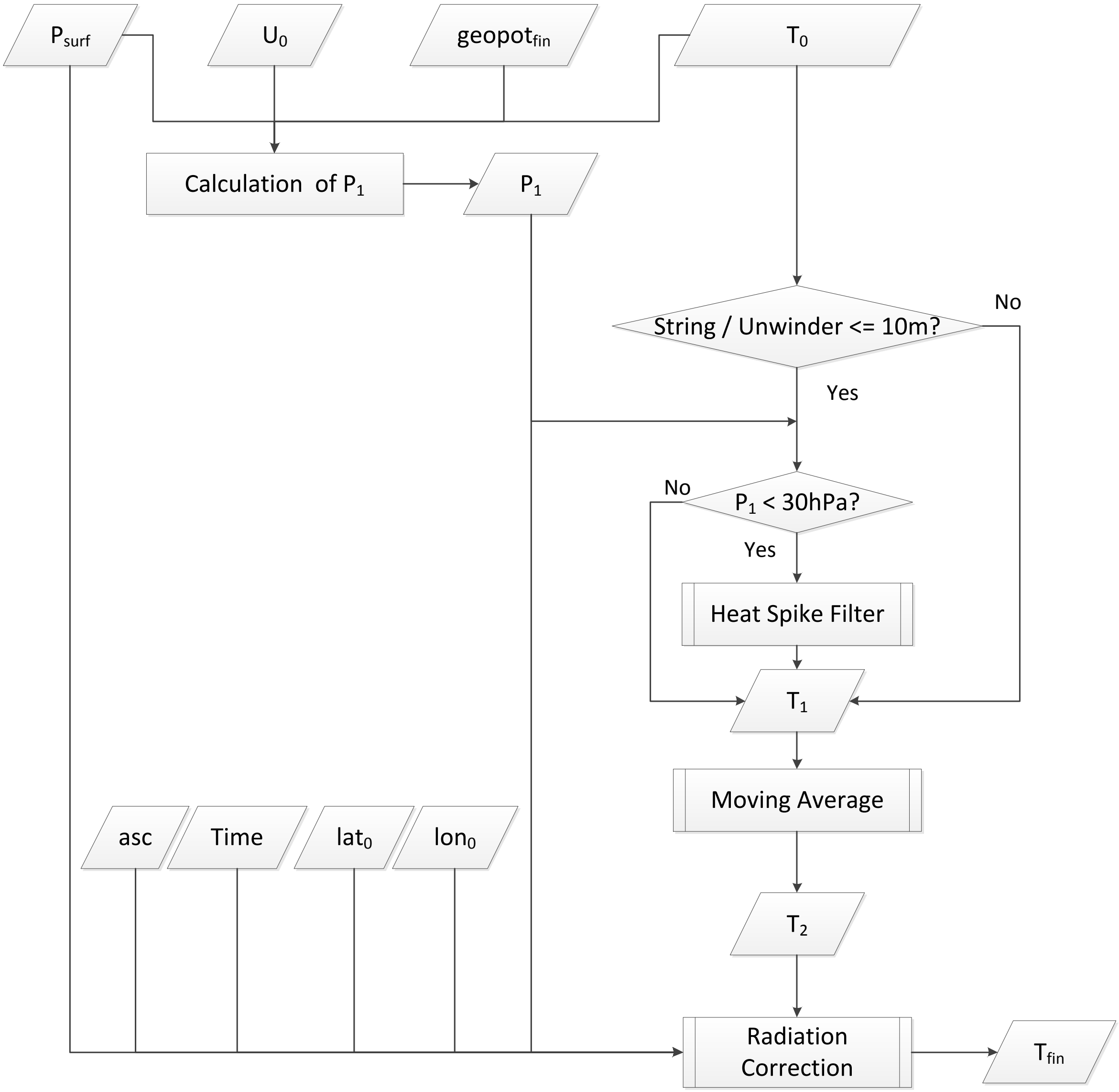

Figure H.2: The workflow to derive T_{fin}.

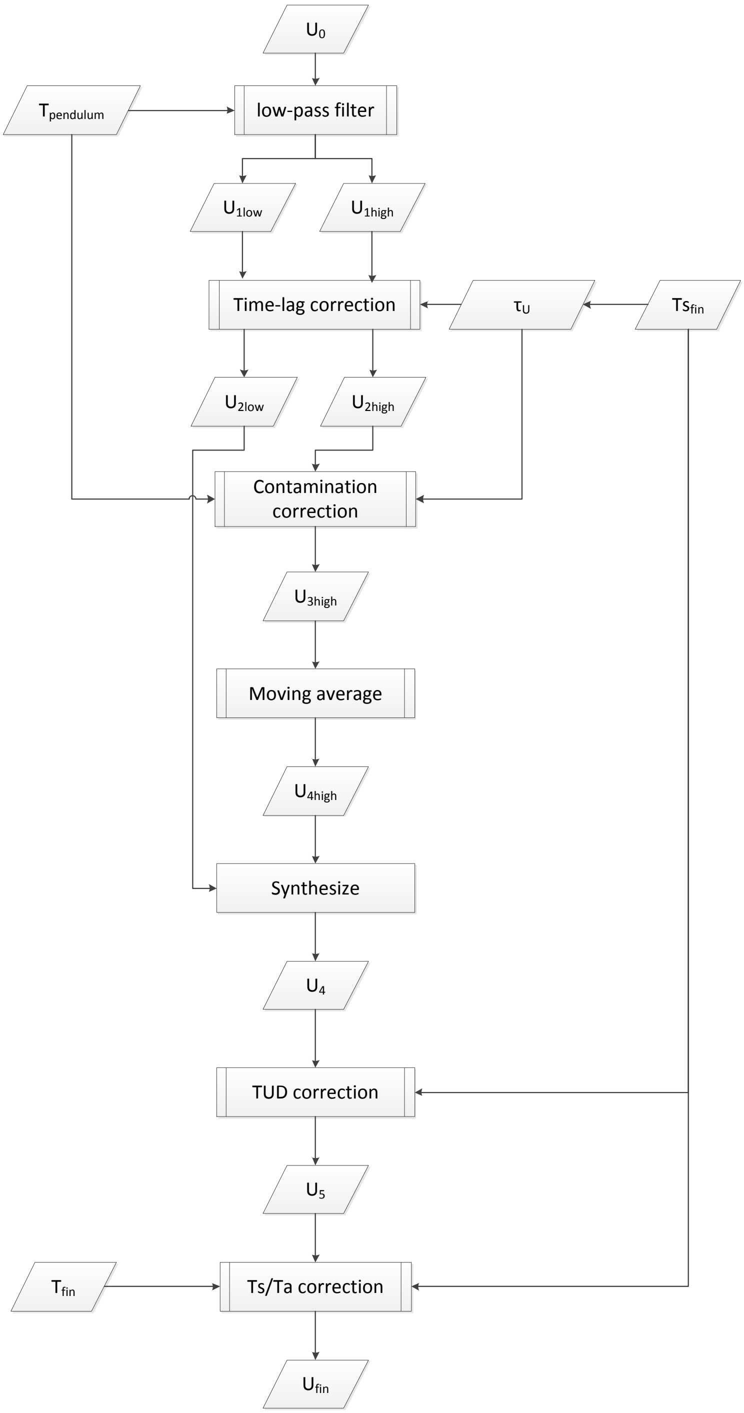

Figure H.3: he workflow to derive U_{fin}.

I Acronym list

BC	Base line check
CFH	Cryogenic Frostpoint Hygrometer
CIMO	WMO Commission for Instruments and Methods of Observation
CMO	Central Meteorological Observatory
DGPS	Differential GPS
FLASH	Fluorescent Advanced Stratospheric Hygrometer
GC	Ground check or Ground checker
GCOS	Global Climate Observing System
GDP	GRUAN Data processing
GNSS	Global Navigation Satellite System
GOS	Global Observing System
GPS	Global Positioning System
GRUAN	GCOS Reference Upper Air Network
GUAN	GCOS Upper Air Network
GUM	Guide to the Expression of Uncertainty in Measurement
ICM	Implementation and Coordination Meeting
IrDA	Infrared Data Association
JMA	Japan Meteorological Agency
JMAFMT	JMA transmission Format
Meisei	Meisei electric co., LTD
MTR	Meisei Temperature Reference (sensor)
NCEI	NOAA National Centers for Environmental Information
NOAA	National Oceanic and Atmospheric Administration
OPC	Optical Particle Counter
PDOP	position dilution of precision (for GPS)
PLL	Phase-Locked Loop
RMS	Root Mean Square
SBAS	Satellite-Based Augmentation System
SHC	Standard Humidity Chamber
TUD	Temperature-hUmidity Dependence
UERE	User Equivalent Range Error
WG GRUAN	Working Group on GRUAN
WMO	World Meteorological Organization

Acknowledgments

We would like to thank Dr. Holger Vömel, Dr. Ruud Dirksen, Dr. Michael Sommer, Ms. Marion Fiedler, and Ms. Tatjana Naebert for their great support when we carried out several laboratory experiments and comparison flights at the GRUAN Lead Centre in the Lindenberg Aerological Observatory, Deutscher Wetterdienst (DWD), Germany.

We also deeply thank the colleagues of the JMA Aerological Observatory at Tateno, Japan and of the Meisei Electoric Co. Ltd. for their cooperation for the laboratory experiments and radiosonde soundings.

We thank Drs. Ruud Dirksen, Christoph von Rohden, Rolf Philipona, and Martial Haefelin as well as Hannu Jauhiainen for reviewing this document, and for their valuable comments and suggestions that contributed to its improvement.

Finally, we thank Dr. Ruud Dirksen for editing the document.

References

Abe, T., The historical changes of upper-air observation and the characteristics of aerological data at Japan Meteorological Agency. Part 1: The historical changes of instruments and methods about upper-air observation, *TENKI*, **62**, 161–185, 2015, in Japanese.

Bodeker, G. E., S. Bojinski, D. Cimini, R. J. Dirksen, M. Haeffelin, J. W. Hannigan, D. F. Hurst, T. Leblanc, F. Madonna, M. Maturilli, A. C. Mikalsen, R. Philipona, T. Reale, D. J. Seidel, D. G. H. Tan, P. W. Thorne, H. Vömel, and J. Wang, Reference upper-air observations for climate: From concept to reality, *Bull. Amer. Meteor. Soc.*, **97**, 123–135, 10.1175/bams-d-14-00072.1, 2016.

Buck, A. L., New equations for computing vapor pressure and enhancement factor, *J. Appl. Meteor.*, **20**, 1527–1532, 1981.

Dirksen, R. J., M. Sommer, F. J. Immler, D. F. Hurst, R. Kivi, and H. Vömel, Reference quality upper-air measurements: GRUAN data processing for the Vaisala RS92 radiosonde, *Atmos. Meas. Tech.*, **7**(12), 4463–4490, 10.5194/amt-7-4463-2014, 2014, URL http://www.atmos-meas-tech.net/7/4463/2014/.

Fujiwara, M., T. Sugidachi, T. Arai, K. Shimizu, M. Hayashi, Y. Noma, H. Kawagita, K. Sagara, T. Nakagawa, S. Okumura, Y. Inai, T. Shibata, S. Iwasaki, and A. Shimizu, Development of a cloud particle sensor for radiosonde sounding, *Atmos. Meas. Tech.*, **9**(12), 5911–5931, 10.5194/amt-9-5911-2016, 2016, URL http://www.atmos-meas-tech.net/9/5911/2016/.

Hayashi, M., Size Distribution of Aerosol in the Stratosphere and Troposphere Observed with Air-Borne 1765 Optical Particle Counter, *Earozoru Kenkyu*, **16**, 118–124, 2001.

Hodge, M. W., Superadiabatic lapse rates of temperature in radiosonde observations, *Monthly Weather Review*, **84**(3), 103–106, http://dx.doi.org/10.1175/1520-0493(1956)084<0103:slroti>2.0.co;2, 1956.

Hyland, R. and A. Wexler, Formulations for the thermodynamic properties of the saturated phases of H_2O from 173.15 K to 473.15 K, *ASHRAE Trans.*, **89**, 500–519, 1983.

Immler, F. J., J. Dykema, T. Gardiner, D. N. Whiteman, P. W. Thorne, and H. Vömel, Reference Quality Upper-Air Measurements: guidance for developing GRUAN data products, *Atmos. Meas. Tech.*, **3**(5), 1217–1231, 10.5194/amt-3-1217-2010, 2010, URL http://www.atmos-meas-tech.net/3/1217/2010/.

Japan Society of Mechanical Engineers (JSME), *Heat transfer* (1975), 3rd edition, in Japanese.

JCGM/WG 1, *Evaluation of measurement data – Guide to the expression of uncertainty in measurement*, International Bureau of Weights and Measures / Bureau International des Poids et Mesures, 2008, URL http://www.bipm.org/utils/common/documents/jcgm/JCGM_100_2008_E.pdf.

JMA, A hundred years memorial magazine of japan meteorological agency, Technical report, Japan Meteorological Agency, 1975, in Japanese.

JMA, Comparison of the Meisei RS2-80 rawinsonde and Meisei RSII-56 rawinsonde, *Meteorological Research Note*, **50**, 373, 1983, in Japanese.

JMA, Guidelines of radiosonde soundings, Technical report, Japan Meteorological Agency, 1995, in Japanese.

JMA, Verification provisions for meteorological instruments, Technical report, Japan Meteorological Agency, 2002, in Japanese.

Kobayashi, E., Result of comparison and verification with RS2-91 Rawinsonde and RS92-DGP GPSsonde, *Kishou Kenkyuu Note*, **229**, 27–36, 2014, in Japanese.

Kobayashi, E., Y. Noto, S. Wakino, H. Yoshii, T. Ohyoshi, S. Saito, and Y. Baba, Comparison of Meisei RS2-91 Rawinsondes and Vaisala RS92-SGP Radiosondes at Tateno for the Data Continuity for Climatic Data Analysis, *Journal of the Meteorological Society of Japan. Ser. II*, **90**(6), 923–945, 10.2151/jmsj.2012-605, 2012a.

Kobayashi, E., H. Yoshii, T. Abe, and Y. Kaneko, Investigation of characteristic of temperature at cloud top and stratosphere in the rainy weather with comparison observation data of RS2-91 Rawinsonde and RS92-SGP GPSsonde, *Journal of the Aerological Observatory*, **70**, 13–22, 2012b, in Japanese.

Kobayashi, K., GPS Wave Reception and Measurement of Position, *KODEN TECH.*, **22**, 1–11, 2006.

Komhyr, W. D., R. A. Barnes, G. B. Brothers, J. A. Lathrop, and D. P. Opperman, Electrochemical concentration cell ozonesonde performance evaluation during STOIC 1989, *J. Geophys. Res.*, **100**(D5), 9231–9244, 10.1029/94JD02175, 1995, ISSN 2156-2202, URL `http://dx.doi.org/10.1029/94JD02175`.

Kuo, F. F. and J. F. Kaiser, *System analysis by digital computer* (John Wiley & Sons, New York, 1966), 438 pp.

Miller, D., *Water at the surface of the Earth* (Academic Press, New York, USA, 1977).

Miloshevich, L. M., A. Paukkunen, H. Vömel, and S. J. Oltmans, Development and Validation of a Time-Lag Correction for Vaisala Radiosonde Humidity Measurements, *J. Atmos. Ocean. Technol.*, **21**(9), 1305–1327, http://dx.doi.org/10.1175/1520-0426(2004)021<1305:DAVOAT>2.0.CO;2, 2004.

Morrissey, J. F. and F. J. Brousaides, Temperature induced errors in the ML-476 humidity data, *J. Appl. Meteor.*, **8**, 805–808, 1970.

Murphy, D. M. and T. Koop, Review of the vapour pressures of ice and supercooled water for atmospheric applications, *Quart. J. Roy. Meteor. Soc.*, **131**, 15391565, 10.1256/qj.04.94, 2005.

Nakamura, K., N. Hayashi, and K. Masuda, The estimation of some error in the RS2-80 temperature measurements. -solar radiation correction-, *Sokko Jiho*, **50**, 117–138, 1983, in Japanese.

Nash, J., T. Oakley, H. Vömel, and L. Wei, WMO Intercomparison of High Quality Radiosonde Systems Yangjiang, China, 12 July – 3 August 2010, Technical report, WMO, 2011, URL `https://www.wmo.int/pages/prog/www/IMOP/publications/IOM-107%_Yangjiang/IOM-107_Yangjiang.zip`, WMO/TD-No. 1580, Instruments And Observing Methods Report No. 107.

NOAA, NASA, and USAF, *US Standard Atmosphere* (US Government printing office, Washington DC, 1976), 241 pp.

Sakoda, Y., K. Naganuma, H. Ogihara, N. Inoue, and A. Mita, RS-91 Rawinsonde, *Kishou Kenkyuu Note*, **194**, 3–24, 1999, in Japanese.

Savitzky, A. and M. J. E. Golay, Smoothing and differentiation of data by simplified least squares procedures, *Anal. Chem.*, **36**, 16271639, 10.1021/ac60214a047, 1964.

Seidel, D. J., F. H. Berger, F. Immler, M. Sommer, H. Vömel, H. J. Diamond, J. Dykema, D. Goodrich, W. Murray, T. Peterson, D. Sisterson, P. Thorne, and J. Wang, Reference upper-air observations for climate: Rationale, progress, and plans, *Bull. Amer. Meteor. Soc.*, **90**(3), 361–369, 10.1175/2008bams2540.1, 2009.

Shimizu, K., T. Asanuma, K. Yamaguchi, and K. Yoshikawa, Upgraded thermistor for unbiased measurements evaluation of new gps radiosonde rs-06g, *IOM 97, Papers presented at the WMO technical Conference on Instruments and Methods of observation (TECO 2008)*, 2008.

Shimizu, K. and F. Hasebe, Fast-response high-resolution temperature sonde aimed at contamination-free profile observations, *Atmos. Meas. Tech.*, **3**(6), 1673–1681, 10.5194/amt-3-1673-2010, 2010.

Sommer, M., GRUAN Technical document 3 - User Guide of GRUAN RsLaunchClient, Technical report, GRUAN Lead Centre, Lindenberg, 2014, version 1.0.

Sugidachi, T. and M. Fujiwara, Correction of the Stepwise Change Observed at 0°C in Meisei RS2-91, RS-01G, and RS-06G Radiosonde Relative Humidity Profiles, *Journal of the Meteorological Society of Japan. Ser. II*, **91**(3), 323–336, 10.2151/jmsj.2013-306, 2013.

Tateno Aerological Observatory, Intercomparison and verification of the Meisei RS2-91 rawinsonde and Vaisala RS92-SGP, *Sokko Jiho*, **50**, 373–384, 2011, in Japanese.

Uesato, I., T. Ito, M. Kumamoto, R. Shigebayashi, and M. Nakamura, Temperature trend considering histrical changes of radiosonde (part 1), *Journal of the Aerological Observatory*, **68**, 15–22, 2008, in Japanese.

Vömel, H., D. E. David, and K. Smith, Accuracy of tropospheric and stratospheric water vapor measurements by the cryogenic frost point hygrometer: Instrumental details and observations, *J. of Geophys. Res. Atmos.*, **112**(D8), D08,305, 10.1029/2006jd007224, 2007.

Vömel, H., T. Naebert, R. Dirksen, and M. Sommer, An update on the uncertainties of water vapor measurements using cryogenic frost point hygrometers, *Atmos. Meas. Tech.*, **9**(8), 3755–3768, 10.5194/amt-9-3755-2016, 2016, URL `http://www.atmos-meas-tech.net/9/3755/2016/`.

Williams, S. L. and D. T. Acheson, Thermal time constants of u. s radiosonde sensors used in gate, *NOAA Tech. Memo. EDS CEDDA-7*, 1976, (Available from U. S. Govt. Printing Office, Washington, DC 20402.).

WMO, *Guide to Meteorological Instruments and Methods of Observation*, World Meteorological Organization, Geneva, 7th edition, 2008, URL `http://library.wmo.int/pmb_ged/wmo_8_en-2012.pdf`, [Accessed 3 December 2014].

Yushkov, V., V. Astakhov, and S. Merkulov, Optical balloon hygrometer for upper-troposphere and stratosphere water vapor measurements, in J. Wang, B. Wu, T. Ogawa, and Z.-H. Guan, eds., *Optical Remote Sensing of the Atmosphere and Clouds*, *Proc. Soc. Photo-Opt. Instrum. Eng.*, volume 3501, pp. 439–445 (1998), 10.1117/12.317759.